Advanced transmission electron microscopy studies of semiconductor nanocrystals synthesized by colloidal methods

Fabio Agnese

Communauté UNIVERSITÉ Grenoble Alpes

THÈSE

Pour obtenir le grade de

DOCTEUR DE LA COMMUNAUTÉ UNIVERSITÉ GRENOBLE ALPES

Spécialité : NANOPHYSIQUE

Arrêté ministériel : 25 mai 2016

Présentée par

Fabio AGNESE

Thèse dirigée par **Jean luc ROUVIERE**, CEA
et codirigée par **Frédéric (phy) CHANDEZON**, CEA
préparée au sein du **Laboratoire Modélisation et Exploration des Matériaux**
dans **l'École Doctorale Physique**

Etudes par microscopie électronique en transmission avancée de nanocristaux semiconducteur synthétisé par méthodes colloïdaux

Advanced Transmission Electron Microscopy Studies of Semiconductor Nanocrystals Synthesized by Colloidal Methods

Thèse soutenue publiquement le **16 octobre 2018**,
devant le jury composé de :

Monsieur NICOLAS LEQUEUX
PROFESSEUR, ESPCI - PARIS, Rapporteur
Monsieur NICOLAS MENGUY
PROFESSEUR, SORBONNE UNIVERSITES - PARIS, Rapporteur
Madame EIRINI SARIGIANNIDOU
MAITRE DE CONFERENCES, GRENOBLE INP, Examinateur
Monsieur ALAIN IBANEZ
DIRECTEUR DE RECHERCHE, CNRS DELEGATION ALPES, Président

Abstract

The rapid progress in semiconductor nanocrystal synthesis that enables the design of materials down to the nanoscale also demands the development of characterisation techniques able to analyse the materials down to the same scale, such as transmission electron microscopy (TEM). In this thesis, we apply a variety of advanced microscopy techniques to unravel the morphology, crystal structure and chemical composition of the state-of-the-art nanocrystal materials.

The first part of the work deals with the optimisation of the synthesis and sample preparation for high-resolution (HR)TEM. The ligands bound to the surface of the nanocrystals pose issues for the observation by TEM. Conventional cleaning methods are found insufficient. After literature review from different scientific areas, acetic acid was found to be suitable in the purification procedure as an effective antisolvent. Ligands and residual contamination on the sample are revealed when graphene is used as a sample support in TEM. The second part of the thesis provides new contributions on the characterisation of two promising materials: Cu_2ZnSnS_4 (CZTS) and $CsPbBr_3$ NCs. Firstly, a previously described synthesis procedure for CZTS NCs is examined step by step. During the synthesis of multinary products, different secondary phases tend to form in the initial reaction stages due to the difference in the reactivity of the cationic precursors. Morphology and stoichiometry of the samples extracted at different time intervals are characterised by HRTEM and chemical mapping by electron dispersive X-ray spectroscopy (EDS). These observations are compared with synchrotron Small-Angle X-ray Scattering (SAXS) and Wide-Angle X-ray Scattering (WAXS) techniques. Subsequently, a growth mechanism is proposed. Next, crystal structure of CZTS is determined by two complementary methods: Nanobeam Precession Electron Diffraction (NPED) and High-Resolution Scanning Transmission Electron Microscopy by High Angle Annular Dark-Field Imaging (HRSTEM-HAADF). We show that the nanoparticles are constituted of subdomains with different cation ordering. In particular, the metastable PMCA structure is identified in this material for the first time.

Secondly, we apply TEM techniques to investigate the crystal structure of $CsPbBr_3$ NCs. Previous reports based on benchtop X-ray diffraction are conflicting as to whether the correct crystal structure of $CsPbBr_3$ NCs is cubic or orthorhombic. Our approach compares STEM-HAADF experimental images with simulations. The influence of different STEM detectors on the visualisation of the tilting of the octahedra is explored. Precision is enhanced with the acquisition of image stacks. These strategies suggest an

orthorhombic phase.

Resumé

Les recherches sur les nanocristaux semiconducteur (NCs) ont conduit à des résultats scientifiques fascinants, spécialement pour l'application en dispositifs optoelectroniques. Afin de répondre à certaines exigences comme des coûts mineurs, des gains d'efficacité et l'utilisation des composants respectueux de l'environnement, des nouvelles méthodes sont explorées : dans les procédés en solution, dans l'ingénierie de bande et des niveaux d'énergie. En particulier, la méthode de synthèse peut influencer les propriétés optoélectroniques. Par conséquent, une meilleure compréhension des facteurs complexes pendant la synthèse entraînera une amélioration considérable des performances. La microscopie électronique avancée fournit un moyen précis de recueillir des informations sur la morphologie, la structure cristalline et la composition chimique des matériaux avec une résolution spatiale au niveau atomique. La première partie de cette thèse traite de la synthèse et de la préparation des échantillons pour la microscopie électronique à transmission en haute résolution (HRTEM). La deuxième partie traite du mécanisme de croissance des NCs Cu_2ZnSnS_4 synthétisés par une méthode colloïdale. La morphologie et la stoechiométrie des intermédiaires de réaction extraits après différents intervalles de temps sont déterminés par HRTEM et analyse dispersive de rayons X en énergie (EDS). Deux méthodes complémentaires, la diffraction par nanofaisceau d'électrons en précession (NPED) et la microscope électronique en transmission par balayage à haute résolution avec imagerie en champ sombre avec détecteur annulaire à grand angle (HRSTEM-HAADF) permettent une profonde caractérisation de la structure cristalline. En outre, la structure cristalline de NCs $CsPbBr_3$ est résolue avec comparaison entre images expérimentales et simulations de STEM-HAADF. Cet approche peut différencier entre structures cristallines cubiques et orthorhombiques, difficile avec techniques de diffraction traditionnelles.

Contents

List of abbreviations **10**

Preface **13**
Thesis timeline . . . 13

1 Introductory chapter **17**
1.1 Introduction and objectives . . . 17
1.2 Semiconductor colloidal nanocrystals . . . 19
1.2.1 Ternary and quaternary NCs . . . 23
1.2.2 Cu_2ZnSnS_4 . . . 24
1.2.3 $CsPbBr_3$ . . . 27
1.2.4 $CuFeS_2$ . . . 29
1.3 Transmission Electron Microscopy . . . 30
1.3.1 Interaction of the electron beam with the specimen . . . 30
1.3.2 Imaging modes . . . 30
1.3.3 Multislice simulations . . . 33
1.3.4 Energy Dispersive X-ray Spectroscopy (EDS) . . . 35
1.3.5 Electron Energy Loss Spectroscopy (EELS) . . . 41
1.3.6 Nanobeam Precession Electron Diffraction (NPED) . . . 41

2 Preparation of colloidal nanocrystals for TEM observations **45**
2.1 Introduction . . . 45
2.2 Standard colloidal NC deposition methods in TEM . . . 46
2.3 Purification procedures . . . 48
2.3.1 Solvent-antisolvent and centrifugation cycles . . . 48
2.3.2 Heating the sample . . . 48
2.3.3 Plasma cleaning . . . 49
2.3.4 Cooling . . . 50
2.3.5 Beam showering . . . 50
2.4 Innovative purification strategies . . . 51
2.4.1 Fast thermal annealing on semiconductor NCs . . . 51
2.4.2 Purification of Cu_2ZnSnS_4 NCs by acetic acid . . . 56
2.5 Graphene as a sample support for TEM . . . 59

2.5.1 Preparation of graphene . . . 61
2.5.2 Ultrathin amorphous carbon vs graphene film . . . 61
2.5.3 Monochromated HRTEM imaging of nanomaterials supported on graphene . . . 64
2.5.4 Accelerating voltage on graphene . . . 66
2.6 Conclusion . . . 67

3 Investigation of the growth mechanism and structural characterization of Cu_2ZnSnS_4 colloidal nanocrystals 68
3.1 Introduction . . . 68
3.2 Overview of colloidal synthesis methods for Cu_2ZnSnS_4 nanocrystals . . . 70
3.3 Synthesis and sample preparation . . . 71
3.4 STEM-EDS analysis . . . 76
3.4.1 Experimental methods . . . 76
3.4.2 Summary . . . 99
3.5 Crystal growth mechanism . . . 100
3.6 Structural characterisation of Cu_2ZnSnS_4 colloidal NCs . . . 104
3.7 Sample preparation for structural characterization . . . 108
3.8 Nanobeam Precession Electron Diffraction . . . 108
3.8.1 Influence of stoichiometry on the lattice parameters . . . 108
3.8.2 Acquisition parameters for NPED . . . 111
3.8.3 Template matching strategy . . . 112
3.8.4 Imaging procedure . . . 113
3.8.5 Filtering and digital imaging strategies . . . 113
3.9 Experimental structure determination by HRSTEM . . . 120
3.9.1 Multislice simulations . . . 120
3.9.2 Comparison of simulations from different structures: $\langle 1\,0\,0 \rangle$ direction 121
3.9.3 Comparison of simulations from different structures: $\langle 2\,2\,1 \rangle$ or $\langle 1\,1\,1 \rangle$ direction . . . 123
3.9.4 STEM-HAADF images . . . 125
3.10 Conclusion . . . 131

4 Morphology and structural characterisation of $CsPbBr_3$ nanocrystals 133
4.1 Introduction . . . 133
4.2 $CsPbBr_3$ sample preparation . . . 134
4.3 Cubic and orthorhombic $CsPbBr_3$ structures . . . 136
4.4 Structural analyses of $CsPbBr_3$ nanocrystals in the literature . . . 142
4.5 Experimental results and analysis . . . 145
4.5.1 Standard HRTEM . . . 145
4.5.2 C_s-corrected HRTEM . . . 152
4.5.3 HRSTEM . . . 154
4.5.4 STEM simulations . . . 161
4.5.5 SAED . . . 163
4.5.6 STEM-EDS . . . 165

4.5.7 X-ray powder diffraction . . . 167
4.6 Conclusion . . . 169

5 Conclusions and perspectives 170
5.1 Conclusions . . . 170
5.2 Perspectives . . . 173

A Synchrotron and laboratory WAXS and SAXS studies for CZTS NC growth 176
A.1 Experimental methods . . . 176
A.2 *In situ* synchrotron WAXS and SAXS . . . 177
A.3 *Ex situ* laboratory WAXS and SAXS . . . 181
A.3.1 First stage: 110 °C pre-heating of the precursors in oleylamine . . . 181
A.3.2 Following stages: 280 °C heating . . . 182

B Selection of X-ray techniques: nanocrystals growth studied by *in situ* methods 185

C Surface science of NCs 187
C.1 Structure and bonding at the inorganic-organic interface . . . 187
C.2 Characterisation of the nanocrystal surface . . . 189
C.3 Effect of ligands on the electronic structure . . . 190
C.4 Ligands for synthesis, ligands for applications . . . 191

D Inspiring ligand removal methods in literature 193
D.1 Fast thermal annealing . . . 193
D.2 Purification by acetic acid . . . 194
D.2.1 Surface treatment by acetic acid on $CuInS_2$ NCs . . . 194
D.2.2 Ligand exchange in PbS:P3HT . . . 195

E Examples of clean graphene as sample support for other classes of materials 197

F STEM-EELS 198

G Additional STEM-EDS acquisitions in CZTS synthesis 200

H Additional STEM-HAADF simulations 206

I Perovskite structure 208
I.1 FFTs from single NCs from HRTEM micrographs . . . 210
I.2 Structure factors from cubic and orthorhombic $CsPbBr_3$ . . . 214

J Morphology and structural characterisation of $CuFeS_2$ nanocrystals and composite pellets **219**
J.1 Introduction . . . 219
J.2 Synthesis and sample preparation . . . 221
J.2.1 Heat-up method . . . 221
J.2.2 Hot-injection method . . . 222
J.2.3 Purification . . . 223
J.3 Morphology analysis of $CuFeS_2$ NCs by TEM . . . 223
J.4 Structural analysis of $CuFeS_2$ nanocrystals by TEM . . . 224
J.4.1 Rotational average of FFT from several randomly oriented hot-injection NCs . . . 225
J.4.2 Modeling of hot-injection $CuFeS_2$ platelets . . . 225
J.5 Nanocomposite materials . . . 228
J.5.1 Fabrication of composite $CuFeS_2$/Sn pellet . . . 228
J.5.2 STEM-EDS of the pellet . . . 228
J.6 Conclusion . . . 232

List of Figures **233**

List of Tables **240**

Bibliography **242**

Publications and communications **263**

List of abbreviations

Abbreviations	
NC	NanoCrystal
QD	Quantum Dot
CEA	Alternative Energies and Atomic Energy Commission
DRF	Direction de la Recherche Fondamentale
INAC	Institute for NAnoscience and Cryogenics
MEM	Modeling and Exploration of Materials
LEMMA	Laboratoire d'Etude des Matériaux par Microscopie Avancée
SyMMES	SYstèmes Moléculaires et nanoMatériaux pour l'Energie et la Santé
NREL	National Renewable Energy Laboratory
UCA	University of Cadiz
TEM	Transmission Electron Microscope
HR	High Resolution
EFTEM	Energy Filtered TEM
EDS	Energy Dispersive X-ray Spectroscopy
EELS	Electron Energy Loss Spectroscopy
ED	Electron Diffraction
SA(E)D	Selected Area (Electron) Diffraction
(N)PED	(Nanobeam) Precession Electron Diffraction
(LA)CBED	(Large Angle) Convergent Beam Electron Diffraction
STEM	Scanning Transmission Electron Microscope
HAADF	High Angle Annular Dark Field
ADF	Annular Dark Field
BF	Bright Field
DF	Dark Field
IBF	Incoherent Bright Field
SEM	Scanning Electron Microscope
XRD	X-Ray Diffraction
SC	Single Crystal
PDF	Pair Distribution Function
(U)SAXS	(Ultra) Small Angle X-ray Scattering

Abbreviations

WAXS	Wide Angle X-ray Scattering
DLS	Dynamic Light Scattering
UV-vis	UltraViolet visible
FTIR	Fourier Transfrom InfraRed
TGA	ThermoGravimetric Analysis
DSC	Differential Scanning Calorimetry
ICP-OES	Inductively Coupled Plasma - Optical Emission Spectrometry
NMR	Nuclear Magnetic Resonance
JEMS	Java Electron Miscroscopy Software, written by P. Stadelmann
DP	Diffraction Pattern
FEG	Field Emission Gun
CCD	Charge Coupled Device
SDD	Silicon Drift Detector
FT	Fourier Transform
FFT	Fast Fourier Transform
SDSD	Statistically Determined Spacial Drift
SQ	Shockley and Queisser
HOMO	Highest Occupied Molecular Orbital
LUMO	Lowest Unoccupied Molecular Orbital
V_{OC}	Open-circuit voltage
BG	Band Gap
EQE	External Quantum Efficiency
QDSSC	Quantum Dot Sensitized Solar Cell
DSSC	Dye-Sensitized Solar Cell
DFT	Density Functional Theory
MD	Molecular Dynamics
TDS	Thermal Diffusion Scattering
σ	bonding orbital
σ^*	antibonding orbital
KS	Kesterite
ST	Stannite
PMCA	Pre-Mixed Cu-Au
η	tetragonal distortion parameter (or efficiency)
ZT	figure of limit
σ	electrical conductivity
S	Seebeck coefficient
κ	thermal conductivity
CVD	Chemical Vapour Deposition

Abbreviations

CZTS	Copper Zinc Tin Sulfide
CIGS	Copper Indium Gallium Selenide
HAc	Acetic Acid
MeOH	Methanol
TOPO	Tri-n-OctylPhosphine Oxide
OA	Oleic Acid
DDT	1-DoDecaneThiol
PMMA	PolyMethyl MethAcrylate
P3HT	Poly(3-HexylThiophene)
PEDOT	Poly(3,4-EthyleneDiOxyThiophene)
PSS	PolyStyrene Sulfonate
ODE	OctaDEcene
OLA	OleyLAmine
DNA	DeoxyriboNucleic Acid

λ	wavelength
ψ	wave function
Z	atomic number
C	weight percentage
k_{AB}	Cliff-Lorimer factor
I	Intensity (X-ray)
i	beam current
ρ	mass thickness
t	Thickness
ζ- factor	zeta-factor
N_0	Avogadro's number
SNR	Signal-to-Noise Ratio
$Q(i)$	image correlation index
$P(x, y)$	experimental diffraction pattern
$T(x, y)$	simulated template
d	lattice spacing
R	Reliability
CTF, $T(k)$	Contrast Transfer Function
C_s	spherical aberration
k	spatial frequency
Δf_s	Scherzer Defocus
Δx	point resolution
F_{hkl}	structure factor
$S(Q)$	normalized total structure factor
DOSY	Diffusion-Ordered SpectroscopY
D	Diffusion coefficient

Table 1 – Abbreviations

Preface

This thesis was financed by Ecole Doctorale for Physics in Grenoble Alpes University and performed between October 2013 and October 2018 in French Alternative Energies and Atomic Energy Commission (CEA) centre in Grenoble. The whole project took place in the DRF/INAC/MEM/LEMMA laboratory.

The goal of the project is to apply advanced microscopy techniques to the field of semiconductor nanocrystals which have applications in photovoltaics, thermoelectrics and medical field. Electron microscopy allows the direct visualisation of atomic positions and morphology of the single nanocrystals, as well as chemical information (mainly from spectroscopic techniques).

The inspiration for this project originates from the collaboration of two laboratories from CEA Grenoble. LEMMA group is an advanced microscopy group, mainly involved in the characterisation of materials and nanostructures at a sub-nanometer scale. The investigation of nanomaterials requires the development of new characterisation tools: for that purpose, LEMMA not only develops and optimise new microscopy techniques to give information on the structural and chemical properties with the better resolution but also to probe other physical properties of the materials.

All the samples presented in this thesis are synthesised in SyMMES laboratory in CEA Grenoble. Research in the domain of photovoltaics (organic, nanocrystals, hybrid) is developed in SyMMES, with particular attention in the synthesis of new nanomaterials and the optimisation of performance for application in devices.

Thesis timeline

A summary of the progress of the thesis from the first year to the final is given in the following.

The goal of the first year has been to master the HRTEM and HRSTEM techniques with aberration-corrected microscopes; in parallel, an examination of the most promising semiconductor NCs has been done to focus on the key points concerning the structure, the properties and the growth mechanisms. We obtained significant results on Cu_2ZnSnS_4 [1] and $CuFeS_2$ NCs. The PMCA structure was observed for the first time in Cu_2ZnSnS_4 NCs by STEM-HAADF. Nevertheless, the results were hardly reproducible, as the contamination of the sample made the observations very difficult. In the meanwhile, we have studied other samples, but the advanced characterisation was

not possible due to contamination problems. In particular, core/shell, core/shell/shell and alloyed InP samples were synthesised (main doping elements: Zn, Sn, As, structures: InPZnS@ZnSe/ZnS). These syntheses provided a great framework for elemental quantification in such nanostructures, but the tiny size ($< 4\,\mathrm{nm}$) and the contamination made such a characterisation impossible. TEM analysis was therefore limited to size distribution [2]. Later on, the same InPZnS@ZnSe/ZnS NCs were functionalised with fragmented antibodies for medical applications [3]; the comparison between the size of the semiconductor part (measured by TEM), and the values of the hydrodynamic radius as obtained by dynamic light scattering (DLS), was necessary to create the fragmented antibody-quantum dot conjugates among the smallest antibody functionalized nanoprobes ever reported.

In the second year, the goal was to apply advanced microscopy to fully retrieve the atomic positions in CZTS NCs. Chemical mapping at 2D atomic resolution had been previously demonstrated by Trasobares on Ce-Zr mixed oxide nanocrystals, combining HAADF and experimental and simulated EELS mapping [4]. We aimed to extend the applicability of the technique to discriminate the positions of the isoelectronic Cu and Zn cations. In particular, the presence of a monochromator in our EELS apparatus would theoretically allow the analysis of the oxidation state of the cations. However, the unsolved contamination issue once again interfered with the analysis. The reason why Trasobares managed to obtain chemical mapping at 2D atomic resolution is probably that the oxides materials support the radiation and the heating treatments better than the chalcogenide CZTS NCs. In our case, since the traditional purification methods were found insufficient, atomic resolution EELS was unsuccessful. It was clear that spectroscopy from STEM was particularly affected by this phenomenon when focusing on core-loss EELS. To acquire a high signal, the energy window has to extend up to 900-1000 eV energy loss. On the one hand, the exposure time needs to be in the order of hundreds of milliseconds and in this case, significant radiation damage is induced inside the nanocrystal (creation of great holes and no signal). On the other hand, if the exposure time is kept low to avoid NC destruction, the signal is extremely low and no significant signal can be extracted, even by using modern PCA (principal component analysis) and ICA (independent component analysis) deconvolution processes. HRTEM was found to be less impacted by ligand contamination, as the beam is spread over a large area and total dose can be reduced. The availability of an aberration-corrected and monochromated HRTEM led us to test focal series reconstruction using the FEI software TrueImage. Coene and Thust [5, 6] developed a software to reconstruct the complex-valued electron wave at the exit plane of the specimen including correction for the aberrations of the microscope, with a focal series of HRTEM images as input. This routine was developed before the conception of aberration-corrected microscopes; for us, it was interesting to understand how these routines work and their applicability with an AC-TEM, with the precise measure of the residual aberrations as measured from the monochromator program routine. More recently, Van Dyck [7] presented an electron tomography method to determine, from only one viewing direction and with sub-Å precision, the position of individual atoms in the plane of observation and their

vertical position. Our laboratory was interested in understanding and developing this technique. In principle, the focal series were acquired on graphene: we planned to start from a "simple" 2D material to understand the principles and to later extend over the 3D reconstruction of a NC. Unfortunately, it was found that minimal variations in the input aberration values gave non-physical and multiple solutions for the wave function at the exit of the sample. Simulations also confirmed this fact. Therefore, the activity was not continued further on complex systems. This part of the study is not presented in this manuscript.

A change in the strategy started at the beginning of the third year, with the research on innovative methods for sample purification, and on the use of graphene as a sample support layer. We extended the bibliographic research to other research fields, such as catalysis and surface science. The use of graphene improved the contrast and allowed to visualise the organic components which remain after purification. Therefore, it was easier to observe the effect of the novel purification procedure less empirically. Solving the contamination issue was challenging, but necessary. In the remaining half of the third year, we decided to focus on a few crucial samples: in particular, CZTS needed complementary information to clarify the whole picture. The arrival of the FEI Themis microscope with a SuperX detector system allowed us to perform a *ex situ* STEM-EDS study on the nucleation and growth during synthesis of CZTS NCs, which was complementary to the WAXS and SAXS study performed earlier in ESRF synchrotron facility. The new dedicated FEI system and the laboratory expertise on nano-beam electron diffraction techniques allowed a broader investigation of the crystalline structure by NPED, thanks to the precessing cone illumination, even on such small crystals. We applied NPED coupled with template matching to identify kesterite, stannite and PMCA structures in CZTS NCs. In our laboratory, Brunetti previously applied a similar template-matching strategy to lithium battery materials. They distinguished between $LiFePO_4$ and $FePO_4$ phase mapping at the nanometer-scale level on a large number of particles of sizes between 50 and 300 nm in a partially charged cathode [8]. Nowadays, the NPED system better controls the probe aberrations, precession and convergence angle can be finely tuned, and a smaller aperture is available. We confidently applied the same strategy with a better spatial resolution for nanocrystals which are considerably smaller (and thinner). We adapted his strategy to discriminate very similar structures, which possess a minimal lattice mismatch.

Moreover, other exciting samples were characterised. During the three years, we also studied $CuFeS_2$ NCs by TEM and HRTEM to provide complementary structural information. These NCs, which are interesting for their thermoelectric properties, were synthesised and investigated by Louis Vaure during his PhD in LEMOH [9]. At the end of his project, he prepared a composite $CuFeS_2$-Sn: the information from our exploratory observation by STEM-EDS provided the first model to understand how the thermoelectric properties of the composite improved with respect to pure $CuFeS_2$ pellets. Perovskite $CsPbBr_3$ NCs soon became a promising material for solar cell applications. They were synthesised and investigated by Mathilde Bouchard during her PhD in CEA (in progress). As an advanced microscopy laboratory, we took an interest in the detection

of the tilt of the $PbBr_6$ octahedra. Nevertheless, the sample is sensible to the electron beam and undergoes structural modifications for long beam exposure. A more detailed diffraction study was not possible, as the sample destroyed before the forecast observation by NPED, and there was no time for preparing a new sample. This is currently a debated open question.

In parallel to the research activity in the laboratory, I had the opportunity to teach at the Grenoble Institute of Technology (INP Grenoble). In particular, I lectured during my second and third year of the PhD, for a total of 128 hours. I taught material science for future engineers in Physics Materials Processes and in Physics Electronics Telecommunications. Moreover, I had the chance of supervising two Long Term Practical Work with two small groups of international students from the "Functionalized Advanced Materials Engineering" master. During this time, I had the chance of being formed by the doctoral school in the framework of the "Label RES" to improve the skills of a teacher. I hope I will have the possibility to work as a teacher in the future.

Chapter 1

Introductory chapter

1.1 Introduction and objectives

Many of the environmental problems the world faces today, including climate change, air pollution and oil spills, result from our dependence on fossil fuels. The burning of fossil fuels produces greenhouse gases that are the main cause of the ongoing rise in global atmospheric temperatures. In the meantime, the research on renewable energy sources has been flourishing. Clean energy investment brakes new records and is now seeing twice as much global funding as fossil fuels. The majority of solar cells fabricated to date have been based on silicon because of its high stability and abundance. However, crystalline silicon does not absorb sunlight as efficiently as some other materials do, since it is an indirect band gap semiconductor. Besides, silicon is expensive to purify, and it requires a large thickness due to its indirect band gap of 1.1 eV [10]. Therefore, new technologies which are based on thin layers of direct band gap materials represent an alternative. However, the scarcity of materials used in these thin layers (e.g. indium, gallium, tellurium) seems to overwhelm this solution before its industrial deployment. It is therefore essential to find suitable materials for the replacement of silicon that are abundant, non-toxic and efficient in absorbing solar radiation.

Concerning material choice, a wide range of semiconductor nanocrystals (NCs) have so far been studied. Especially, colloidal semiconductor NCs have attracted significant interest since their discovery about three decades ago [11–13]. Among the most studied NCs, the binary II-VI and III-V compounds of MX, where M^{2+} = Cd, Hg, Pb (all toxic elements) and X^{2-} = S, Se, Te, take the lead in the research for electronic, optoelectronic and photovoltaic applications. However, the interests have shifted towards toxic element-free and more abundant binary ($Cu_{2-x}S(Se)$), ternary ($CuInS_2$, $CuFeS_2$, $CsPbBr_3$) and quaternary (Cu_2ZnSnS_4, $Cu_2ZnSnSe_4$, $Ag_2ZnSnSe_4$) compounds. One of the advantages of using ternary/quaternary compounds is the flexible combination of a range of elements to tune the energy band gap and control other material parameters.

It has been shown that the optical and electrical properties of these nano-scaled NCs could be tailored with size, composition, shape and surface state [14]. Consequently, numerous studies focused on the development of chemical synthesis methods, to obtain NCs

of precisely controlled dimensions, shape and composition. Syntheses of colloidal semiconductor NCs by wet-chemical methods are valid alternatives to traditional physical deposition techniques. As compared to the bulk materials, the ternary and quaternary semiconductor NCs provide several distinct advantages, such as tuning the band gap and electronic energy levels by merely changing the size. They also provide excellent control of the composition and internal structure before materials' processing. Moreover, they can be deposited on various substrates without the need for high-cost vacuum deposition techniques [15].

One of the challenges during the synthesis of the ternary and quaternary NCs is the control of their composition and crystal structure: they tend to form different compositional phases in the initial reaction stages due to the difference in the reactivity of the cationic precursors. By understanding the growth mechanism, it should be possible to identify the crucial steps during nucleation and crystal growth and predict modifications to growth conditions to enhance the probability of forming homogeneous nanoparticles of desired phase [16]. A full description of the crystal structure and morphology of the nanocrystals would bring us one step closer to designing materials for desired applications.

Analysis of core/shell structures, elemental segregation, alloying and secondary phases inside each NC through powder X-ray diffraction is a challenging task, as the peak broadening hampers the detection of subtle differences and the accurate determination of the lattice parameters for NCs in a size range of 1 nm to 20 nm. However, these features play a crucial role when dealing with rather complex quaternary alloys, where several phases may coexist [17]. Other characterisation techniques such as neutron diffraction and Raman spectroscopy have been previously utilised to bring complementary information [18, 19]. Nevertheless, the results are averaged over the ensemble of nanoparticles, thus neglecting the radial compositional variations in single particles as well as the variations from nanoparticle to nanoparticle. Only advanced characterisation techniques such as STEM-EDS make the elemental quantification as well as the detection of secondary phases feasible down to nanometric resolution.

To this end, we present a comprehensive study by coupling high-resolution microscopy techniques, diffraction, simulation and spectroscopy methods to provide further information that is not typically possible to get with traditional characterisation methods. This thesis is divided into four main chapters.

Chapter 1 presents the objective of this thesis, the studied materials and the main technique: transmission electron microscopy (TEM)

Chapter 2 is dedicated to the optimisation of the sample preparation.

Chapter 3 is devoted to the investigation of Cu_2ZnSnS_4 NCs in two different perspectives. At first, the NC growth mechanism is explored by Scanning Transmission Electron Microscopy-Electron Dispersive Spectroscopy (STEM-EDS), *in situ* synchrotron and laboratory Small Angle X-Ray Scattering (SAXS) and Wide Angle X-Ray Scattering (WAXS) techniques. Then, the crystal structure of the final synthesis product is investigated by Nanobeam Precession Electron Diffraction (NPED) and High-Resolution Scanning Transmission Electron Microscopy by High Angle Annular Dark-Field Imaging

(HRSTEM-HAADF).

Chapter 4 presents the structural and morphological investigation of $CsPbBr_3$ NCs.

Finally a general conclusion with perspectives is given in chapter 5.

1.2 Semiconductor colloidal nanocrystals

Nanosystems are structures in which at least one dimension is smaller than 100 nm. Nanocrystals are crystals with reduced size in all the three directions. Firstly, materials in small size exhibit new and unique properties that are different from the bulk material. In particular, the influence of the higher ratio of surface atoms of the NC can significantly influence the properties of the NC. For instance, figure 1.1 shows the evolution of the band gap of a crystal in function of its diameter. Secondly, nanosystems are economically and ecologically interesting as they need less matter to be constructed. The birth of modern nanoscience with NCs began in the early 1980s as a response to the oil crisis in the late 1970s. Early photochemistry studies were conducted on tailored colloidal CdS and TiO_2 [12], and semiconductor NCs with enhanced surface chemistry were considered important for efficient harvesting of solar energy through photoelectrochemistry [13, 20]. Semiconductor NCs were termed quantum dots (QD) after the discovery and explanation of quantum size effects in the optical spectra of CuCl NCs embedded into glass and alkali-halide matrices [11] and in an aqueous solution of colloidal CdS NCs [13]. The impulse of the mid-1990s put colloidal QD in the stream of modern nanoscience, thanks to the emergence of surfactant-assisted precision synthesis, providing narrow size distributions, well-controlled surface chemistry, enhanced optical properties such as bright, spectrally tunable, stable photoluminescence [21]. Chemically synthesised NCs form a colloid, in which the NCs are separated from each other and homogeneously distributed within a solvent. Colloidal NCs became versatile nanoscale materials, thanks to composition and morphology tunability. Their unsupported nature allows the deposition onto different surfaces or integration into various matrices. At the beginning of 2000s, a multitude of semiconductor NCs has been developed.

As evoked previously, one of the most remarkable properties of semiconductor NC is the variation of their band gap as a function of the crystal size when it is lower than a certain value corresponding to the exciton Bohr radius (figure 1.1). In bulk, semiconductors present a valence band and a conduction band, separated by a band gap E_g. A photon with $E \geq Eg$ can be absorbed, exciting an electron e^- from the valence band to the conduction band and creating a hole h^+ in the valence band. Electron and holes are charged and are linked by Coulomb interaction; the linked pair e^--h^+ is an excited electron state, called exciton. Its energy is slightly lower than E_g: it corresponds to E_g minus the Coulomb interaction between electron and hole. At the same time, its wavelength is extended to a large region: the radius is large, as the effective mass of the charge carrier is small and the dielectric constant of the material is large.

When the particle size is in the nanometric range, the exciton radius can be larger than the NC size. To be confined inside the crystal, charge carriers will possess higher kinetic energy, increasing the E_g and moving from continuum to discrete energy levels.

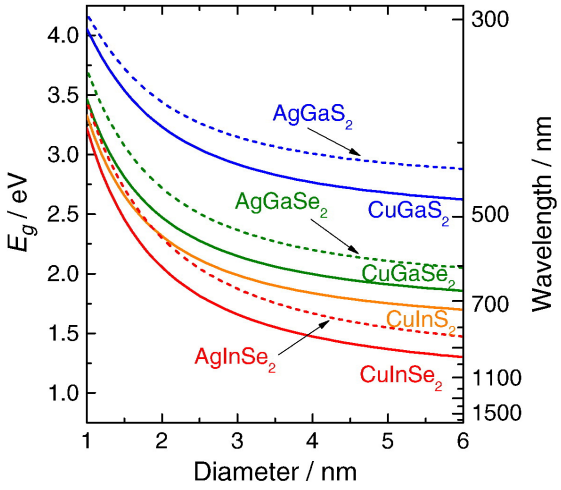

Figure 1.1 – Calculated evolution of the band gap with size for various ternary I-III-VI$_2$ semiconductor NC. Reprinted from [22].

This phenomenon is called quantum confinement. The nomenclature of the energy levels follows the terms defined in the molecular orbital theory: HOMO (Highest Occupied Molecular Orbital) and LUMO (Lowest Unoccupied Molecular Orbital) correspond to valence band and conduction band, respectively. The properties of these materials are in between bulk semiconductors and molecular assemblies.

An important characteristic of semiconductor NCs concerns the influence of the surface on optical and electrical properties. Ideally, a perfect compositionally pure collection of atoms isolated in a gas phase would result, from the point of view of semiconductor physics, in a highly defective system; substantial reconstruction occurs, leading to additional energy levels within the band gap. These states degrade the electrical and optical properties of the material, as they trap electrons or holes and can induce alternative relaxation pathways. Surfaces can be passivated by an inorganic semiconductor with a higher band gap, or with organic ligands: successful passivation inhibits atomic recombination on the surface, leaves no strain, and confines the charge carriers in the semiconductor cluster [14].

The synthesis of monodispersed colloidal NCs is a major goal in chemistry. "Top down" and "bottom up" methods exist. Top down methods involve for instance the mechanical milling of bulk materials to a fine powder, which can be dispersed in a surfactant solution [23]. Despite a large output, the nanoparticles suffer from uncontrolled sizes and shapes. A bottom up strategy consists in building the nanomaterials from molecular precursors in the presence of ligands which protect each object from further growth and coalescence. One of the main factors to obtain NCs with a low size dispersion is the separation between nucleation and growth steps. If these are simultaneous, new germs could form at the same time with others which are growing, implying a polydisperse sample. LaMer proposed a model to explain this phenomenon, to explain the growth of sulphur colloidal particles [24]. This model explains the formation of monodisperse

particles, starting from a supersaturated solution. Three steps are involved:

1. pre-nucleation, where the concentration of reactive species increases; this concentration reaches the solubility level, and then the critical level of nucleation.

2. When this level is reached, nucleation starts spontaneously in a homogeneous manner. If the nucleation is fast enough, the concentration of the reacting species lowers below the critical level for nucleation, and therefore the nucleation stops. In these conditions, the nucleation step is short.

3. Consequently the growth of the nuclei is homogeneous and uniform, as the concentration of reactive species is sufficiently high.

In the LaMer model, the growth is controlled by the diffusion of the solute towards the particle surface. A strategy commonly used to obtain uniform nanocrystals, with fast nucleation separated by the growth step, is the hot-injection method [21]. This method consists in the addition of one reactant in the already warmed solution: in this way, the critical level of nucleation is suddenly reached. The theory of LaMer can be applied not only for the hot-injection but also for the heating-up method, where all the precursors are mixed in the same pot and heating simultaneously [25].

The growth mechanism is influenced mainly by two factors, namely the diffusion (monomers moving from the solution to the NC surface) and the reaction kinetics of the monomers with the NCs. H. Reiss, observing the growth of colloidal dispersion, showed that if the NC growth is limited by the diffusion process, it is possible to obtain a lowering of the size distribution (size-focusing) [26]. The same principle was demonstrated for nanocrystals by Peng [27]. Crystal growth is also strongly influenced by the variation of surface energy as a function of the size. For any monomer concentration, it exists an equilibrium critical radius r^*: crystals smaller than this size will be dissolved, and the ones with a larger size will have a positive growth which depends on the size. Size-focusing is confirmed when the nanocrystals are slightly larger than the critical radius: the smaller NCs will grow faster than the larger ones. With crystal growth, the monomer concentration diminishes, and the critical size is larger than the average size of nanocrystals. Size distribution gets larger, as the smaller NCs get smaller or disappear to favour bigger NCs growth. This process is defined as Ostwald ripening.

Ligands are fundamental for the semiconductor NC synthesis, as they control the kinetics of nucleation and growth of the crystal facets. In the case of colloidal NC synthesis, surface-bound surfactants cause a reduction of the surface energy and are necessary for NC stability and homogeneity in size, composition, shape. The organic ligands are usually compounds of amphiphilic nature and contain a polar hydrophilic unit linked to a nonpolar hydrophobic hydrocarbon chain. The ligands attach through the polar group to the NC surface (figure 1.2). Several kinds of ligands exist and are usually classified depending on the nature of the polar group: carboxylic acids (-COOH), phosphines (>P-), thiols (-SH), amines ($-NH_2$), and others. They provide steric (or electrostatic) repulsion between NCs, stabilising the colloidal suspension. Remarkably, this organic shell can also be very detrimental to the observation in the electron microscope.

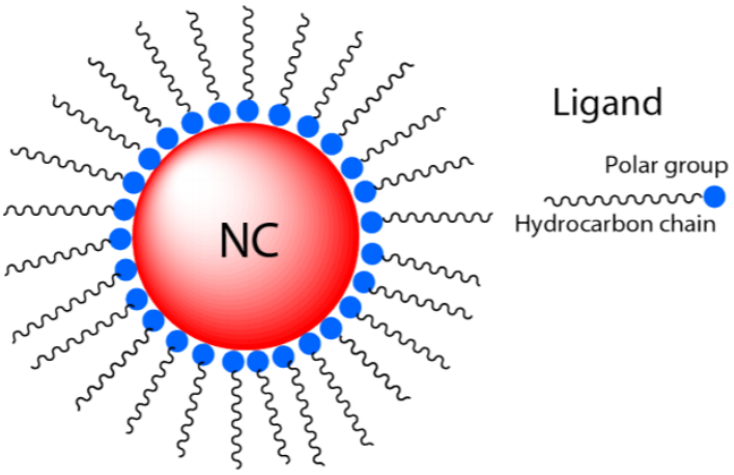

Figure 1.2 – Schematic representation of a nanocrystal which is capped by ligands.

In fact, electron beam contamination is observed when the beam is concentrated on a small area (especially in high magnification modes, or in case of a convergent beam). High energy electrons interact with the organic molecules tethered to the bombarded surfaces. As a result, the exposed area gets dark in TEM imaging mode, or "foggy"[1] in STEM mode. This effect negatively influences the imaging at high magnification. It limits the precision in correcting aberrations or defocus and limits the acquisition time (typical of spectroscopic methods such as scanning TEM EDS and EELS) [28]. For these reasons, the contribution of electron microscopy is generally limited to large field views of dispersed NCs. Only size dispersion, ambiguous morphology and self-organisation of NCs on the carbon grid can be observed. Often, the composition is measured from a reasonably thick film of deposited NCs by SEM-EDS, providing an average composition over some million NCs, without information on the single crystal composition and the homogeneity. Even more difficult is the determination of secondary phases inside a NC, the effective creation of a core-shell structure, or material segregation between crystallites[2].

The most popular strategies to achieve ligand removal are thermal treatments at low temperature [32,33], solvent extraction [34], chemical treatments to separate the ligands

[1] In STEM mode, the image intensity grows where the beam impinges an area; the more the beam stays in a position, the more intensity is observed at this point, hiding the structure and the information from the sample.

[2] Of course, microscopy is actively interested in nanoobjects, and several extraordinary accomplishments have been reached, such as atomic level three-dimensional tomographic reconstruction. On the one hand, nanoobjects allow testing of the most advanced microscopy techniques, on the other hand, the information obtained from single objects is often beneficial for material labs as it is complementary to other techniques and permits to input correctly the structural information to simulate accurately optoelectronic properties. Nevertheless, most of these studies are conducted on models which are "simple", such as monometallic nanoparticles [29, 30] or heavy-atoms CdSe-CdS NCs [31], which often have a limited interest for applications in real-world.

from the particles [35], plasma cleaning [36] or UV-ozone [37]. Too mild methods leave residues; too harsh methods would cause changes in the NCs, atomic diffusion, surface rearrangement and sintering [38]. An overview of the most common ligand removal procedures is presented in section 2.3.

1.2.1 Ternary and quaternary NCs

Since quantum confinement widens the band gap with a decrease in size, it is essential to explore semiconductors with a relatively narrow band gap in the bulk material, with an upper limit of 1.55 eV. Most binary compounds responding to this requirement contain toxic heavy metals, such as Cd, Pb or Hg. Ternary and quaternary compounds offer flexibility of tuning the band hap without relying on toxic elements. Novel NCs of controlled size dispersions and homogeneous composition need a development. The latest strategies in novel materials and architectures for QD-based solar cells have been reported in recent reviews [39, 40].

The evolution towards more complex NCs responds to the growing demand for earth-abundant and nontoxic chemical compositions. One example is the gradual move from binary II-VI to ternary I-III-VI_2 and quaternary I_2-II-IV-VI_4 NCs with excellent size, shape and composition control. Initial binary nuclei can dissolve or fuse together to form multinary NCs or serve as seeds for the growth of the multinary compound by cation exchange or ionic diffusion [41]. Besides size and shape uniformity, composition and phase homogeneity within the NC are critical parameters for tuning optical characteristics. Secondary phases often possess nearly the same crystal structure and lattice parameters as the multinary compound and therefore are hardly discernible. Besides detection of secondary phases by ensemble-averaging techniques, particle-to-particle composition dispersion requires single-particle analyses and high-resolution spectroscopic methods.

Tetrahedrally bonded ternary and quaternary chalcogenide phases can be formed by more than 30 elements; within these compounds, several polymorphs are possible: cation-disordered zinc-blende and wurtzite phases to cation-organised chalcopyrite, CuAu-like and orthorhombic wurtzite-chalcopyrite and wurtzite-CuAu-like ternary phases, and kesterite, stannite, wurtzite-kesterite and wurtzite-stannite quaternary phases [42]. The favoured crystal phase depends on the cation's nature; moreover, the organisation can be kinetically controlled by a chosen selection of precursors, surfactants and synthesis conditions. X-ray or electron diffraction studies easily differentiate between cubic and hexagonal structures, but the atomic site ordering is difficult to determine experimentally. Controlling the cation order requires not only a better understanding of the nucleation and growth mechanisms but also more accurate insight from the characterisation methods. This necessity requires moving from conventional X-ray diffraction (XRD), which suffers from severe peak broadening due to the nanomaterial size (1 nm to 20 nm), and high-resolution transmission electron microscope (HRTEM) to neutron diffraction and aberration-corrected microscopy, with analytical mapping at atomic resolution. Tunable site occupancy of cations in multinary NCs offers the opportunity of controlling optical and electronic properties while maintaining compositions with abundant nontoxic elements. The tuning of the band gap is done not only from quantum size

effects but also by the compositional control at anion and cation sizes [43]. A complete review of multinary NCs is beyond the goals of this introduction. The reader may refer to recent reviews [44–47].

In the following, the materials studied in this manuscript are briefly presented.

1.2.2 Cu_2ZnSnS_4

Quaternary Cu_2ZnSnS_4 has been developed as an alternative material to the high-performance pseudo-quaternary $I-(III,III)-VI_2$ material $Cu(In,Ga)S$ for the application in thin film solar cells. As indium is likely to become scarce in the near future, a replacement is necessary. Particularly, Cu_2ZnSnS_4 takes the lead in the research, as it consists of only earth-abundant, non-toxic and cheap elements. It is a *p*-type semiconductor with a direct band gap ($\approx 1.45\,eV$) and a high absorption coefficient [48]. CZTS can be synthesised using vacuum based methods: in this case, CZTS films are processed by co-evaporating/co-sputtering precursors in high vacuum to obtain desired stoichiometric CZTS films. Nevertheless, the synthesis and successive spin-coating deposition of CZTS NCs is interesting, as composition and crystalline phase can be controlled *ex situ*, and treatments can be performed before integration to the solar cell substrate. The most efficient solar cells involve a step of selenization, to obtain a CZTSSe material [17]. Figure 1.3 shows the phase diagram of CZTS. Only a small spot in the quaternary phase is suitable for photovoltaic applications.

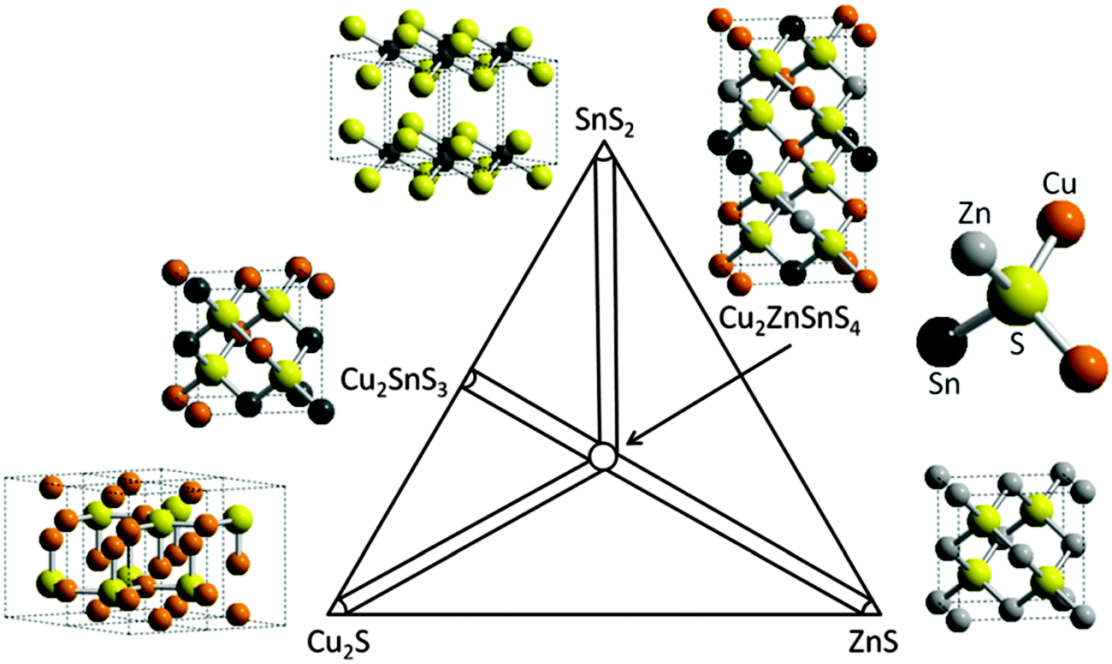

Figure 1.3 – The pseudoternary phase diagram to form CZTS phase and other secondary phases along with their crystal structures. Reprinted from [17].

It is often mentioned as an empirical rule that Cu-poor and Zn-rich conditions give the best solar cell efficiency [49]. A class of known secondary and ternary phases can be formed by a combination of the four elements: CuS, Cu_2S, ZnS, SnS, Sn_2S_3 and Cu_2SnS_3. In particular, ZnS is a wide band gap and insulating material which reduces the final device active area. Cu_2S is highly conductive in nature and may short solar cells. SnS_2 is a *n*-type semiconductor with a band gap $\approx 2.2\,\mathrm{eV}$, which may form a secondary diode inside the absorbing layer, or be insulating. SnS is a *p*-type semiconductor (band gap 1.11 eV), and Sn_2S_3 is a mixed phase showing a band gap of 1.09 eV. Cu_2SnS_3, ofter referred to as CTS, is a *p*-type semiconductor with a band gap similar to CZTS; nevertheless, this material is reported to be less efficient than CZTS. These phases can be unintentionally synthesised together with the quaternary stoichiometric phase and form energy levels in the band gap, which act as recombination or trap sites. Moreover, standard characterisation methods (XRD) cannot reliably discriminate between the crystalline phases of tetragonal CZTS, as Cu and Zn are isoelectronic. Kesterite, stannite and PMCA are three CZTS tetragonal structures which obey the octet rule; they are similar in the crystallography point of view, but they possess a different electronic structure (and band gap) [50, 51].

It is possible to show that Cu_2ZnSnS_4 can be derived from binary II-VI analogues and respective ternary I-III-VI_2 structures. Two fundamental ternary structures obey the octet rule: chalcopyrite and CuAu-like structures. It has been demonstrated that ternary wider band gap chalcopyrite is thermodynamically always more stable [52]. Three quaternary structures of Cu_2ZnSnS_4 obey the octet rule. They are represented in figure 1.4: kesterite, stannite and pre-mixed copper-gold structures. These structures share an equivalent anion S^{2-} lattice, only the cation sublattice changes: bulk CZTS adopts preferentially the tetragonal kesterite structure (space group $I\bar{4}$, figure 1.4d) which consists of cation layers of CuSn alternating with cation layers of CuZn in the direction of crystallographic *c*-axis. It derives from ternary chalcopyrite. Stannite structure (space group $I\bar{4}2m$, figure 1.4e) is also observed in this class of quaternary materials, differing in the composition of the alternating layers: SnZn layers alternate with pure Cu layers in the *c* direction. It derives from ternary Cu-Au structure. Pre-Mixed Copper-Gold (PMCA) structure (space group $P\bar{4}2m$, figure 1.4f), has only two alternating cation layers: one pure Cu layer and one SnZn layer. It also derives from ternary Cu-Au structure [52].

As shown in table 1.1, the crystallographic parameters such as the lattice constant a and the tetragonal distortion parameter η are very similar; the energy difference per atom Δ_E is relatively small. Therefore, the three structures can thermodynamically coexist, and it is experimentally difficult to distinguish these three structures [18, 50].

The presence of these three structures in the same device can lead to variations of the order of 100 mV in the band gap [52], which could cause a lower open-circuit voltage in CZTS cells, in addition to fluctuations due to defect concentration variations.

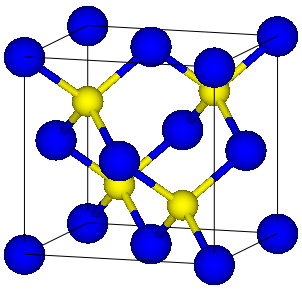

(a) Sphalerite ZnS

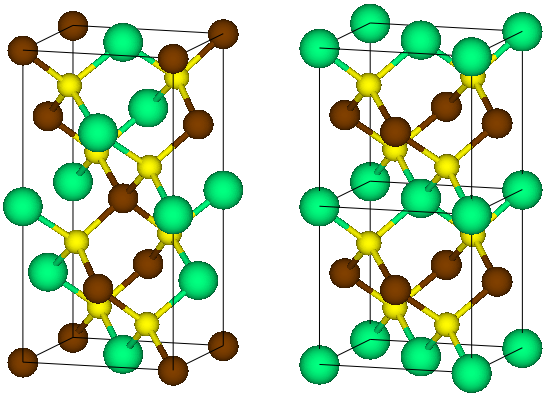

(b) Chalcopyrite $CuInS_2$ (c) CuAu $CuInS_2$

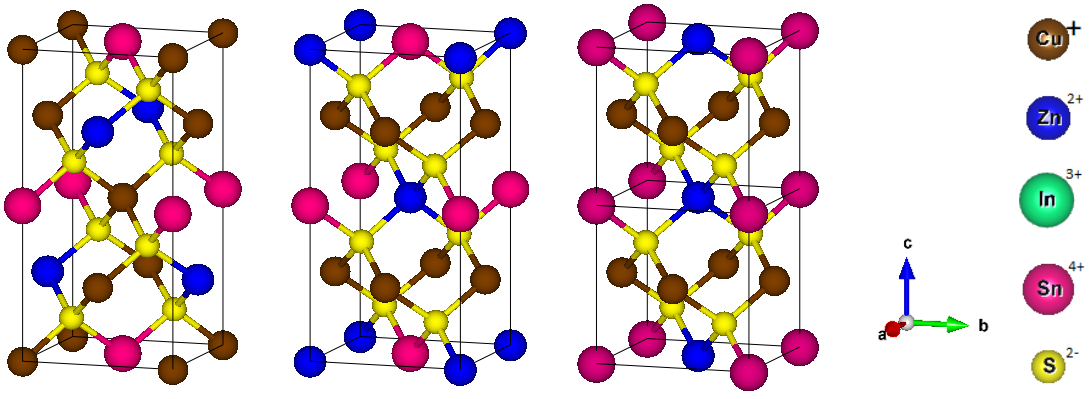

(d) Kesterite CZTS (e) Stannite CZTS (f) PMCA CZTS

Figure 1.4 – Structural relationships in ternary and quaternary metal chalcogenides. The typical zinc-blende binary structure (a) (space group $F\bar{4}3m$) transforms in chalcopyrite (b) ($I\bar{4}2d$) or in CuAu (c) ($P\bar{4}2m$) structures, after replacement of the single cation with two distinct cations. Kesterite (d) ($I\bar{4}$) is derived from the ordered chalcopyrite structure (b) ($I\bar{4}2d$), while stannite (e) ($I\bar{4}2m$) derives from the CuAu ordering (c). Both structures differ in the ordering of the Cu-Zn sublattice. The PMCA structure (f) (primitive mixed CuAu-like, $P\bar{4}2m$) derives from the CuAu ordering (c) too and features a 90° rotation of one of the II-IV layers with respect to stannite.

Structure	a [Å]	η	Δ_{CF} (eV)	Δ_E (meV)	E_g (eV)
Kesterite	5.467	0.999	-0.065	0	1.50
Stannite	5.458	1.004	0.138	2.86	1.38
PMCA	5.459	1.005	0.128	3.15	1.35

Table 1.1 – Calculated lattice constant a, tetragonal distortion parameter $\eta = \frac{c}{2a}$, crystal field splitting Δ_{CF}, energy difference per atom relative to the lowest-energy structure Δ_E, and direct band gap E_g. Adapted from [50].

Moreover, due to the chemical similarity between Cu and Zn, the concentration of point defects provides a specific influence on the properties. The presence of complex and competitive secondary phases and defects and the variations in crystal structure may explain local fluctuations of the open circuit voltage V_{OC} and the consequent performance gap with respect to CIGS.

1.2.3 $CsPbBr_3$

In the past few years, perovskite structures have grabbed much interest for various applications such as photovoltaic and light-emitting devices (LEDs) due to their colour-tunable and narrow-band emission as well as easy synthesis, convenient solution-based processing, and low fabrication cost. In particular, lead halide perovskites (LHPs) in the form of hybrid organic-inorganic compounds, such as $CH_3NH_3PbX_3$, investigated as semiconducting absorber layers in solar cell showed a record power conversion efficiencies from 3.8% in 2009 [53] to 22.1% in 2017 [54]. Recent advances showed that LHPs are not only potential candidates for high-performance solar cells but also in light-emitting devices [55]. Colloidally synthesised LHPs exhibit very high photoluminescence quantum efficiency (PLQY), narrow emission linewidths and colour tuning over the entire visible spectrum. PLQY of I-based NCs have reached 60-70% [56] while Br-based NCs up to 100% [57]. On the other hand, Cl-based NCs are typically less luminescent, and PLQY of maximum 10% have been reported. In films, efficiencies as high as 30% were measured [58]. In case of emission linewidths, typical full width at half maximum values are in the order of 0.1 eV, corresponding to 12 nm to 15 nm in the blue-violet, approximately 20 nm in the green and 35 nm in the red region of the visible spectrum [59, 60].

In 2015, a new type of all-inorganic cesium lead halide perovskites $CsPbX_3$ as promising QDs was reported by Protesescu [60]. As shown in figure 1.5 a-c, the authors reported the synthesis of cuboid shape (4 nm to 15 nm in edge length), monodisperse $CsPbX_3$ (X = Cl, Br, and I) nanocrystals with cubic perovskite crystal structure. Owing to the exciton Bohr diameter of up to 12 nm, $CsPbX_3$ NCs exhibit compositional bandgap engineering as well as size-tunability of their bandgap energies through the entire visible spectral region of 410 nm to 700 nm (figure 1.5 d and e). Protesescu reported emission line-widths of 12 nm to 42 nm, PLQY of 50-90%, and PL lifetimes of 1-29 ns.

LHPs are practical for tuning the optical properties thanks to various mixed-halide compositions. Two ways have been shown; the first is the combination of appropriate

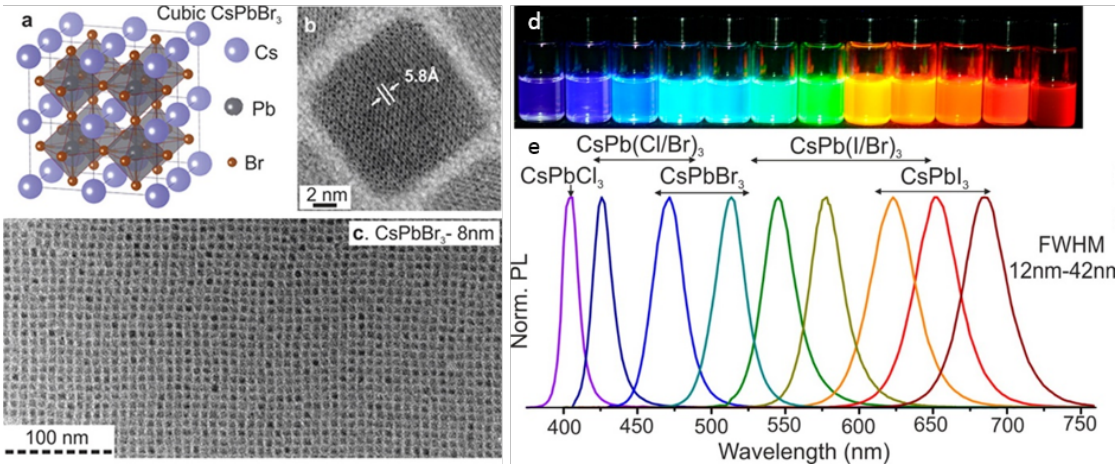

Figure 1.5 – Monodisperse $CsPbX_3$ NCs and their structural characterisation. (a) Schematic of the cubic perovskite lattice; (b,c) typical transmission electron microscopy (TEM) images of $CsPbBr_3$ NCs; (d) colloidal solutions in toluene under UV lamp ($\lambda = 365\,\text{nm}$); (e) representative PL spectra ($\lambda_{exc} = 400\,\text{nm}$ for all but 350 nm for $CsPbCl_3$ samples). Reprinted from [60].

ratios of halogen precursors (PbX_2 salts) as previously described by Protesescu [60]. The second is to take advantage of the mobility of the halide anions in the crystal lattice. Akkerman demonstrated that Br ions in $CsPbBr_3$ NCs could be replaced by either Cl or I, resulting in a blue shift of the PL peak in the case of chloride and red shift in the case of iodine [59]. Quantum confinement has also been shown to control the perovskite nanocrystals emission. The size of the NCs was shown to be tunable down to the quantum confinement regime by changing the synthesis conditions (reaction temperature, pH of the reaction medium or chain length of the organic molecules used as surfactants) [61–64].

Reports on the structure of nanometer-sized $CsPbBr_3$ conflict between either $Pm\bar{3}m$ cubic [60, 65, 66] or *Pnma* orthorhombic [67, 68] structure (figure 4.3). Also, mixed structures [69], where both phases exist simultaneously, have been reported. A clear description of the crystal structure is crucial for the physical interpretation of the electronic structure. In particular, the lower conduction band of $CsPbBr_3$ is generally considered to originate from the overlap of lead *p*-orbitals [60], in which case the rotation of $PbBr_6$ octahedra is likely to have a substantial impact on the band structure. This structure uncertainty may result in the inaccurate determination of electron and hole effective masses from band structure calculations based on the cubic structure of $CsPbBr_3$ and may cause deviations in the band gap-size dependence for $CsPbBr_3$ QDs.

1.2.4 $CuFeS_2$

The characterization of $CuFeS_2$ NCs is presented in appendix J. The material is rapidly introduced in the following.

$CuFeS_2$ is a non-toxic and earth-abundant material which offers unique properties as an antiferromagnetic semiconductor, with a narrow band gap of 0.5 eV to 0.6 eV. The thermoelectric performance of this material is best at low temperatures (0 °C to 400 °C), where few other materials (which rely on heavy metals) are available to date (Bi_2Te_3, PbTe). Greener semiconductors, although much less efficient as bulk materials are gaining novel interest in this end, especially since nanostructuring was proven able to improve their thermoelectric properties remarkably. Possibilities for the preparation of both *n*- and *p*-type materials are possible by tuning the cation ratio Cu : Fe, as well as cation-anion ratio ($Cu^+ + Fe^{3+} : S^{2-}$); this flexibility has an influence on carrier density, electrical conductivity and Seebeck coefficient. Chalcopyrite is a semiconductor with high electrical conductivity; its high thermal conductivity must be improved to enhance its thermoelectric performance, which can be done by tuning the material nanostructure. In the bulk form, doming allows to increase electrical conductivity σ but with the concomitant drop in Seebeck coefficient S and a rise in thermal conductivity κ. The maximum figure of merit $ZT = \frac{\sigma S^2}{\kappa}$ is therefore obtained for an optimal doping level. To improve ZT above the maximum limit in bulk, the size of semiconductors can be tuned to reduce phonon mean free path and therefore lower κ, while preserving a high mean free path for the charge carriers and therefore a high σ. In semiconductors, the mean free path of phonons is generally higher than the mean free path of electrons: for chalcopyrite compounds, the mean free path for phonons ranges between 100 nm and few µm, whereas it is $\approx$ 2 nm for electrons. Grain boundaries or impurities regularly integrated into the material structure can work as scattering elements and decrease the thermal conductivity. $CuFeS_2$ nanocrystals with a diameter ranging between 30 nm to 50 nm are particularly interesting for limiting phonon-related conductivity; nevertheless, the reported synthesis by colloidal methods yield NCs of 5 nm to 10 nm. For this reason, the properties of $CuFeS_2$ NCs need to be carefully controlled during the synthetic procedure.

From the synthetic point of view, both in hydrothermal or in organic synthesis, the material tends to crystallise in anisotropic shapes (nanowires, nanorods, platelets, pyramids) and have too small sizes with respect to requirements for thermoelectrics. The size distributions are usually not highly controlled; Gabka synthesised the smallest $CuFeS_2$ nanocrystals, with a diameter < 3 nm [70]. Ghosh obtained 10 nm monodispersed NCs [71]. However, the existing synthesis procedures are not optimised for the production of hundreds of milligrams of NCs, required for the making of thermoelectrics pellets. The link between structure, morphology, composition and physical properties needs a proper investigation to obtain the best $CuFeS_2$ based thermoelectric devices [9]. TEM can provide complementary information about the structure of the synthesised NCs, in particular when dealing with the analysis of the homogeneity of the NCs and the structure inside the single NCs.

1.3 Transmission Electron Microscopy

The first TEM was built by Max Knoll and Ernst Ruska in 1931 [72], and the first commercial TEM was available in 1939. Ruska was awarded the Nobel Prize in physics for its development later in 1986. Since then, TEM is amongst the most powerful tools for materials science. A high energy electron beam is shone through a thin sample, and the interactions between the electrons and the atoms are used to observe the crystal structure and features in the structure like dislocations and grain boundaries.

The TEM operates on the very same principles as the light microscope but uses electrons instead of light. Because the wavelength of electrons is several orders of magnitude smaller than that of light, the theoretical optimal resolution attainable for TEM images is many orders of magnitude better with respect to light microscopes. In real life experiments, the resolution has higher values than the wavelength, because of the aberrations induced by electron lenses. Last generation TEMs can reach an information limit on the order of 50 pm [73]. Thus, TEM reveals the finest details of internal structure, sometimes as small as individual atoms.

1.3.1 Interaction of the electron beam with the specimen

As illustrated in figure 1.6, when energetic electrons in the microscope interact with the sample, a wide variety of signals can be formed. Relatively thick samples produce secondary or backscattered signals with higher probability; electrons are transmitted when the sample is sufficiently thin. The desired thickness of a TEM sample is a function of the electron beam energy and the average atomic number of the elements in the sample. In general, samples with a thickness less than 100 nm should be used wherever possible. The transmitted electrons can be either elastically or inelastically scattered.

Different TEM imaging techniques exist based on elastically scattered electrons, depending on the angle of scattering. Electrons scattered at low angles are used for conventional TEM, High-Resolution TEM (HRTEM) imaging and Electron Diffraction (ED), whereas in the so-called High Angle Annular Dark Field Scanning Transmission Electron Microscopy (STEM-HAADF) imaging, electrons are scattered to higher angles ($\theta > 50$ mrad off axis) corresponding to Rutherford and thermal diffuse scattering (TDS). However, as discussed above, also inelastic scattering occurs, yielding different types of signals such as X-rays, Auger or secondary electrons, plasmons, phonons and cathodoluminescence, which can be exploited by different techniques in the microscope, such as Energy Dispersive X-ray Spectroscopy (EDS) and Electron Energy Loss Spectroscopy (EELS).

1.3.2 Imaging modes

As previously discussed, the different signals emerging after the interaction of the electron beam with the specimen give rise to different TEM techniques. In this part, we present a short description of these techniques. The reader can refer to existing literature for a detailed and comprehensive description [74].

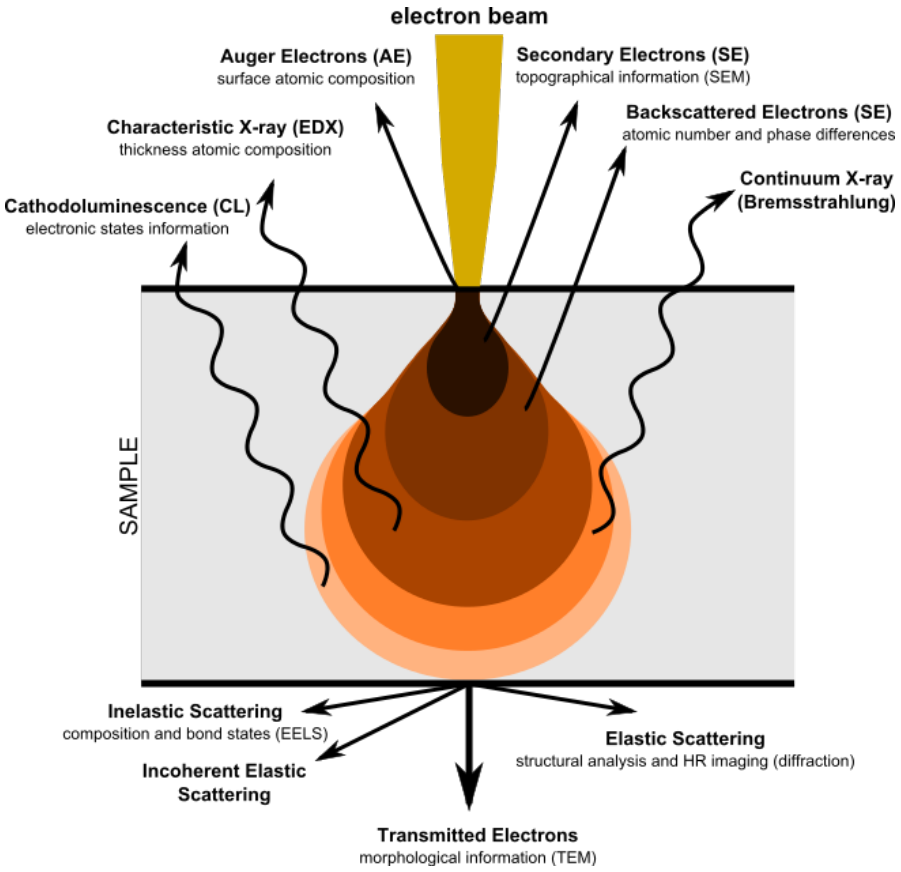

Figure 1.6 – Schematics of the STEM electron beam-sample interaction and the different signals emerging from the sample.

Bright Field and Dark Field TEM imaging

In the bright field (BF) mode of the TEM an aperture is placed in the back focal plane of the objective lens which allows only the direct beam to pass. In this case, the image results from a weakening of the direct beam through its interaction with the sample. Therefore, mass-thickness and diffraction contrast contribute to image formation: thick areas, areas in which heavy atoms are enriched, and crystalline areas appear with dark contrast. It should be mentioned that the interpretation of images is often impeded by the simultaneous occurrence of the contrast-forming phenomena.

In dark field (DF) images the direct beam is blocked by the aperture while one or more diffracted beams are allowed to pass the objective aperture. Since diffracted beams have strongly interacted with the specimen, very useful information is present in DF images, e.g. about planar defects, stacking faults or particle size.

High Angle Annular Dark Field Scanning Transmission Electron Microscopy (HAADF-STEM)

STEM is a particular mode of TEM in which the beam has a convergence angle: the lenses of the illumination system focus the electron beam into a fine probe, which is scanned across the sample using deflection coils (in contrast of the parallel plane wave illumination of conventional TEM). The image formation mechanism is different compared to TEM. Briefly, the signal is generated at the position of the beam and, for every pixel, the number of electrons scattered to the annular detector is detected. Scanning and acquisition of a signal build an image. One of the main advantages of the technique is that the image quality is only affected by the aberrations of the probe. The first scanning TEM was built by Von Ardenne in 1938 [75], only five years after the first TEM. Several improvements were the introduction of field emission source [76] and the visibility of single heavy atoms on a C support film [77] for which an annular dark field detector (ADF) was used. Another significant development is based on the development of high-angle annular dark field (HAADF) for Z contrast imaging [78] and the application for high-resolution imaging by Pennycook [79]. Finally, the first sub-angstrom STEM images were obtained with the help of a C_s corrector by Batson and Nellist [80, 81].

As discussed above, different detectors can be used, each yielding different types of information from the sample. The most widely used detector is the Annular Dark Field (ADF) detector, for which the collection angle range can be modified by changing the camera length. When using a high camera length, more coherent electrons are collected ($10\,\text{mrad} < \theta < 50\,\text{mrad}$) and the resulting images are influenced by diffraction contrast. By using a low camera length, electrons scattered to high angles are collected ($\theta > 50\,\text{mrad}$). Since the scattering, in this case, is Rutherford-like, the intensity of the formed images is proportional to Z^n ($0.6 < n < 2$) of the elements under investigation and the thickness of the sample. As a result, the high-resolution HAADF-STEM images are more straightforward to interpret in comparison to HRTEM images for which image simulations are generally needed. Often, a BF-STEM detector is also available which has a disc-shaped detector located in the central part of the annular detector and collects the central beam and coherent electrons which are scattered at low angles. An illustration

of the STEM system including the detectors is presented in figure 1.7.

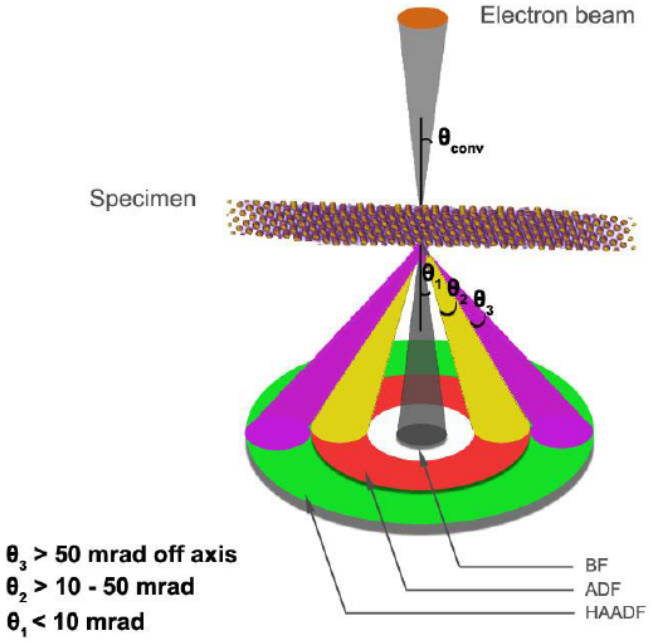

Figure 1.7 – Setup of STEM imaging. Retrieved from [82].

1.3.3 Multislice simulations

Image simulation consists of numerical calculations of electron microscope images from first principles and from a detailed description of the specimen and the instrument. There are two general types of image simulations:

1. the first group involves Bloch wave eigenstate and a matrix formulation in reciprocal space; the Bloch-wave method is adapted to the calculation of crystalline solids with small unit cell and in any $[u\,v\,w]$ orientation. The Bloch-wave method also has several advantages (speed, ease of use) for simulating CBED, LACBED or PED patterns and for polarity and chirality determination.

2. The other group involves mathematically slicing the specimen along the beam direction (multislice method). This method was initially proposed by Cowley [83] and optimised thanks to the utilisation of the fast Fourier transform by Ishizuka [84]. In principle, the specimen is decomposed into sub-volumes perpendicular to the beam direction; the potential contained in these sub-volumes is projected into one plane. These slices generally are of equal volume. Propagation of the wave function through a specimen is approximated by transmitting it through the first slice; propagate the outcome through the vacuum; repeat for the next slice. The

wave function at the $i+1$th slice is

$$\Psi(\vec{x}, z_{j+1}, \vec{x_0}) = [\Psi(\vec{x}, z_j, \vec{x_0}) t(\vec{x}, z_j)] \otimes P(\vec{x}, \Delta z_j) \tag{1.1}$$

where $\vec{x}$ denominates a vector in the plane of the slice, $\vec{x_0}$ is the position of the probe at the entrance surface of the specimen and z is the coordinate perpendicular to $\vec{x}$. For semplicity, the beam direction is considered to be perpendicular to slices. The transmission function t reads

$$t(\vec{x}, z_j) = \exp\left\{\frac{2\pi i m}{h^2 k_0}[V(\vec{x}, z_j) + iV'(\vec{x}, z_j)]\right\} \tag{1.2}$$

The potential is split into a real component and an imaginary component. The propagator function is defined as:

$$P(\vec{x}, \Delta z_j) = \frac{1}{i\lambda\Delta z_j} \exp\left(\frac{i\pi x^2}{\lambda \Delta z_j}\right) \tag{1.3}$$

Computationally, it is convenient to make use of the Fourier Transform FT by means of the Fourier convolution theorem and calculate

$$\Psi(\vec{x}, z_{j+1}, \vec{x_0}) = FT^{-1}\left\{FT[\Psi(\vec{x}, z_j, \vec{x_0}) t(\vec{x}, z_j)] FT[P(\vec{x}, \Delta z_j)]\right\} \tag{1.4}$$

In order to reproduce high-resolution STEM images the transmission and propagation needs to be calculated for every position of the probe. However, the projected potential (often referred to as phase gratings) and the propagator function can be maintained and reused in the whole specimen calculation.

The multislice method offers much flexibility, allowing for drastic changes in structure and composition in between successive slices. It is often chosen for simulating crystalline or amorphous solids with a large unit cell, or solids which contain defects. Multislice calculations are handy and offer an advantageous strategy to handle non-periodicity.

Image simulation helps the interpretation of recorded images in the microscope. It is also adapted to adjust instrumental parameters by changing microscope conditions (such as beam energy, spherical aberration): this is relatively fast and simple, rather than modifying conditions in the microscope (or changing the microscope design). Image simulation is used both as an aid in image interpretation, both as a mean of exploration of new kinds of imaging modes in the microscope. In the presented study, simulations were performed using the multislice method on the program autostem [85], developed by the team of Earl J. Kirkland in Cornell University.

It is possible to define the minimum and maximum allowed angle for integrating scattered electrons: all the possible camera lengths which are defined in the alignment of the microscope can be explored, by inserting as input the angles for bright field and for high angle annular dark field detectors.

Thermal Diffuse Scattering

Atoms in the sample are slightly vibrating, in a spatial range which is sensibly smaller than the interatomic distances. Nevertheless, they can lead to interesting effects, such as a diffuse background intensity due to thermal vibrations.

Optical phonons have a typical maximum frequency of about 10^{12} Hz, which is higher than acoustic phonons. As it takes about 10^{-16} s for one electron to traverse the sample, atoms seem stationary but slightly out of equilibrium positions to the imaging electrons. The final image is an average of several different imaging electrons, each of them seeing a slightly different configuration of atoms in the specimen. Each atomic configuration is not correlated with the previous one but randomly generated. The final image is the time average of many imaging electron intensities.

In numerical simulations from Kirkland programs, the approach for approximating thermal diffuse scattering is called "frozen phonon approximation":

1. from the list of specimen atomic coordinates, a small random offset is assigned to each atom;
2. perform a normal multislice simulation to get an image;
3. repeat the process with a different random offset for each atomic coordinate (from the initial atomic coordinates, to avoid cumulative effects);
4. the final image is the average of the intensity $\left(|\psi|^2\right)$ calculated from different randomly perturbed atom configurations.

The random offset is generated using a random number generator within a Gaussian distribution. When all of the atoms have a slightly offset position, there is no residual periodicity in any direction, and the specimen must be considered amorphous.

1.3.4 Energy Dispersive X-ray Spectroscopy (EDS)

Atoms in a sample contain ground state electrons which are present in discrete energy shells bounded to the nucleus. When the incident electron beam interacts with the sample, electrons from the inner shells are excited and ejected from these shells, creating an electron hole at their former position. Next, an electron from a higher energy shell can occupy the hole, and the difference in energy between the high and the low energy shell can be released as an X-ray. An energy dispersive X-ray spectrometer can measure the number an the energy of the emitted X-rays. Since the energy of the X-rays is characteristic for the energy difference between the two shells, which is dependent on the element from which they are emitted, an elemental analysis of the specimen can be performed. An illustration of the interaction together with an example of an extracted spectrum is presented in figure 1.8. The technique is not regarded as ideal for the detection of light elements ($Z < 8$) but recently, after the development of new systems for X-ray detection where four windowless detectors are combined, the detection sensitivity

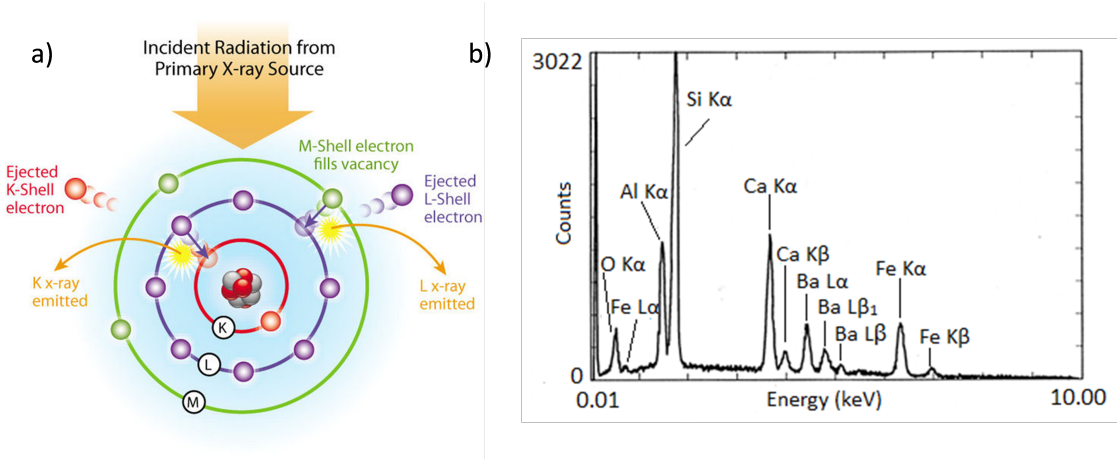

Figure 1.8 – (a) X-ray generation mechanism in the electron microscope, (b) an example of an EDS spectrum. Retrieved from [82].

has been strongly improved. By combining EDS with STEM imaging, detailed 2D chemical mapping can be obtained.

In the sample analysed in this thesis, NCs are smaller than 20 nm, and compositional quantification is calculated from X-rays having an energy higher than 2 keV. We can assume that absorption processes are negligible and therefore use a standardless Cliff-Lorimer quantification method, which is detailed in the following.

Cliff-Lorimer equation [86] reads

$$\frac{C_A}{C_B} = k_{AB}\frac{I_A}{I_B} \tag{1.5}$$

where C_A and C_B are the weight percentage of each element A and B; I_A and I_B are the measured intensity emerging from the specimen. k_{AB} is the Cliff-Lorimer factor. k_{AB} is not a constant, it varies with the microscope and the electron energy.

This formula is expressed for a binary system, but it can be extended to multinary systems by adding some extra equations:

$$\begin{cases} \frac{C_A}{C_B} = k_{AB}\frac{I_A}{I_B} \\ \frac{C_B}{C_C} = k_{BC}\frac{I_B}{I_C} \\ \frac{C_C}{C_D} = k_{CD}\frac{I_C}{I_D} \\ C_A + C_B + C_C + C_D = 100\% \end{cases} \tag{1.6}$$

Therefore, k-factors of different elements relate as follows:

$$k_{AB} = \frac{k_{AC}}{k_{BC}} \tag{1.7}$$

This ratio approach is the basis for most quantifications in TEM for thin samples [74].

When performing an EDS experiment, a spurious signal is created from the interaction of electrons with the components of the microscope, such as the sample holder. To minimise the influence of the environment surrounding the area of interest, beryllium (Be) clamps and rings are used. Be is a low-atomic number element: therefore its characteristic X-rays have low energy, and its X-ray emission is relatively low when compared with the one from standard copper clamps.

Another important factor is about the material selected for the grids where the sample is deposited during this kind of quantification elemental studies. This choice has to be taken according to the elements composing the sample: if the sample has a common element with the grid, the latter will produce X-rays overlapping with the sample signal. Grids usually give a quite strong signal, with peaks characteristic of the material; to a first approximation, the signal from the grid is uniform in all the pixels of the spectrum image (spatially uniform). In the study case, copper is present inside the sample: a copper grid would consequently make quantification impossible. Gold M-line (approximately 2.1 keV) is partially overlapping with S K-line (2.3 keV), so gold should also be avoided, for compounds containing this particular element. Ni fluorescence spectrum is only partially overlapping with Cu, but not in such a decisive way: in fact, it is possible to deconvolute the two peaks (see figure 3.4). Following these considerations, Ni grids were chosen for all the analyses presented in this section.

Here we list the elements needed for quantification in the Cu_2ZnSnS_4 growth study presented in chapter 3, and some of their characteristic X-ray lines. Characteristic energies are presented; the lines chosen for quantification are underlined.

- Copper (Cu):
  - $\underline{K_\alpha : 8.040\,\text{keV}}$
  - $K_\beta : 8.904\,\text{keV}$
  - $L : 0.293\,\text{keV}$
- Zinc (Zn):
  - $\underline{K_\alpha: 8.629\,\text{keV}}$
  - $K_\beta: 9.570\,\text{keV}$
  - $L: 1.012\,\text{keV}$
  - $m: 0.009\,\text{keV}$
- Tin (Sn):
  - $K_\alpha: 25.271\,\text{keV}$
  - $K_\beta: 28.485\,\text{keV}$
  - $\underline{L_\alpha: 3.443\,\text{keV}}$
  - $L_\beta: 3.719\,\text{keV}$
  - $M_Z: 0.397\,\text{keV}$

- sulfur (S):
  - K_α: 2.309 keV
  - K_β: 2.65 keV
- Nickel (Ni)
  - K_α: 7.474 keV
  - K_β: 8.267 keV[3]
  - L: 0.84 keV

In the NC community, EDS is a routine technique which is usually coupled with SEM. SEM offers the main advantage of the easiness of operation. Nevertheless, it has some limitations as compared to STEM:

1. the electron beam energy is lower (10-20 keV for SEM, compared with the standard 200 keV for TEM), therefore higher energy lines are not visible and usable for quantification;
2. the spatial resolution is limited. STEM uses a probe of nanometric size, with a thin sample, which produces a small widening of the beam; the interaction pear of SEM widens laterally in the material, degrading the lateral spatial resolution. The volume analysed is, therefore, smaller in STEM;
3. the counting rate is generally low[4];
4. usually the elemental quantification is done on a film of NCs deposited on a flat support (typically silicon): solution dries on the support surface. The film needs to be thick, to obtain more counts and therefore a better statistics. Information about the single particle is lost and only average composition can be obtained.

STEM is therefore more adapted for chemical analysis at nanometric scale [87].

The Zeta-factor method

The Cliff-Lorimer ratio needs for accurate enough k-factors; Cliff-Lorimer factors can be determined both theoretically and experimentally. Theoretical calculations of k-factors from first principle are fast and easy, but may produce significant systematic error (in the order of 20 %). Experimental determination of k-factors requires multielement thin-specimen standards with known composition. These standards may not be available.

[3] Ni-K_β line is overlapping partially with Cu-K_α line. Deconvolution is used to avoid mistakes in the quantification.

[4] Some SEM detectors have been developed to increase the counting rate and optimise detection for low-energy X-rays. Bruker's FlatQUAD is a retractable annular silicon drift detector that can be inserted between SEM pole piece and sample to achieve maximum solid angle in EDS. Its counting rate is comparable to STEM-EDS techniques with the Super-X system.

Standards may also be difficult to thin to electron transparency without modifying the elemental ratio or without inducing damage.

Another problem for the Cliff-Lorimer method is X-ray absorption, even in thin specimens. X-ray absorption correction terms have been proposed [88], but prior knowledge of the specimen thickness and density is required for each analysis point.

The ζ-factor method is a quantitative thin-film analysis procedure which overcomes the described limitations in the Cliff-Lorimer method. In this method, all the parameters associated with x-ray generation in a thin specimen and x-ray detection are incorporated in the ζ-factor, which reads

$$\zeta_A = \frac{M_A}{N_V Q_A \omega_A a_A \left[\frac{\Omega}{4\pi}\right] \epsilon_A} \tag{1.8}$$

where M_A is the atomic weight, N_V is the Avogadro's number, Q_A is the ionization cross-section, ω_A is the fluorescence yield, a_A is the relative transition probability, $\frac{\Omega}{4\pi}$ is the detector collection-angle in the whole 4π space and ϵ_A is the detector efficiency. The ζ-factor is therefore dependent only on the x-ray energy and the accelerating voltage, but is independent of the total electron dose, specimen composition, thickness and density. This independence notably simplifies the absorption correction.

C_A, C_B and ρt can be determined simultaneously from measured x-ray intensities, without k-factors. However, the *in situ* beam current measurement during the analysis is the primary necessary value.

The absorption-correction term for a single x-ray line from a thin specimen can be given as

$$A_A = \frac{(\frac{\mu}{\rho})^A_{sp} \rho t \mathrm{cosec}\alpha}{1 - \exp[-(\frac{\mu}{\rho})^A_{sp} \rho t \mathrm{cosec}\alpha]} \tag{1.9}$$

where $(\frac{\mu}{\rho})^A_{sp}$ is the mass absorption coefficients of the characteristic x-ray line in the specimen and α is the x-ray take-off angle. This absorption-correction term is incorporated into the ζ-factor by multiplying it by the corresponding x-ray intensities. Therefore the general expressions can be written as:

$$\rho t = \sum_j^N \frac{\zeta_j I_j A_j}{D_e}, C_A = \frac{\zeta_A I_A A_A}{\sum_j^N \zeta_j I_j A_j}, \ldots, C_N = \frac{\zeta_N I_N A_N}{\sum_j^N \zeta_j I_j A_j} \tag{1.10}$$

and they are solved with an iterative process to obtain composition and thickness. Typically, the convergence rate is very fast. The absorption-corrected composition can be determined simultaneously with the specimen-mass thickness only from x-ray intensity data.

The ζ-factor is generated from data of only a single element; therefore pure elements thin films can be used as standards: they are robust, cheap, easy to fabricate, and their composition is stable. Other advantages with respect to the Cliff-Lorimer method, which will not be detailed here, are the easy calculation of the spatial resolution; the mapping

of composition in terms of the absolute number of atoms; and the determination of the minimum detectable mass values (the smallest amount of a material that can be detected).

The limit of simple Cliff-Lorimer approach is when thin-foil criterion is invalid, because of absorption and fluorescence. It means that the measured counts are lower than the generated ones, making C_A non-proportional to I_A. This problem arises in particular for thick specimens, for characteristic X-ray energies are lower than 1-2 keV, or if X-ray lines differ in energy by more than 5-10 keV (as the higher energy X-ray are less absorbed than the lower energy ones) [89].

In the presented study, Cliff-Lorimer approach is preferred because its approximation is sufficient to model the observation. The sample is thin and all the characteristic X-rays used for quantification are in the range 2-8 keV. The NC thickness is often unknown and changes in every point, due to the shape or due to the irregularity of the NCs, but is typically lower than 10 nm. Absorption is considered to be negligible.

However, being the emission of photons proportional to the quantity of ionised matter, the exposure time is an essential criterion of the quality of signal-to-noise ratio. To improve the analysis time, the technology Super-X has been developed offering a ratio signal/exposure time almost 100 times superior.

FEI Titan Themis

Classical EDS studies are hampered by the sample-detector geometry since the EDS detector is typically placed under a specific tilt angle to the specimen. The number of detected x-rays, therefore, depended on the sample position with respect to the detector, with the highest signal collected when the sample is tilted towards the detector. Contrariwise, at specific tilt angles the signal will be hampered by shadowing effects.

The FEI Titan Themis used in the presented work is an aberration-corrected S/TEM with Super-X technology. It has a broad availability of techniques, but it is optimised for the EDS chemical analysis (figure 1.9a). A key performance metric of EDS is the net measured X-ray count rate, which depends on the count generation rate (set by beam current) and by the collection efficiency (set by the detector system). X-FEG Schottky electron source ensures the higher beam current; therefore, a high localised dose can be applied, and the subsequent nanometer-sized probe has enough current to generate more photons. The Super-X system integrates 4 Silicon Drift Detector (SDD) detectors which are placed very close to the sample area (figure 1.9b). These detectors are windowless to ensure light element detection capability. The system features a 0.9 sr solid angle and collects the emitted photons more symmetrically, limiting the shadowing during sample tilting or in complex samples, especially for low-energy photons. All for detectors sit at a "take-off" angle and location, so that the detectors are better illuminated at 0° tilt, with no shadowing loss [90].

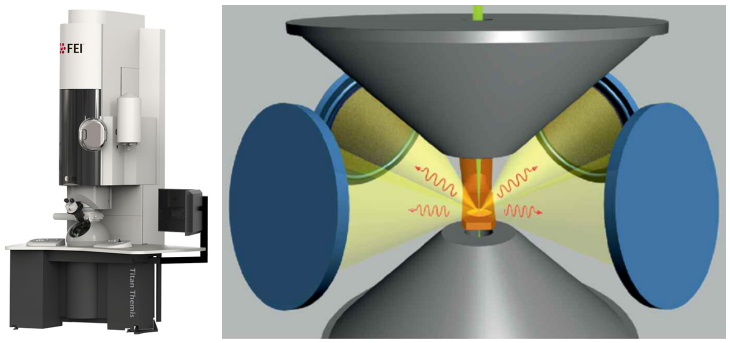

(a) (b)

Figure 1.9 – (a) FEI Titan Themis and (b) schematic of the EDS system design, including X-FEG high-brightness, Schottky electron source, and the Super-X geometry including four SDD detectors arranged symmetrically around the sample and the objective lens pole pieces (not to scale; retrieved from [90]).

1.3.5 Electron Energy Loss Spectroscopy (EELS)

Another spectroscopic technique in the electron microscope is so-called Electron Energy Loss Spectroscopy (EELS), a technique which is often considered as being complementary to EDS. The technique is based on inelastically scattered electrons from the sample under investigation. Elemental composition, atomic bond state as well as valency can be determined by analysing the energy using a spectrometer, which is located under the sample.

STEM-EELS has been attempted extensively during this study, given the advantages of high spatial resolution and chemical information (with valence state) [4]. We aimed to extend the applicability of the technique to discriminate the positions of the isoelectronic Cu and Zn cations. In particular, the presence of a monochromator in our EELS apparatus would theoretically allow the analysis of the oxidation state of the cations. However, the unsolved contamination issue once again interfered with the analysis. Nevertheless, they were not successful. Appendix F shows a typical STEM-EELS experiment on Cu_2ZnSnS_4 NCs; the related obstacles are also described.

1.3.6 Nanobeam Precession Electron Diffraction (NPED)

Scanning nano-beam diffraction is a powerful method, traditionally used to map crystal phases and orientations in different materials. A review of the technique can be found in [91]. The combination of small scanning probe and the use of diffraction allows extracting valuable local information. The technique is extraordinarily powerful when combined with precession of the beam: precession diffraction was first proposed by Vincent and Midgley [92]. Nanobeam precession electron diffraction (NPED) uses a STEM probe formed by a small aperture. The beam is then focused onto the sample; the beam rocks around a cone with a precession angle of some tenths of degrees, the

beam being descanned (the diffraction beam is brought back from a ring to a spot in the diffraction pattern). The probe is small (it is typically formed by a 10 µm aperture) and can give crystallographic information about a small volume. As in STEM imaging, the probe scans the interest object, forming a matrix where each element is associated with a diffraction pattern [93]. To minimise dynamical effects, the incident beam precesses by using deflections coils above the sample. The beam pivot point is placed precisely on the sample plane during alignment routine, and the transmitted beam is re-centred using an additional group of deflecting coils located below the sample (descan). Diffraction patterns are strongly affected by precession: the final image is a merging of the full series of slightly tilted diffraction patterns. Tilting of the beams modifies the dynamical interaction, which fluctuates while the beam orientation changes. The dynamical signal is smoothed out, and the kinematical signal is enhanced[5] [94]. Typically the use of a precessing beam doubles the number of visible spots, with respect to a classic conical illumination. A typical example is shown in figure 1.10 for CZTS NCs .

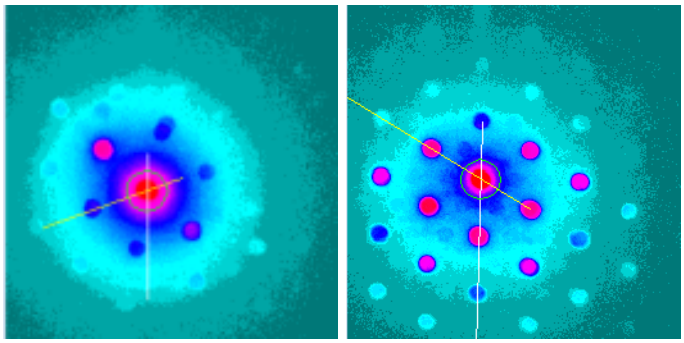

(a) (b)

Figure 1.10 – Nano-beam Electron Diffraction from CZTS NCs (a) by classic conical illumination and by (b) 0.7° precessing beam

It is possible to apply NPED on a large field of view, or on a single NC. In case of a large field of view, a standard application of the method is the calculation of an orientation map [91]. More interestingly, it is possible to perform a phase recognition from a database of given possible structure. If a reference diffractogram is acquired on a reference material (e.g. silicon on a known direction, or any well-defined material) by using the same conditions, it is possible to determine lattice differences which are in the optimum theoretical case better than 2×10^{-4} [93], with a spatial resolution of 1 nm. It is relatively easy to calculate simulated diffraction patterns for a known phase and orientation, and compare them with the experimental diffractograms. The theoretical

[5] In kinematic diffraction, beams diffract only once; in dynamical diffraction, multiple diffraction events occur inside the sample. Considering a beam diffracted in a $\vec{G}_1$ direction, it can be re-diffracted by $\vec{G}_2$ and the final diffracted beam direction will be $\vec{G}_1 + \vec{G}_2$. The intensity of the diffracted spot is therefore redistributed, and if $\vec{G}_1 + \vec{G}_2$ lies on a forbidden reflection, the corresponding spot will be present on the diffraction pattern because of double diffraction.

diffraction pattern is the product between the reciprocal lattice (readily calculated from a known phase) and the Ewald sphere (having radius proportional to the inverse of wavelength). In Bragg conditions[6] the intensity of each node depends on the structure factor; whereas out of Bragg angles intensity drops, and this decrease is set proportional to the distance between reciprocal lattice and Ewald sphere. The main adjustable value for template generation is the maximum excitation error, over which intensity vanishes. This value can be tuned for having simulated diffractograms similar to experimental ones. Templates are calculated for most of the possible orientations (a typical value being each 3° for each axis). Collections of simulated diffractograms are created and compared to acquired patterns; the strongest resemblance indicates the best choice for phase and orientation identification.

The whole identification process is reduced to an image recognition problem. The identification process speeds up by reducing the template information in a limited number of non-zero points (each reflection is characterised by the spot coordinates (x, y) and its intensity). The following image correlation index is calculated for every template:

$$Q(i) = \frac{\sum_{j=1}^{m} P(x_j, y_j) T_i(x_j, y_j)}{\sqrt{\sum_{j=1}^{m} P^2(x_j, y_j)} \sqrt{\sum_{j=1}^{m} T_i^2(x_j, y_j)}} \tag{1.11}$$

where the experimental diffraction pattern is represented by $P(x_j, y_j)$ and every simulated template is represented by $T_i(x_j, y_j)$. The highest Q value corresponds to the solution. Reliability is defined as:

$$R = 100\Big(1 - \frac{Q_2}{Q_1}\Big) \tag{1.12}$$

where Q_1 and Q_2 are respectively the highest and the second highest image correlation indices; in other words, R describes how close the two most probable solutions are. A safe indexing is obtained for $R > 15$. Reliability maps are automatically generated by the program and are used to understand whether indexing was successful in the crystalline zones; artificial misinterpretations[7] must be discarded.

The measurements presented in this work are done using an alpha version of the FEI Epsilon software for acquisition of the data, and a DigitalMicrograph based script, written by Jean-Luc Rouvière for processing. The Epsilon software was available in the framework of the "common lab" project between CEA Grenoble and FEI company. It facilitates the precession, scanning and synchronised acquisition on the FEI Ceta camera (CMOS). It allows tuning the precession and de-rocking of the beam to obtain a stationary, small beam and a focused diffraction pattern at the same time [95]. Considering

[6] Bragg's law reads $2d \sin\theta = n\lambda$ and defines the scattering angle θ in which constructive interference is at its strongest. d is the lattice spacing, λ is the electron wavelength.

[7] The software finds a solution in phase and orientation for each diffractogram. Attention must be taken in the amorphous part of the sample, or on the support. Reliability values in these areas are usually very low. A significant phase mapping is then obtained by combining (i.e. by multiplying) phase map and reliability map.

a standard acquisition time of 0.2 s per pixel, a complete acquisition of a hypermap of $60 \times 60 = 3600$ pixels takes 12 minutes.

When NPED is used with a reference, it is possible to measure strain and relative distance which are in the optimum theoretical case better than 2×10^{-4} [93], with a spatial resolution of 1 nm. A significant application of NPED in the field of Li-ion battery materials was demonstrated in our lab by Brunetti [8]. The phase mapping of lithium iron phosphate $LiFePO_4$ was performed in a large number of particles between 50 and 300 nm in size. Precession electron diffraction was used to sort $LiFePO_4$ and $FePO_4$ at the nanometer scale, despite the similarity of the two phases (difference of lattice parameters <5%).

Chapter 2

Preparation of colloidal nanocrystals for TEM observations

2.1 Introduction

The samples characterised in this thesis are small. Their diameters are generally lower than 50 nm and so they do not need to be thinned to be observed in a TEM. So one could think that a standard deposition of these semiconductor NCs on a thin substrate would be sufficient. Indeed, in general, classical NCs are deposited on amorphous or crystalline films. Generally, amorphous thin films are preferred. Since the user is not particularly interested in visualization of the support film, there is a need of reducing its effect on the image: for that, it should have a minimum and uniform thickness; its interaction with the beam should be minimized, and therefore be constituted of light elements; diffraction or diffusion effects should be avoided. Typically, thin amorphous carbon films with or without holes (holey carbon film) covering standard grids of 3 mm diameter are used. Their thickness is 2 nm to 3 nm. Alternatively, SiN films with thickness ranging from 10 nm to 100 nm can be used. They are more robust and are used mainly for *in situ* experiments [96]. These substrates can be bought at any TEM accessory suppliers. In 2012 graphene layers were used in a liquid cell to replace the SiN films [97] and were rapidly chosen as support for electron microscopy of NCs and nanomaterials. Specimen preparation is a vast subject, and the purpose of this chapter is not to describe all the different methods. A good review can be found elsewhere [98]. This chapter focuses on the processes carried out after the synthesis, performed for the preparation of TEM samples from colloidal nanoparticles.

Section 2.2 presents a concise overview of the traditional NC sample preparation for TEM observation, which is the deposition of the NCs on a thin membrane by drop casting.

As already reported in section 1.2 and as explained in more detail in appendix C, colloidal NCs have a ligand shell, which has many functions: control of the nucleation during growth, stabilisation in solution, agglomeration inhibition, surface passivation. Unfortunately, these organic molecules are a drawback for electron microscopy, as they

undergo degradation under the electron beam, preventing in particular longer time acquisitions necessary for advanced microscopy studies. Section 2.3 reviews the specificities of colloidal NC preparation and in particular their purification.

In section 2.4 the optimisation techniques performed in the frame of the presented work are illustrated. They are inspired by publications from fields and domains which are close to the subject, such as catalysis.

Section 2.5 describes our use of graphene as a support for the NCs.

2.2 Standard colloidal NC deposition methods in TEM

Colloidal NCs are usually synthesised in a high boiling point solvent, which withstands the high temperatures required for nucleation and controlled growth of the crystals. Typical solvents are oleylamine (OLA), octadecene (ODE), tri-n-octylphosphine oxide (TOPO), oleic acid (OA) and 1-dodecanethiol (DDT). When the sample is cooled down to room temperature, NCs need to be transferred from the synthesis solution to another solvent. This step is important. Firstly, right after the synthesis, the solution contains lots of unreacted or degraded precursors which need to be excluded. Also, ligands which are not sufficiently bound to the semiconductor core must be eliminated. Secondly, NCs must be transferred in media allowing processability in the desired application[1] or stability for long-term storage. The suitable solvent depends on the desired application (processability) and the hydrophobicity and polarity of the NC surfaces. These characteristics can be modified by performing a ligand exchange, which is a common strategy to transfer NCs from organic solvents to water.

The purification is performed by flocculation with the addition of an antisolvent. The solvents and antisolvents usually used for purification on the samples are listed in table 2.1. After centrifugation, the precipitant contains most of the NCs; the supernatant is discarded. The precipitant can be redispersed in the desired solvent, with the help of some seconds of shaking. Then another centrifugation cycle is ready to be applied. Not all the solvents and the antisolvents have the same specifications. Solubility as well

Class of NCs	Solvent	Antisolvent
Binary	chloroform, hexane, decane, hexane:decane 8:1 (vol.)	ethanol, methanol, acetone
Ternary, quaternary	chloroform, toluene	ethanol, methanol, acetone, acetonitrile

Table 2.1 – Solvent and antisolvent used for the materials analysed.

as the stability of NCs change in time. For long-term storage, it is important to have non-volatile solvents. Also, 2D and 3D arrangements of NCs on the supporting film are

[1]The medium can be aqueous, in case of applications in biology, such as biomarkers, FRET spectroscopy for diagnosis in living beings; or in apolar solvents, such as toluene, which ensures a long-term stability for storage thanks to the low volatility, or hexane.

influenced by the evaporation rate of the solvent. On the grid, the droplet remains on the support until the solvent evaporates. Hexane is a highly volatile solvent, and NC ring formations are often observed with such fast evaporation. This volatility gives a high temperature gradient between interface and substrate, which perturbs the surface tension and produces convective flow. To decrease the evaporation rate, a low-volatility solvent, such as decane, can be added. In case of low size distribution, the NC organise in a hexagonal array. If the size distribution is broader, the NCs are randomly dispersed on the substrate. The ordering or scale of self-assemblies is considered as a competition between the diffusion of the NCs and the solvent dewetting occurring at the liquid-substrate interface. If the particle diffusion speed in the colloidal solution is slower than the solvent evaporation speed [99], the particle concentration increases below the liquid forces: capillary forces induced by surface tension drive the assembly into a 2D array. It has been shown that under defined conditions of one-drop deposition, the process arises at the liquid/air interface, or even in the bulk solution. When the solvent is completely evaporated, often the distance between NCs is smaller than the sum of two lengths of the ligand crystals, showing an interpenetration of these molecular tails.

Specimens should be observed in TEM as soon as possible after preparation. Otherwise, they should be stored in special conditions, such as in dry air (as water vapour affects the surface), inert atmosphere (dry nitrogen or oil-free vacuum), and in an inert container (glass and filter paper). For long-term storage (up to one month), the previously described strategy works fine. Old specimens can be cleaned by plasma cleaning or chemical cleaning. Nevertheless, the process may thin the specimen further and modify surfaces. The effect of plasma cleaning on NCs can be seen in figure 2.1: atoms are displaced, and the NC surface is damaged. Nanoparticles are often very reactive and

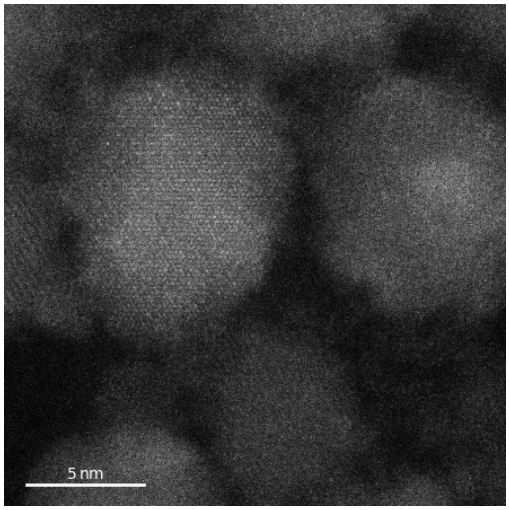

Figure 2.1 – STEM-HAADF acquisition of NCs treated by O and H plasma.

change before observing by TEM. Sometimes, the specimen must be transferred in a controlled environment, by using vacuum-transfer holders or by maintaining them in an

inert atmosphere.

In the following section, some strategies that we applied to allow the use of advanced microscopy techniques are presented. Some of them are routinely used and common in the community. Unfortunately, these procedures did not help to avoid the contamination in the samples. Therefore, new strategies have been proposed and tested. In section 2.3 they are described in detail, and their effect on the samples are analysed.

2.3 Purification procedures

All the reported tests were performed on semiconductor NCs with different composition, ranging from binary to quaternary, and from simple to core-shell structures: PbS, InP and doped InP or core-shell structured InP such as InPZnS, InPZnAs and InPGa, $CuFeS_2$, CuInSSe, Cu_2ZnSnS_4, $CsPbBr_3$.

2.3.1 Solvent-antisolvent and centrifugation cycles

The principle of the purification of the NC solution by a cycle of solvent-antisolvent cycles is described in detail in section 2.2.

2.3.2 Heating the sample

One strategy to remove the organic ligands from the surface of NCs is heating. Heat can be applied at different rates for different periods, under vacuum or air. More importantly, heat can be applied by different means. Here, the standard methods used in our laboratory are listed.

Heating lamp

One method of heating is exposing the grid to a light, emitted by an incandescent light bulb, which concentrates on the grid on an in-house built sample holder. Incandescent light bulbs emit a spectrum which follows approximately a black body radiation. The light emitted is controlled by the voltage applied to the filament. As the temperature cannot be measured directly, a calibration has been made previously to obtain a temperature-voltage relationship. During the calibration, it has been observed that approximately ten minutes are necessary to ramp the temperature up to the steady level. With this in-house built system, it is possible to reach temperature ranging from 60 °C to 230 °C. The sample is kept under secondary vacuum (in particular, a Gatan turbo pumping station). The light passes through glass before hitting the sample. Vacuum is necessary to avoid combustion of the carbonaceous species, and oxidation of the sample. Moreover, the grid is cooled down before extraction from vacuum (fast cooling would make water vapour condensation possible).

Heating sample holder (GATAN)

Microscope manufacturers have developed many heating holder systems in recent years. They feature a furnace, designed for direct *in situ* observation of microstructural phase changes, nucleation, growth and dissolution processes at elevated temperatures. The furnace is made of tantalum or nickel-chrome-iron alloys, and good thermal contact is ensured between specimen and furnace. Miniature heater wires ensure a rapid response to changes in current, as the specimen furnace system has a low mass. A stage controller is used to control the temperature, which can reach 800 °C. It has been reported that the minimum temperature to remove organic ligands is at 300 °C [100]. Unfortunately, at such a high temperature, atomic diffusion is activated, and sintering of NCs is observed. Moreover, the low dimensionality can drastically diminish the melting temperature with respect to bulk material properties. Therefore, the temperature for such heating treatment under vacuum is kept way below this limit. If not stated differently, all samples analysed during this thesis have been heated at 100 °C for at least 1 h by using the heating holder. The light bulb heating system damages the sample more easily. The ligands which are firmly tethered to the semiconductor surface are not entirely removed, but at least the crystalline section does not undergo modifications. At higher temperatures, the NCs are often observed to sinter.

2.3.3 Plasma cleaning

Plasma cleaners are used for removing surface contamination and modifying surfaces. Modern units are small boxes which can accommodate one specimen holder. The tip of the holder is placed in a plasma chamber just before inserting in the TEM. Surface modification and cleaning is possible on glass, semiconductors, ceramics, metal, and more recently polymers and biomaterials. Processes occurring during exposure under plasmas are complicated, but the basic idea is the removal of hydrocarbon contamination on the specimen. Plasma consists of a mixture of energetic electrons and ions which bombards the surface, breaking C−H bonds. With a short enough exposure, the surface of the specimen itself should remain essentially unaffected [74]. Hydrocarbon residuals are gradually reduced in low molecular weight entities and pumped away in the vacuum of the cleaner. The choice of plasma gas is limited to H, O, Ar.

During this thesis H, O and Ar plasmas were tested. Two are the main effects of plasma cleaning:

1. if a sample gives a lot of contamination under electron exposure, plasma cleaning does not provide a solution, the sample is not observable.

2. if a sample has a small amount of contamination, a small exposure to plasma cleaning can improve the observability. As an example, for HR-STEM imaging, a sample can be exposed the double of time (before the “organic cloud” gets significant in the imaging) after plasma cleaning (example, from 30 seconds to 1 minute).

Nevertheless, this minor improvement costs a lot on the surface of the NCs. Plasma impacts on the microstructure of the surface, as from HR-STEM micrographs a diffusion

of the elements composing the NCs are spread nearby. Therefore, plasma cleaning damages the NCs, which are fragile and weak objects. Structural damages and atomic diffusions occur as well. After exposure to plasma over 20 seconds, some heavy atoms composing the NCs diffused away from the semiconductor core. After the tests, our choice has been to reduce the use of this method. The maximum plasma treatment applied was selected to be 10 seconds with a mixture of Ar and H.

Plasma cleaning deserves a particular note when applied to graphene. In fact, it is highly destructive on the carbon monolayer structure, even at low power and short times. Consequently, no plasma cleaning was used on samples deposited on this material.

2.3.4 Cooling

The contamination process typically involves the diffusion of hydrocarbons. The diffusion rate will be therefore an exponential function of the temperature, following an Arrhenius relationship. Cooling is reported to reduce the effect of electron beam damage in crystalline structures [101].

This strategy was discarded in our study as the general problem is not the stability of the crystalline part, but the contamination due to ligands on the surface of the nanocrystals; moreover, generally, the stability and available resolution of cooling holders are inferior when compared with that of room temperature equivalents [102]. Test conducted on the laboratory on similar samples and on graphene [103] did not show any improvement in the quality of contamination.

2.3.5 Beam showering

Beam showering irradiates a vast area of the specimen with a high electron flux so that hydrocarbons which might have otherwise migrate are cracked and form an extremely thin layer of immobile carbon. In principle, the showered area can be examined quite in detail without contamination occurring in the short-term. The showered area forms a "safe zone" around the area of interest. However hydrocarbons may migrate from outside the showered region, and therefore contamination may begin to occur after an interval which is shorter for more heavily contaminated specimens [102]. As this method leaves a thin contamination layer, it should be used as the last form of attack. In particular, for a STEM experiment, the beam showering involves the change of the mode (TEM); change of magnification; retracting HAADF detectors and lowering the fluorescent screen; insert the largest C1 aperture (150 µm); setting spot size to 1 (the largest). Showering times were chosen between 5 and 15 minutes.

The method was efficient for already quite clean samples. Nevertheless, the working time after beam shower is quite short, as consistent contamination builds up again for 5-10 minutes. Moreover, with the high flux of electrons, beam damage is induced in sensitive materials. Beam shower was shown inducing diffusion in semiconductor constituents for long exposure; therefore, these changes in NC morphology are discordant with a solid characterisation. Besides, even though the most recent microscopes are

supposed to be stable, and should charge an alignment configuration without any problem, often that was not the case. Moving several apertures in the microscope, changing the magnification, and mostly changing the beam spot size and the alignment mode from TEM to STEM can provoke a misalignment of the microscope, which is tedious to reset in an aberration-corrected microscope (as it requires extracting the sample and reinserting the cross grating).

In conclusion, beam showering can be used punctually, on already quite clean samples. Nevertheless, care must be taken in considering the changes due to electron damages induced into the sample, and in the alignment of the microscope, particularly when using aberration-corrected machines.

2.4 Innovative purification strategies

As the previously described standard and routinely used purification methods were not successful[2], an in-depth investigation in the literature has been made.

We have searched:

1. samples similar to semiconductor NCs, which share similar drawbacks in surface contamination (metallic NCs, or bulk semiconductors);

2. other research fields where controlling surface properties is crucial.

A review of some of the works that inspired our strategies can be found in appendix D. We found interesting concepts on fast thermal annealing and on purification by acids, and elaborate on these methods in detail.

2.4.1 Fast thermal annealing on semiconductor NCs

Our tests have been performed on InPZn/ZnSe/ZnS core/shell/shell NCs of approximately 4 nm to 5 nm[3]. They are synthesised in the non-coordinating solvent 1-octadecene (ODE) in the presence of myristic acid, a saturated fatty acid. The primary purification of all the samples is made by centrifugation with non-solvent (methanol-ethanol 3:1 vol.), followed by redispersion in $CHCl_3$. InP-based NCs were chosen because they are particularly tricky to observe in electron microscopy. Since they are small, to obtain quantum confinement effect, the size must be contained under the exciton Bohr radius

[2]Some of the samples treated by solvent-antisolvent cycles are not even visible in HR-TEM, degradation occurs in a few seconds. Contamination does not even allow focusing. The only information available is low-magnification STEM. Some other samples are "acceptable" and allow HR-TEM, but no HR-STEM and spectroscopy (EDS and EELS) have been possible. The only two samples that did not show contamination were one batch of Cu_2ZnSn_4 and $CuInS_2$, but the results are not reproducible: by replicating the same procedure to the same batch, contamination appears again and again. The difference in behaviour under electron beam was attributed to the composition of the NCs and the strength of bonding between ligands and semiconductor core, and to the presence of organic molecules in the solution, even after several purification cycles.

[3]These samples are not described in the material characterisation part in this thesis, nevertheless they have been described elsewhere [2, 3].

(10 nm). Usually, to tune the suitable band gap, the synthesis conditions are arranged to obtain diameters ranging from 2 nm to 5 nm. Moreover, they usually do not have a faceted shape but are somewhat spherical. Therefore, the contrast obtained with the supporting film is often small. Lastly, it is complicated to get rid of the excess ligands present on the surface.

Three samples have been tested:

sample A the sample as sorted from the synthesis, i.e. with only primary purification;

sample B the sample deposited on an ultrathin carbon film on copper grid and then treated at 700 °C at 30 s;

sample C dried at 70 °C in a crucible for two hours in order to evaporate the solvent; treated two times at 700 °C for 30 s, then redispersed in $CHCl_3$ and deposited on an ultrathin carbon film on copper grid.

These three samples were then observed by HRTEM to investigate whether fast thermal annealing could be appropriate for these materials.

sample A: standard purification

The micrographs, taken by TEM on the sample processed through the standard purification by centrifugation with non-solvent (methanol-ethanol 3:1 vol.) followed by redispersion in $CHCl_3$, allow the observation of the single isolated NCs. They do not agglomerate and are well dispersed on the carbon film, as observed in figure 2.2a. The shape and the size distribution of the NCs can be easily determined, and the contrast is sufficient to apply automated software routines (such as ImageJ plugins [104]). However, when observing the sample at higher magnification, the surface ligands in excess attached onto the semiconductor part strongly influences the quality of acquisitions. A halo (highlighted by red arrows) appears in the zones exposed to the beam: high resolution is impossible. The interaction of the electron beam with the organic molecules rapidly forms a dark halo in the zone of illumination (figure 2.2b). It is therefore very difficult to operate the TEM in a fruitful manner: regulation of defocus is cryptic, as it is the correction of astigmatism. Neither atomic column resolution is possible under these conditions, nor single particle elemental quantification after spectroscopy studies (EDS, and even more complicated EELS).

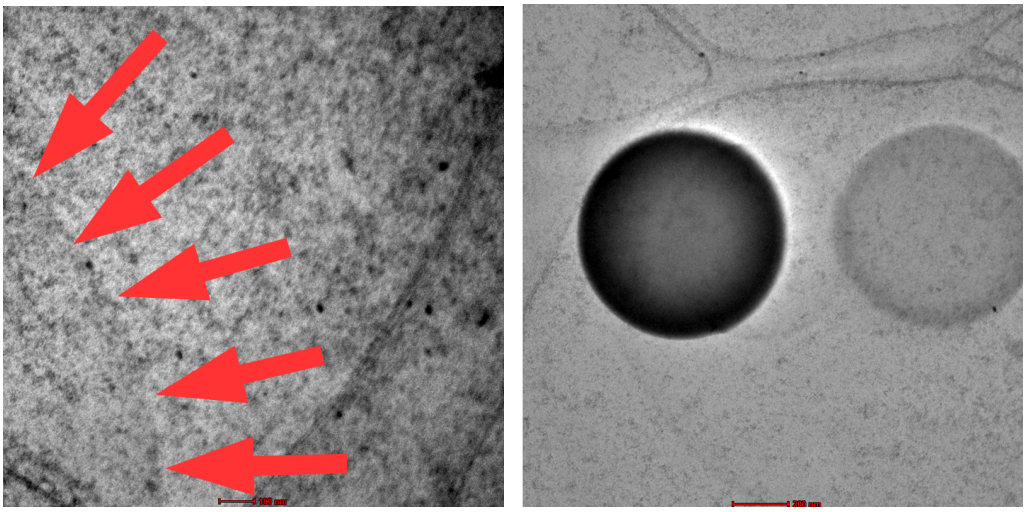

(a) Scale bar 100 nm (b) Scale bar 200 nm

Figure 2.2 – TEM over the InPZn/ZnSe/ZnS core/shell/shell NCs after standard purification (sample A). The halo is produced by contaminants at higher exposure times.

sample B: fast thermal annealing on TEM grid

In this test, after the standard purification by centrifugation with non-solvent (methanol-ethanol 3:1 vol.) followed by redispersion in $CHCl_3$, the solution is deposited by drop casting on an ultrathin carbon film on a copper grid. After complete drying of the solvent, the grid is inserted in a furnace at 700 °C for 30 s under air, then quickly extracted at ambient temperature.

Observation in TEM shows that no amorphous carbon film is left, most of the areas are very dark and much less transparent than usual (figure 2.3a). The supporting layer looks thicker and transparency is greatly reduced. The main limitation arises from the thermal stability of the grid. Carbon supporting films are not mechanically stable at high temperature. They break in vacuum or burn away in air upon heating [105]. Carbon gets oxidised at high temperatures. Moreover, the carbon film exposed to such a high-temperature gradient substantially suffers from strain due to different thermal expansion coefficient with the metallic grid, and it breaks. The ultrathin film certainly breaks, only very thick carbon resists, although in an oxidised form. With such modifications in transparency, the effect on NCs is hardly noticeable. However, some dark areas which are much larger than the original NCs (dark areas have a lateral size of 20 nm to 50 nm) are observed in figure 2.3b. They are likely the result of the aggregation of the semiconductor component.

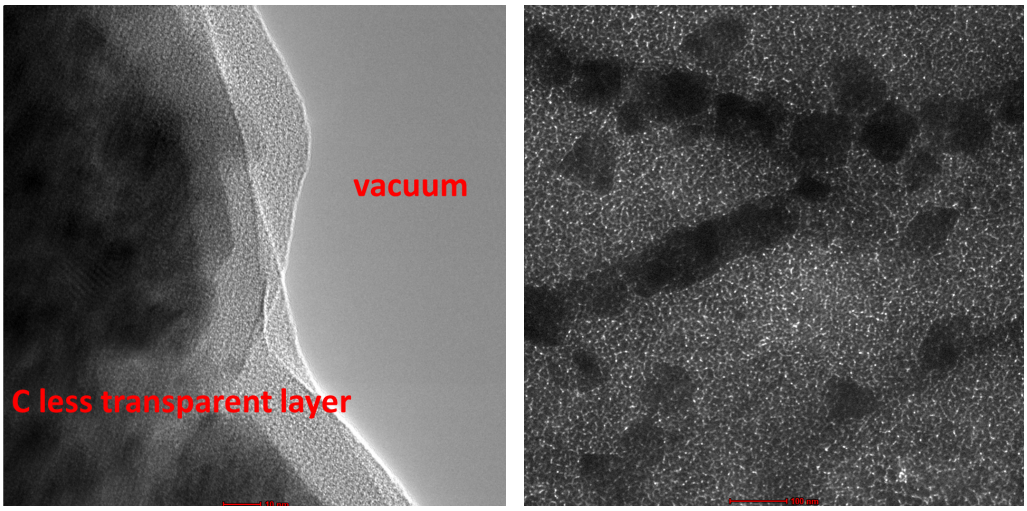

(a) Observation next to a hole formed in the carbon layer. Scale bar 20 nm.

(b) Scale bar 100 nm.

Figure 2.3 – TEM over the InPZn/ZnSe/ZnS core/shell/shell NCs after standard purification and fast thermal annealing at 700 °C for 30 s, performed on the grid (sample B).

sample C: (dry) fast thermal annealing in a crucible, followed by deposition onto a TEM grid

To avoid thermal instability of the ultrathin carbon film at high temperature, the fast thermal annealing is performed in a crucible. After the standard purification by centrifugation with non-solvent (methanol-ethanol 3:1 vol.) followed by redispersion in $CHCl_3$, a small amount of solution is deposited in a crucible. To optimise the efficiency of the thermal treatment, the crucible was put in an oven at a temperature of 70 °C up to complete but mild solvent evaporation (2 hours). The crucible is then inserted in the furnace for 30 s, then extracted and cooled in ambient temperature; then the treatment is repeated. In total the crucible is exposed to 700 °C for one minute. $CHCl_3$ is used to redisperse the NCs in solution: a drop of the obtained liquid is drop cast on an ultrathin carbon film on copper grid.

This testing sample still shows the presence of a contamination halo, which appears more slowly than in the previous samples. In fact, higher magnification images are possible (figure 2.4a), but not enough to obtain atomic resolution, nor images of the crystalline structure[4]. By leaving the electron beam on the grid for 2-3 minutes, the contamination halo appears again (figure 2.4b). Following the promising micrographs obtained by TEM, a test has been performed in STEM-HAADF (figures 2.4c and 2.4d). Here the contamination appears like a white cloud when acquiring high-resolution images. At high magnification, the bright NCs are indistinguishable from the contamination cloud.

[4]Powder X-ray diffraction previously assessed crystallinity, and NC size was calculated from the full-width half maximum of the most intense diffraction peaks using Scherrer equation.

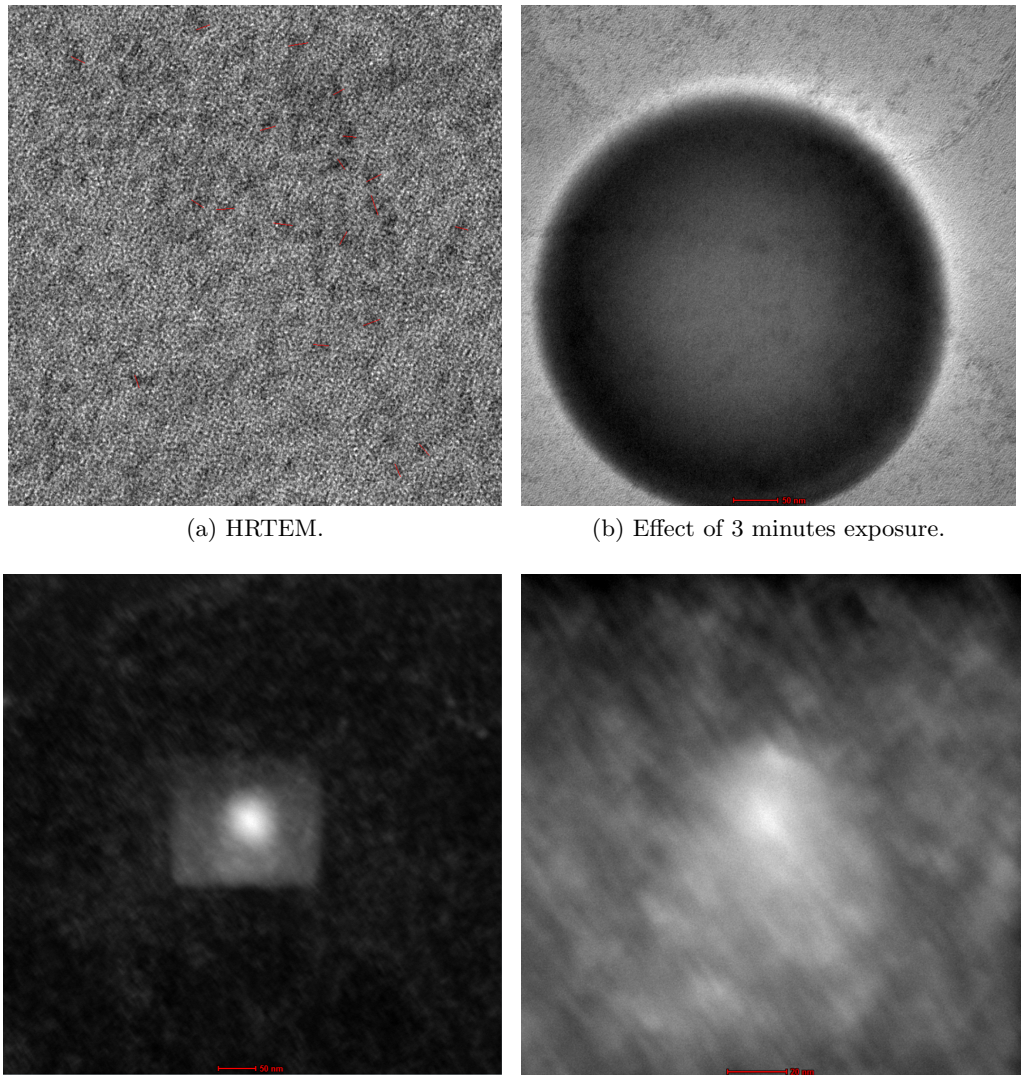

(a) HRTEM.

(b) Effect of 3 minutes exposure.

(c) STEM-HAADF

(d) Detail of (c)

Figure 2.4 – TEM over the InPZn/ZnSe/ZnS core/shell/shell NCs after standard purification and fast thermal annealing at 700 °C for 30 s (sample C).

At low magnification, only the size distribution of NCs is measurable; however atomic resolution is not possible.

2.4.2 Purification of Cu_2ZnSnS_4 NCs by acetic acid

The reports from Akdaş and Seo reviewed in appendix D.2 inspired our next strategy. Although we share similar issues, there are some remarkable differences:

- sample is a chalcogenide in which the anion is S.
- in our case, Zn and Sn replace In, making the NC quaternary.
- ligands are different: Akdaş used a thiol as the sulfur source and surfactant; the solvent is a long chain alkene. For Seo, the ligand is a carboxylic acid and is "replaced" by acetic acid (both molecules have a carboxyl group, the length and saturation of moieties are different). In our study, the sulfur source is elemental sulfur, and the solvent and surfactant is oleylamine, which is a primary unsaturated amine.
- our main interest differs, as our goal is finding a reliable procedure for cleaning NCs for electron microscopy studies.

Solid state purification by acetic acid

At first, we preferred depositing the sample on TEM grids by drop casting. The grid is successively dipped in an antisolvent which contains acetic acid. Three baths were chosen:

1. 3 eq. acetone, 1 eq. acetic acid for 20 s;
2. 0.1 M acetic acid in acetonitrile (CH_3CN) for 40 s;
3. 0.1 M acetic acid in water for 40 s.

Such short bath times[5] were chosen in order not to attack the metal grid (in the test case, the grid was Cu; Au would have been more appropriate, as it is resistant to acid corrosion). The first bath was chosen in relationship to Akdaş antisolvent used for centrifugation purification, Seo's work inspired the second bath. The third bath uses water, where samples are not soluble. These baths were followed by rinsing with chloroform and followed by heating under vacuum at 100 °C. The three grids were therefore observed by HRTEM.

In the sample exposed to the bath in acetone:HAc 3:1 eq. (figure 2.5a), we observe that the film is quite clean. Nevertheless, it is still possible to observe some organic contribution on the surface of all NCs considered.

[5] As a reminder, in Seo's work the ligand exchange is completed in 30 min, despite a ten times lower concentration of the acetic acid with respect to second and third solutions.

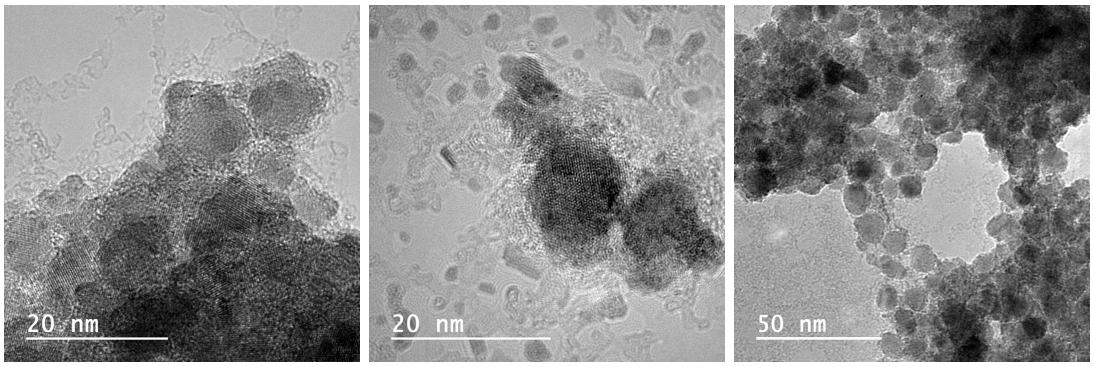

(a) acetone:HAc 3:1 eq. (b) 0.1 M HAc in CH_3CN (c) 0.1 M HAc in H_2O

Figure 2.5 – Comparison of the three baths proposed for Cu_2ZnSnS_4 NCs.

In the case of the bath in 0.1 M HAc in CH_3CN (figure 2.5b), the cleaning is not so successful: some large stains in the carbon film are visible. These stains demonstrate that the purification was not completely successful.

For the sample dipped in 0.1 M HAc in water (figure 2.5c), it was tough to observe isolated samples; some ligands are on the surface of the NCs, and on the carbon film as well. Nevertheless, observation by HRTEM was possible in this case.

Following the results of this procedure, more tests were conducted by analysing the sample by STEM. Some STEM-HAADF micrographs were acquired, and some STEM-EDS mappings were launched to simulate a real experiment and observe the influence of contamination[6].

The acquisitions have microscope parameters (exposure times and electron dose) comparable to the ones in real spectroscopy experiments. In the case of samples which undergo a bath acetone-HAc 3:1, the stability under electron beam improved, and the background contamination is strongly limited. Figure 2.6a has been acquired right after the STEM-EDS acquisition. The visible "fog" concentrates around the NCs, but the form and the position of the NCs are recognisable. Figure 2.6b shows the same area acquired by STEM HAADF at slightly lower magnification: the cloud in the square in the centre is due to the long acquisition time necessary for spectroscopy experiments. Therefore, the effect of contamination coming from organic ligands excess appears to be softened, at least when compared with the previously analysed samples.

[6]Particularly for long-time and high magnification acquisitions, automatic drift correction is necessary for piling up scans of the same area. This drift correction works by autocorrelation of two successive images. If these two images are changing because of the contamination, the autocorrelation algorithm will calculate a displacement which is different from the real one and will cause problems in the final acquisition.

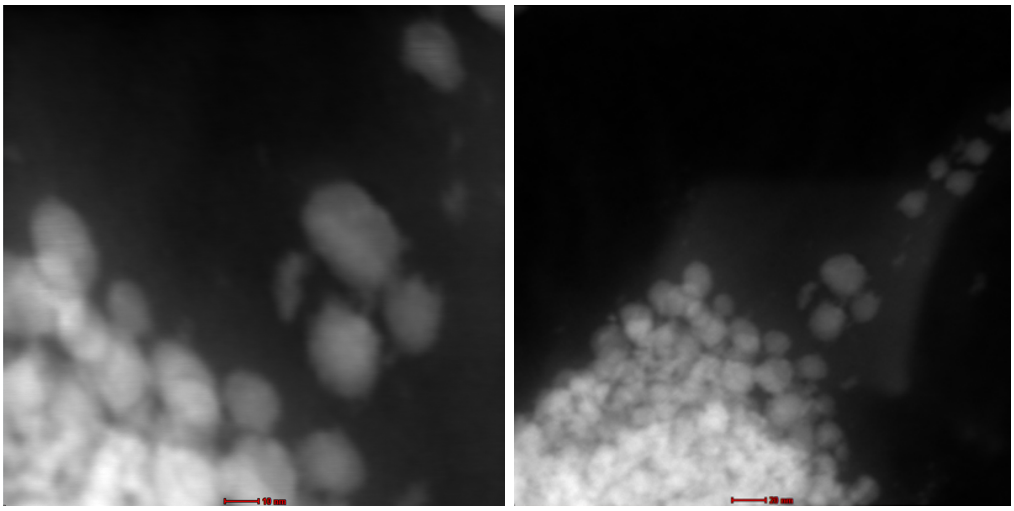

(a) Acquisition zone (scale bar 10 nm)

(b) General plan at lower magnification (scale bar 20 nm

Figure 2.6 – STEM-HAADF images from STEM-EDS acquisitions; 400 s, 1024 × 1024 px. CZTS NCs were poured in an acetone-HAc 3:1 bath. Shape and positions of NCs are clearly recognisable.

Acetic acid as antisolvent in centrifugation purification

As the best results for purification in solid state Cu_2ZnSnS_4 NCs were obtained by the acetone:acetic acid 3:1 eq. solution, this liquid phase was used as antisolvent in ulterior purification tests.

Purification of the reaction solution was performed by 3 cycles of

1. addition of 1 eq. of solvent $CHCl_3$;
2. flocculation by addition of 1 eq. of acetic acid plus 3 eq.s of acetone (HAc - acetone);
3. centrifugation for 5 min at 12000 rpm;
4. discard of supernatant.

Even after three solvent - antisolvent cycles, the solvent is redispersible in $CHCl_3$. After drop casting, the TEM grid (graphene) was heated under vacuum at 100 °C. In this case, the preparation is easier than the dipping treatment performed previously. The efficiency is better, as demonstrated in figure 2.7. Also, there is no issue about the compatibility of grids to acid attack: acid is never directly in contact with the metallic grid.

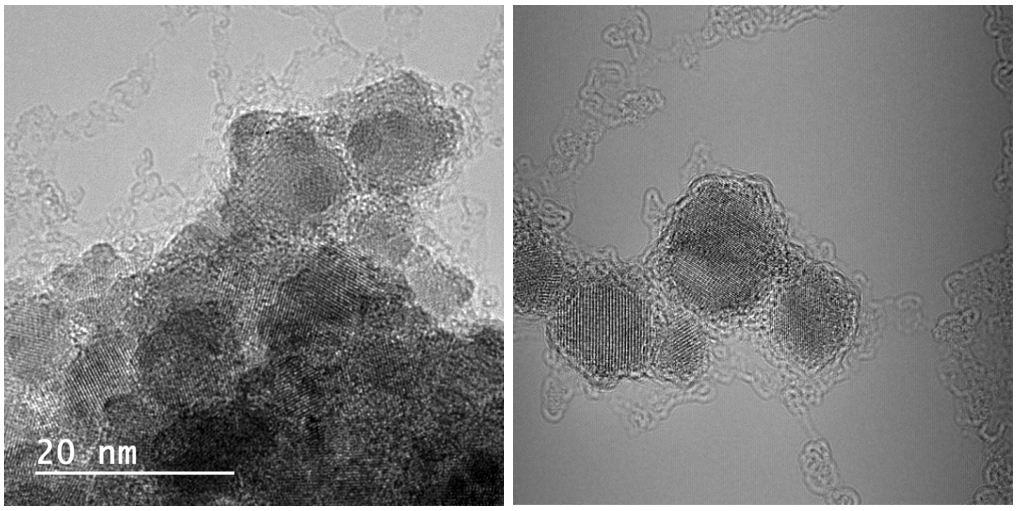

(a) Sample purified in solid state in acetone:HAc 3:1 eq. solution bath

(b) Sample purified with acetone:HAc 3:1 eq. solution as antisolvent

Figure 2.7 – Comparison of purification performed in (a) solid state or in (b) solution.

2.5 Graphene as a sample support for TEM

To control the final efficiency of purification methods for electron microscopy, the real point is to test the application of TEM techniques to the sample, obtain meaningful images and exploitable spectrum images, without modifying the semiconductor core. Even by depositing NCs on ultrathin amorphous carbon film ($< 3\,\mathrm{nm}$), the background signal is relatively high. In particular, the contrast with the ligands is very low: the semiconductor part is visible, but the same is not true for the carbonaceous corona surrounding it. Ligands are in fact relatively light molecules (composed mostly by C and H, and marginally by O, N, S). Growth and transfer methods for graphene have been developed in the last years. In particular, graphene can be readily deposited on a holey carbon grid and be the support for colloidal NC deposited by drop casting. In this case, there is an amorphous carbon film which has holes covered by a freestanding graphene monolayer: the observation of the objects of interest is performed on these holes, where the thickness and the background are minimal. In this section, the preparation of such sample support is explained, and the advantages (and drawbacks) of this approach are analysed.

Graphene is the two-dimensional atomic-scale allotrope of carbon, and in the last years it was an enormous explosion in nanotechnology: its popularity exploded after Andre Geim and Konstantin Novoselov were awarded physics Nobel prize in 2010 “for groundbreaking experiments regarding the two-dimensional material graphene”, and several novel applications have been proposed in many fields of nanoscience and nanotechnology [106]. Recently, graphene has been proposed as support for samples in TEM thanks to its properties. Graphene is thin but highly conductive and can avoid charging

effects, such as charge accumulations in the sample, which can repel the electron beam and create an artificial beam shift in the sample. In fact, amorphous carbon films are not electrically conductive for thickness lower than 4 nm [107]. In the specific field of material science, it is fundamental to image at the atomic resolution to understand three-, two- and one-dimensional volume defects, interfaces and dopants, nanoscale materials. These objects cannot always be prepared as free-standing samples: isolated objects such as nanoparticles, inorganic molecules, NCs, quantum dots and nanotubes - nanowires introduce unique challenges in sample preparation. Of course on ultrathin films, individual heavy atoms can be easily visualised, as beam-induced migration is still slow in comparison with the time needed to obtain high-resolution images. However, it is clear that imaging of low-dimensional and light element materials is limited when using amorphous carbon support: numerous examples include atomic resolution imaging from single-walled carbon nanotubes, single-atom vacancies, topological defects, exact atomic configurations along grain boundaries, and amorphous inclusions.

Crystalline support demonstrates almost no phase contrast down to the resolution of their periodicity, regardless of thickness. By reducing the thickness of the support, the background amplitude contrast (noise) by secondary and multiple electron scattering can thus be minimised. Graphene has renewed interest in crystalline TEM supports: it is essentially electron transparent down to a resolution of 2.13 Å. In HRTEM, the periodic structure of graphene yields a diffracted signal which can be easily Fourier filtered from the images. The single-layer thickness of 0.34 nm contributes only minimally to the background. Graphene is remarkably robust both mechanically and elastically; it is a ballistic electric conductor and shows electrical conductivity more than six orders of magnitude higher than amorphous carbon. The growth of continuous, large-area graphene by chemical vapour deposition (CVD) was essential for allowing a natural application as supports. The changing corner has been CVD growth on Cu foils, thanks to the low carbon solubility and large obtained grain size (solubility lower than 0.001 atom% at 1000 °C, versus earlier production on Ni foils, which has a solubility of 1.3 atom%). Direct transfer of CVD graphene from Cu foils to perforated amorphous carbon supports provides freestanding areas of graphene. When using graphene as sample support in HRTEM and HRSTEM studies, atomic-resolution images inevitably require relatively high electron doses, which can introduce knock-on damage across the support. Radiation damage is limited by lowering the acceleration voltages, below the knock-on threshold for bulk graphene (86 kV) [108]. Normally a voltage of 80 kV is applied, in some cases 60 kV; corrected TEM imaging at even lower voltages (20 kV) is currently under development [109]. When exposed to air, graphene accumulates a significant amount of adsorbed contamination. It contributes to background signal; it can be cleaned by heating (in vacuum at 200 °C to 300 °C) before sample deposition and insertion in TEM.

Graphene is also promising for in situ studies as heating platforms: its transparency, chemical inertness, mechanical and thermal stability make it ideal as a wall for liquid cells [97]. Also, thanks to the transparency of the sample support, it allows the visibility of soft-hard interface in the case of organic-inorganic composite materials [110,111], such as the interface between semiconductor quantum dot and ligands.

2.5.1 Preparation of graphene

While some companies commercially propose suspended monolayer graphene on TEM grids, we decided to transfer graphene from a Cu foil to a holey carbon Quantifoil grids, to better control the different process steps.

A monolayer graphene CVD-grown on a Cu foil, spin-coated by polymethyl methacrylate (PMMA) (which acts as protecting layer), was acquired from Graphenea (schema in figure 2.8). An electrolytic bath (NaOH 1M in water) is used to separate the graphene

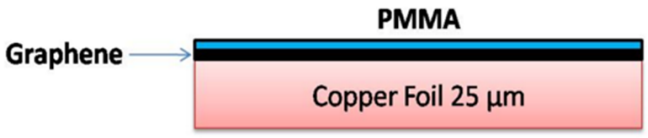

Figure 2.8 – Structure of the purchased graphene from Graphenea.

from the Cu foil. The anode (Pt wire) is immersed in the electrolyte, while the cathode is connected to the side of a square of the copper foil (3×3 mm). The voltage is set to 3.6 V. By holding the corner of the Cu foil, H_2 bubbles separate Cu and graphene. The Cu foil is transferred to a beaker with purified water, and thanks to the separation, the graphene - PMMA floats on the surface. Graphene alone would be transparent if floating on water; the PMMA layer makes it practical to find and manipulate. The floating graphene - PMMA square is transferred to several other beakers, to better wash the surfaces. Then the graphene - PMMA film is "captured" by a holey carbon grid. A graphene - PMMA film deposited on a classic holey carbon grid is obtained after drying. The grid is dipped in acetone to dissolve PMMA. After one hour, the solvent is removed, and the grid dried. The grid can typically be manipulated, with precaution due to the fragility of pristine graphene. To eliminate surface contaminants, the grid is heated at 300 °C for 1 hour before drop casting the sample (solution containing semiconductor NCs).

2.5.2 Ultrathin amorphous carbon vs graphene film

Figure 2.9 demonstrates the potential of graphene as sample support. Figures 2.9a and 2.9b show some of the best images obtained by HRTEM on CZTS NCs, with a voltage of 200 kV on a standard TEM grid. The amorphous carbon signal produces a strong background signal. Moreover, the potential contamination deposited or accumulating on the amorphous carbon is not distinguishable from the support. In case of NCs deposited on graphene (figures 2.9c and 2.9d), for the initial tests an accelerating voltage of 80 kV was chosen to avoid knock-on damage on graphene[7]. It is possible to observe three different zones:

- the crystalline core (in case of exposition of a zone axis and at high resolution, atomic columns are visible);

[7] Knock-on damage threshold at 86 kV

- ligand layers, which are between the NCs or on the surface of NCs: some filiform features are visible. Even though single (light) atoms cannot be resolved, the shape of these ligand chains are clear.
- clean graphene, which for non-monochromated beam appears uniform (except for some bends, tilt-effects, and adsorbates).

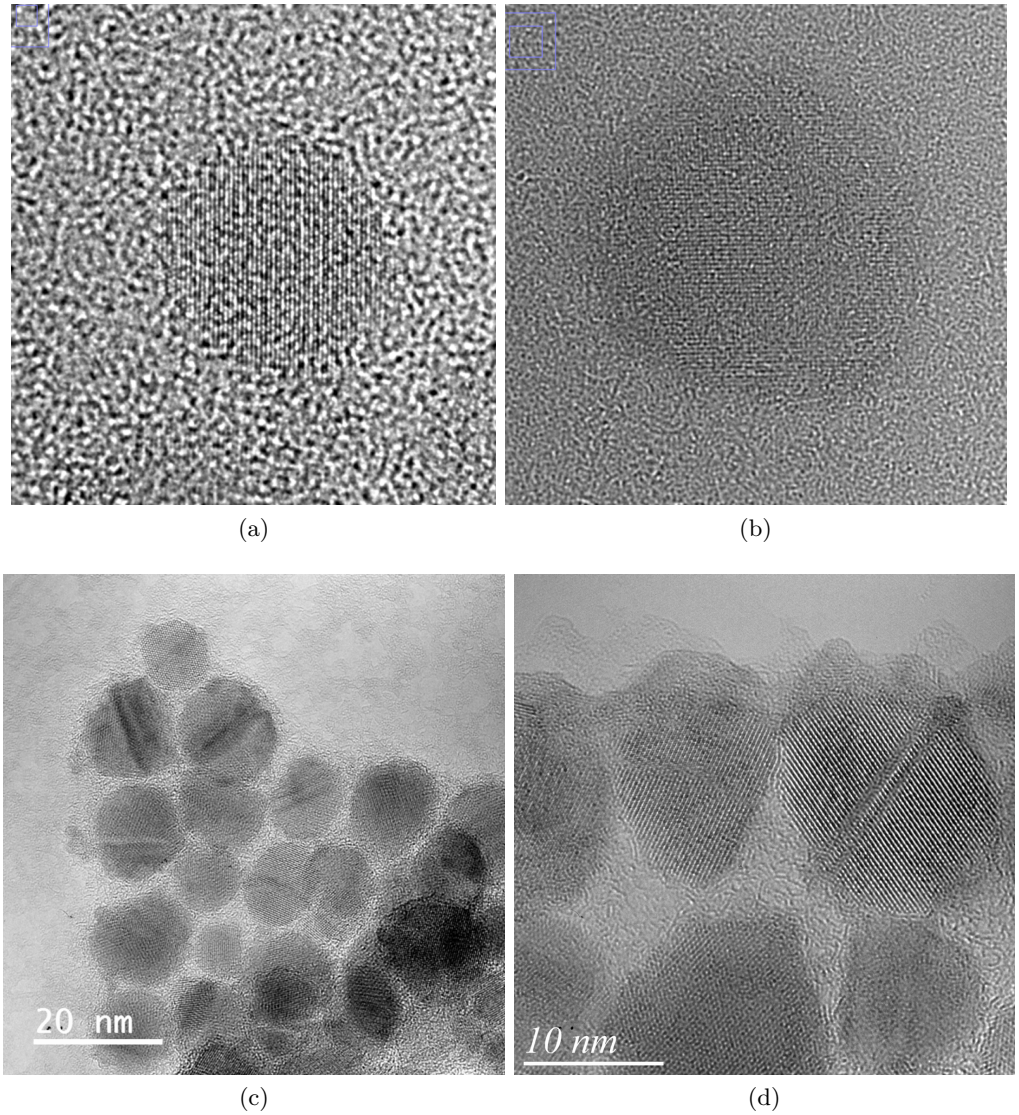

(a) (b)

(c) (d)

Figure 2.9 – Comparison between (a) (b) the best HRTEM images obtained on CZTS NCs deposited onto a ultrathin amorphous carbon at 200 kV and (c) (d) images obtained by non-monochromated HRTEM at 80 kV of NCs deposited onto graphene, where the background contribution is minimized. All the NCs underwent the same purification process. Graphene allows the visualization of the remaining organic molecules on the surface of the semiconductor NCs.

2.5.3 Monochromated HRTEM imaging of nanomaterials supported on graphene

With a monochromator, it is possible to reduce the effects of chromatic aberration (beam energy dispersion lower than 0.3 eV). This microscope component is essential for 80 kV studies of graphene to obtain the atomic resolution on this light and bidimensional material. With the presence of pristine and clean graphene, it is possible to tune the corrector precisely, and therefore minimise the aberrations. Obtaining a higher signal-to-noise ratio, some new features are now visible. Figure 2.10 displays a typical micrograph of a CZTS NC deposited on graphene and acquired with a monochromated beam. The detail of the clean graphene in figure 2.10b shows the characteristic hexagonal pattern. In some areas, there is some amorphous adsorbate, which produces only a marginal noise. Of course, during drop casting of NC solution, the liquid covers the graphene grid completely. Interestingly, some areas of graphene are maintained pristine and clean even after solvent evaporation. The adsorbates on graphene are likely to be:

- PMMA due to incomplete removal of the spin-coated protection layer (1 h bath in acetone is supposed removing that completely);
- oleylamine and unreacted (or deteriorated) precursors still present in the solution (which should have been eliminated by centrifugation purification).

The same effect can also be attributed to areas where more than one graphitic layers are overlapping[8]. The "hard" component of the NC, the semiconductor core, is shown in figure 2.10c. The interpretation of the contrast between atomic columns requires a profound knowledge of the aberrations values and the use of simulation tools, to describe thickness variations and, possibly, elemental distribution in the structure. No particular background noise from the support disturbs the analysis of the crystal structure.

Figure 2.10d shows the advantage of graphene support: a clear visualisation of the hard-soft interface, which separates the atomic columns from the ligands on the surface. There is also a difference between the adsorbates on graphene, which appear brighter in intensity, and the ligands on the surface, which have a filiform appearance. In all the micrographs analysed, NCs are always sitting onto adsorbates of graphene, suggesting that some organic molecules are necessary to "glue" the NCs on the graphene layer, probably thanks to the affinity of organic chains. A complete surface organics removal in the liquid phase[9] appears being detrimental to the deposition on TEM carbon grids.

It is not trivial to distinguish between adsorbates on graphene and ligands and to establish where exactly the interface organic-inorganic stands[10]. Basing the separation only on the intensity variation, a difference in thickness can be observed, ranging from 0.5 nm to 1.5 nm (figure 2.11). Therefore, the observed organic shell is not homogeneous all over the surface: the purification treatments affect likely more efficiently ligands which are tethered on facets with determined orientations.

[8] A quite clean graphene support on another kind of material is shown in appendix E.

[9] Furthermore, complete ligand removal in solution would influence negatively the solubility and aggregates would precipitate.

[10] Because of the quite similar composition, even spectroscopic methods with high spatial resolution cannot distinguish the two components.

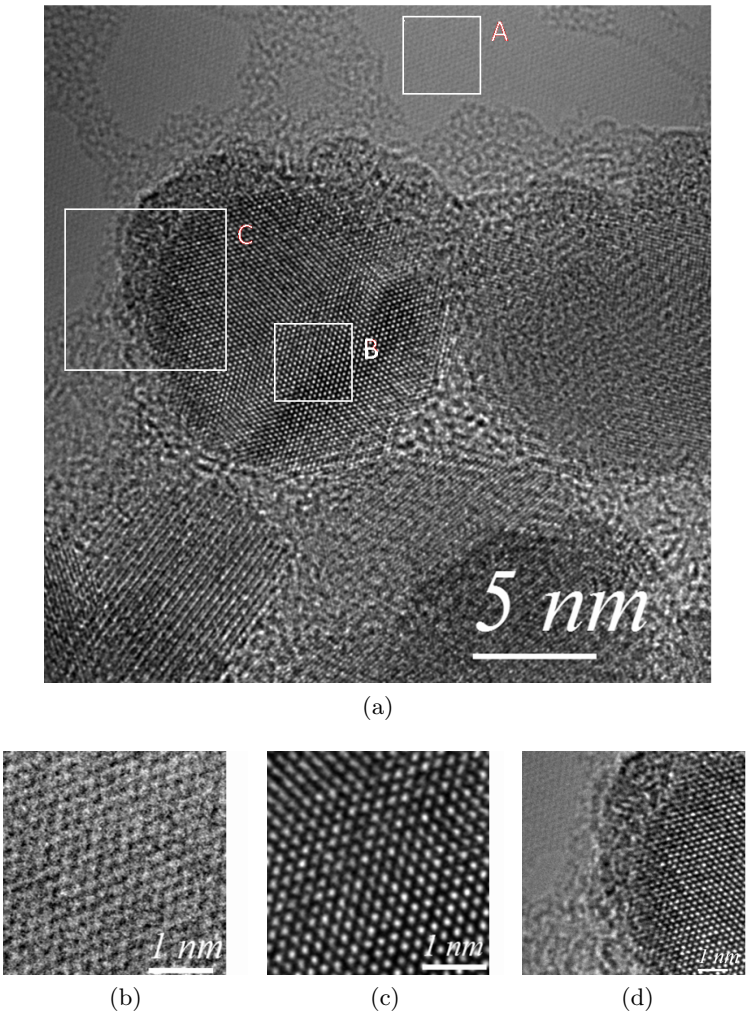

(a)

(b) (c) (d)

Figure 2.10 – (a) Image of CZTS NCs with monochromated 80 kV and details of (b) clean graphene in zone A, (c) NC in zone B, (d) the hard-soft interface in zone C.

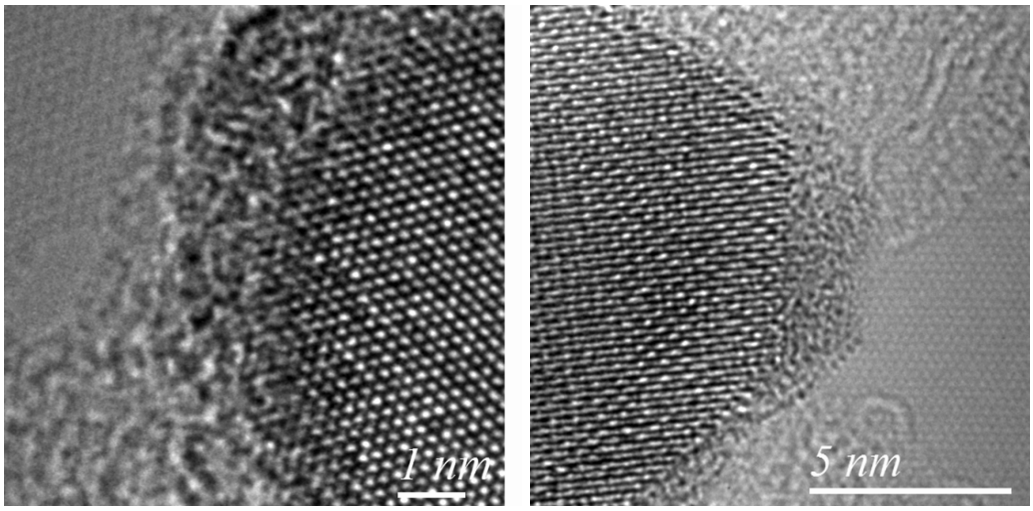

Figure 2.11 – Selected details of the hard-soft interface.

2.5.4 Accelerating voltage on graphene

The first tests by HRTEM and HRSTEM were conducted at 80 kV: knowing the knock-on threshold voltage, the primary concern is about the stability of the graphene film. 80 kV is also the voltage used in electron microscopy of pristine graphene, and most of the novel bidimensional materials. However, good high-resolution images and STEM-EDS acquisitions were taken with an accelerating voltage of 200 kV. No particular degradation of the film has been observed: graphene remained stable under electron irradiation. The explanation is that the 200 kV TEM voltage, used to observe the structure of graphene, creates point defects. Electron beam induces these defects, so the atom position observed in microscopy does not correspond to the genuine pristine graphene structure. Nevertheless, our work only concerns NCs. Therefore, diffusion of carbon atoms in graphene are allowed as long as mechanical stability is maintained (i.e. no vibrations or shifts are observed).

The possibility of using 200 kV accelerating voltage is advantageous for many reasons. First, a higher accelerating voltage means a lower wavelength for the electrons ($\lambda_{80\,\mathrm{kV}} = 0.004\,18\,\mathrm{nm}$, $\lambda_{200\,\mathrm{kV}} = 0.002\,51\,\mathrm{nm}$) and an higher resolution.

Secondly, from the practical point of view, with the advent of correctors, most of the TEM users[11] are routinely operating the microscope at 200 kV. A modification in the accelerating voltage requires a stabilisation time of approximately 8 hours to stabilise the current in the lenses and as well the emission of the gun. This time may disturb other users and requires a rigorous organisation for the planning of the microscope. Last but not least, the manual aberration correction and the corrector converge more efficiently and faster at 200 kV.

[11] Practically, all the ones which are not working with 2D materials

2.6 Conclusion

Ligands surrounding the NCs complicate the observation of NCs by TEM. Sample preparation is, therefore, a critical point, in particular for high magnification studies, for advanced spectroscopy studies (EELS in particular), and for the reproducibility of the experimental results. During this work, several classical physical and chemical methods for the purification of colloidal NCs were tested: solvent-antisolvent dispersion cycles, heating up the sample, plasma cleaning. These methods were not sufficient for obtaining good observations on the samples. Results were hardly reproducible. Moreover, some parameters needed a careful control to avoid damages in the NC (e.g. exposure time to plasma, excessive temperature). In summary, we propose two strategies:

- **Fast thermal annealing** was inspired by a procedure applied in catalysis to activate surface sites of metallic NCs [112]. The sample was heated to high temperature (700 °C) for a short time (30 seconds). The tests were not successful when applied to semiconductor NCs. In fact, when the treatment was applied on the support grid, the damages induced to the grid and the amorphous carbon film were significant; if the treatment was applied over the dried solution, a great change in the size of the NCs and agglomeration were observed. The concentrated electron beam still induced dark halos.

- **Acid treatment**: purification by using an acetic acid solution as an antisolvent in solvent-antisolvent cycles had been tested on $CuInS_2$ and PbS NCs, and was proposed as a good way of removing excess ligands [113], and as a substitutional ligand (in the case of oleic acid ligands) [114]. In particular, we successfully applied Akdaş's procedure to CZTS, inspired by the similarity in structure with $CuInS_2$ and in the synthesis method. Our work extended the applicability of acid antisolvent to one additional material and ligands. A great improvement in TEM image quality was obtained. The study of reaction steps during the synthesis is thus possible, as well as an unprecedented structural characterisation on this kind of nanomaterials. It would be interesting to broaden this cleaning procedure to other kinds of materials and tethered molecules.

An essential contribution to the optimisation of sample preparation also comes from the adoption of graphene as a TEM sample support. This two-dimensional material is becoming widely available; protocols are available for the transfer of the monolayer grown on Cu to the sample grid. Despite a certain fragility, graphene provides a unique level of contrast; due to its atomic monolayer thickness, it allows direct visualisation of the organic corona surrounding the NCs. Moreover, the observation of the contamination deposited on the clean graphene provides an empirical measure of the efficiency of the cleaning procedures precedently tested.

Chapter 3

Investigation of the growth mechanism and structural characterization of Cu_2ZnSnS_4 colloidal nanocrystals

3.1 Introduction

Syntheses of colloidal NCs by wet-chemical methods are interesting alternatives to traditional physical deposition techniques for applications in photovoltaics and devices. As compared to the bulk materials, ternary and quaternary semiconductor nanocrystals provide several distinct advantages, such as tuning the band gap and electronic energy levels by merely changing their size. They also provide excellent control of the composition and internal structure before materials' processing. Moreover, they can be deposited on various substrates without the need for high-cost vacuum deposition techniques. One of the challenges in the synthesis of the quaternary NCs is the control of their composition and crystal structure. By understanding the growth mechanism, it should be possible to identify the crucial steps during nucleation and crystal growth and predict modifications to growth conditions to enhance the probability of forming homogenous nanoparticles of desired phase [16]. However, quaternary NCs tend to form secondary phases in initial reaction stages due to the different reactivity of cation precursors. Detailed structural characterisation of the final synthesis product is therefore needed.

Copper zinc tin sulphide (Cu_2ZnSnS_4) is an important example of this family of compounds (subsection 1.2.2). It emerged as an attractive non-toxic and earth-abundant compound, which also makes it well suited for use as a photovoltaic absorber [48].

Several characterisation techniques including neutron diffraction and Raman spectroscopy have been previously reported for the determination of the crystalline structure of the semiconductor NCs [18,19]. Nevertheless, the results are averaged over the ensemble of nanoparticles, thus neglecting the radial compositional variations in single particles as well as the variations from nanoparticle to nanoparticle. Only advanced characterisation techniques such as STEM-EDS make the elemental quantification as well as the detection of secondary phases feasible down to nanometric resolution. Currently, few are

the reported advanced microscopy studies in the characterisation of semiconductor NCs produced by organometallic synthesis. This scarcity is due to the relative complexity of the task, the low availability of dedicated equipment and the difficulties in obtaining reproducible and effective purification routines (see chapter 2).

Several synthetic approaches have been reported in the literature for the synthesis of CZTS NCs (hot-injection, heating up) [115–118]. Nanocrystals of kesterite and wurtzite crystal structures have been obtained by both techniques. However, according to the recent reports, a photovoltaic device made up of wurtzite CZTS (4.3 % [119]) is less efficient than the one made up of kesterite form (over 9 % [120]). Although the reason is still unclear, this difference might be the result of complex factors including particle size, shape, phase, ligands. For that reason, a number of parameters impacting the synthesis have been investigated in the literature, comprising the precursor concentration [121], precursor reactivity [122], reaction temperature [123], reaction time [121], the coordinating solvent [118], the concentration of the alkylthiol [118,122,124], all of which provided a reaction mechanism and ways to improve the synthetic procedure. Since the objective of this work is to show the applicability of advanced microscopy techniques on the study of reaction mechanisms, we focus on one approach that has received a great deal of attention in the literature: the Steinhagen's heat-up method [117]. We study the reaction mechanisms in detail by advanced microscopy techniques and provide nucleation and growth mechanisms accordingly. In a similar approach undertaken by Coughlan [125], the reaction intermediates of CZTS hot-injection synthesis process has been analysed by STEM-EDS. However, the information was limited to qualitative interpretation, as the study was performed only on line profiles. Here, we present a comprehensive study by combining advanced microscopy and diffraction techniques on the reaction intermediates of Steinhagen's heat-up method. We analyse the aliquots of the reaction medium by STEM-EDS, SEM-EDS and compare them with *in situ* SAXS and WAXS measurements. Following the analysis, we propose a crystal growth mechanism.

Section 3.2 presents an overview of the colloidal synthesis methods developed for CZTS NCs.

Section 3.3 describes the synthesis procedure and gives some hints on the precautions needed to obtain good experimental images by TEM.

In section 3.4, the growth mechanism is studied in detail by Scanning Transmission Electron Microscopy (STEM) in selected reaction steps (*ex situ*). In particular, images are acquired in STEM-HAADF as they provide detailed information about morphology. The quantitative chemical composition is explored by STEM-EDS: the evolution of stoichiometry in the species during the crystal growth is reported from the first steps up to the final sample. The nanometer resolution allows not only size analysis of the sample population, but also composition analysis inside single particles.

In appendix A, the results obtained from the previous section are compared with the findings of *in situ* synchrotron and laboratory diffraction studies (Wide Angle X-ray Scattering (WAXS) and Small Angle X-ray Scattering (SAXS) performed on samples prepared by the same synthesis process. The two studies provide complementary information.

Accordingly, a mechanism of crystal growth during the whole reaction (from the degassing of the precursors under Ar to the final stages of the reaction) is proposed in section 3.5.

An in-depth investigation of the crystal structure determination is presented in the second part of this chapter. A concise description of possible crystal structures of CZTS is given in section 3.6.

Two complementary methods are presented: NPED in section 3.8, and High-Resolution Scanning Transmission Electron Microscope by High Angle Annular Dark-Field imaging (HRSTEM-HAADF) in section 3.9.

Comparison of experimental images with templates and simulations allows resolving the structure for some well-oriented NCs. These findings might shed light on the electronic structure and explain the parasitic exciton recombination pathways in this promising energy material.

3.2 Overview of colloidal synthesis methods for Cu_2ZnSnS_4 nanocrystals

By forming NCs in solution-based routes, elements can be arranged with the proper composition before film deposition for absorber layer formation, and volatile phases or kinetically stable secondary phases can be avoided. Three main crystallographic forms have been obtained for Cu_2ZnSnS_4: the thermodynamically stable kesterite and stannite phases (tetragonal) and the metastable wurtzite phase (hexagonal). Stabilisation depends not only on the reaction temperature but also on the precursors and solvents used in the reaction [47]. Usually, metal salts with elemental sulphur powder lead to the formation of kesterite NCs at high temperature [115–117, 126, 127]. Sulphur powder precursor is generally dissolved in oleylamine solvent: it exists as an alkylammonium polysulfide at low temperatures and transforms to H_2S through the reaction of the polysulfide ions with excess oleylamine at higher temperatures, where it combines with the metal precursors to form metal sulfide NCs [128]. The metal salt and the sulphur precursor can be replaced by one-component precursors, such as metal diethyldithiocarmate complexes, which produces kesterite NCs [129]. Conversely, thiols have a strong coordination ability with the metal cations and favour the stabilisation of the metastable wurtzite structure. Dodecanethiol has been used in the reaction with metal salts [121, 124, 130] and in the presence of metal dithiocarbamate complexes [118], allowing the formation of NCs in the wurtzite structure. The formation of wurtzite CZTS NCs in solution synthesis methods has been attributed to the induced growth of $Cu_{2-x}S$ NCs at the start of the reaction, due to the high reactivity of the Cu precursor toward the thiol precursor, and the resultant formation of Cu-thiolate which decomposes to form the metal sulfide NCs.

The solution synthesis of CZTS NCs began in 2009, with three concurrent group reporting the colloidal synthesis of kesterite phase CZTS NCs with slight differences between the synthetic protocols.

Guo first reported the formation of CZTS NCs by injection of a solution of elemental sulfur in oleylamine into a reaction flask containing the metal precursors at 225 °C with a 30 min growth time. The obtained NCs had a slightly Cu-rich composition of $Cu_{2.12}Zn_{0.84}Sn_{1.06}S_4$ and showed particles falling in the range of 15 nm to 25 nm [115].

Riha reported a hot-injection method improving the monodispersity (12.8 ± 1.8 nm): metal and sulphur precursors were simultaneously injected into a hot solution of trioctylphosphine oxide at 300 °C [116].

Steinhagen preferred a heating-up approach, in which the precursors were mixed together in oleylamine with elemental sulphur, then mixed up at 110 °C for 30 min and heated up at 280 °C for 1 h to obtain kesterite NCs 10.9 ± 2.9 nm [117].

The first report of wurtzite CZTS was described by Lu in 2011, two years after the initial observation of the kesterite phase. The authors stated that using dodecanethiol was prerequisite to stabilise the metastable wurtzite phase, with oleylamine and oleic acid cooperating with dodecanethiol to form nanoprisms and nanoplates respectively [130].

Regulacio reported the formation of wurtzite nanorods in a heat-up procedure [118], monitoring the growth process as a function of reaction time by TEM and XRD. The authors observed that the crystal structure of the resultant CZTS NCs is determined by the structure of the starting seed, that is initially forming binary copper sulfide (monoclinic $Cu_{1.94}S$) NCs. Anisotropic growth started at one side of $Cu_{1.94}S$, inducing the formation of two-component nanostructures consisting of $Cu_{1.94}S$ (10 nm) and wurtzite-type CZTS (5 nm). After 30 minutes, interdiffusion of cations led to wurtzite CZTS elongated in shape. In the presence of oleylamine, cubic $Cu_{1.8}S$ seeds were formed in the first reaction stages, and finally, only zinc-blend derived CZTS phase were produced. This observation confirmed that quaternary Cu chalcogenide NCs shared the same underlying formation pathways of ternary Cu chalcogenides [47]. Liao obtained wurtzite CZTS NCs from a heating-up method, following the formation mechanism by XRD, TEM and EELS [131]. The process is found to begin with nucleation of djurleite ($Cu_{1.94}S$) and the subsequent growth of CZTS - $Cu_{1.94}S$ heterostructures and inter-diffusion of cations, finally leading to single phase and single crystal wurtzite CZTS NCs.

3.3 Synthesis and sample preparation

The synthesis procedure of this thesis employs the optimised parameters from the inspirational work of Steinhagen [117]. The original paper from Steinhagen's group constitutes a pillar in the class of heat-up synthetic method for obtaining CZTS NCs. Nevertheless, the paper presents the results in a rapid communication focusing on the final material and its performance as a solar light absorber, partially neglecting the details of the reaction intermediates and reaction pathways [117]. This method is particularly attractive for CZTS synthesis since the metal precursors are affordable and stable [132]. All precursors are used as received from Aldrich. They were stocked and weighted in a glovebox, as some of them are hydrophilic. A precursor salts solution was prepared by dissolving

adequate amounts of copper(II) acetylacetonate $Cu(acac)_2$ (99.99+%)[1], zinc(II) acetate $Zn(OAc)_2$ (99.99%)[2], tin(II) chloride anhydrous $SnCl_2$ (99.99+%) in oleylamine (OLA) (70%)[3].

OLA is commonly used in the chemical synthesis and capping of various semiconductor nanoparticles. It is a long chain primary alkylamine, which acts as an electron donor at elevated temperature. It is liquid at room temperature and has a high boiling point (358 °C to 360 °C). It exhibits affinity to metals through NH_2 functional groups. OLA acts as a strong reducing agent as well as a stabilizer in the synthesis of nanoparticles [133, 134].

The amount of precursors (table 3.1) is chosen to obtain Cu-poor and Zn-rich NCs. This stoichiometry shows the best properties in photovoltaic cells. Chen [49] summarized the relationship between the cell efficiencies and atomic ratio. The authors elucidated that all the solar cells with efficiencies higher than 8% have $\frac{Cu}{Zn+Sn}$ ratio of approximately 0.8 and a $\frac{Zn}{Sn}$ ratio of approximately 1.2.

The authors indicate two possible reasons for non-stoichiometry: the coexistence of secondary phases and the high concentration of intrinsic defects or defect clusters. Possible defects include Cu, Zn or Sn vacancies (V_{Cu}, V_{Zn}, V_{Sn}), interstitials (Cu_i, Zn_i, Sn_i, S_i) and antisites A_B with A replacing the element B (Cu_{Zn}, Zn_{Sn}, etc.). Defects may also compensate and attract each other, forming defect clusters. Although TEM technique is not able to detect these different types of punctual defects, we recall here these effects of non-stoichiometry and justify why we decided to aim at this composition. When Cu becomes poorer, the *p*-type conductivity is enhanced and V_{Cu} becomes dominant than Cu_{Zn}. Also, the concentration of the $[V_{Cu} + Zn_{Cu}]$ and $[Zn_{Sn} + 2Zn_{Cu}]$ defect cluster increases exponentially, causing severe non-stroichiometry. These two defect clusters have little influence on the electronic structure of kesterites and are electrically benign, so their high population does not affect the solar cell performance negatively. Even, $[V_{Cu} + Zn_{Cu}]$ defect clusters downshift the valence band, enhancing the electron-hole

[1] 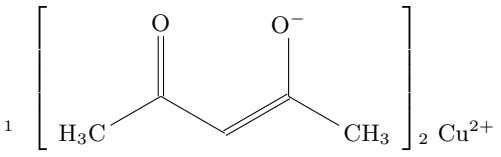

Copper(II) acetylacetonate

[2] 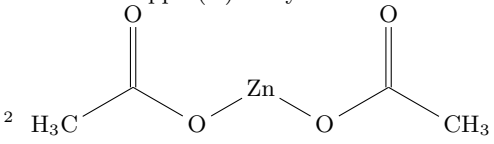

Zinc(II) acetate

[3] 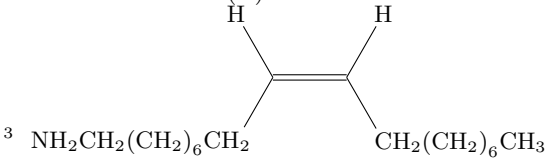

Oleylamine

separation in the light-absorber layer and therefore the overall performance. Under the condition of $\frac{Cu}{Zn+Sn}$ ratio around 0.8, the detrimental $[2Cu_{Zn} + Sn_{Zn}]$ defect clusters have a low population. These defect clusters induce electron-trapping states in the absorber materials and are thus detrimental to the solar cell performance. Indeed, in the same conditions a reasonably high concentration ($10^{15}\,cm^{-3}$ to $10^{16}\,cm^{-3}$) of holes is achieved from ionized $V_{Cu}{}^{+}$.

When Zn becomes rich, the hole population decreases; Sn richness has weak influence on the hole concentration. When either Zn is very rich or Sn is very poor, the concentration of the innocuous $[Zn_{Sn} + 2Zn_{Cu}]$ and $[V_{Cu} + Zn_{Cu}]$ can be very high; on the contrary, when either Zn is very poor or Sn is very rich, the detrimental $[2Cu_{Zn} + Sn_{Zn}]$ defect cluster concentration becomes high [49].

Chemical name	Formula	Amount	Quantity [mmol]
Copper(II) acetylacetonate	$Cu(acac)_2$	0.471 g	1.8
Zinc(II) acetate	$Zn(OAc)_2$	0.240 g	1.3
Tin(II) chloride anhydrous	$SnCl_2$	0.183 g	1
Elemental sulfur	S	0.133 g	4
Oleylamine	OLA	40 µL	

Table 3.1 – Precursors and solvent used in the synthesis of CZTS NCs.

The reaction steps employed in this thesis work are shown in figure 3.1. The whole synthesis process is done under Ar flow. Precursors are poured in oleylamine and put under vacuum (2.9×10^{-2} mbar) in a Schlenk line for some hours at room temperature under vigorous stirring for degassing. Bubbles are continuously created from the solution, that has a dark black colour with some greenish reflections. Several processes occur before reaching the final composition: Cu oxidation state passes from II to I, Sn also changes oxidation state, acetylacetonate is highly reactive. Green colour is due to $[CuCl_4]^{2-}$ complexes.

After 3 hours, argon flow is turned on, and a first aliquot is extracted from the solution (sample 1). Some solid powder is visible, and the solution is blackish.

Then the solution is heated to 110 °C, with a heating ramp rate at $20\,°C\,min^{-1}$. Control of temperature is fundamental to obtain good quality NCs and reproducible results. The reaction mixture is usually heated with standard electric heaters: they can be relatively slow and imprecise, and the highest temperature is usually reached with excessive fluctuations. In our case, the flask is submersed into molten salt at the heating stage at the maximum temperature (280 °C). Molten salts are used to increase the temperature more rapidly than with standard heaters.

After 30 minutes at 110 °C, sample 2 is extracted. This solution shows a dark colour with green hints. A lot of bubbles appear as vacuum line is opened. It has a higher viscosity with respect to the initial stage.

At the initial stage, heating is very fast at the desired temperature (280 °C) when molten salts are used. After 5 minutes from stage 2, the solution reaches already 265 °C, and sample 3 is extracted.

Then the solution stabilizes at 280 °C. Samples 4, 5 and 6 are extracted respectively after 10, 15 and 30 minutes at 280 °C.

After 1 hour at 280 °C, the flask is removed from molten salts and it slowly cools down. In 5 minutes, the temperature reaches 160 °C. In 15 minutes, 86 °C. After 30 minutes, 55 °C. 40 minutes after flask removal from the hot molten salts, solution temperature is 40 °C and the final sample (sample 7) is taken.

All aliquots extracted at high temperature were taken by glass syringes.

The reaction temperature curve is represented in figure 3.1 for clarity. A description of the sample with the numbering of each reaction intermediate is available in table 3.2.

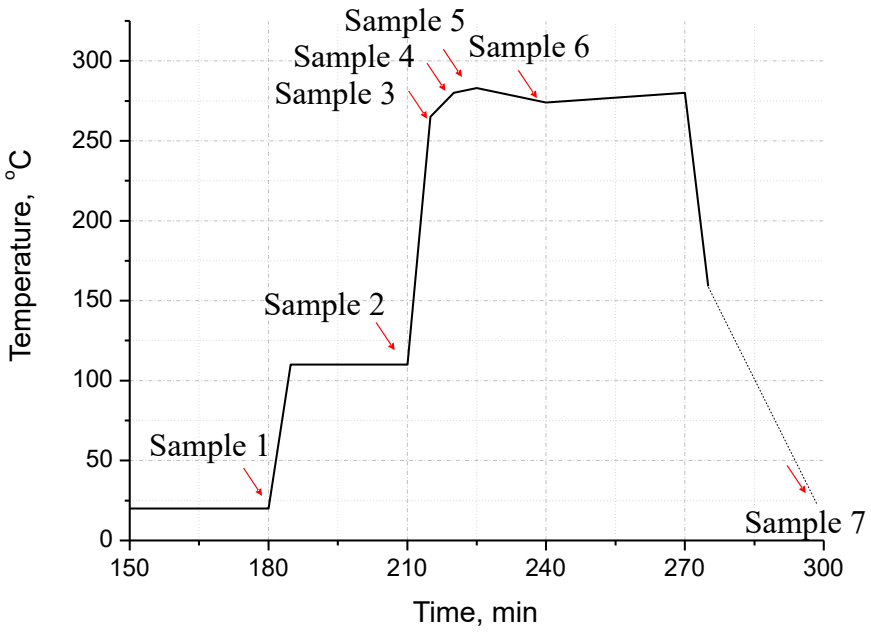

Figure 3.1 – Temperature of the system as a function of time. Arrows indicate the moment of sample extraction (see also 3.2).

Sample number	Denomination
1	mixture of reactants under vacuum, ambient temperature
2	30 min @ 110 °C
3	5 min @ 280 °C
4	10 min @ 280 °C
5	15 min @ 280 °C
6	30 min @ 280 °C
7	final 60 min @ 280 °C, cooled down to RT

Table 3.2 – Samples and reaction steps.

Samples were purified to eliminate all contaminants and organic ligands in excess that could affect TEM characterisation negatively. General strategies and further details are presented in chapter 2. Samples from the most interesting intermediate steps were selected. Purification is done by solvent dispersion - precipitation with antisolvent. In particular, a purification method involving the use of an acid antisolvent such as acetic acid developed in section 2.4.2. Here are recalled the exact purification steps:

1. addition of chloroform (or toluene) followed by precipitation by a solution of methanol-acetone 1:1 vol.;
2. centrifugation at 14 krpm for 5 minutes;
3. removal of supernatant;
4. dispersion in 400 µL of chloroform (or toluene);
5. precipitation with 700 µL of acetic acid-acetone 1:3 eq. solution and centrifugation;
6. removal of supernatant;
7. dispersion in 400 µL chloroform;
8. precipitation with 700 µL acetic acid-acetone 1:3 eq. solution and centrifugation;
9. removal of supernatant;
10. addition of chloroform or toluene[4].

Lacey carbon Ni grids are chosen as sample supports for TEM. They are covered with graphene from Graphenea. The sample is directly deposited onto the carbon-coated side of the TEM grid by drop casting (15 µL). More details for the in-house graphene TEM support preparation can be found in section 2.5. Right before the insertion in the microscope, the grid is heated under secondary vacuum for 1 h at 100 °C by means of

[4]For samples 3 and 7, chloroform is used, and three cycles of purification are performed. Sample 2 was too diluted after the second precipitation; therefore it was purified only in two cycles. Sample 1, 4 and 5 were purified with toluene as a solvent and with two cycles of purification.

a Gatan heating holder. This procedure allows for degassing and eliminating some of the ligands from the surface of the NCs. It was reported in [100] that ligand removal is effective only by heating over 300 °C: however, at such a high temperature, coalescence of NCs is observed. Thus, to avoid crystal modification and thermal excitation-induced atomic diffusion, the temperature is kept relatively low. No noticeable difference in the crystal habit or structure is observed between pre-heating and post-heating specimens at 100 °C; the observation of heated samples is remarkably easier.

3.4 STEM-EDS analysis

3.4.1 Experimental methods

STEM-EDS analysis was performed on the FEI Titan Themis 80-200 kV operated at 200 kV, with a convergence angle of 18 mrad. Gun lens was tuned to obtain a relatively high number of electrons interacting with the sample (0.6 nA current measured on the lower fluorescent screen) and therefore to collect more strong X-ray signal. The Themis microscope is equipped with a Super-X windowless EDS system: four quadrant SDD EDS detectors cover a solid angle of at least 0.7 sr. The specific symmetric geometry of this system avoids artefacts due to X-ray absorption issues, in particular for low-energy photons and thick and heavy materials.

Details on the quantification methods and on the theory of EDS, as well as the details of the spectrum lines used for the quantification can be found in subsection 1.3.4.

Acquisitions have been taken on a 256×256 pixels area at different magnification, to investigate chemical composition at different scales. All acquisitions (except where indicated differently) are about 10 minutes long to have a sufficient signal for a good statistics, without damaging the sample[5]. The chosen acquisition time is a compromise between the need for a high number of electrons and sample stability. Dwell time of the probe for each pixel is chosen to be 100 µs: each pixel spectrum is the sum of the spectra taken for the same point during several scans. The distortion in the image due to sample drift is minimized, and the sample is less damaged (the beam impinging one small area for some seconds would make a hole in the NCs and in the support film, in this case, graphene, which is somewhat fragile). The total integration time for each pixel results to be approximately 10 ms. A drift correction tool is needed to avoid misinterpretation in the final mappings: even with an extremely stable microscope, drift is a real problem in long acquisitions. Drift correction software calculates the correlation between two successive images, and therefore the correction to be applied via the scanning coils. The efficiency of this strategy usually is excellent, under condition where shift is limited, and where successive images are comparable (different successive images are typical for beam-sensitive or contaminating materials; on the other hand, alignment routine usually

[5]With the relatively high current hitting the sample, several damages can occur, such as atom diffusion. During STEM-EDS acquisitions, a control STEM-HAADF image is acquired at every scan; this is a great tool to observe potential crystals shape changes or modifications in the border which get less sharp. These changes would prove whether the beam energy corrupts the sample.

works well on low magnification acquisitions, as drift is relatively low and details are often very sharp). In this study, drift correction is applied every 3 seconds, after each probe scan.

Subtraction of the background is necessary to obtain reliable quantification. An optimised physical bremsstrahlung model for TEM is provided for perfect fitting to some selected intervals, which do not present elemental characteristic lines (11 intervals for this sample).

Sample 1

Sample 1 has been taken from the mixture of reactants in oleylamine, after degassing under vacuum for 3 hours at ambient temperature. Interestingly, NC formation is already observed as shown in figure 3.2. Their size is approximately 12 nm, with a quite irregular shape.

Some bright zones are visible: they are due to segregation of Zn element, as will be shown later in figure 3.5.

In fact, the mixture already turned black-green, indicating the formation of NCs in the solution. During the purification process and after centrifugation, a deposit of a blackish mass on the bottom of the eppendorf is visible. The supernatant is dark green, indicating the presence in the solution of complex species $[CuCl_4]^{2-}$. The composition

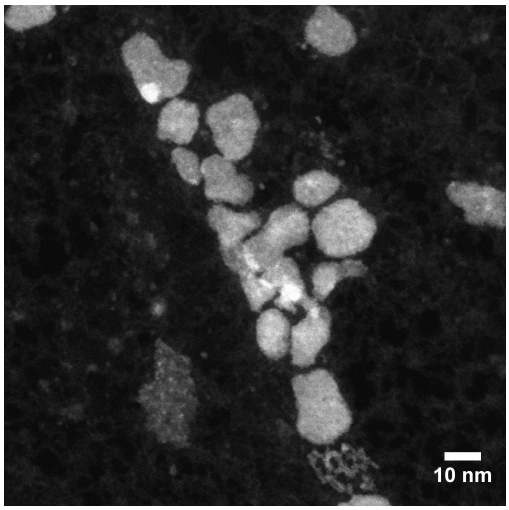

Figure 3.2 – Sample 1 is the reactants solution extracted after mixing and degassing.

of these NCs is analysed by STEM-EDS and homogeneity is studied.

The analysis presented in figure 3.3 shows some irregularly shaped aggregates, as well as a portion of free graphene (support). The particles are mainly composed of Cu and S. Sn is either not present, or its signal is under the noise level. Zn seems to be confined in zones which are smaller than 2 nm. It is not possible to distinguish whether those clusters are incorporated inside the NCs, or if they lay on the surface. Isolated zinc clusters, far from NC, were not observed.

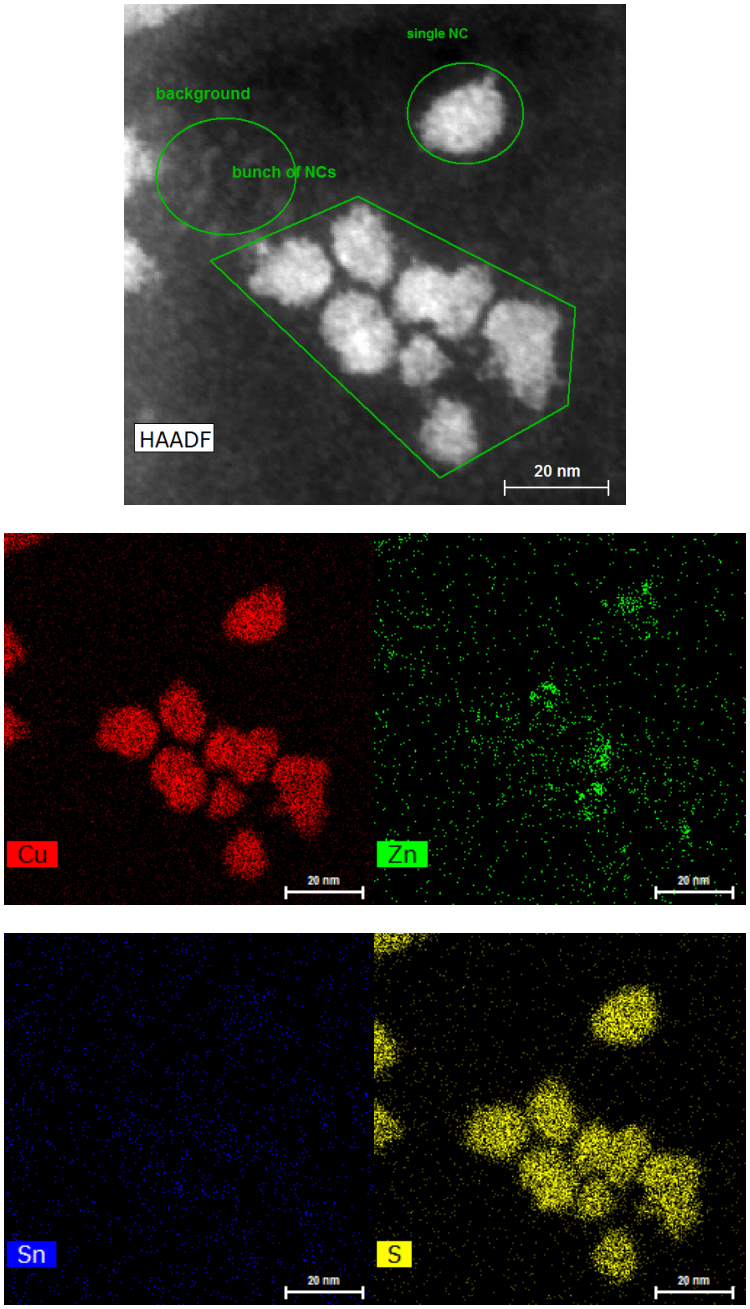

Figure 3.3 – General plan of acquisition area and elemental maps (Cu-K_α, Zn-K_α, Sn-L_α and S-K_α) in sample 1. Spectra from pixels delimited by green lines are integrated and used for elemental quantification in table 3.3.

In figure 3.4, EDS spectra integrated from different areas are shown. Cu and S signals are originated from NCs. While Zn signal is very low, Sn signal is either absent or under the noise level. In the background zone (graphene monolayer), there is not any detectable signal from the elements constituting CZTS. The composition calculated from the single NC and the one from the bunch of NCs are presented in table 3.3: these values are comparable, suggesting a homogeneous composition which indicates binary crystals. Values correspond to a stoichiometry of $Cu_{5.18}Zn_{0.06}Sn_{0.00(3)}S_4$. Nevertheless, these are not values for the usual stoichiometric copper sulfide compounds. The stoichiometric ratio $\frac{Cu}{S}$ is approximately 1.3.

The organometallic copper precursor is copper(II) acetylacetonate, where Cu has an oxidation state of (II). In Cu_2ZnSnS_4, Cu has an oxidation state of (I): Cu oxidation state changes during the reaction. At this stage of the reaction, following the stoichiometric ratio between copper and sulfur, it is possible to speculate the ratio between Cu^{I} and Cu^{II} in the solid already formed in the solution. Cu_2S only contains Cu^{I}, whereas CuS only contains Cu^{II}. If we approximate a binary composition, the following equations can be set:

$$Cu_{5.18}S_4 = Cu_{1.295}S = xCu_2S + yCuS = Cu_{2x}S_x + Cu_yS_y \tag{3.1}$$

$$Cu_{1.295}S = Cu_{2x+y}S_{x+y} \tag{3.2}$$

$$\begin{cases} 2x + y = 1.295 \\ x + y = 1 \end{cases} \quad \begin{cases} x = 0.295 \\ y = 0.705 \end{cases} \quad \begin{cases} [Cu^{I}] = 0.295 \\ [Cu^{II}] = 0.705 \end{cases} \tag{3.3}$$

As shown in equation 3.3, in sample 1 Cu^{I} represents 29.5% of the total copper amount, Cu^{II} represents the remaining 70.5%.

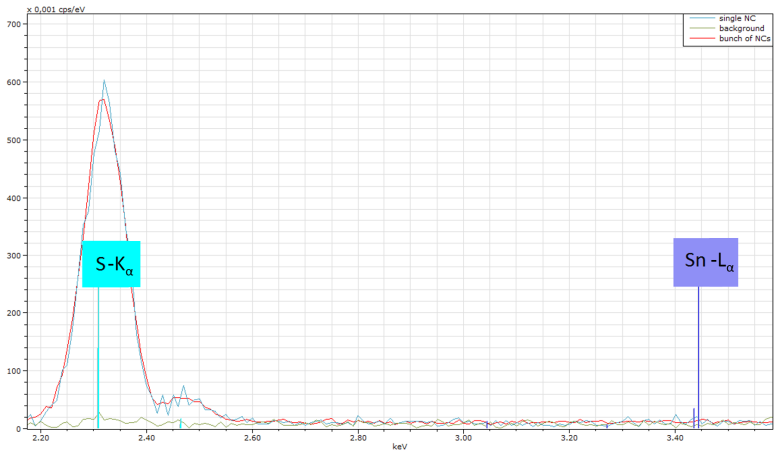

(a) Characteristic lines for Sn and S.

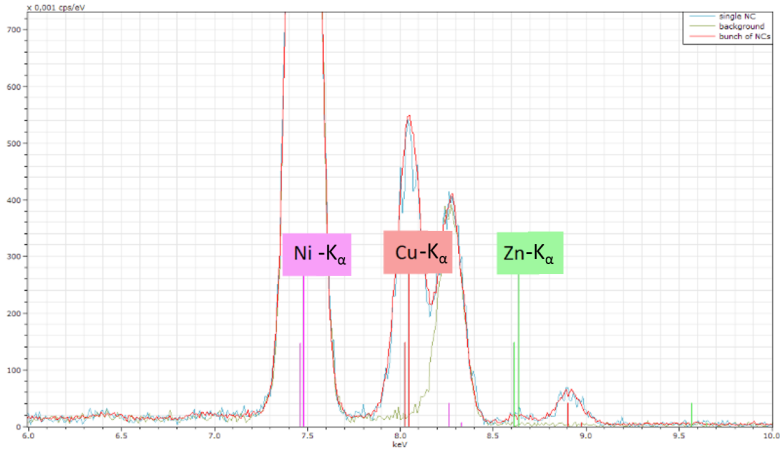

(b) Characteristic lines for Cu and Zn, with the parasitic signal from the Ni grid.

Figure 3.4 – EDS spectra of nanoparticles observed in figure 3.3.

	Single NC		Bunch of NC	
Element	Atom C. [at %]	Rel. error ($\frac{\sigma}{c}$)	Atom C. [at %]	Rel. error ($\frac{\sigma}{c}$)
Cu	56.0	3.45	57.8	3.11
Zn	0.68	18.18	1.78	6.81
Sn	0.03	106.35	0.20	33.25
S	43.3	3.68	25.7	3.22

Table 3.3 – Elemental quantification of sample 1 in the zones labelled "single NC" and "bunch of NCs" in figure 3.3.

The acquisition presented in figure 3.5 is taken at a higher magnification (1.8 Mx). Four NCs have a size of approximately 10 nm and are surrounded by some smaller particles. Cu and S are homogeneously distributed in the nanoparticles as shown in figure G.1, while Zn is concentrated on the surface of the NCs. Sn signal is under the noise level. Elemental mapping of Zn and Sn show that only these two elements are forming the smaller objects presented in this acquisition.

Figure 3.5b shows a partial chemical map of the largest NCs obtained by superimposing Cu (red) and Zn (green) maps. Segregation of Zn is evident. Smaller NCs contain only Zn and a tiny amount of Sn, while Cu and S are absent.

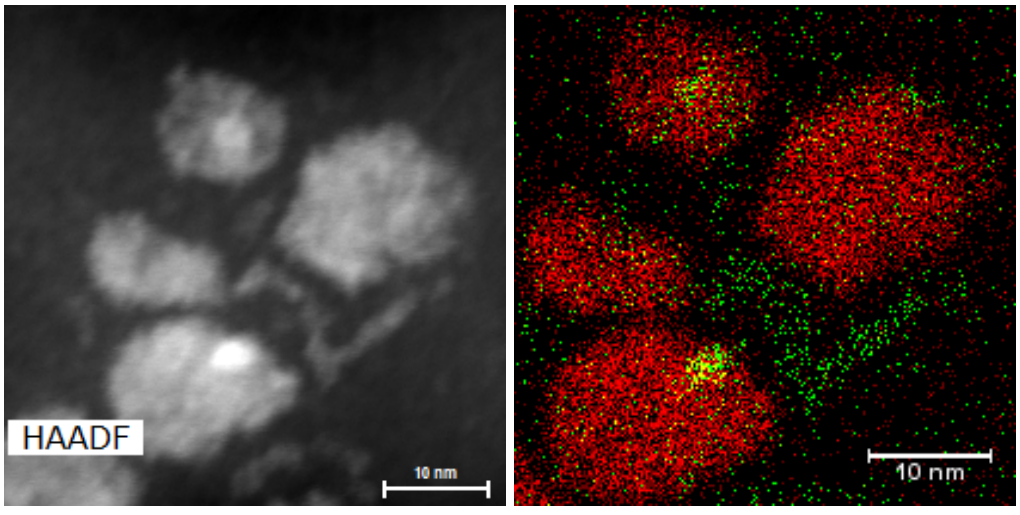

(a) (b)

Figure 3.5 – (a) General plan of acquisition area and (b) Cu-K_α and Zn-K_α chemical mapping of the same area (sample 1).

The next acquisition presented in figure 3.6 is taken at a magnification of 640 kx. It shows a dozen of NCs, with an irregular habit, approximately 10 nm in size. Also, some smaller objects are observed in the image. Some of the larger NCs are labelled in the image, and their X-ray spectra are integrated: quantification results are presented in table 3.4. NCs (and the area that they cover) are small and thin in absolute scale.

Therefore noise is relatively high. Nevertheless, the homogeneity in the composition can be properly investigated.

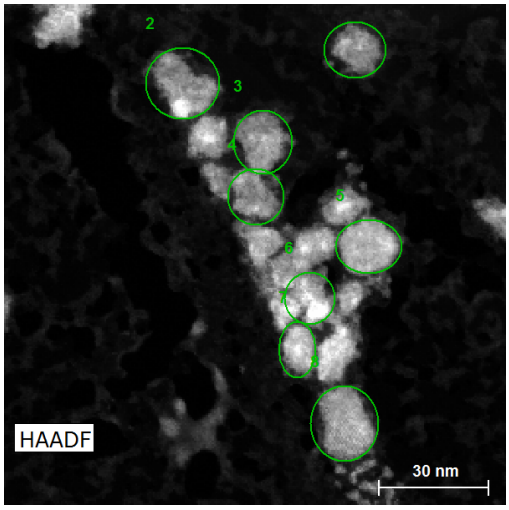

Figure 3.6 – STEM-HAADF general plan of acquisition area at a magnification of 640 kx of sample 1.

Atomic concentration [%]				
NC label	Cu	Zn	Sn	S
1	56.22	0	0.80	42.98
2	53.94	1.69	0	44.37
3	56.30	1.26	0.26	42.17
4	56.85	0.75	0.36	42.04
5	55.45	0	0.26	44.28
6	54.25	3.18	0	42.57
7	51.58	6.57	0.93	40.91
8	56.12	0.38	0.24	43.26
average	55.1	1.7	0.4	42.8
standard deviation	1.7	2.2	0.3	1.2

Table 3.4 – Elemental quantification of sample 1 from spectra integrated from labelled zones in figure 3.6.

Average composition corresponds to $Cu_{5.14}Zn_{0.15}Sn_{0.04}S_4$ ($Cu_{1.295}S$); standard deviation is relatively low for Cu and Sn, and no noticeable fluctuations in composition are observed.

Sample 2

Sample 2 was taken from the flask after purging under Ar for 30 minutes at 110 °C. The sample tolerated only two purification cycles rather than the three that are usually performed.

In the STEM-HAADF images acquired in this sample, interesting features are observed (figure 3.7). The sample is not uniform, as three different morphologies are observed:

1. spherical particles of approximately 10 nm;
2. two-dimensional platelets-disks, which pile up and show their lateral projection: they are 10 nm wide and 3 nm thick;
3. smaller particles of < 2 nm.

The difference between spherical particles and two-dimensional platelets is confirmed by profiles in STEM-HAADF and in STEM-EDS signal. Integrated spectra (table 3.5) acquired on the whole image give an average composition of $Cu_{2.97}Zn_{1.04}Sn_{0.52}S_4$. These values represent an excess of Cu and a lack of Sn cations in comparison to the stoichiometric compound.

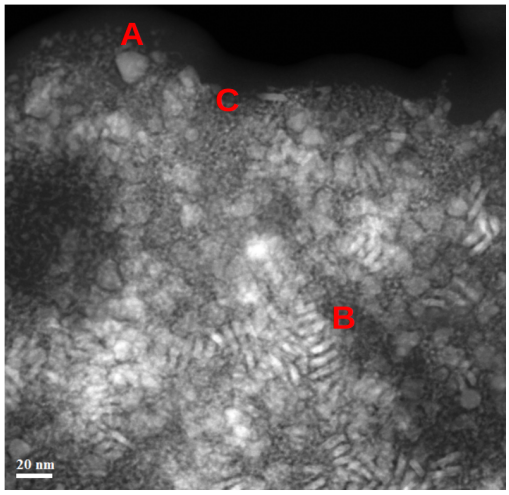

Figure 3.7 – STEM-HAADF image of sample 2 acquired at a magnification of 320 kx. A) Spherical particles, B) 2D platelets, C) smaller particles with $d < 2$ nm

Overall composition		
Element	Atom C. [at %]	Rel. error ($\frac{\sigma}{c}$)
Cu	34.85	3.09
Zn	12.13	3.25
Sn	6.14	10.23
S	46.87	3.11

Table 3.5 – Elemental quantification of sample 2 for all the particles in figure 3.7.

The next acquisition shows the presence of small and large particles (figure 3.8). The top left zone is occupied exclusively by the smaller particles, while the rest contains the larger particles. Thus, the composition difference between the two populations can be distinguished. It is important to note that small particles could be found near large particles; however, their contribution to the EDS signal is relatively small. By observing Cu and S elemental mapping in figure 3.8, these two elements are the main constituents of larger size NCs and platelets. On the other hand, Zn and Sn signals are quite homogeneous in the whole zone. Elemental compositions are listed in table 3.6 for the smaller nanoparticles and for the larger objects (platelets and large NCs). Atomic composition for the smaller objects corresponds to $Cu_{1.64}Zn_{1.62}Sn_{1.71}S_4$, and for the larger objects corresponds to $Cu_{2.75}Zn_{0.66}Sn_{0.45}S_4$ (smaller NCs may also be present in this zone). The composition is considerably different in the two populations. The atomic ratio $\frac{Cu}{Zn+Sn}$ is 0.49 in the area occupied only by smaller particles, while it is 2.47 in the area populated by larger particles (we remind that in final stoichiometric Cu_2ZnSnS_4, $\frac{Cu}{Zn+Sn}$ is 1).

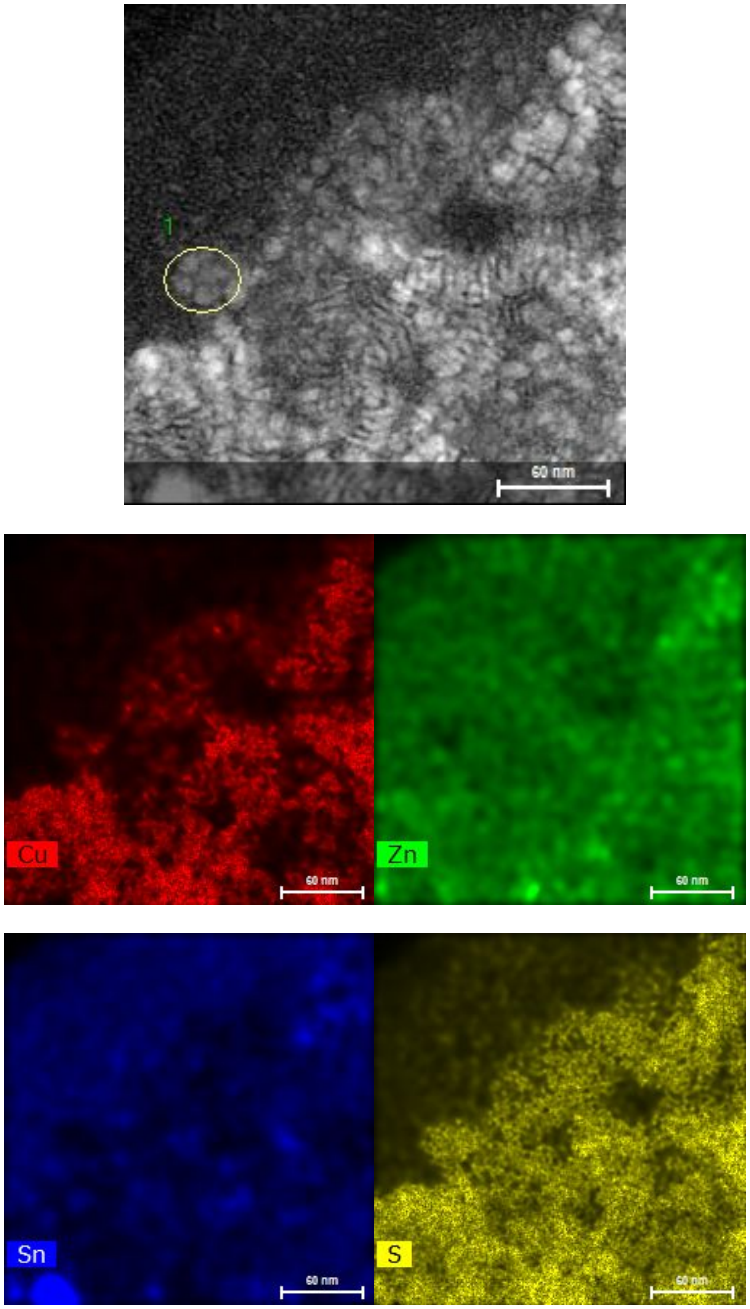

Figure 3.8 – HAADF-STEM image and elemental mappings (Cu-K_α, Zn-K_α, Sn-L_α and S-K_α) of sample 2.

	Smaller particles		Larger particles	
Element	Atom C. [at %]	Rel. error ($\frac{\sigma}{c}$)	Atom C. [at %]	Rel. error ($\frac{\sigma}{c}$)
Cu	18.23	3.26	35.00	3.06
Zn	18.16	3.26	8.44	3.26
Sn	19.05	10.10	5.73	10.2
S	44.57	3.17	50.83	3.08

Table 3.6 – Elemental quantification of sample 2 of smaller and larger particles.

In the next acquisition (figure 3.9) all three kinds of particles are present (small nanoparticles, large nanoparticles, platelets) and they are better separated. Small nanoparticles composition corresponds to $Cu_{1.38}Zn_{2.30}Sn_{1.61}S_4$, whereas the large nanoparticles and the platelets contain mostly Cu and S ($Cu_{2.60}Zn_{1.07}Sn_{0.58}S_4$ and $Cu_{2.43}Zn_{1.00}Sn_{0.74}S_4$ respectively). Large nanoparticles and platelets have similar compositions.

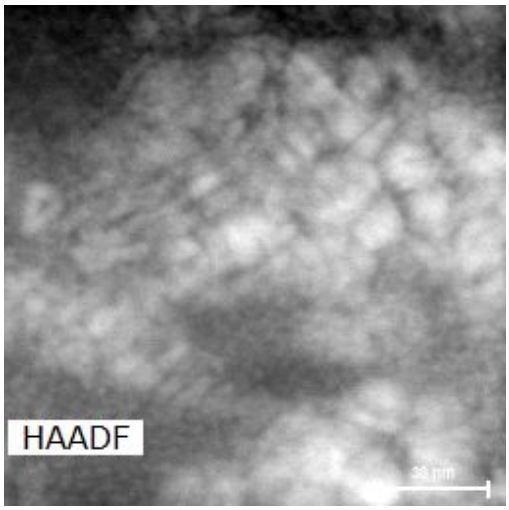

Figure 3.9 – HAADF image of sample 2. Labelled areas are integrated for quantification.

Atomic concentration [%]				
Label	Cu	Zn	Sn	S
Small NCs	14.82	24.76	17.35	43.08
Platelets	32.13	13.48	7.26	46.81
Largest NCs	30.32	12.52	9.37	47.79

Table 3.7 – Elemental quantification of sample 2 for different objects.

Figure 3.10 compares the EDS spectra of an isolated large NC and of a group of small NCs normalized over the Ni peak. The absolute amount of Zn and Sn are constant for both species, whereas the amount of Cu and S are remarkably higher for the large NC.

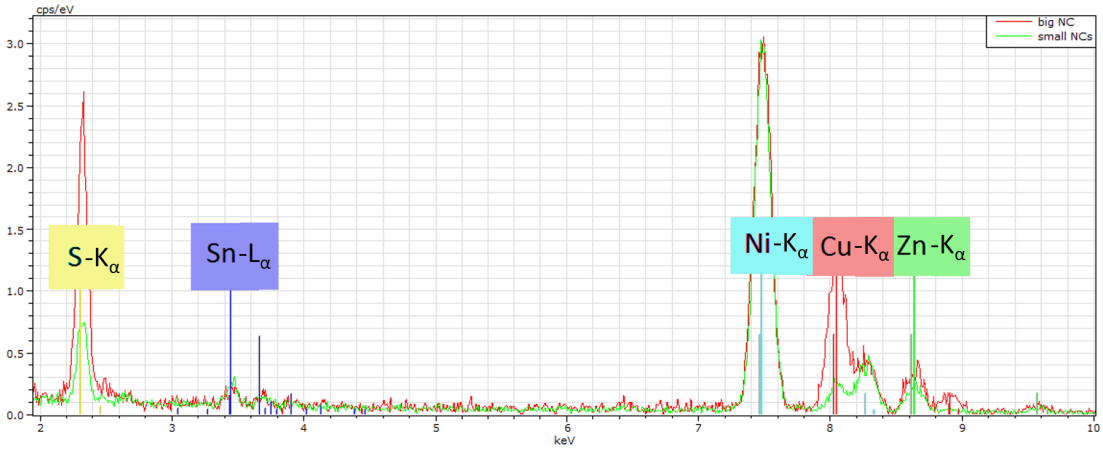

Figure 3.10 – Comparison of normalized EDS spectra in sample 2 between one isolated large NC (red) and a group of small NCs (green).

Sample 3

Sample 3 is taken after 5 minutes heating (110 °C to 280 °C). The temperature of the reaction mixture after 5 minutes reaches 265 °C.

Acquisition in figure 3.11 shows a bimodal size distribution for this sample. Two populations of NCs are observed. The presence of smaller NCs (< 2 nm) population is evident; large NCs are quite homogeneous in elemental composition. The elimination of impurities through effective purification improved the contrast. Spectra from some particular areas of interest have been integrated:

1. large nanocrystal 1;
2. large nanocrystal 2;
3. area with small nanocrystals;
4. most of the larger nanocrystals.

Larger and smaller NCs are well separated, allowing the resolution of composition differences between the two populations. The quantification of smaller and larger NC groups is presented in table 3.8. Larger NCs have a composition of $Cu_{2.63}Zn_{0.91}Sn_{1.15}S_4$, and smaller NCs $Cu_{2.58}Zn_{0.46}Sn_{1.35}S_4$. The difference in the composition of Cu and S between the two populations is minimal. On the contrary, small NCs contain half the amount of Zn in comparison to larger NCs. Smaller NCs are also slightly more abundant in Sn. The composition of the larger NCs in sample 3 is quite similar to the ones in sample 2, with an increase in Sn content. Concerning the small nanoparticles, while Cu content increases, Zn content decreases.

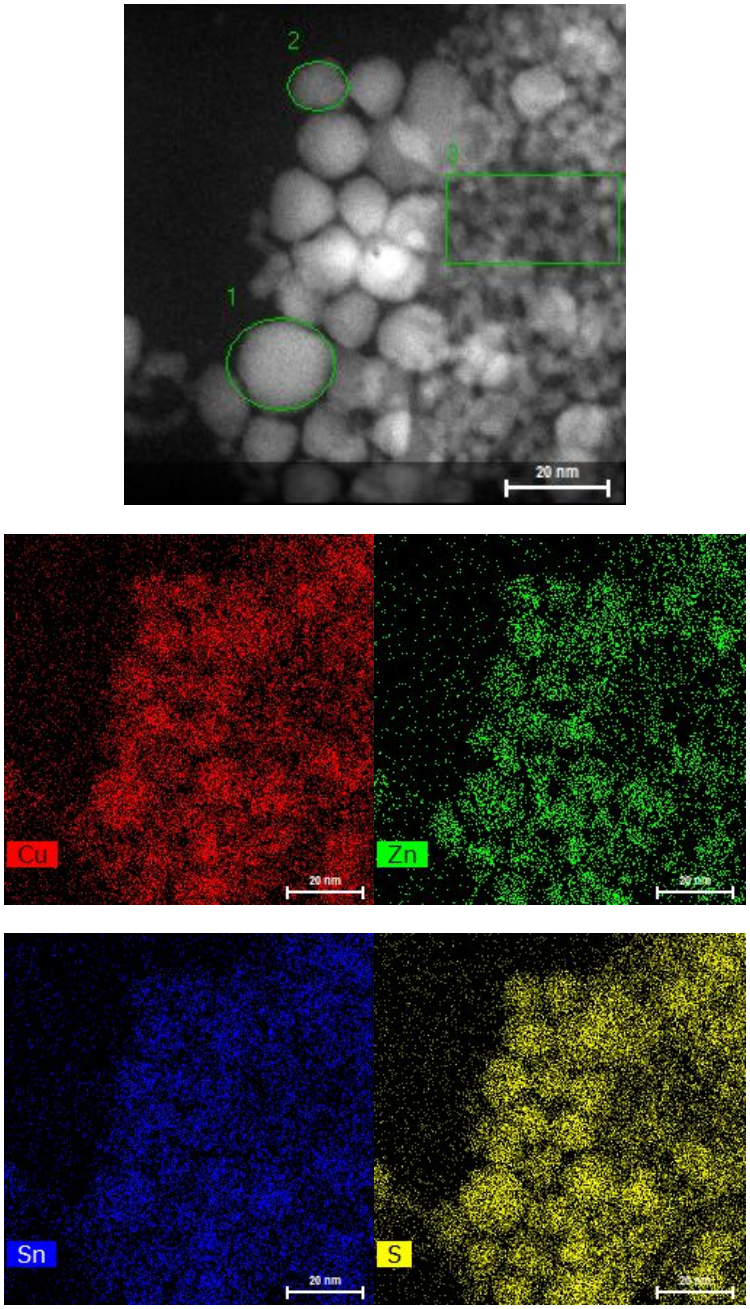

Figure 3.11 – General plan of acquisition area at a magnification of 910 kx of sample 3, and elemental mapping (Cu-K_α, Zn-K_α, Sn-L_α and S-K_α) of the same zone.

Atomic concentration [%]				
Label	Cu	Zn	Sn	S
Smaller NCs	30.72	5.53	16.09	47.65
Larger NCs	30.26	10.45	13.23	46.07

Table 3.8 – Elemental quantification (Cu-K_α, Zn-K_α, Sn-L_α and S-K_α) of sample 3 from figure 3.11.

Next acquisition (figure 3.12) has been taken at a higher magnification to investigate the homogeneity of composition between larger NCs. The three NCs have a diameter of approximately 10 nm and show similar compositions. Their average composition is equivalent to $Cu_{5.93}Zn_{0.94}Sn_{1.22}S_4$. An excess in Cu and a deficiency in S are observed in comparison to the previous acquisition, probably because of the high electron dose impinged on the sample.

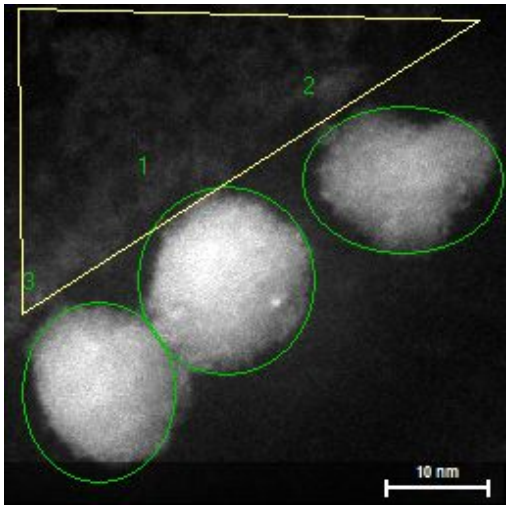

Figure 3.12 – General plan of acquisition area at a magnification of 1.8 Mx of sample 3.

Atomic concentration [%]				
Label	Cu	Zn	Sn	S
NC1	45.62	9.38	9.97	35.03
NC2	53.70	6.01	9.39	30.9
NC3	47.62	8.05	10.93	33.4
average	49	7.8	10.1	33
standard deviation	4	1.7	0.8	2

Table 3.9 – Elemental quantification of sample 3 for three NCs from image 3.12.

Sample 4

This sample is taken after 10 minutes of heating from 110 °C to 280 °C. The temperature of the reaction mixture after 10 minutes is 280 °C and is stable. The sample has been purified with the standard procedure used in all this study (by using methanol-acetone and acetic acid-acetone as antisolvents). It is particularly clean, contamination is not important, and STEM-HAADF images are particularly good. It is possible to acquire stacks of images, which allow an improvement of image quality.

In this reaction step, the population of small NCs (< 2 nm), which was identified in the previous batches, are not observed anymore. Only the ones having diameters of approximately 10 nm are observed in the solution.

Five NCs are observed, and a spectral STEM-EDS mapping is acquired as shown in figure 3.13. Their shape appears to be quite irregular. Qualitatively, NCs look rather homogeneous, except in Zn distribution: some zones appear richer in Zn (distribution map in figure G.2). The mean value for the five NCs corresponds to $Cu_{2.51}Zn_{1.16}Sn_{1.38}S_4$ (table 3.10). Therefore, the composition is close to stoichiometric values. The five NCs seem homogeneous in composition, with the exception of NC1, which is Cu- and Sn-poor and Zn-rich. Its intensity in the HAADF image is also different from the others.

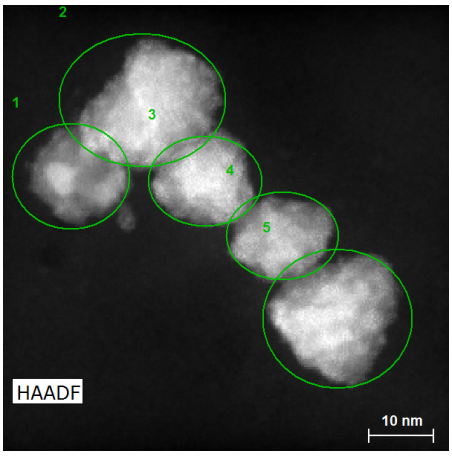

Figure 3.13 – HAADF image of sample 4.

Atomic concentration [%]				
Spectrum	Cu	Zn	Sn	S
NC1	23.49	19.46	12.70	44.35
NC2	29.39	9.18	15.32	46.11
NC3	28.22	11.96	15.40	44.42
NC4	28.49	12.79	16.73	41.99
NC5	28.89	10.68	16.27	44.15
Mean value:	27.70	12.82	15.28	44.20
Sigma:	2.39	3.96	1.56	1.47
Sigma mean:	1.07	1.77	0.70	0.66

Table 3.10 – Elemental quantification of sample 4 from 5 NCs from figure 3.13.

Next acquisition shows one single NC (figure 3.14). Despite a quite long acquisition (11 minutes), no particular sample degradation is observed. In the NC in the centre, the composition is practically constant all over the volume. Conversely, the NC on the top left of the image has a band rich in Cu and poor in Zn; and the NC on the top right has a zone rich in Zn and poor in Cu, as shown in a qualitative linescan in figure 3.15. The linescan is taken from the bottom right to the top right of the image: there is one band, approximately in the middle of the NC, which is Zn-rich and Cu- and Sn-deficient. Consequently, at this growth stage, some of the NCs are homogeneous; in other cases, cation ratio can vary locally, giving rise to secondary phase-like domains. NCs showing local composition inhomogeneities in the elemental maps have no remarkable differences in total stoichiometry with respect to homogeneous ones (see table G.1). These composition fluctuations inside a single crystal form a peculiar nanostructure which may have novel (and inhomogeneous) properties inside the sample batch. Only advanced spectroscopy study could detect this phenomenon.

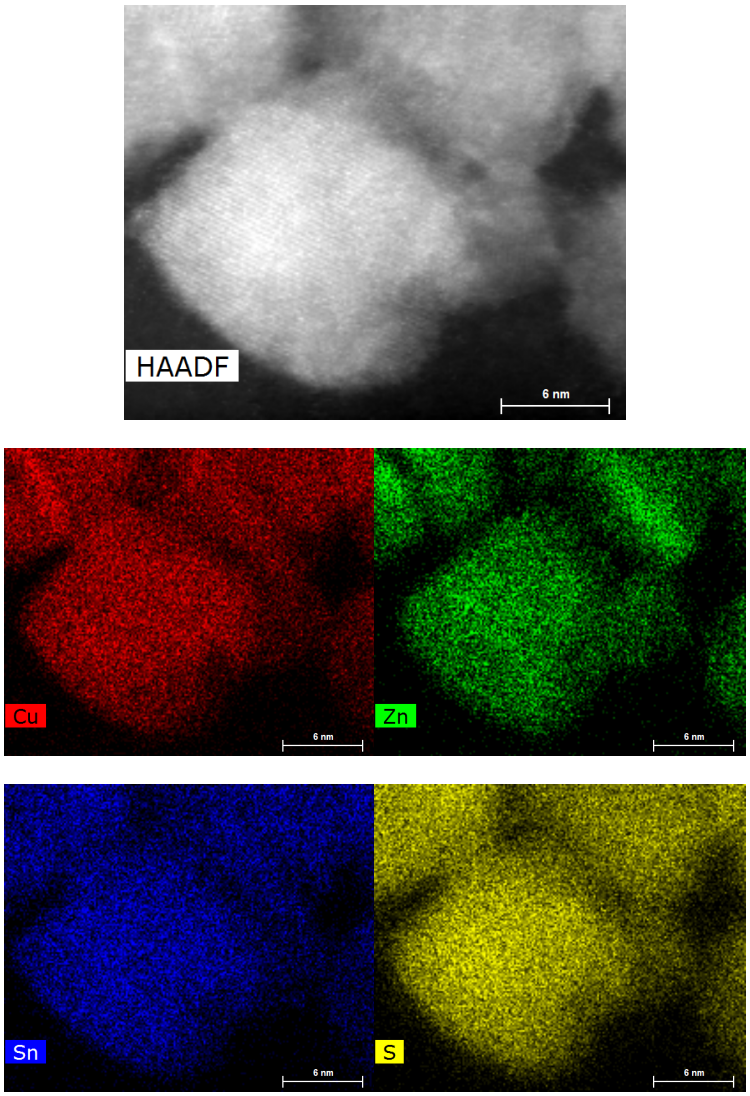

Figure 3.14 – General plan of acquisition area and elemental mapping (Cu-K_α, Zn-K_α, Sn-L_α and S-K_α) of sample 4.

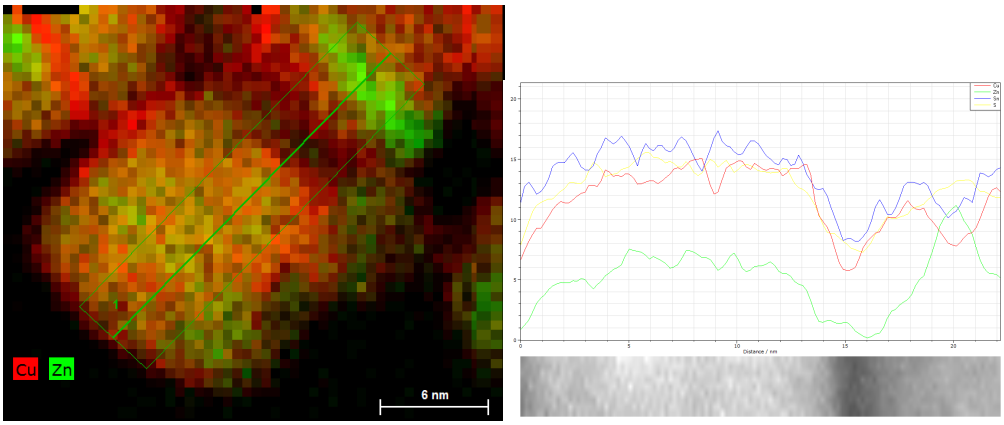

(a) Cu-K_α and Zn-K_α elemental mapping. (b) Line profile from bottom left to top right.

Figure 3.15 – Line profile of a compositional homogeneous NC and of a NC presenting a Zn-rich domain in sample 4.

Sample 5

Sample 5 is taken after 15 minutes heating at 280 °C. Similarly to sample 4, only 10 nm sized NCs are present. This sample is very clean. For the first time in this study, it was possible to acquire some atomic column resolution images are taken by STEM-HAADF (figure 3.16). Some atomic columns show also interesting contrast motifs. Atomic column resolution could not be achieved in samples 1 to 4, possibly because of unreacted reagent and contamination. All acquisition presented here were acquired at the same magnification of 91 kx.

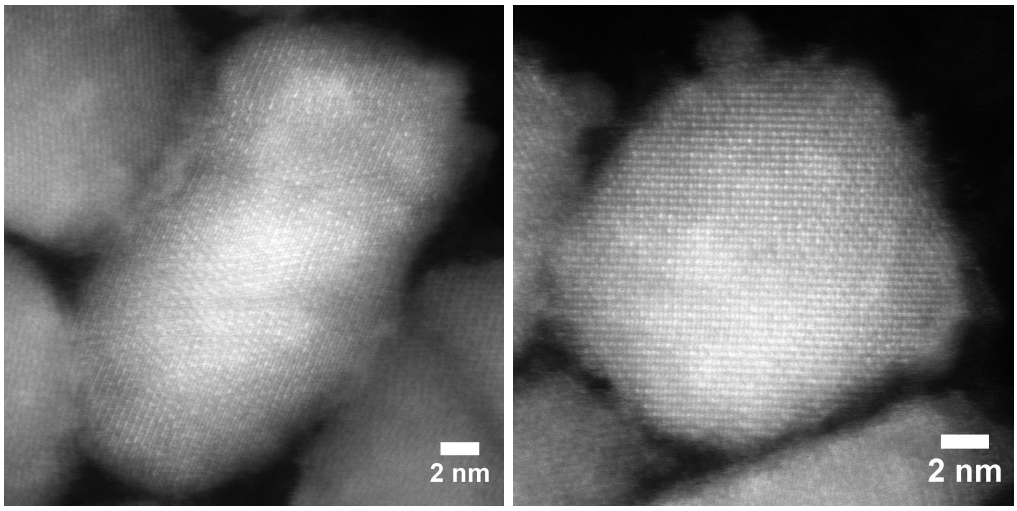

Figure 3.16 – HAADF images of NCs from sample 5, showing some atomic column contrast.

Like in the previous stage (sample 4), several NCs show zones which are particularly rich in Zn. Surprisingly, a binary NC composed of Cu and S only is found (61.54 at% Cu and 39.46 at% S): it can be observed in red colour in figure 3.17c. In the same position, there is no signal from the other cations (Sn and Zn), as shown in figure 3.17b.

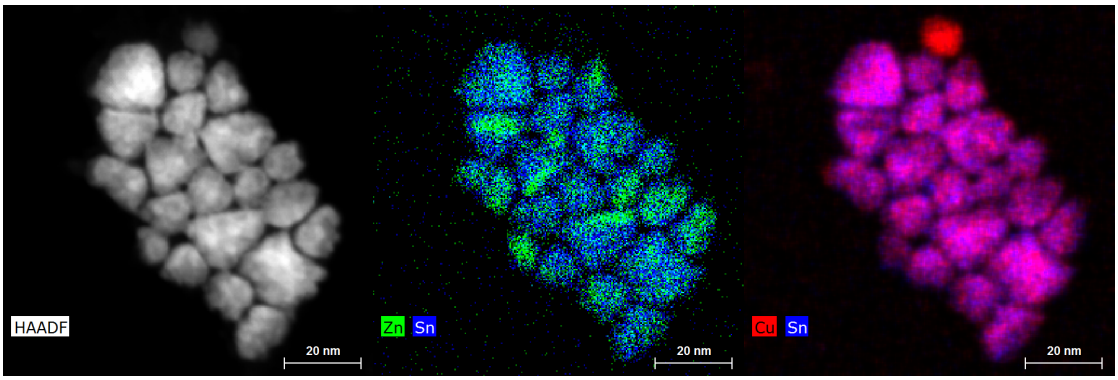

(a) (b) (c)

Figure 3.17 – (a) HAADF image, (b) sum of Zn-K_α (green) and Sn-L_α (blue) and of (c) Cu-K_α (red) and Sn-K_α (blue) elemental maps.

Figure G.3 presents a zone with more homogeneous NCs. The NCs are very close to each other. Therefore only an overall quantification is performed, which is equivalent to $Cu_{2.06}Zn_{0.84}Sn_{1.28}S_4$.

Sample 6

This sample, extracted 30 minutes after heating at 280 °C, has not been considered for the electron microscopy study. Despite several efforts, the complete solvent evaporation made it impossible to redisperse the sample in standard solvents.

Sample 7

Sample 7 is the final sample. Similarly to samples 4 and 5, only 10 nm sized NCs are present. At this stage, chemical homogeneity and the composition must be studied accurately to provide a complete characterisation at a nanometric scale.

In the first acquistion (figure 3.18), when referring to elemental maps, the sample looks very homogeneous. An average quantification (table 3.11) is performed over approximately 70 NCs: their composition reads $Cu_{2.23}Zn_{0.96}Sn_{1.23}S_4$.

Average composition		
Element	Atom C. [at %]	Rel. error (σ)
Cu	26.44	3.14
Zn	11.38	3.32
Sn	14.67	10.11
S	47.52	3.13

Table 3.11 – Elemental quantification of sample 7 from figure 3.18.

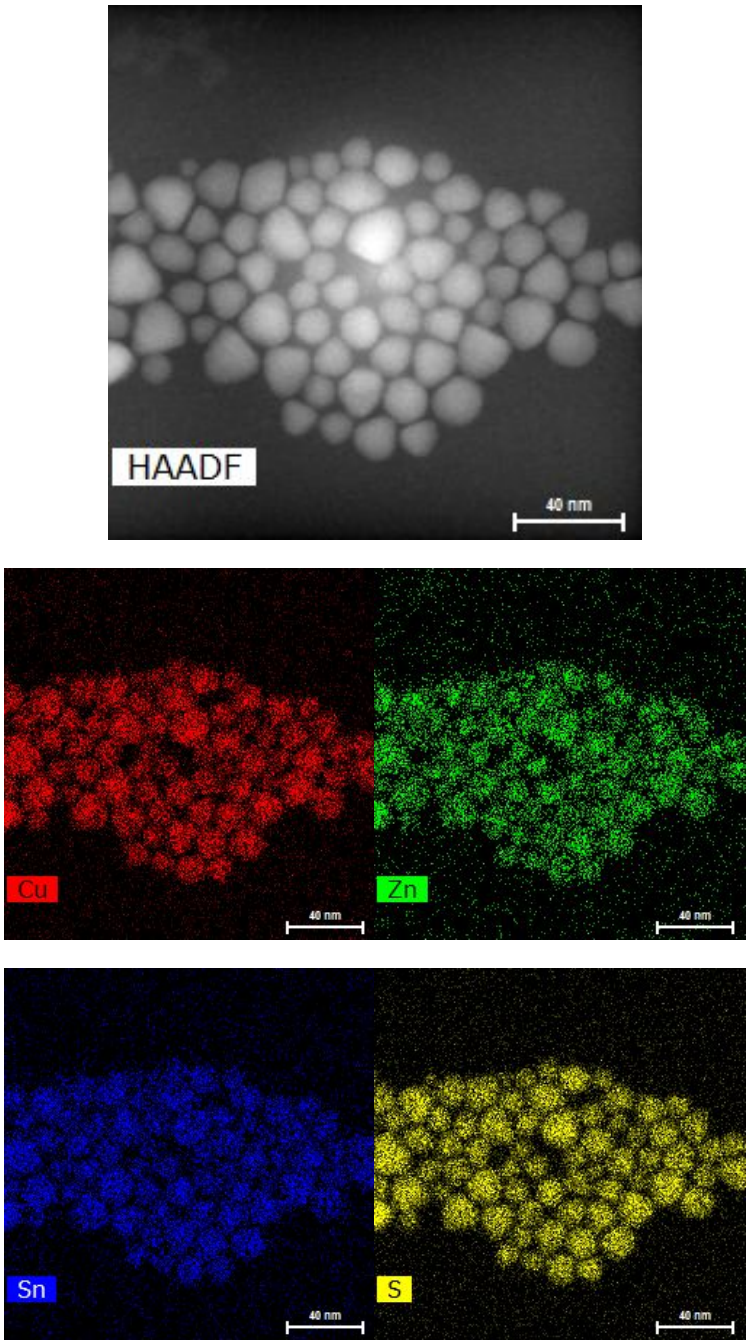

Figure 3.18 – General plan of acquisition area and elemental mapping (Cu-K_α, Zn-K_α, Sn-L_α and S-K_α) of sample 7.

In the following acquisition, elemental distribution in each NC is observed at high magnification (1.3 Mx) (figure 3.19). The X-ray signal is integrated from each single NC, and the homogeneity in the NC population is analysed (table 3.12). The mean stoichiometry of the single NCs is $Cu_{2.21}Zn_{0.99}Sn_{1.24}S_4$, highly comparable to the sum of the whole spectrum $Cu_{2.21}Zn_{0.99}Sn_{1.22}S_4$. These results confirm that the composition and habit do not change significantly after stage 5. Nevertheless, an improvement of the homogeneity is observed at the end of the synthetic procedure.

The values of the standard deviation are 10 to 20 times lower than the ones reported by Haas who investigated inhomogeneities in $Cu_2ZnSnSe_4$ NCs [135]. Haas used STEM-EDS (using a Schottky, non-corrected TEM, and with single EDS detector) and STEM-EELS to investigate single $Cu_2ZnSnSe_4$ NCs, with high spatial resolution. EDS and EEL spectra of individual nanocrystals were recorded. Only EDS quantitative measurements were considered. Their results from NCs from the same batch show substantial variations in the Cu:Zn:Sn:Se ratios. While the overview measurements show good stoichiometric composition, measurements of individual particles show a considerable variation in cation content. The authors, therefore, speculated that, due to the similarity of the systems, the compositional inhomogeneities observed in $Cu_2ZnSnSe_4$ NCs should be extended to Cu_2ZnSnS_4 NCs. Nevertheless, Haas did not perform any experiments on Cu_2ZnSnS_4 NCs. They merely reevaluated Steinhagen's STEM-EDS elemental mapping [117] and declared a slight but visible spatial separation which can be seen best in the distribution of Zn and Sn. Our findings over individual nanoparticle STEM-EDS elemental composition quantification reported in table 3.12 show a excellent homogeneity in composition. We speculate that the spatial separation observed in Steinhagen's STEM-EDS chemical map are due to artefacts from image filters, presumably necessary because of the probably low EDS counting (as obtained by non-dedicated equipment).

Figure G.4 shows the detail of a Zn-rich band in the middle of one NC. The related line profile shows clearly that this Zn-rich band (in green in the graph) is about 1 nm large. The amount of S (yellow) is constant all along the NC. A lower ratio of Cu (red) and Sn (blue) is observed where Zn is more abundant.

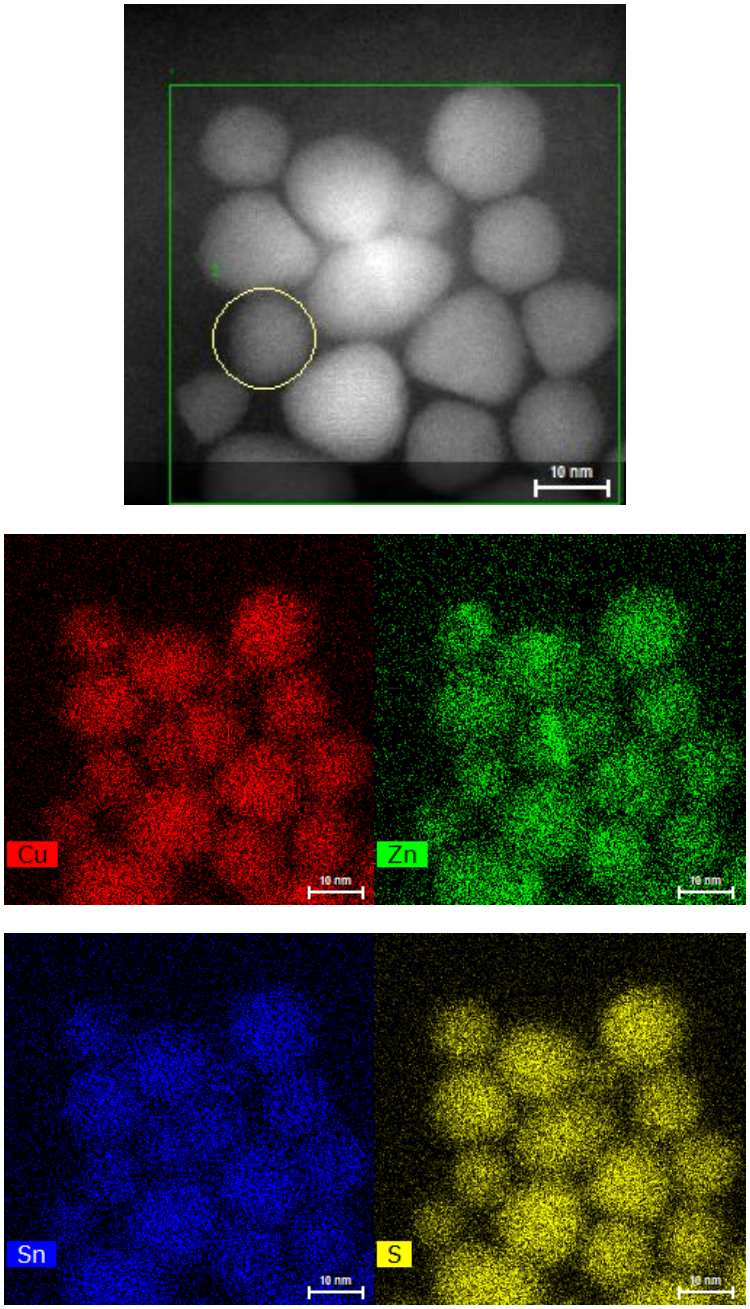

Figure 3.19 – General plan of acquisition area and elemental mapping of sample 7.

Atomic concentration [%]				
Label spectrum	Cu	Zn	Sn	S
NC2	27.13	10.95	15.01	46.91
NC3	25.88	11.28	14.96	47.89
NC4	26.56	10.63	14.96	47.85
NC5	26.50	11.97	14.72	46.81
NC6	26.80	10.38	15.05	47.77
NC7	25.56	12.77	14.19	47.48
NC8	25.40	13.44	13.59	47.58
NC9	25.70	12.21	15.08	47.01
Mean value:	26.19	11.70	14.69	47.41
Sigma:	0.64	1.08	0.53	0.44
Sigma mean:	0.23	0.38	0.19	0.16
area of all NCs	26.23	11.77	14.46	47.54
sigma relative	3.11	3.24	10.10	3.11

Table 3.12 – Elemental quantification of most of the NCs of sample 7 in figure 3.19.

3.4.2 Summary

The stoichiometry obtained by STEM-EDS after each reaction steps is summarized in table 3.13. After the mixing of the precursors in oleylamine at room temperature (sample 1), there is already the formation of NCs, as confirmed by the black colour of the sample and by the presence of a consistent solid precipitate after centrifugation. These nanoparticles are visible after purification by TEM: their size is comparable to the one of the final sample. NCs are practically binary, with a composition of $Cu_{1.1-1.3}S$. Some zones with a concentration of Zn are present, but their position is undefined (they could either be inclusions in the NCs or be attached to the surface). After 30 minutes at 110 °C (sample 2), different populations of NCs are observed:

- larger NCs (10 nm are still rich in Cu and S. Zn and partially Sn appear in these species. Their size is the same as the NC observed in sample 1;
- platelets, whose three-dimensional information is visible because of the spontaneous organisation in stacks. They have a similar composition in comparison to the larger NCs;
- smaller NCs (2 nm to 4 nm). With respect to stoichiometric Cu_2ZnSnS_4, they are particularly rich in Zn and Sn. Their composition is measured to be $Cu_{1.4-2}Zn_{1.6-1.9}Sn_{1.2-1.7}S_4$.

Larger NCs are very rich in Cu, while Zn value is already similar to stoichiometry. Sn is not fully incorporated yet. Small NCs are rich in Zn and Sn.

After 5 minutes at 280 °C (sample 3) the distribution of NCs sizes is still bimodal. On the one hand, larger NCs have still an excess in Cu, on the other hand, Zn and Sn

are approximately in the good proportion. Smaller NCs are richer in Sn. We assume that in the high-temperature regime the smaller NCs are vanishing and there is a cation exchange in the larger NCs through Ostwald ripening, up to the good stoichiometry. This is confirmed by the trend observed in the following samples extracted after 10 (sample 4) and 15 minutes (sample 5) at 280 °C. The small NC population vanishes, and the stoichiometry tends progressively to become more homogeneous between the NCs towards the final stoichiometry.

Nevertheless, the final sample (sample 7) is not stoichiometric. Precursors were weighted to obtain a Cu-poor and a slightly Zn-rich material; the final material shows the opposite, with Sn slightly over-represented. Some Zn-rich bands can be observed in the centre of some of the NCs: in these positions, the amount of the other cations (Cu and Sn) is decreasing.

Sample	Larger NC	Smaller NC
1	$Cu_{1.1-1.3}S$	
2	$Cu_3Zn_{0.7-1}Sn_{0.3-0.5}S_4$	$Cu_{1.4-2}Zn_{1.6-1.9}Sn_{1.2-1.7}S_4$
	average: $Cu_{3.0}Zn_1Sn_{0.5}S_4$	
3	$Cu_{2.6-5.9}Zn_{0.9}Sn_{1.2}S_4$	$Cu_{2.6}Zn_{0.5}Sn_{1.4}S_4$
4	$Cu_{2.5}Zn_{0.9-1.2}Sn_{1.3}S_4$	
5	$Cu_{2.1-2.6}Zn_{0.9}Sn_{1.3}S_4$	
6	\	\
7	$Cu_{2.2}Zn_{0.9}Sn_{1.2}S_4$	

Table 3.13 – Summary of composition measurements on larger and smaller NCs by STEM-EDS.

A complete discussion, including complementary results of Small Angle X-ray Scattering (SAXS) and Wide Angle X-ray Scattering (WAXS) experiments performed by our group and described in appendix A, is presented in section 3.5.

3.5 Crystal growth mechanism

This study investigated the growth mechanism of CZTS by coupling STEM-HAADF and STEM-EDS[6], SAXS and WAXS. The elemental quantification results by STEM-EDS and SEM-EDS are summarized in table 3.14 and cation ratios are demonstrated in Figure 3.20.

[6]SEM-EDS was performed in a previous study [136]. The results are not displayed here as redundant with STEM-EDS results which can benefit from a higher spatial resolution.

Sample	Large NC: STEM-EDS	Small NC: STEM-EDS	SEM-EDS
1	$Cu_{1.1-1.3}S$		\
2	$Cu_3Zn_{0.7-1}Sn_{0.3-0.5}S_4$ average: $Cu_{3.0}Zn_1Sn_{0.5}S_4$	$Cu_{1.4-2}Zn_{1.6-1.9}Sn_{1.2-1.7}S_4$	$Cu_{3.1}Zn_{1.5}Sn_{0.1}S_4$ $Cu_{3.1}Zn_{1.5}Sn_{0.1}S_4$
3	$Cu_{2.6-5.9}Zn_{0.9}Sn_{1.2}S_4$	$Cu_{2.6}Zn_{0.5}Sn_{1.4}S_4$	
4	$Cu_{2.5}Zn_{0.9-1.2}Sn_{1.3}S_4$		\
5	$Cu_{2.1-2.6}Zn_{0.9}Sn_{1.3}S_4$		
6	\	\	\
7	$Cu_{2.2}Zn_{0.9}Sn_{1.2}S_4$		$Cu_{2.1}Zn_{1.1}Sn_1S_4$

Table 3.14 – Summary of composition measurements on larger and smaller NCs by STEM-EDS and SEM-EDS.

Figure 3.20 reveals the change in cation composition ratios in NCs as a function of reaction time. The points in the figure represent the relative composition (obtained by STEM-EDS measurements) plotted as a function of reaction time when the samples 2, 3, 4, 5 and 7 are extracted, respectively[7].

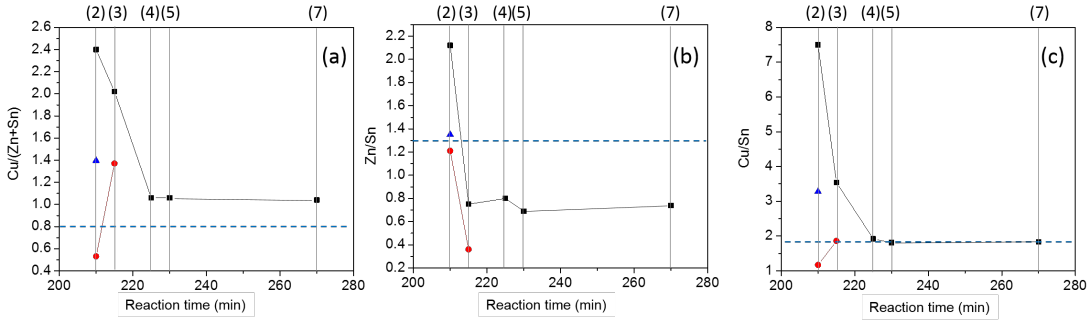

Figure 3.20 – The change in cation ratios for large NCs (black square), small NCs (red circle) and platelet NCs (blue triangle) as a function of time. The points correspond to samples 2, 3, 4, 5 and 7. The composition was determined using STEM-EDS. The average elemental composition is used for the calculation of cation ratios. The blue dashed line indicates the starting value for the precursor. After 3 hours degassing at room temperature (sample 1), only a binary Cu_xS specie is observed. Moreover, no sample could be observed by TEM at 30 minutes at 280 °C (sample 6). Therefore, the cation ratios for the two samples (sample 1 and 6) are excluded in the figure.

After the mixing of the precursors in oleylamine at room temperature (sample 1), the formation of NCs is confirmed by the blackish colour of the sample and the presence of a consistent solid precipitate after centrifugation. These nanoparticles are visible after purification by TEM: their size is comparable to the final sample. These are binary NCs with a composition of $Cu_{1.1-1.3}S$. Some zones with a concentration of Zn are

[7]Sample 1 is not represented, as no Zn nor Sn are observed. Sample 6 composition was not measured.

present, but their position is undefined (they could either be inclusions in the NCs or be attached to the surface). The formation of binary Cu_xS is commonly observed in the first stages in the synthesis of wurtzite CZTS by the heat-up method as reported by Regulacio [118], Liao [131] and Li [121], and in the early stages of ternary and quaternary copper chalcogenides [122, 137], where a strong coordinating ligand (such as an alkylthiol) is present even at low temperatures and can strongly bind the metal precursors, preventing the interaction of Cu and Sn [138].

As the temperature is ramped, the chemical transformation from binary Cu_xS to quaternary CZTS is complete already after 30 min at 110 °C (sample 2) which was previously observed at 220 °C by Li [121]. Zn and Sn are gradually incorporated into the crystal lattice of formed Cu_xS and replaced parts of Cu, which is confirmed by the $\frac{Cu}{Zn+Sn}$ ratio evolution (figure 3.20a). At this stage, three populations of quaternary CZTS NCs with different stoichiometry are observed: they are denoted as large (10 nm), small (< 2 nm) and platelet NCs (10 nm × 3 nm). Large and platelet NC populations have similar average compositions, and they are both extremely Cu-rich and Sn-poor. On the other hand, smaller NCs are rich in Zn and Sn. Laboratory WAXS also indicates two sets of diffraction peaks associated with two crystalline particle families with sizes corresponding to 4 nm and 9 nm. The overall sample composition shows a larger Cu while right Zn stoichiometry with respect to Cu_2ZnSnS_4. On the other hand, Sn is not fully incorporated in the large NCs' crystal structure. This assumption is in agreement with the WAXS data, as the stoichiometric Cu_2ZnSnS_4 phases are found not to be present at this stage. Similar behaviour has been previously observed by Li [121] in which has been referred to as asynchronous doping of Zn^{2+} into the larger NCs. The authors explain this according to the similarities of the ionic radius of Zn^{2+} (74 pm) and Cu^{+} (77 pm) compared to Sn^{4+} (69 pm). Zn^{2+} will be preferentially doped into Cu_xS over Sn^{4+}, resulting in a so-called asynchronous doping[8] [121].

A different formation mechanism was proposed by Tan [122] and Coughlan [125] for hot-injection CZTS NC synthesis. These authors observed a first nucleation of Cu_xS, followed by the formation of Cu_2SnS_3 intermediates. Zn was later incorporated to form the final close-to-stoichiometry Cu_2ZnSnS_4. Our findings are similar to the reports of Li [121] and Collord [138], where Zn incorporation is observed in earlier stages.

As the temperature is further increased at 280 °C (sample 3), only two populations of NCs remain as the platelet NCs disappear. At this stage, smaller NCs (2 nm to 3 nm) become very Zn-poor. Meanwhile, in the larger (10 nm) NCs the concentration of Cu decreases as Sn gets incorporated. The $\frac{Zn}{Sn}$ ratio already gets closer to those of the final sample. The observation of smaller nanoparticles with larger nanoparticles suggests a transfer of cations from smaller to larger nanoparticles via Ostwald ripening as previously reported by Tan [122] and Collord [138], which suggest a slow Ostwald

[8]Li observed rice-shaped pure wurtzite CZTS NCs. By HRTEM, they measured the distance of atomic columns, and the morphology of as-synthesized CZTS NCs. EDS was performed on CZTS products synthesised by changing the reaction times. The proposed formation process of final CZTS nanorice is divided into three steps: rapid nucleation of Cu_2S occurring with the help of oleylamine; asynchronous doping of Zn and Sn assisted growth (as little lattice distortion) and shape transformation to rhombus-like intermediate shaped NCs; completed transformation.

ripening mechanism to change particle size and composition after all free precursors have been consumed. Tan used Surface-enhanced Raman scattering (SERS) spectroscopy to differentiate the mixed compositional phase. Growth mechanism is revealed to involve three steps. $Cu_{2-x}S$ nucleate, followed by diffusion of Sn^{4+} into Cu_{2-x} nanoparticles to form Cu_3SnS_4 (CTS) phase. This result agrees with reports on the unfavourable formation of the Cu-Zn-S ternary system with respect to heterogeneous $Cu_{2-x}S$-ZnS nanoparticles. Zn^{2+} diffuses into CTS to form CZTS phase. The observation of smaller nanoparticles along with larger ones during CZTS NCs suggests the growth to proceed via Ostwald ripening. A stronger binding ligand is used to reduce the reactivity of cations at each step. Aliquots were also examined by TEM [122]. Collord considers a hot-injection CZTS NC synthesis method using oleylamine. Three different particles groups were isolated using size selective precipitation (big, small, and big + small). SEM-EDS was performed on films from the three different size fractions. Only average compositions are measured. Composition differences are significant between the biggest and the smallest particles. Under 30 min reaction times, small NCs are Cu- and Sn-rich, whereas the standard-NC is very Zn-rich. The first stage is the nucleation and growth stage, starting with the injection of sulphur up to 30 minutes. After 30 minutes, the mass yield reaches a plateau, indicating almost all the free precursors have been consumed. Changes in particle size and composition still occur after this time, by the slower Ostwald ripening mechanism. XRD and absorption data indicating the presence of Cu_xS allows concluding that the formation pathway involves either the nucleation of Cu_xS followed by very rapid Zn addition or the simultaneous nucleation of both Cu_xS and ZnS. An unspecified interaction of Cu with Sn creates a secondary small particle fraction which has near constant composition for all reaction times [138]. Following our data, the size of larger NCs does not vary considerably from sample stage 2 to 7; we speculate that Zn and Sn are incorporated by the cationic exchange.

As the time proceeds, only larger NCs (10 nm) remain in sample 4, which was also confirmed by the vanishing of WAXS peaks corresponding to smaller NCs. Moreover, the peak corresponding to 1.9 Å shifted to the position of corresponding tetragonal-like CZTS crystal structure. From sample 4 to sample 7, the average composition changes very slowly, but the NCs gain a more homogeneous composition. The average $\frac{Cu}{Zn+Sn}$ ratio reduces from 1.06 to 1.04, while the $\frac{Zn}{Sn}$ ratio reduces from 0.8 to 0.74 and a best stoichiometric composition of $Cu_{2.2}Zn_{0.9}Sn_{1.2}S_4$ is obtained after 1 hour at 280 °C (sample 7). We point out that initially, the precursors were weighted in order to obtain a Cu-poor and a slightly Zn-rich composition to optimize the photovoltaic properties [49].

Contrary to expectations, the final composition showed a slightly rich Sn amount. Some Zn-rich bands can be observed in the centre of few NCs: in these positions, the amount of the other cations (Cu and Sn) decreased. The elemental distribution maps show that Cu, Zn, Sn, and S are homogeneously distributed throughout the NCs, contrasting the findings of Haas [135], for inhomogeneities in the similar compound $Cu_2ZnSnSe_4$. Binary or tertiary sulfides are not present in the final product.

On the basis of the above detailed time-dependent shape and elemental composition evolution, a possible formation mechanism is proposed and summarised in figure 3.21.

The formation process of final CZTS NCs may be divided into three steps. At room temperature, irregular Cu_xS NCs (10 nm) form under simple mixing. At intermediate temperatures, new nucleation and growth processes are favoured, as unstoichiometric CZTS nanocrystal populations with different sizes and shapes (extremely Cu-rich 10 nm spherical NCs and 10×3 nm platelets, and Zn- and Sn-rich smaller < 2 nm NCs) appear. At higher reaction temperatures, the population of the smaller NCs progressively dissolves in the solution. Asynchronous doping of Zn and Sn in the large NC proceeds comprising cation-transfer via Ostwald ripening. Finally, conversion is completed by reaching the final stoichiometry, and pure monodisperse CZTS NCs are obtained.

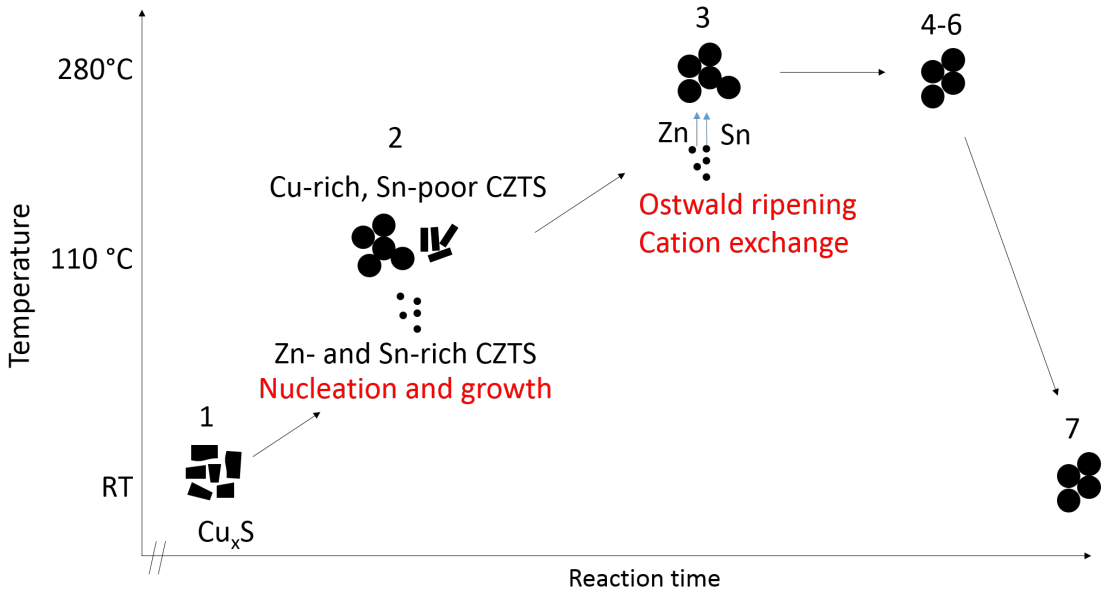

Figure 3.21 – Scheme summing up the different steps of NC formation during Steinhagen's synthesis: from the precipitation of Cu_xS to the nucleation and growth of two populations of off-stoichiometric quaternary NCs to the final homogeneous CZTS NCs.

3.6 Structural characterisation of Cu_2ZnSnS_4 colloidal NCs

A differentiation between isoelectronic cations Cu^+ and Zn^{2+} is almost impossible, as their scattering power is similar for both standard X-rays and for electrons in imaging modes. These methods cannot reliably discriminate between the crystalline phases of tetragonal CZTS, see figure 3.22. Kesterite, stannite and PMCA are three CZTS tetragonal structures which obey the octet rule; they are similar in the crystallography point of view, but they possess a different electronic structure (and band gap) [50, 51]. Neutron diffraction can solve this problem, as neutron scattering lengths of copper and zinc are different (b_{Cu}=7.718 fm, b_{Zn}=5.680 fm) [18]. This approach has been already used for bulk samples [18].

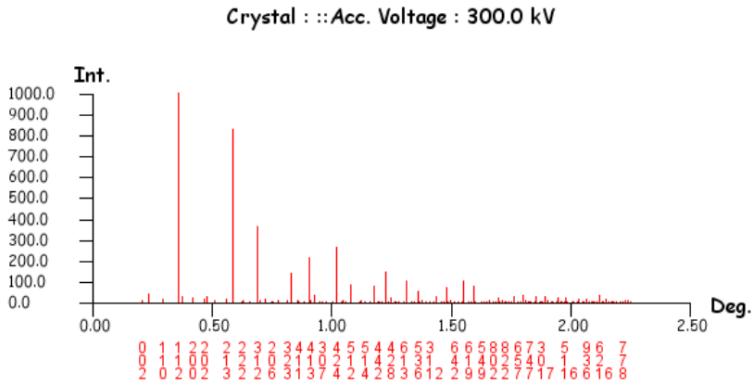

(a) Kesterite

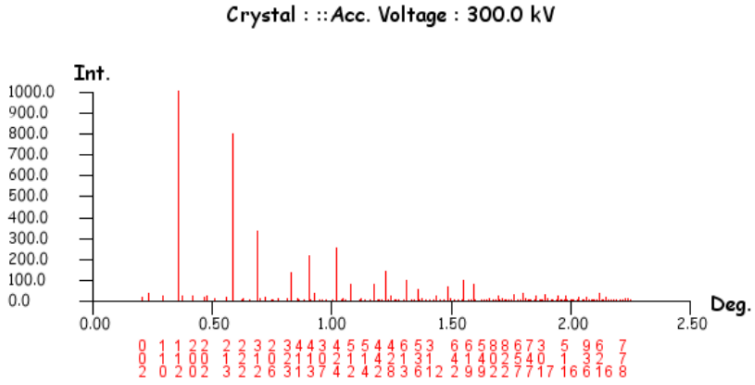

(b) Stannite

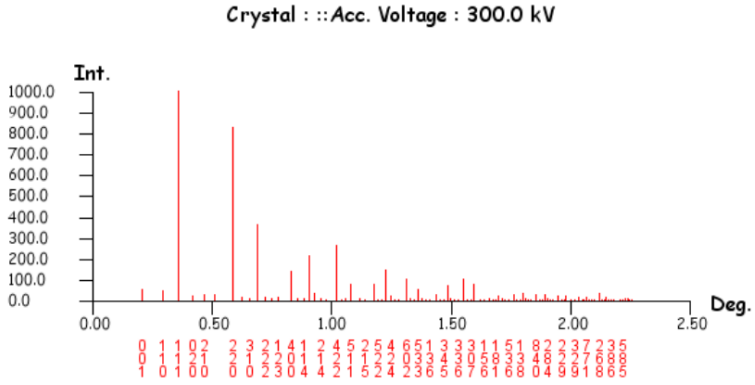

(c) PMCA

Figure 3.22 – The almost-indistinguishable powder electron diffraction pattern for the three structures.

Concerning bulk Cu_2ZnSnS_4, chemical analysis of individual atom columns was carried out by Mendis to determine the crystal structure [139]. The authors used the aberration-corrected STEM to measure compositions of Cu/Zn atom columns along [0 0 1] *c*-axis. They observed cation disorder, but they speculated that this could also be a result of beam spreading artefacts. Attempts to use convergent beam electron diffraction (CBED) to characterise the crystal structure at the nanoscale were unsuccessful due to electron scattering from Cu and Zn cations being indistinguishable. The STEM-HAADF images showed bright Sn-containing columns, with a motif compatible with both kesterite and stannite structure.

Concerning nanocrystal Cu_2ZnSnS_4, few studies are conducted using TEM to analyse the crystal structure. Kattan [140] acquired sets of SAED and CBED patterns of individual crystals after annealing, over prominent zone axis: some weak reflections due to cation ordering were observed, confirming a tetragonal unit cell consistent with kesterite or stannite. The authors demonstrated these approaches to distinguish CZTS from the secondary phases such as ZnS. Moreover, they studied dislocations, lamellar twins and stacking faults. Two sets of nanostructures were considered: as-grown NCs (7±3 nm) and annealed particles (53±13 nm). The detailed characterisation was performed solely on the annealed particles, which contain no surface ligands (annealing performed in vacuum at 550 °C, where oleylamine evaporates).

In a successive paper, the same authors employed atomic resolution STEM-HAADF to examine antisite defects in the annealed CZTS particles [141]. Kikuchi bands seen in thicker regions were used to orient the particles in the exact [0 1 0] zone axis, and high-resolution imaging studies were carried out on thin edges overlapping holes in the carbon support film. The brightest spots for Sn columns were imaged, and the superstructure typical of kesterite-stannite phases were observed by HAADF contrast. The authors stated that the structure was confirmed to be kesterite by EDS mapping at atomic resolution, which was not presented in the cited work to be instead published elsewhere.

Both papers use a similar approach to us, nevertheless we point out that the as-grown CZTS nanocrystals were never taken into consideration for detailed microscopy study, but only the larger, ligand-free annealed particles were examined in detail. In particular, the work from 2016 analysed particles of approximately 200 nm in diameter, whereas our interest lies in the understanding of the structure of as-grown CZTS NCs, before possible treatments for final use in applications.

An exciting contribution of STEM-HAADF to discern a stannite structure in the similar material $Cu_2Cd_xSnSe_y$ was presented by Zamani [142]: in particular, the object of the study was a polytypic branching consisting of wurtzite extensions out from a zinc-blende seed. STEM-HAADF was used for polarity determination in the wurtzite branches; the narrowest part of the zinc-blende-like monopod was magnified, deconvolved and frequency-filtered. The resulting intensity profile, after comparison with image simulations, allows the determination of the position of cations, with Sn-Cu-Cd-Cu-Sn stannite ordering.

It has been calculated theoretically that the three possible Cu_2ZnSnS_4 relaxed structures have slightly different lattice parameters [50]. In principle, it would be possible to

distinguish them by determining the lattice parameter with high accuracy, or alternatively, the tetragonal distortion parameter $\eta = \frac{c}{2a}$. As shown in table 3.15, determination of lattice parameter constant must be at the picometer level to be able to discern the three structures.

Structure	a [pm]	c [pm]	η
Kesterite	546.7	1092	0.999
Stannite	545.8	1096	1.004
PMCA	545.9	1097	1.005

Table 3.15 – Calculated lattice parameters and tetragonal distortion parameters of the three structures [50].

Table 3.16 gives an idea of the relative precision that is necessary to discriminate between the three structures.

$\frac{a_{KS} - a_{ST}}{a_{KS}} = 1.646 \times 10^{-3}$	$\frac{a_{KS} - a_{PCMA}}{a_{KS}} = 1.463 \times 10^{-3}$	$\frac{a_{ST} - a_{PMCA}}{a_{ST}} = 1.832 \times 10^{-4}$
$\frac{c_{ST} - c_{KS}}{c_{ST}} = 3.339 \times 10^{-3}$	$\frac{c_{PMCA} - c_{KS}}{c_{PMCA}} = 4.513 \times 10^{-3}$	$\frac{c_{PMCA} - c_{ST}}{c_{PMCA}} = 1.178 \times 10^{-3}$
$\frac{\eta_{ST} - \eta_{KS}}{\eta_{ST}} = 4.980 \times 10^{-3}$	$\frac{\eta_{PMCA} - \eta_{KS}}{\eta_{PMCA}} = 5.970 \times 10^{-3}$	$\frac{\eta_{PMCA} - \eta_{ST}}{\eta_{PMCA}} = 9.950 \times 10^{-4}$

Table 3.16 – Relative differences between a and c lattice parameters and tetragonal distortion η for the kesterite (KS), stannite (ST) and pre-mixed Cu-Au (PMCA) structures.

In the last years with the rising of the aberration-corrected STEM, the spatial resolution of the microscope has improved to about 50 pm. Different approaches can further enhance this value:

- by using HAADF detectors, which significantly avoid coherent effects leading to artefacts [74];
- with acquisitions of a series of rapid STEM images and successive alignment [143, 144]. Hence scanning and drift artefacts are minimized[9]. These kinds of algorithms calculate estimated drift positions by correlating each frame to multiple frames and minimising the error in order to obtain the best estimate for frame positions relative to each other;
- the obtained aligned frames are then averaged, and peak positions are then deter-

[9]Another approach reported by Sang [145] reports the acquisition of an image series while rotating the scan coordinate system between successive frames to capture the information necessary to analyse sample drift and direction. This approach, named RevSTEM, is reported to correct distortion without the need for a priori structure information, to improve signal-to-noise ratio, picometer precision (1.5 pm) and accuracy regardless of drift rate

mined via geometric phase analysis[10] [146] or template-matching algorithms (such as Zuo template-matching analysis algorithm TeMA [147]). The precision of atom position determination from TeMA from registered series of HgCdTe in [1 1 0] zone axis shows errors of 1.26 pm and 1.46 pm for the horizontal and vertical axis, and 1.36 pm and 0.95 pm for GaN in $[1\,1\,\bar{2}\,0]$ zone axis for the horizontal and vertical axis [95]. This approach has proved to be very powerful, for example in atomic structure solution of inversion domains in GaN nanowires [148], or in strain determination. Nevertheless, one of the limitations is that unstrained reference material is needed in order to calibrate pixel size accurately and to have a significant template for template matching. Moreover, the reference material must be in the same image as the interesting feature, as minimal changes in height, defocus or aberrations can influence the precision of the measurement. In our case, only bunches of NCs are present in the image; they are deposited on graphene, which is not an optimal reference material (as it can quickly show ripples, and is barely imaged in STEM mode, as carbon atoms are relatively light). Some NCs are also deposited on thicker amorphous carbon, which indeed cannot be the reference material for any template matching strategy.

3.7 Sample preparation for structural characterization

Structural characterisation is performed over the final sample (sample 7). After the previously described purification involving acetic acid as an antisolvent, the sample was deposited by drop-casting on a graphene layer transferred on a lacey carbon gold grid. The grid is successively heated at 100 °C right before observation at the microscope.

3.8 Nanobeam Precession Electron Diffraction

Each experimental diffractogram obtained by NPED can be compared with simulated diffractograms created from a database of structures in order to identify the phase and orientation of each crystalline domain. The details of this approach can be found in the introductory section 1.3.6.

3.8.1 Influence of stoichiometry on the lattice parameters

In this discussion, as a first approximation, we use lattice parameters from stoichiometric structures. Nevertheless, STEM-EDS quantification on the final sample indicated a final composition of $Cu_{2.2}Zn_{0.9}Sn_{1.2}S_4$. Here, we discuss how this approximation affects the results and discussion.

Ritscher performed neutron scattering investigations on off-stoichiometric CZTS powders that are mechanochemically synthesized with cation ratios ranging between 0.90 to

[10] Hytch measured continuous displacement fields at the nanometre scale to an accuracy of 3 pm from the geometrical phase analysis of a HRTEM image of a non-corrected JEOL 200CX with 220 pm resolution

1.15 for $\frac{Cu}{Zn+Sn}$ and between 0.74 to 1.09 for $\frac{Zn}{Sn}$ [149]. Structural characterisation was performed by X-ray and neutron powder diffraction. The kesterite-type structure (space group $I\overline{4}$) was used as the starting model for Rietveld refinements. The refined lattice parameters of all off-stoichiometric samples are summarised in figure 3.23. Only a small variation of the lattice parameter is observed for the off-stoichiometric CZTS samples. Looking at the behaviour of the lattice parameter a as a function of the cation ratio $\frac{Cu}{Zn+Sn}$, only a slight alteration of 0.4 pm is observed, whereas the change of $\frac{c}{2}$ is more significant for Cu-poor/Zn-rich to Cu-rich/Zn-poor samples. Both lattice parameters decrease when cation ratio $\frac{Zn}{Sn}$ increases [149].

To understand the influence of the off-stoichiometry over the lattice parameters on our sample, the data presented by Ritscher have been fitted with a linear function. The linear fit is therefore used for interpolation to obtain a reasonable estimation of the influence of off-stoichiometry in the synthesised $Cu_{2.2}Zn_{0.9}Sn_{1.2}S_4$ NCs. By considering the relationship between lattice parameters and cation ratio $\frac{Cu}{Zn+Sn}$ (figure 3.23a), the value of the lattice parameter a obtained by extrapolation for a stoichiometric Cu_2ZnSnS_4 is 543.2 ± 0.2 pm, which is the same value for a cation ratio of $\frac{Cu}{Zn+Sn}$ of 1.04 (543.2 ± 0.2 pm). The variation reads 0.014 pm. Concerning the halved lattice parameter $\frac{c}{2}$, the extrapolation gives 542.1 ± 0.3 pm for both the stoichiometric and non-stoichiometric values (difference is 0.05 pm). The interpolation performed in the relationship between lattice parameters and cation ratio $\frac{Zn}{Sn}$ gives the calculated values of 543.24 ± 0.11 pm and 542.18 ± 0.16 pm for the lattice parameters a and $\frac{c}{2}$ respectively for Cu_2ZnSnS_4. Interpolation for the cation ratio $\frac{Zn}{Sn} = 0.75$ gives 543.28 ± 0.10 pm and 542.3 ± 0.14 pm for a and $\frac{c}{2}$, respectively. Our Zn-poor/Sn-rich material presents therefore a larger unit cell when compared with the stoichiometric material: we calculate variations of 0.04 pm for a and 0.16 pm for $\frac{c}{2}$. By plotting the tetragonal distortion parameter η (measured by Ritscher in [149]) as a function of the lattice parameter, no linear dependence appear. In the considered compositions range, η varies between 0.998629 and 0.996953 ($\Delta\eta = \eta_{MAX} - \eta_{min} = 0.001676$, $\frac{\eta_{MAX}-\eta_{min}}{\eta_{MAX}} = 0.001678$). These results obtained from interpolation are listed in table 3.17. Here, only the result reported in Ritscher [149] are exploited; nevertheless, similar work was performed by Valle Rios [150] over 20 off-stoichiometric CZTS powders synthesised by a solid-state reaction from pure elements. The primary outcome of this study was to demonstrate that the kesterite type structure can self-adapt to Cu-poor and Cu-rich compositions in CZTS without any structural change except for the cation distribution. The cation ratio interval which produces single phase CZTS is smaller for CZTS obtained by solid-state reactions and larger for CZTS obtained by mechanochemical synthesis route, due to the difference in the synthetic processes.

To resume, in the following we apply NPED for discriminating between kesterite, stannite and PMCA for CZTS NCs synthesised by Steinhagen method. We use Astar strategy to do so (creation of a dataset for several orientations, and comparison of experimental and simulated DP; the one with the best correspondence provides a chemical phase and the orientation). In a first approximation, the stoichiometric models have been considered. This approximation is made without taking into account that the

NCs are off-stoichiometric $Cu_{2.2}Zn_{0.9}Sn_{1.2}S_4$, which would have an influence over the lattice parameters and could influence the DP identification. Few experimental data were available when the experimental work was performed. In the meanwhile, Valle Rios [150] and Ritscher [149] performed structural characterisation on off-stoichiometric kesterite CZTS sampes obtained by solid state reactions [150] and mechano-chemical synthesis [149]. We exploit the data from Ritscher, who obtained a larger range of single-phase compositions, to extract the relationship between lattice parameters a and c and the cation ratios $\frac{Cu}{Zn+Sn}$ and $\frac{Zn}{Sn}$. Linear dependences are obtained so that it is possible to interpolate the variation in lattice parameters as a function of cation ratios. However, the variations obtained from $\frac{Cu}{Zn+Sn}$ differ from the ones obtained from $\frac{Zn}{Sn}$ cation ratio. In fact, the composition $Cu_{2.2}Zn_{0.9}Sn_{1.2}S_4$ does not exactly fit on the line represented by Ritscher, in particular for Cu-rich/Zn-poor/Sn-rich compositions (composition $Cu_{2+2z}Zn_{1-3z}Sn_{1+z}S_4$) and therefore the two considered cation ratios might not correspond to the same sample. Nevertheless, we observed the variation of the tetragonal lattice distortion $\eta = \frac{c}{2a}$ for Ritscher data, which does not show any observable dependence with the lattice parameter a.

Furthermore, this interpolation is valid only for kesterite which, in the cited works, was in powder state: it is risky to extend the lattice parameter values for the material in micrometric size to nanomaterials, which may show peculiar atom position relaxation and strain effects, especially in the proximity to the surface. Moreover, to the best of our knowledge, there is no experimental data reported in the literature about the influence of off-stoichiometry on stannite and PMCA CZTS lattice parameters. Finally, the influence of off-stoichiometry is in our case lower than 0.1 Å and does not remarkably influence the determination of the structure from the lattice parameter determination.

	Cu/(Zn+Sn)		Zn/Sn	
	a [pm]	$\frac{c}{2}$ [pm]	$a[pm]$	$\frac{c}{2}$ [pm]
Cu_2ZnSnS_4	543.2 ± 0.2	542.1 ± 0.3	543.24 ± 0.11	542.18 ± 0.16
$Cu_{2.2}Zn_{0.9}Sn_{1.2}S_4$	543.2 ± 0.2	542.1 ± 0.3	543.28 ± 0.10	542.34 ± 0.14
Variation	0.014	0.05	0.04	0.16

Table 3.17 – Table representing the interpolation for cation ratios $\frac{Cu}{Zn+Sn}$ and $\frac{Zn}{Sn}$ from the stoichiometric Cu_2ZnSnS_4 and the off-stoichiometry material $Cu_{2.2}Zn_{0.9}Sn_{1.2}S_4$, observed in the synthesized NCs.

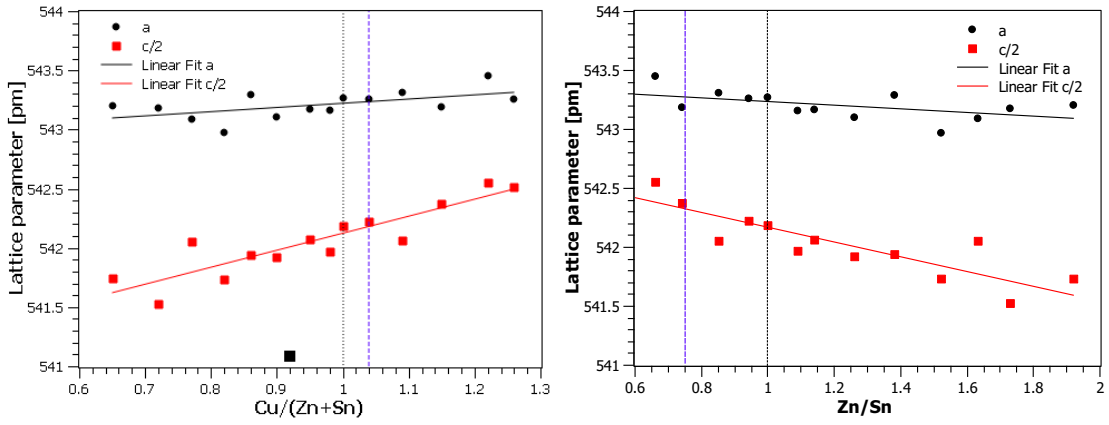

(a) (b)

Figure 3.23 – Lattice parameters vs. cation ratios of CZTS samples, with linear interpolation. Left: Cation ratio $\frac{Cu}{Zn+Sn}$. Right: Cation ratio $\frac{Zn}{Sn}$. Vertical black dotted lines represent the stoichiometric values for Cu_2ZnSnS_4 and vertical blue dashed lines represent the cation ratio measured experimentally on the synthesized CZTS NCs. Data retrieved from [149].

3.8.2 Acquisition parameters for NPED

In the following, an NPED experiment is described, and the Automated Crystal Orientation Mapping tool (ASTAR^{TM} by NanoMEGAS) is applied.

The experiment was performed on a FEI Themis microscope operated at 200 kV in STEM mode. A small probe is created by selecting a 10 µm second condenser aperture. In order to minimise dynamical effects, which are relatively low for these NCs, and to double the number of visible spots, the incident beam precesses by using deflections coils above the sample. The beam pivot point is placed precisely on the sample plane during alignment routine, and the transmitted beam is re-centred using an additional group of deflecting coils located below the sample (descan). Diffraction patterns are strongly affected by precession: the final image is a merging of the full series of slightly tilted diffraction patterns.As precession averages over a broad set of tilt angle, the dynamical contrasts within the disks are smoothed out, and the contrast within the disk is more uniform. Typically the use of a precessing beam doubles the number of visible spots, with respect to a classic conical illumination. During all the acquisitions, the convergence angle was set to 3 mrad. The precession angle was set to 0.7° (12 mrad) with a 100 Hz precession frequency. The size of the diffraction limited beam (FWHM) is 0.75 nm; if the precession is well tuned FWHM slightly increases to 0.85 0.75 nm. This value is valid before interacting with the specimen, and should not be confused with the resolution of the experiment. The camera length was set to 135 mm[11]. HAADF signal

[11]For the HAADF detector. The camera length calculated on the CETA camera, acquiring the diffraction patterns, is approximately three times this camera length value, as determined in subsection 3.8.3.

and diffractogram are simultaneously acquired: the HAADF signal by a Fischione high annular dark field detector, the diffractogram is acquired by a FEI Ceta camera with binning 4 and one quarter active area. Therefore, acquired diffractograms have a format 256×256 pixels, which is a good compromise between speed, intensity, resolution. Then the collection of electron diffraction patterns begins after choosing a square area of interest. The lateral step is chosen manually, so it is possible to scan large areas with reasonably small steps (the limiting factor being not the step size but the probe size, which is in the nanometer range; probe impinges then a specific volume of matter). In our study, most of the acquired maps have a lateral step of about 2 nm. Considering that the NC diameter is approximately 10 nm, the probe interacts with one single NC in roughly 20 different positions: this provides a good statistics and can be useful to detect whether several phases are present in the same NC.

3.8.3 Template matching strategy

It is relatively easy to calculate simulated diffraction patterns for a known phase and orientation, and compare them with the experimental diffractograms. For all phases present in the sample, templates are calculated for most of the possible orientations. In the ASTAR software, the number of simulated patterns is determined by a step count that is the number of steps in which the fundamental directions of the unit cell of the reciprocal space are divided to generate the patterns. Depending on the symmetry of the simulated crystal this unit cell is more or less extended. In our case, a step count of 120 was chosen, resulting in an angular step of approximately 0.7° for each axis. Higher step count values are possible, but the memory of the computer/program is insufficient in the identification process. Nevertheless, the step count of 120 can be considered as a good choice: rotation steps of the order of 1° are proper parameters, as there is some degree of overlap between two successive templates [91]. Collections of simulated diffractogram are created and compared to acquired patterns; the strongest resemblance indicates the best choice for phase and orientation identification.

We remind that reliability is defined as:

$$R = 100\Big(1 - \frac{Q_2}{Q_1}\Big) \tag{3.4}$$

where Q_1 and Q_2 are respectively the highest and the second highest image correlation indices; in other words, R describes how close the two most probable solutions are. A safe indexing is obtained for $R > 15$ [91]. Reliability maps are automatically generated by the program and are helpful to understand whether indexing was successful in the crystalline zones; artificial misinterpretations must be discarded. It must be noted that a solution is always given, even for patterns from vacuum or from materials which are not in the databases. Reliability and image correlation index must be carefully analysed to obtain solid results.

3.8.4 Imaging procedure

First, the camera length for the camera used to acquire the diffraction patterns must be calibrated with a known and well-oriented sample: a well-oriented [1 1 0] silicon sample is used. Diffraction is acquired by keeping microscope conditions constant. Astar^{TM} is then used in order to calibrate the camera length. Crystallographic information on the silicon diamond-like structure is input and a template collection is created (20301 reflections). The best matching is calculated spanning the desired camera length interval: a curve with image correlation index as a function of camera length is plotted. Maxima correspond to the most probable real camera lengths; however, it is always necessary to compare experimental and simulated diffractogram. The image correlation index has an absolute maximum at a camera length of 151 cm (figure 3.24a), but the correspondence between simulated and experimental diffractogram is clearly low. Moreover, the index map (green window) shows that the identified sample direction is wrong with respect to the real one. A second maximum is present at 410 cm as seen in figure 3.24b; there is a perfect agreement between the simulated template and the experimental one, and the [1 1 0] direction is clearly identified, as shown by the index map (window with green background).

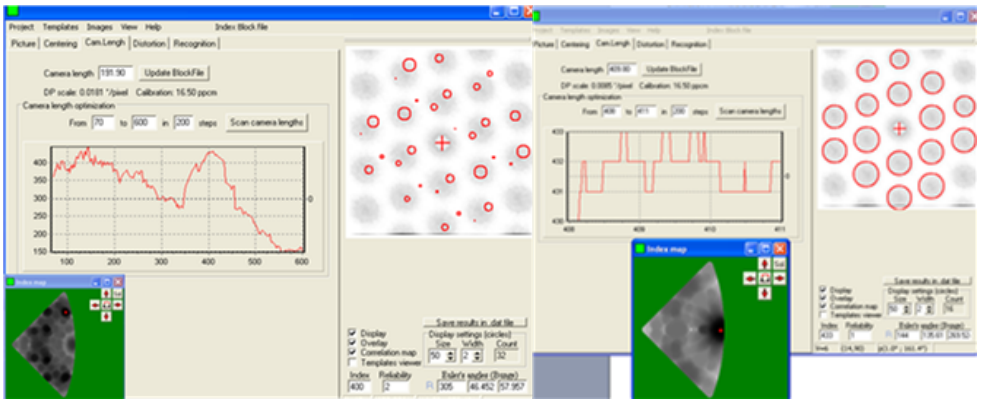

(a) CL 151 cm (b) CL 410 cm

Figure 3.24 – Detail of the template matching at the two maxima.

The best template matching results for a camera length of 410 cm at a direction very close to the zone axis [1 1 0]. This value of camera length is then used for the identification of phase in the diffractograms acquired on Cu_2ZnSnS_4 NCs.

In the presented case, an 80 × 80 pixel map is acquired over a 150 × 150 nm area. The total acquisition time is about 2 hours.

3.8.5 Filtering and digital imaging strategies

The ASTAR software only read Nanomegas proprietary .blo files that have been acquired with the ASTAR software. In our case, diffraction patterns have been acquired on a

TITAN microscope and saved in a .bin format. So we had to write a script to convert the .bin format to the .blo format. Another issue is that the ASTAR software has been optimised to analyse point diffraction patterns and not diffraction pattern with large disks. Filtering acquired diffractograms provides some advantages. One must take into account the following:

- on the one hand, even the lower intensity peaks must be preserved (in fact thanks to them it is possible to distinguish between very similar crystal structure);
- on the other hand, artefacts (i. e additional peaks from background noise) should be avoided;
- for analysis in Astar^{TM}, images need to be centred, and this is easily done by an autocorrelation operation;
- by choosing good threshold values, the best results are obtained with the information first derivative, followed by thresholding under a certain value in the diffractogram intensity.

In order to fulfil the previously cited goals, several filters are tested. All the ones where artificial spots are created, or weak reflections are not considered, are discarded. Threshold values were optimised in order to obtain meaningful identification. Some examples of the filters are shown in figure 3.25.

Here, a homemade script written by Jean-Luc Rouvière is used; it is based on autocorrelation. The periodic nature of diffractograms from crystals leads to a sharply peaked correlation function at the centre position of each diffraction disc, which facilitates the measurement of the disc spacings in different crystallographic directions. These distances are inversely proportional to the respective lattice planes.

Diffraction pattern dataset can be exploited: by applying a digital mask, it is possible to select a part of the diffracted beam to perform virtual imaging (this process mimics the principle of STEM imaging).

Different digital masks (figure 3.26a) are applied on the acquired diffraction patterns, corresponding to Bright Field (figure 3.26b) and Annular Dark Field (figure 3.26c) images, where coherent diffraction effects are evidently playing role in contrast between NCs[12]. A higher angle Annular Dark Field image (figure 3.26d) is influenced mostly by incoherent elastic scattering: diffraction contrast is minimum and contrast is due to difference in atomic number of the material, and to thickness variation. These maps are fundamental in order to correctly interpret Astar^{TM} results.

Lots of NCs exhibit a good number diffraction spots; most of them are exploitable. Some of the most significant diffractograms acquired are shown in figure 3.27.

Firstly, the orientation map[13] (figure 3.28a) shows that most NCs are recognised, and their orientation is consistent in the single NC area.

[12]NCs in diffraction condition appear dark in the Bright Field image (intensity from the transmitted beam to the scattered pattern) and bright in Annular Dark Field image (where diffraction spots are integrated).

[13]The process is comparable to EBSD in a SEM.

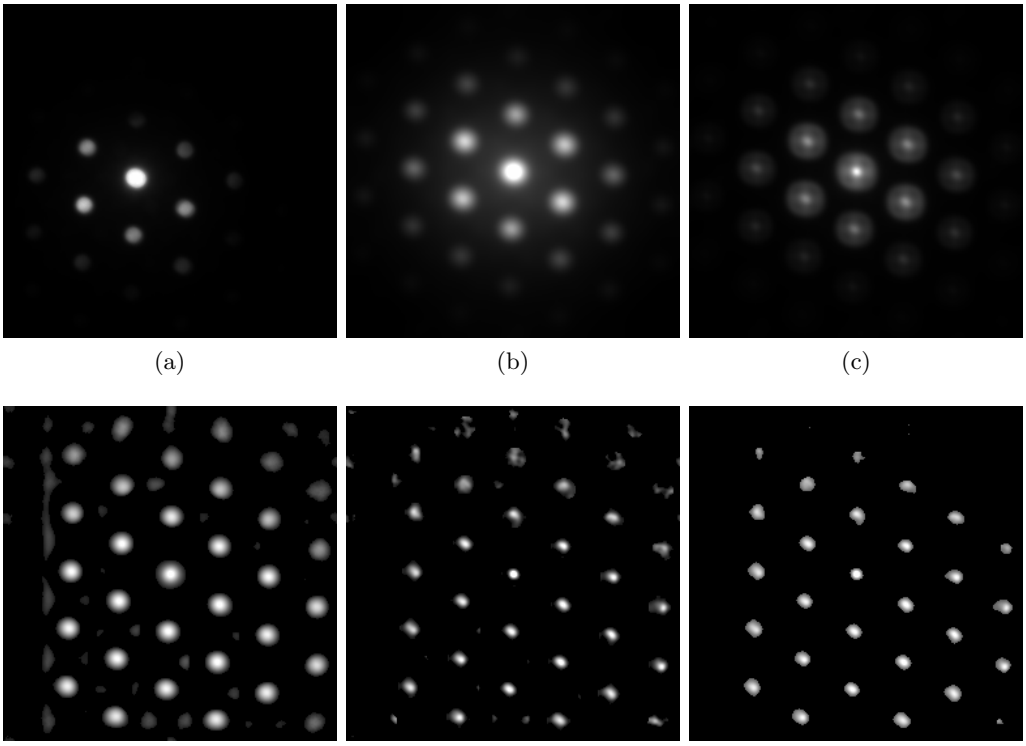

(a) (b) (c)

(d) (e) (f)

Figure 3.25 – Different filters applied on original diffraction patterns.

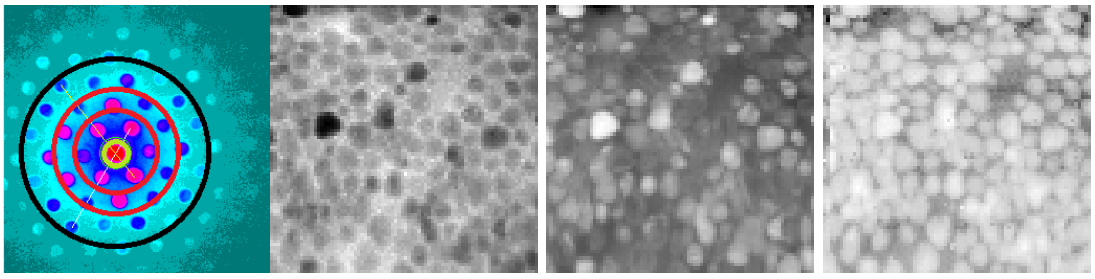

(a) Masks used for virtual BF and ADF images (b) V-BF image (c) V-ADF1 image (d) V-ADF2 image

Figure 3.26 – Digitally created images from NPED. Figure (b) is created by integrating the pixels inside the green circle in figure (a); figure (c) originates from the integration between the two red circles in figure (a); finally, the integration of the pixels outside the black circle in figure (a) originates figure (d).

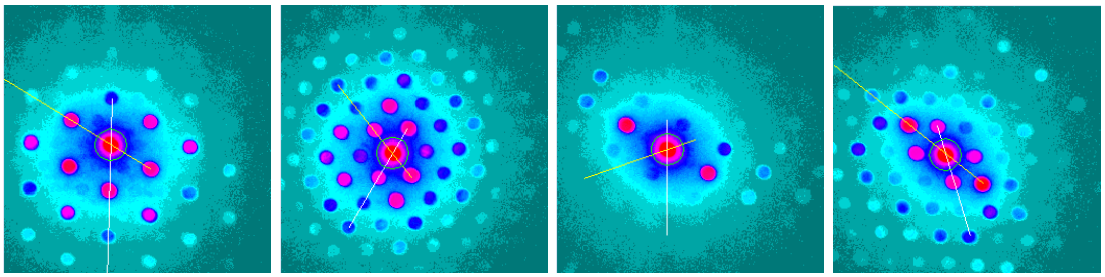

Figure 3.27 – NPED diffractograms from CZTS NCs.

Secondly, the phase identification is made with success, as visible in the phases map (figure 3.28b). All three phases are present there. Nevertheless, it is known that a mathematical solution is always given. Further investigation is necessary to understand which solution are physically significant. Reliability map (figure 3.28c) shows relatively high values (about 40)[14] only is some areas: those areas are the ones where NCs are. By multiplying the reliability map with the phases map, only one phase is conserved in the image (figure 3.28d). It seems that all the identified NCs have a PMCA structure.

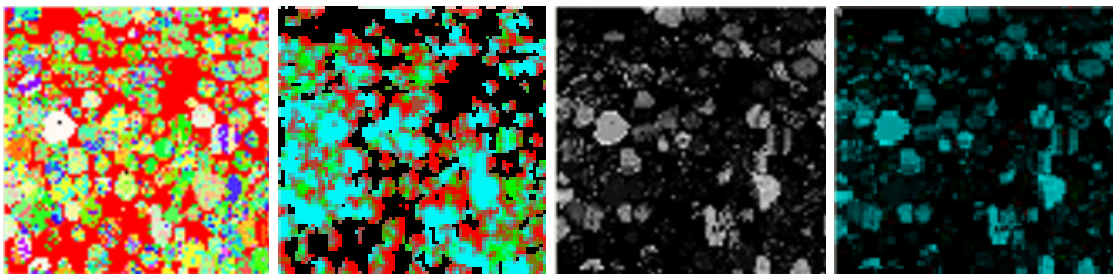

(a) Orientation map

(b) Phases map convoluted with mask from digital HAADF signal (red: kesterite, green: stannite, blue: PMCA)

(c) Reliability map

(d) Phases map multiplied by reliability

Figure 3.28 – Results from nanodiffraction experiment.

Nevertheless, the method applied previously is valid when structures are sufficiently different from each other. For this particular situation, kesterite and stannite are very similar in lattice parameter and in cation positions. In fact, when indexing the same image only by kesterite and stannite structures, we observe that reliability values are extremely low in each pixel (figure 3.29a) and, therefore, only PMCA structure appears in the combination of phase and reliability (figure 3.28d). In order to better identify the real phases in the structure, the phase map is better multiplied by the image correlation index for the most probable phase. The resulting image is presented in figure 3.29b. In

[14] A reliability value over 15 is considered to indicate a reliable matching.

contrast with the previous reliability-linked result, here all the NCs can be recognised and indexed. PMCA structure describes better most of the NCs, but some of them show kesterite or stannite features. Therefore, more structures cohabit in this batch. In some cases, more crystal structures coexist in one single NC.

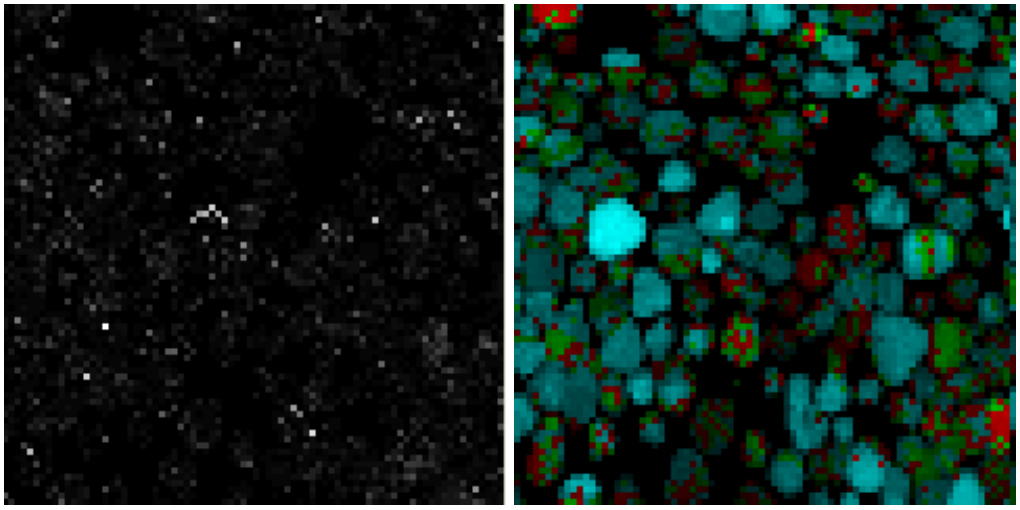

(a) Reliability in indexing with kesterite and stannite templates only.

(b) Image correlation index multiplied by the phase map.

Figure 3.29 – Results from nanodiffraction experiment.

To complete, figure 3.30 shows the same diffractogram of one well-oriented NC[15] matching with each of the three crystalline phases. In this case, PMCA structure is clearly matching better the diffractogram, as many secondary spots of kesterite and stannite structure are not present in the experimental image. The image correlation index is similar for kesterite (figure 3.30a) and stannite (figure 3.30b), respectively 440 and 475; it reaches the highest value 823 for PMCA (figure 3.30c).

The sampling of the templates appears to be sufficient, as the observation of the neighbouring templates which are closer to the solution (figure 3.30) show still high values of image correlation index, and a partial overlapping with the exact solution. In order to investigate sample homogeneity, a lot of NCs have to be observed. A randomly chosen isolated single NC has been analysed. The highest correlation is obtained with the PMCA template (figure 3.31d in most of the zones of the NC area (figures 3.31a and 3.31b. Matching of kesterite (or the almost equivalent stannite) provides an image correlation index of approximately 455, whereas the image correlation index for PMCA is 839. Here, reliability has high values (45).

[15]The diffraction pattern is extracted from the brightest blue NC in image 3.29b.

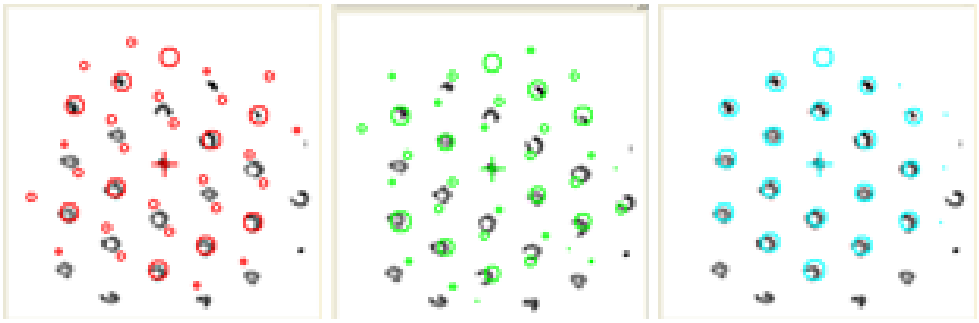

(a) Kesterite (b) Stannite (c) PMCA

Figure 3.30 – Template matching with different phases from the template collection.

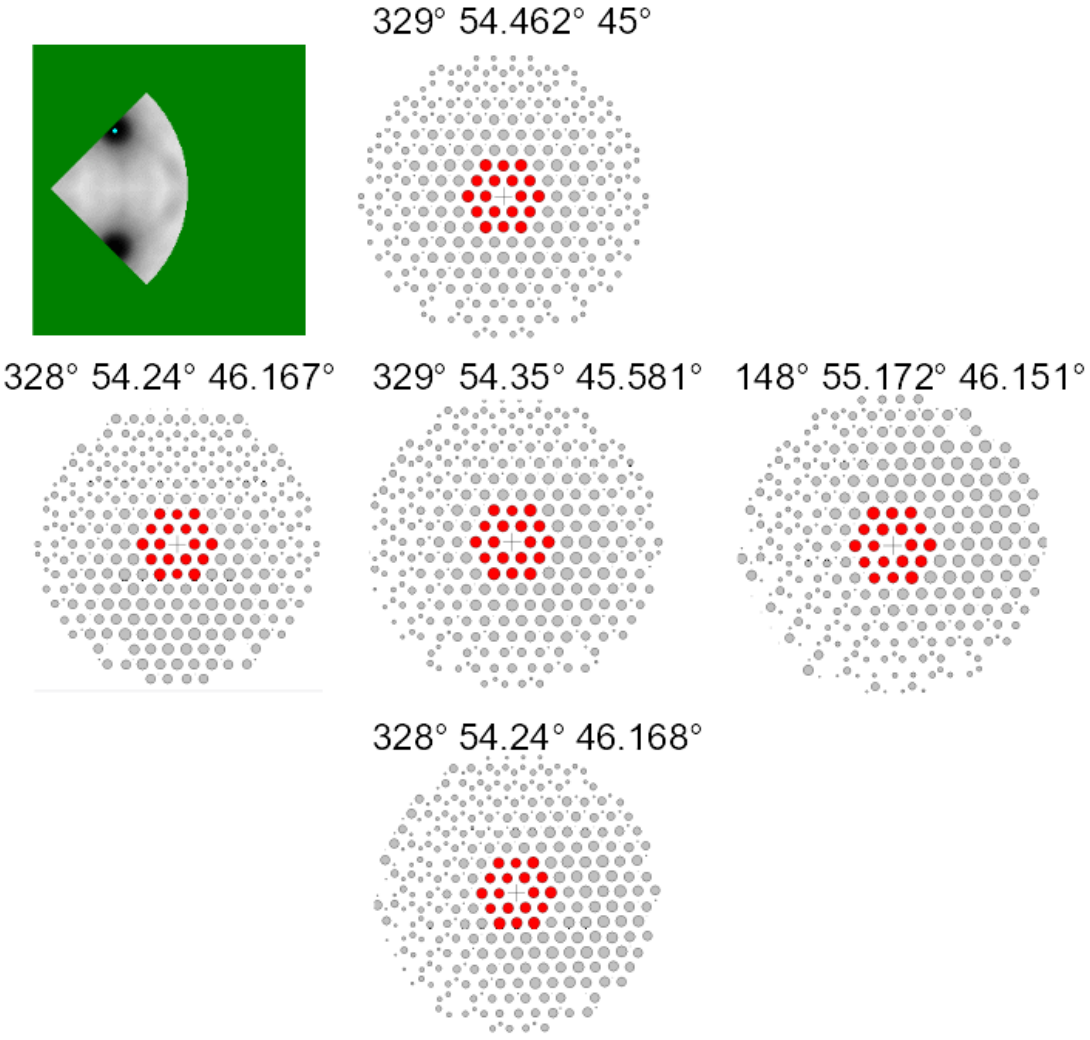

(a)

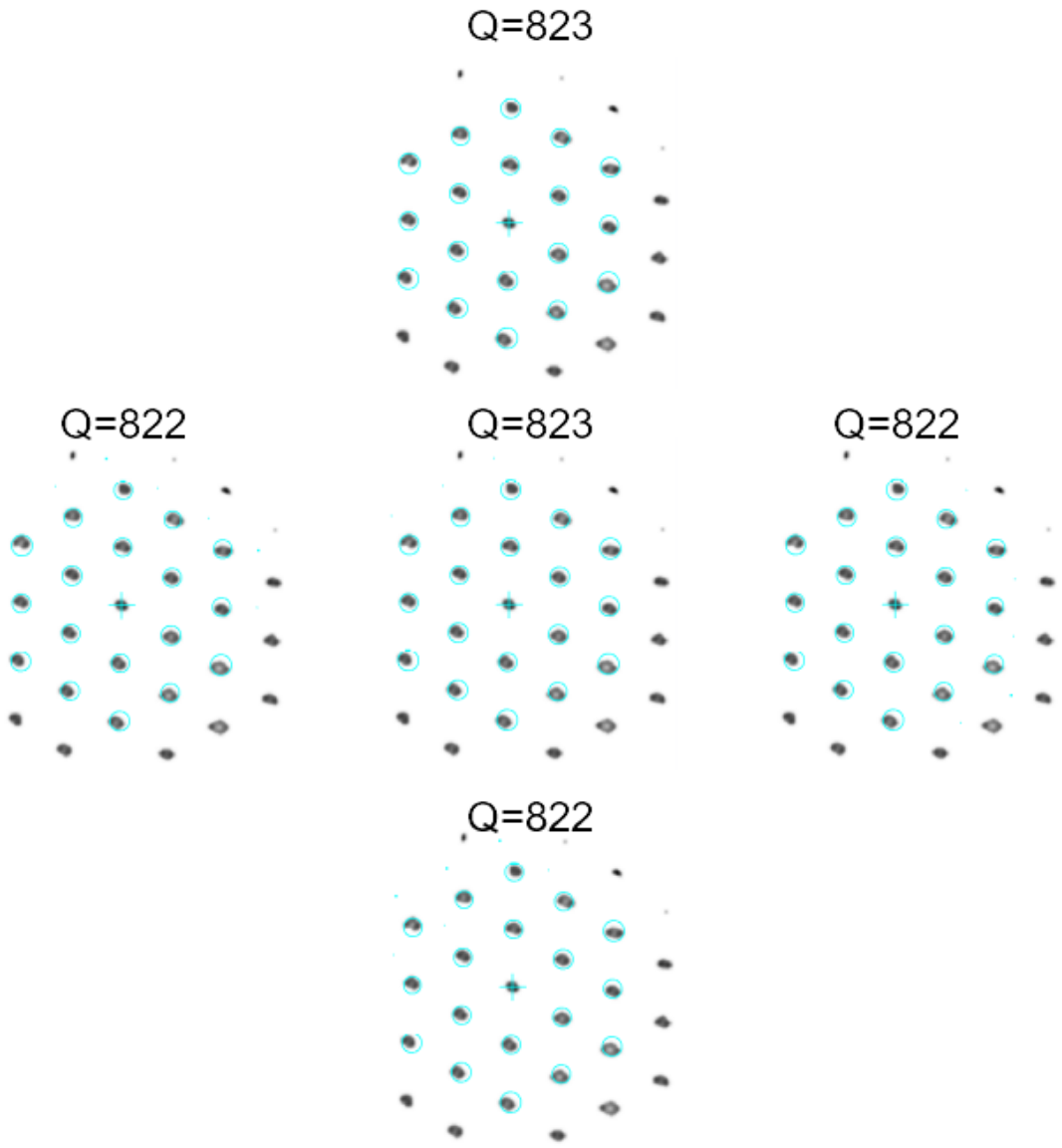

(b)

Figure 3.30 – Comparison of the solution of the template matching (in the centre of the images) with 4 templates with the smallest misalignment. The index map plots the image correlation factor as a function of the direction. The indicated angles are the orientation of the simulated diffractogram following the Euler-Bunge notation. Q represents the image correlation factor.

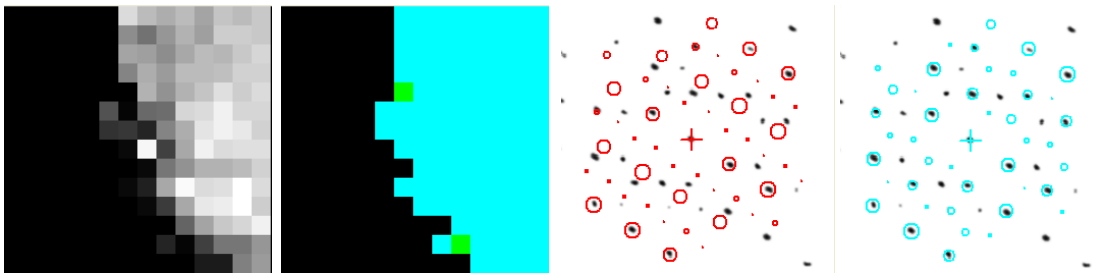

(a) Reliability. (b) Phases map (red: kesterite, green: stannite, blue: PMCA). (c) Kesterite. (d) PMCA.

Figure 3.31 – Results from NPED experiment and template matching with different phases from the template collection.

3.9 Experimental structure determination by HRSTEM

TEM and STEM-HAADF images are used as routine methods to measure size dispersion of the NCs. With the use of aberration-corrected microscope and thanks to the development of efficient purification routines, it is possible to obtain high-resolution images, where atomic columns are imaged even in these sensible materials. In particular, high-resolution STEM-HAADF is quite interesting for discriminating between kesterite, stannite and pre-mixed Cu-Au crystals structures. In the previous sections, it has been discussed that the difference in lattice parameters is relatively small. However, the positions of the cations are sufficient to modify electronic properties. STEM-HAADF is a technique which is sensitive to chemical contrast, the signal increasing monotonically with the atomic number Z: it is then possible to observe the sites occupied by the heavier atoms (Sn). Kesterite (space group $I\bar{4}$) or stannite (space group $I\bar{4}2m$) can be distinguished from pre-mixed Cu-Au (PMCA, space group $P\bar{4}2m$) structures, which show different characteristic "brightness motifs". In this study, multi-slice simulations are calculated on some remarkable directions (kesterite and stannite [1 1 2], equivalent to PMCA [1 1 1]; and [1 0 0] for the three structures). With the help of these simulations, it is discussed whether the structures are distinguishable. Then, experimental images are acquired and analysed. Only a few NCs are conveniently oriented; nevertheless, it is possible to identify the cation ordering in these few NCs.

3.9.1 Multislice simulations

Image simulation consists of numerical calculations of electron microscope images from first principles and from a detailed description of the specimen and the instrument. Image simulation helps the interpretation of recorded images in the microscope. In the presented study, simulations were performed using the multislice method on the program autostem [85], developed by the team of Earl J. Kirkland in Cornell University.

Supercells et simulation parameters

Three equivalent supercells are generated by multiplication of kesterite, stannite and PMCA unit cell. The lateral size of the supercell is twice the size of the simulated images, to avoid artefacts. Supercell is about 20 nm thick, and the STEM image are saved for desired thickness values (here, every multiple of unit cell). In this context only one thickness value is presented: the one comparable to NC size (9.8 nm). Also, it is possible to define the minimum and maximum allowed angle for integrating scattered electrons: all the possible camera lengths which are saved in the alignment of the microscope were explored, by inserting as input the angles for bright field and for high angle annular dark field detectors. In the context of this study, only one chosen camera length is presented, which is quite a standard one for the experimental point of view: a camera length of 115 mm. To realistically simulate the effects of temperature, the averages from ten different atomic configurations were considered for all the simulation presented here. Table 3.18 summarizes the simulation parameters.

Slice thickness	0.543 42 nm
Microscope HT	200 kV
Convergence angle α	21 mrad
Spherical aberration C_s	1.429 µm
Fifth order spherical aberration C_5	50 µm
Defocus	−3 nm
Camera Length	115 mm
Minimum detector angle	51.3428 mrad
Maximum detector angle	173.887 mrad
Sample thickness	9.7812 nm
Thermal diffuse scattering	10 configurations

Table 3.18 – Overview of simulation parameters

3.9.2 Comparison of simulations from different structures: $\langle 1\,0\,0 \rangle$ direction

In $\langle 1\,0\,0 \rangle$ direction, it is possible to observe some differences in the projections for the three structures, even though the distances between peaks are nearly the same. At a first glance, kesterite (figure 3.32a) and stannite (figure 3.32c) simulations are similar, whereas PMCA simulation (figure 3.32e) is different in the intensity patterns.

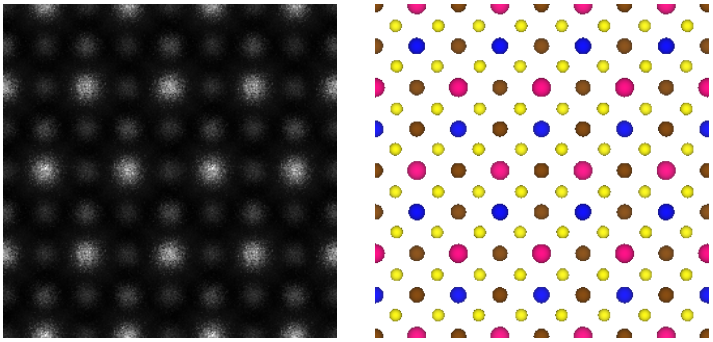

(a) Kesterite simulation (b) Kesterite model

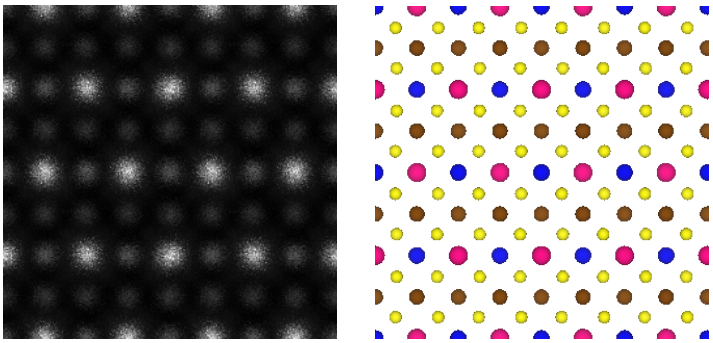

(c) Stannite simulation (d) Stannite model

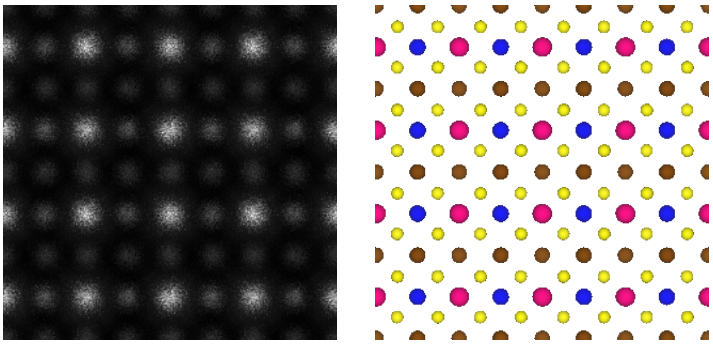

(e) PMCA simulation (f) PMCA model

Figure 3.32 – Simulations and atomistic models for the direction [1 0 0]. Cu: brown, Zn: blue, Sn: fuchsia, S: yellow.

The atomic columns in this projection are composed of the same element respectively. Therefore, Sn columns appear brighter, as it is the heaviest element in the compound. Cu and Zn columns have a comparable intensity as these elements are neighbours in the periodic table. S is barely visible. By assuming a column intensity proportional to Z^2 in STEM-HAADF imaging, we can evaluate that the integrated intensity for each of the column is:

1. for Cu, $Z^2_{\mathrm{Cu}} = 29^2 = 841$, relative value 0.34;
2. for Zn, $Z^2_{\mathrm{Zn}} = 30^2 = 900$, relative value 0.36;
3. for Sn, $Z^2_{\mathrm{Sn}} = 50^2 = 2500$, relative value 1;
4. for S, $Z^2_{\mathrm{S}} = 16^2 = 256$, relative value 0.10.

In particular, bright Sn columns are forming a different pattern depending on the atomic structure, as confirmed by the simulations presented in figure 3.32. Bright columns correspond to Sn positions (in fuchsia in the model). Kesterite (figure 3.32a) and stannite (figure 3.32c) have Sn atoms in the same sites, therefore they present the same "rhombus" projection. Pre-mixed Cu-Au structure (figure 3.32e) shows a "rectangular" bright columns pattern,these last being composed by pure Sn. Accordingly to this feature a distinction between kesterite or stannite phase and pre-mixed Cu-Au phase is possible.

3.9.3 Comparison of simulations from different structures: $\langle 2\,2\,1 \rangle$ or $\langle 1\,1\,1 \rangle$ direction

In case of kesterite $\langle 2\,2\,1 \rangle$, there is two alternating kind of columns:

1. $CuSnS_2$, $\overline{Z}^2 = 27.75^2 \approx 770$, relative intensity value 1;
2. $CuZnS_2$, $\overline{Z}^2 = 22.75^2 \approx 518$, relative intensity value 0.67;

In case of stannite $\langle 2\,2\,1 \rangle$, the alternating columns are:

1. CuS, $\overline{Z}^2 = 22.5^2 \approx 506$, relative intensity value 0.65;
2. $ZnSnS_2$, $\overline{Z}^2 = 28^2 = 784$, relative intensity value 1.

From the simple comparison of intensities, these two structures are indistinguishable, as their patterns are very similar.

In case of PMCA $\langle 1\,1\,1 \rangle$, the alternating columns are:

1. CuS, $\overline{Z}^2 = 22.5^2 \approx 506$, relative intensity value 0.46;
2. ZnS, $\overline{Z}^2 = 23^2 = 529$, relative intensity value 0.49;
3. SnS, $\overline{Z}^2 = 33^2 = 1089$, relative intensity value 1.

Here, three kinds of columns are shown: on the one hand, CuS and ZnS columns show very similar intensity values and comparison is difficult. On the other hand, SnS bright columns are forming a clear separated pattern. Therefore, PMCA is clearly distinguishable from kesterite and stannite phases.

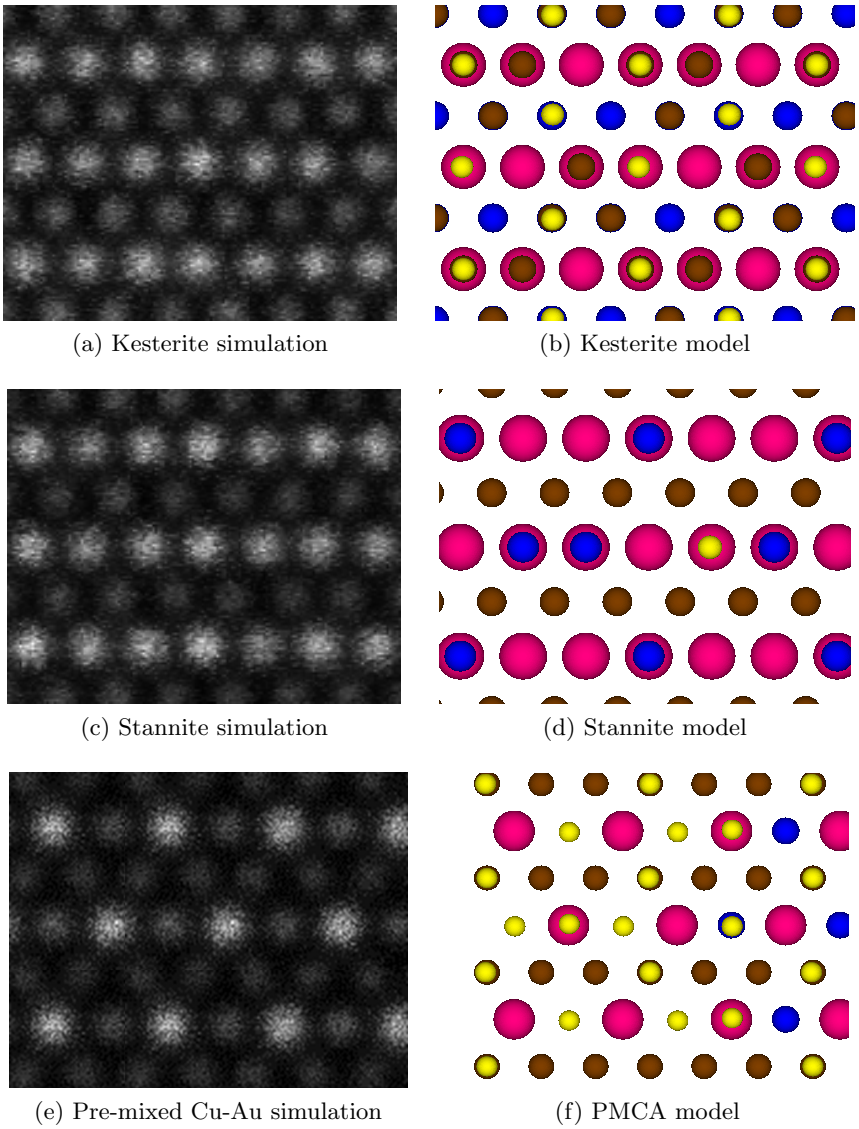

(a) Kesterite simulation (b) Kesterite model

(c) Stannite simulation (d) Stannite model

(e) Pre-mixed Cu-Au simulation (f) PMCA model

Figure 3.33 – Simulations and atomistic models for the direction [2 2 1] ([1 1 1] in the case of PMCA structure). Cu: brown, Zn: blue, Sn: fuchsia, S: yellow. Sn atoms are artificially represented with an enlarged radius, to underline the heaviest atoms and explain the bright columns patterns in simulations.

3.9.4 STEM-HAADF images

STEM-HAADF images were acquired with a FEI Titan^3 microscope. Aberrations were corrected with a CEOS probe corrector; spherical aberration was set to a value around 1 µm. Aberrations were measured after the aligning procedure, by a routine typical of CEOS correctors: aberrations are measured after the acquisition of tilted series of the probe. Values of the principal ones are given in table 3.18. They have been used to simulate the images presented in subsections 3.9.2 and 3.9.3.

The population of NCs is deposited on the ultrathin amorphous carbon film without preferred orientation. At first sight, and as confirmed in the nanodiffraction experiment, they do not show any orientation correlation with their first neighbours. Only a few of them are oriented exactly (or very close) to the zone axes, allowing structural discrimination. It is preferable to explore the grid, looking for well-oriented NCs, rather than aligning the NC manually. In fact, during the sample alignment procedure, the crystal is exposed to the electron beam: the burning of organic contaminants can reduce the observation quality and moreover the energetic beam could modify NC atom positions.

The most significant images are presented here and compared with the corresponding simulation. It is important to underline some important assumptions and limitations of this strategy:

- while simulations are calculated on superstructures with a constant thickness, real NCs have thickness variations (see appendix H for further simulations with different thickness values);
- there is not evident faceting; NCs are assumed to be spheroidal;
- as pointed out in section 3.4.1, NCs do not respect the exact stoichiometry[16]. Nevertheless, simulations are calculated from perfectly stoichiometric structures, as it is assumed that point-like defects do not change the average cation ordering substantially;
- only a very small fraction of NCs are in the proper orientation and show characteristic patterns, however, some common features are recognised;
- the image is a projection on a plane, the NC is a three-dimensional object. Smaller disordered domains can be "hidden" if they are in the same projected area covered by crystal zones with a high cation order;
- kesterite-stannite structure is the name used to indicate zones where features of these structures are present (as kesterite and stannite are practically undistinguishable following this approach).

$\langle 1\,0\,0 \rangle$ projection

As seen in section 3.9.2, it is possible to distinguish between kesterite or stannite structures and PMCA structures by looking at the pattern formed by the brightest columns:

[16] Composition of the final sample is $Cu_{2.2}Zn_{0.9}Sn_{1.2}S_4$ and not the stoichiometric Cu_2ZnSnS_4

the pattern has a rhombohedral shape for kesterite and stannite structures, while premixed Cu-Au structure forms a squared (more precisely, rectangular) motif.

In figure 3.34 it is possible to observe a crystal having an orientation $\langle 1\,0\,0 \rangle$.

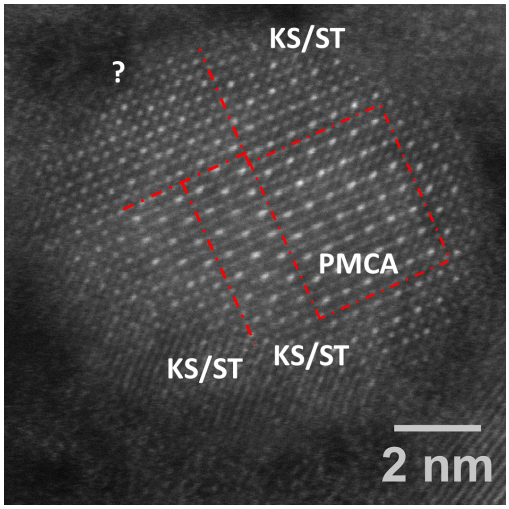

Figure 3.34 – A CZTS NC oriented in direction $\langle 1\,0\,0 \rangle$

Firstly, the crystal cation positions are in an ordered and regular network. Nevertheless, it is possible to divide the NC into at least 5 zones, characterised by different bright atomic columns motifs:

- the largest grain shows PMCA characteristics. This domain has a size of about $2.5\,\text{nm} \times 2.5\,\text{nm}$.
- At its borders, there is a stacking fault. The positions of the atomic columns remain (at a first analysis) substantially the same; nevertheless, the cation ordering changes. The pattern gets typical features of a kesterite-stannite domain.
- A stacking fault is observed between two kesterite-stannite domains: this interface has Sn atoms in the same position as for a PMCA structure (i.e. there is a PMCA monolayer, one unit cell thick, between two kesterite-stannite domains).
- Some zones are not identified. Those are predominantly present in the vicinity of NC surface, in zones where thickness variations are the most significant. Some intensity fluctuations are still present, but not regular.

$\langle 2\,2\,1 \rangle$ (or $\langle 1\,1\,1 \rangle$) projection

Some NCs are found to be oriented in direction $\langle 2\,2\,1 \rangle$ - $\langle 1\,1\,1 \rangle$. Atomic column contrast is weaker with respect to [1 0 0] projection, but some features are still remarkable.

The crystal shown in figure 3.34 shows interesting patterns in its atomic columns. Domain I in figure 3.35b has a pattern characteristic of PMCA structure. Comparison

between line profile from an experimental image in figure 3.34e and a normalized line profile from PMCA simulation in figure 3.34f along $[\bar{1}\,1\,1]$ shows a good agreement.

Domains II, III and IV are equivalent and show a common pattern, typical of the kesterite-stannite structure. These domains share the same zone axis [2 2 1], their difference is a rotation of 60°. This rotation is due to a different cation stacking in each domain. Another NC with zone axis $\langle 2\,2\,1\rangle$ - $\langle 1\,1\,1\rangle$ is shown in figure 3.35. Figures 3.35b and 3.35c show a pattern typical of PMCA structure in the centre of the NC; in the bottom, some bright lines typical of kesterite-stannite structure are visible. Nonetheless, cation network looks continuous. Only the cation ordering is changing in different zones of the NCs.

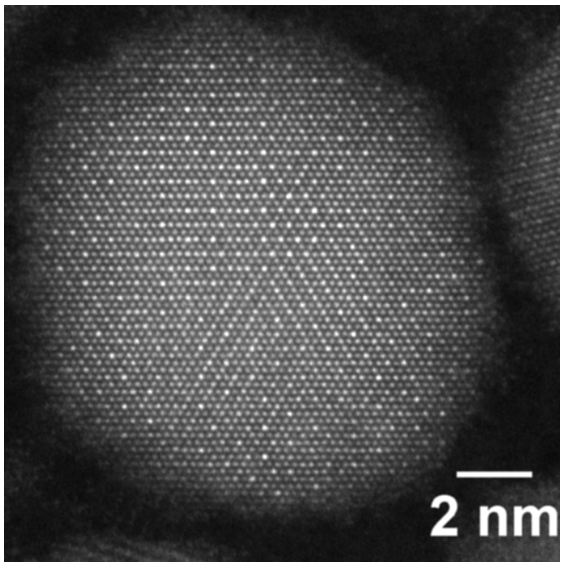

(a) CZTS NC aligned along ⟨2 2 1⟩ (or ⟨1 1 1⟩ for PMCA structure).

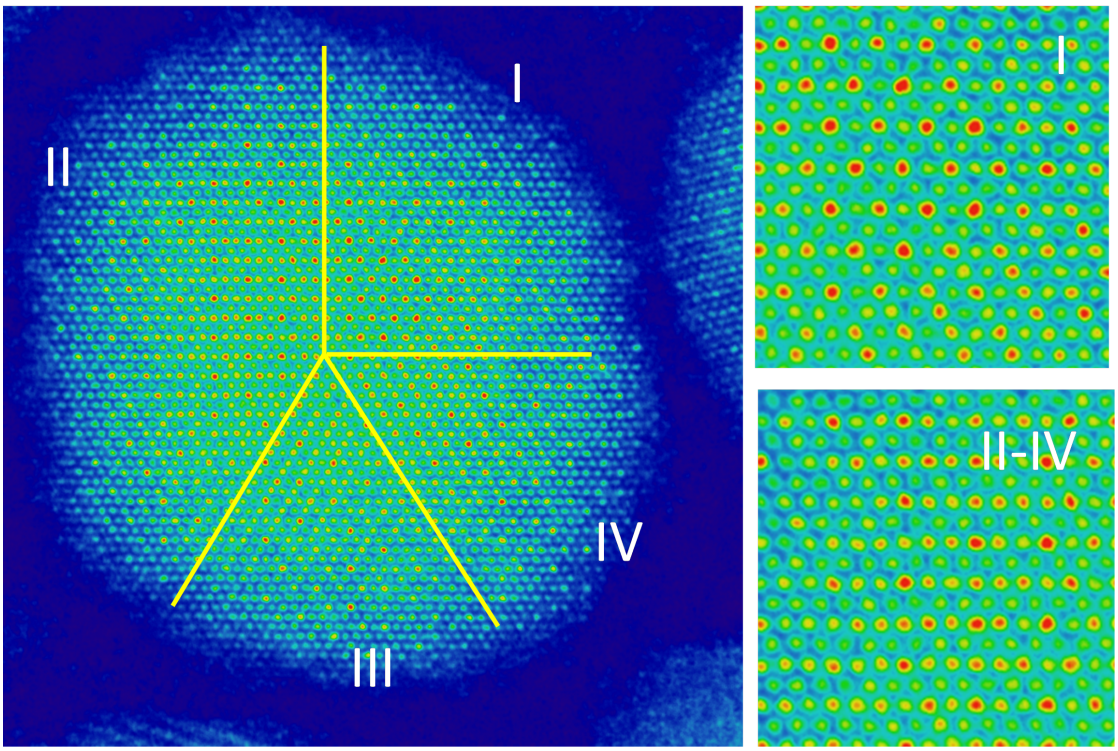

(b) Different domains are present: domain I has a PMCA pattern, whereas II, III and IV have a kesterite-stannite pattern (with different orientation).

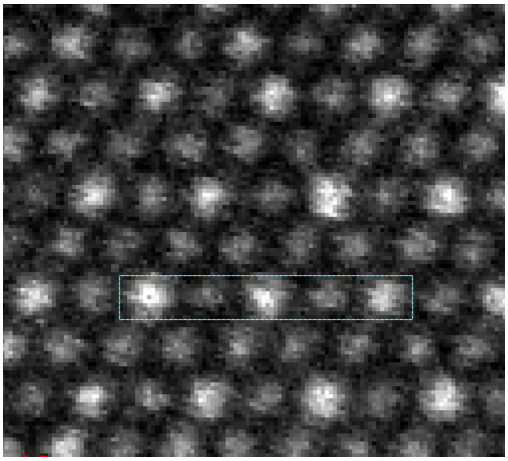

(c) Detail of domain I in figure 3.35a, experimental image.

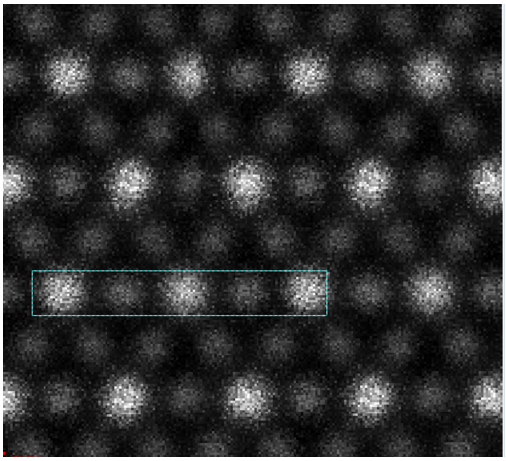

(d) Simulation of PMCA structure in $\langle 1\,1\,1\rangle$ direction.

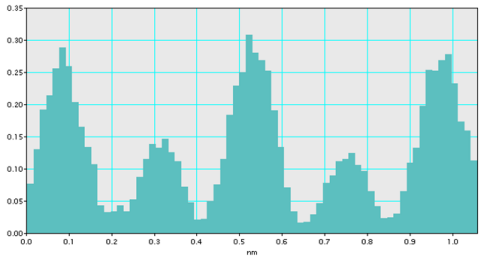

(e) Line profile along $\langle \bar{1}\,1\,1\rangle$ direction from the experimental image presented in 3.34c

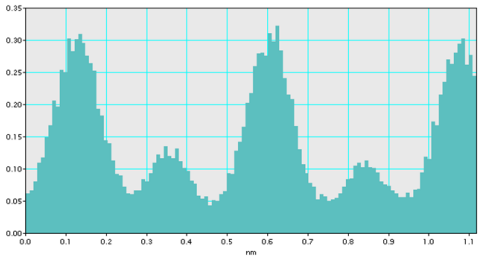

(f) Line profile along $\langle \bar{1}\,1\,1\rangle$ direction from the simulation presented in 3.34d

Figure 3.34 – Details of a well-oriented CZTS NC and comparison of patterns and line profile between experimental image and PMCA structure simulation.

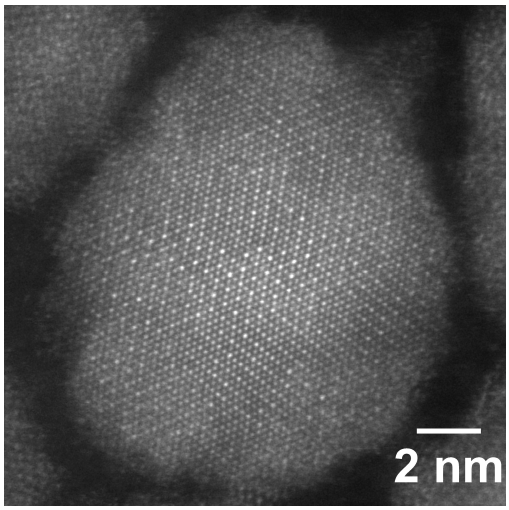

(a) CZTS NC aligned along ⟨2 2 1⟩ (or ⟨1 1 1⟩ for PMCA structure).

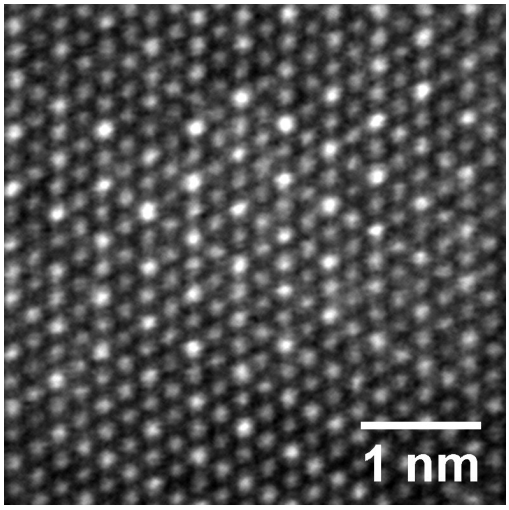

(b) Detail of the pattern due to higher intensity columns.

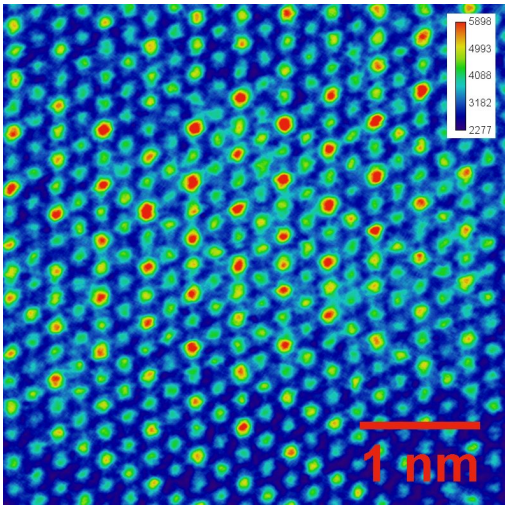

(c) The same zone with rainbow lookup table: see in red the highest intensity columns.

Figure 3.35 – Details of a well-oriented CZTS NC. PMCA structure is clearly recognised thanks to its intrinsic bright column pattern.

3.10 Conclusion

In summary, monodisperse nanocrystalline CZTS has been synthesised colloidally through Steinhagen's heat-up method [117]. We have monitored the temporal evolution of CZTS nanocrystal composition at the nanometric scale with STEM-EDS, SAXS and WAXS and finally proposed a nanocrystal formation mechanism comprising nucleation, growth and cation inter-diffusion.

From the detailed characterisation of several single particles over time, we find that a binary Cu_xS compound is formed already at room temperature. Increasing the temperature at 110 °C results in three distinct particle populations of CZTS: large and platelet nanoparticles that are Cu-rich, and small nanoparticles that are Zn- and Sn-rich. Following the temperature increase at 280 °C, only large and small nanoparticles remain. Small nanoparticles become very Zn-poor. Over time, Ostwald ripening occurs, and the population of small particles decreases resulting in a cation exchange in the larger NCs, in which the concentration of Cu decreases as both Sn and Zn are incorporated. As the time proceeds, small nanocrystals disappear, and large NCs get homogeneous in size and composition, reaching an almost-stoichiometric composition.

It would have been interesting to perform a complementary study by neutron diffraction, which is sensitive to the difference in scattering length between Zn and Sn. However, the times of acquisitions are relatively long due to the low flux of neutrons, and therefore it would have been difficult to perform an *in situ* experiment along with the remarkable intermediate steps occurring during the growth of Cu_2ZnSnS_4 NCs.

Detailed structural characterisation was performed on the final CZTS nanocrystals. Two advanced microscopy techniques were applied: Nanobeam Precession Electron Diffraction (NPED) technique and HRSTEM-HAADF. Literature reports that the CZTS NCs in bulk can crystallise in the kesterite, stannite or pre-mixed Cu-Au (PMCA) crystal structures.

NPED technique was used to characterise several NCs thanks to a large field of view. When multiplying the result of the phase mapping with the reliability value, the PMCA structure appeared to be the dominant one for all the observed NCs. Nevertheless, the reliability in case of kesterite and stannite domains was low, due to the similarity of the two structure: a clear cohabitation of stannite-kesterite NCs and a majority of PMCA NCs were found. More phases were also found in single NCs. To the best of our knowledge, it is the first time that PMCA structure was identified experimentally for a Cu_2ZnSnS_4 NC material.

In the second technique, it has been shown by multislice simulations of STEM-HAADF images that kesterite-stannite and PMCA structure could be distinguished thanks to a peculiar brightness motif due to typical position of the heavier atoms inside the compound (Sn). However, the discrimination was possible only when some particular zone axes were perpendicular to the incident electron beam. Therefore the number of NCs that could be analysed by this technique was relatively low. Nevertheless, the well-oriented NCs clearly showed patterns specific to the PMCA structure, confirming the results obtained by NPED. Moreover, a clear visualisation of PMCA in cohabitation

with smaller kesterite-stannite domains was shown: this implies that the cation order is more complex than expected in this chalcogenide material.

Chapter 4

Morphology and structural characterisation of $CsPbBr_3$ nanocrystals

4.1 Introduction

In the last five years, perovskite-based solar cells have raised a tremendous research interest. This success is principally due to the dramatic evolution of their power conversion efficiency in solar cells, reaching more than 22% today, and the possibility of low-cost processing [54]. Power conversion efficiency of these devices surpassed organic photovoltaics, rivalling established photovoltaic technologies based on Si, CdTe, $CuIn_{1-x}Ga_xSe$ and GaAs. More details on $CsPbBr_3$ are reported in the related introductory section 1.2.3, whereas appendix I recalls some remarkable optical and electronic properties of halide perovskites of the type AMX_3. Protesescu is among the first to demonstrate the successful synthesis of $CsPbX_3$ (X = Cl, Br, I) nanocubes using a hot-injection and fast-cooling approach [60, 151]. Owing to the exciton Bohr diameter of up to 12 nm, $CsPbX_3$ NCs exhibit compositional bandgap engineering as well as size-tunability of their bandgap energies through the entire visible spectral region of 410 nm to 700 nm. Protesescu reported emission line-widths of 12 nm to 42 nm, PLQY of 50-90%, and PL lifetimes of 1 ns to 29 ns.

Regarding crystal structure, at room temperature, bulk or nanowire $CsPbBr_3$ show thermodynamically preferential orthorhombic structure as determined by X-ray diffraction. Reports on the structure of nanometer-sized $CsPbBr_3$ conflict between either $Pm\bar{3}m$ cubic [60, 65, 66] or $Pnma$ orthorhombic [67, 68] structure (figure 4.3). Also, mixed structures, where both phases exist simultaneously, have been reported [69]. A clear description of the crystal structure is crucial for the physical interpretation of the electronic structure of NCs.

In this work, we present a detailed investigation of the structural characterisation of $CsPbBr_3$ NCs prepared following the synthesis of Protesescu [60].

Section 4.2 briefly recalls how the $CsPbBr_3$ NCs have been prepared and describes their morphology.

Section 4.3 presents in details the cubic and orthorhombic $CsPbBr_3$ structures.

Section 4.4 is an overview of the structural studies of this kind of material in the literature.

In section 4.5 the experimental results obtained using different TEM techniques, HRSTEM, HRTEM, SAED, EDS and X-rays, are presented and analysed.

These experimental results are then discussed in section 4.6.

4.2 $CsPbBr_3$ sample preparation

The synthesis of $CsPbBr_3$ follows the procedure described by Protesescu [60]. Briefly, controlled arrested precipitation of Cs^+, Pb^{2+} and Br^- ions into $CsPbBr_3$ is obtained by reacting Cs-oleate with $PbBr_2$ in octadecene (ODE). The mixture ODE and $PbBr_2$ is dried under vacuum for 1 h at 120 °C. Dried oleylamine and dried oleic acid were injected at 120 °C under N_2. After complete solubilization of the $PbBr_2$ salt, the temperature was raised to 200 °C and Cs-oleate solution is quickly injected and, 5 s later, the reaction mixture was cooled by an ice-water bath. The crude solution was cooled down with a water bath and NCs were separated by centrifuging. After centrifugation, the supernatant was discarded and the particles were redispersed in toluene, forming long-term colloidally stable solutions. The TEM grids were prepared by drop casting the solution either on graphene films or more often on standard carbon films with holes. Figure 4.1 displays STEM images of $CsPbBr_3$ NCs. It is evident that the NCs are polydisperse and NCs with a comparable size tend to aggregate and self-organize. TEM or STEM images provides a projection of the NCs along the electron beam. The NCs have a square shape with round corners.

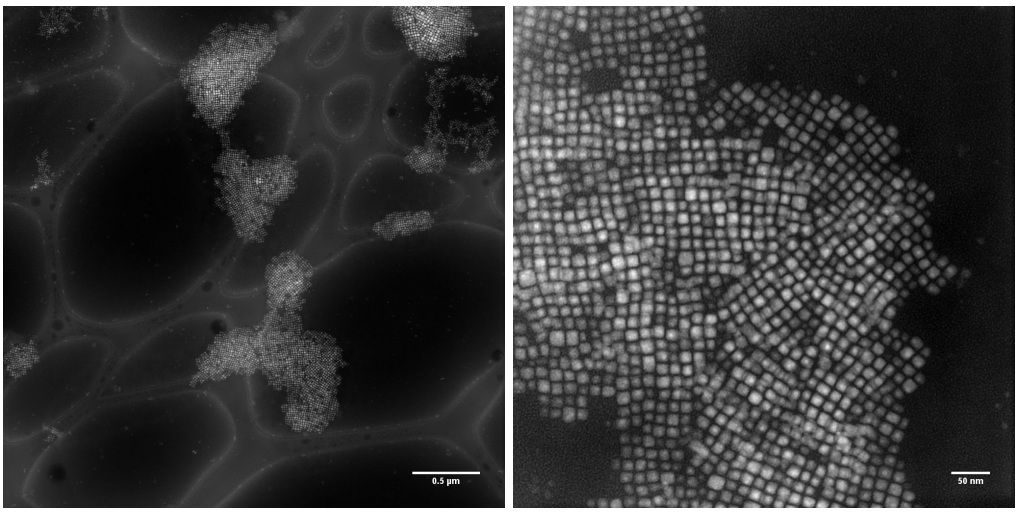

(a) (b)

Figure 4.1 – Typical STEM images of $CsPbBr_3$ NCs.

Using the "analyse particle tool" in ImageJ [104] an estimation of the average NC

size was measured in different regions (see figure 4.2). From the average area, the average edge of the square NC is obtained by taking the square root of the obtained area. The average area in the left part of figure 4.2 is 165.9 nm^2, corresponding to a mean NC size of 12.9 nm. On the other hand, the smaller NCs in the right region of the same image are analysed and their mean area from the region is 74.49 nm^2, corresponding to 8.6 nm.

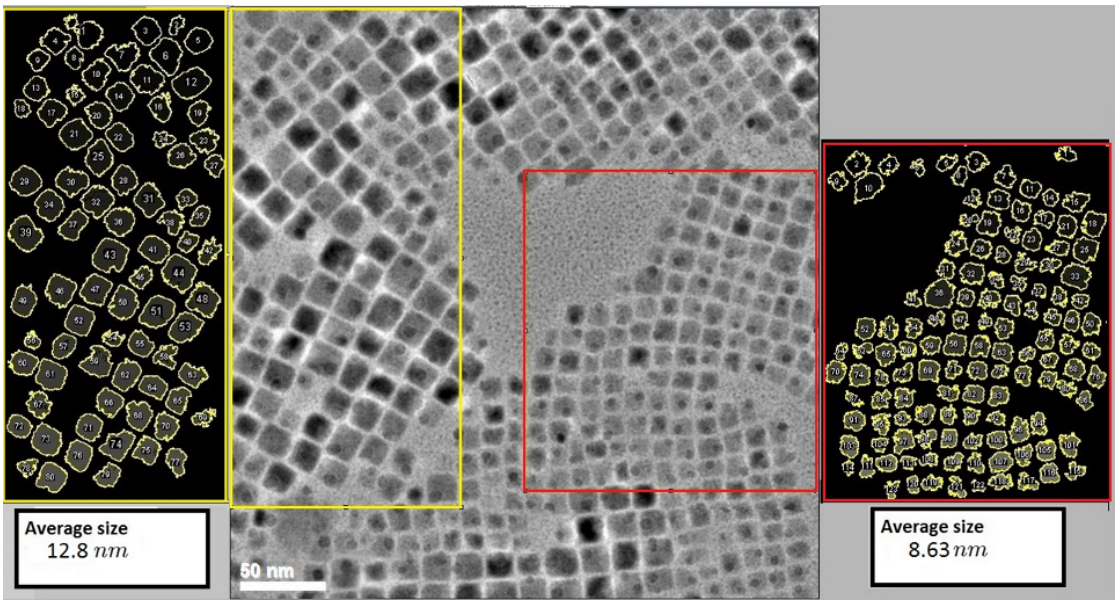

Figure 4.2 – Particle analysis of two separated self-organized domains. Left and right images are binary images created from respectively the yellow and red boxed area of the central image.

The self-organisation probably builds during the drying process, following the drop casting of the solution on the TEM sample grid (surface energy is minimised). The size dispersion in one domain is low, and the passage from one domain to the other is quite smooth. This aspect is typical of systems tending to diminish the surface energy. Some NCs are isolated from the self-organised aggregates, as they are different in shape/size. This isolation can be explained by the short-range influence of surface energy: with irregular shape, a minimal surface-to-surface interaction gives an insufficient force to keep single NCs in contact. Nanoparticles with a cuboid shape tend to maximise the contact with other cubes and, due to the shape, this maximisation is realised when the cubes have the same shape. The cuboid shape allows maximising the contact surface, while round or irregular surfaces lead to less contact area. NCs with irregular shape are isolated because they would create a hollow zone inside the superstructure, and therefore increase the configurational energy.

Determination of the 3D shape of NCs is difficult in standard TEM because the observation is done over a projection, i.e. a 2D image, with no information about the third dimension. Nevertheless, in the case of the $CsPbBr_3$ NCs a cuboid shape can be

reliably assigned. Firstly, following our experience, platelets tend to arrange by piling up, to maximise the contact between the larger area facets. Therefore, some lateral projection of platelet stacks would be observed, but it is not the case in this study. Also, in all the micrographs, quite regular squares are observed (except for few NCs with irregular shapes). Secondly, in high-resolution images, the NCs show a clear crystalline pattern (no moiré fringes nor superposition), showing no 3D stacking of NCs. All the superstructure formed by the cuboid $CsPbBr_3$ NCs dried on an ultrathin carbon layer are observed to be purely bi-dimensional.

4.3 Cubic and orthorhombic $CsPbBr_3$ structures

The unit cell parameters and atomic positions of the cubic and orthorhombic structures are given in table 4.1. Two equivalent ways, which differ only by different reference systems, can describe the cubic structure.For instance, one unit cell of the cubic structure has one Pb atom located at the origin, one Cs atom at the centre of the cubic and 3 Br atoms at the centre of the faces. Alternatively, in another model, the unit cell has one Cs atom at the origin, one Pb atom at the cube centre and 3 Br atoms at the face centres: this is the choice made in this manuscript. Bonds between atoms are ionic. Br atoms are the only anions and are situated in "between" the cations of the structure. To preserve the overall zero charge, the oxidation state of Pb atoms is 2+: the 3 Br atoms of the unit cell accept one electron each, to have 3 Br^- anions; on the contrary, Cs atoms donate 1 electron to fulfil the octet rule. A very convenient way to see the $CsPbBr_3$ structures is to realise that the Br atoms of the unit cell are situated at the corner of octahedra: in one model, octahedra have Cs atoms at their centre or conversely they have Pb atom at their centre. As it is shown in the following, it is better to consider the model based on octahedra with Pb atoms at their centres. Figure 4.3 represents the structure with Pb-centred octahedra in grey (Pb atom in grey) in the centre of the unit cell, and the Br atoms at their corners in brown.

The orthorhombic unit cell is larger than the cubic one, approximately four times bigger, and contains four times more atoms, i.e. 4 Cs, 4 Pb and 12 Br (see table 4.1). The most comfortable discrimination between the two structures is done by looking along the [0 1 0] direction of the orthorhombic structure and compare it to any ⟨1 0 0⟩ direction of the cubic structure (see figure 4.3). The orthorhombic structure maintains the octahedra bone structure of the cubic structure, but in the orthorhombic structure the octahedra are slightly tilted and deformed[1]: symmetry changes as well as the interaction with neighbour atoms. These distortions are widespread in many perovskite structures. Table 4.1 lists the sites, the location and the coordinates of the elements in the $Pm\overline{3}m$ and in the *Pnma* space groups, as defined by Cottingham [67].

Table 4.2 displays atomic number and atomic radius of Cs, Pb and Br. Cs has by far the larger atomic radius.

[1]For the orthorhombic structure, in the octahedron the distance of the vertices (Br) from the centre (Pb) are 2.991 nm, 2.956 nm and 2.964 nm. The distance between Pb and Br column are 2.976 nm and 2.941 nm in the projection [0 1 0].

$Pm\overline{3}m$		
$a = b = c = 5.8445$; $\alpha = \beta = \gamma = 90°$		
Site	Wyckoff letter	Coordinates
Cs cation	a	0,0,0
Pb cation	b	$\frac{1}{2},\frac{1}{2},\frac{1}{2}$
Br anion	c	$0,\frac{1}{2},\frac{1}{2}$; $\frac{1}{2},0,\frac{1}{2}$; $\frac{1}{2},\frac{1}{2},0$
$Pnma$		
$a_o = 8.2609$; $b_o = 11.7650$; $c_o = 8.2124$; $\alpha = \beta = \gamma = 90°$		
Site	Wyckoff letter	Coordinates
Cs cation	c	$x,\frac{1}{4},z$; $\overline{x}+\frac{1}{2},\frac{3}{4},z+\frac{1}{2}$; $\overline{x},\frac{3}{4},\overline{z}$; $x+\frac{1}{2},\frac{1}{4},\overline{z}+\frac{1}{2}$
Pb cation	b	$0,0,\frac{1}{2}$; $\frac{1}{2},0,0$; $0,\frac{1}{2},\frac{1}{2}$; $\frac{1}{2},\frac{1}{2},0$
Br(1) anion	c	$m,\frac{1}{4},n$; $\overline{m}+\frac{1}{2},\frac{3}{4},n+\frac{1}{2}$; $\overline{m},\frac{3}{4},\overline{n}$; $m+\frac{1}{2},\frac{1}{4},\overline{n}+\frac{1}{2}$
Br(2) anion	d	$\pm$ [u,v,w; $\overline{u}+\frac{1}{2}$, $\overline{v}$, $w+\frac{1}{2}$; $\overline{u}$, $v+\frac{1}{2},\overline{w}$; $u+\frac{1}{2}$, $\overline{v}+\frac{1}{2}$, $\overline{w}+\frac{1}{2}$]

Table 4.1 – Unit cell parameters and atomic positions for $CsPbBr_3$ perovskites with $Pm\overline{3}m$ (221) and with $Pnma$ space groups (62).

Atom	Z	Z^2	atomic radius (pm)
Cs	55	3025	334
Pb	82	6724	182
Br	35	1125	112

Table 4.2 – Atomic number and atomic radius of Cs, Pb and Br

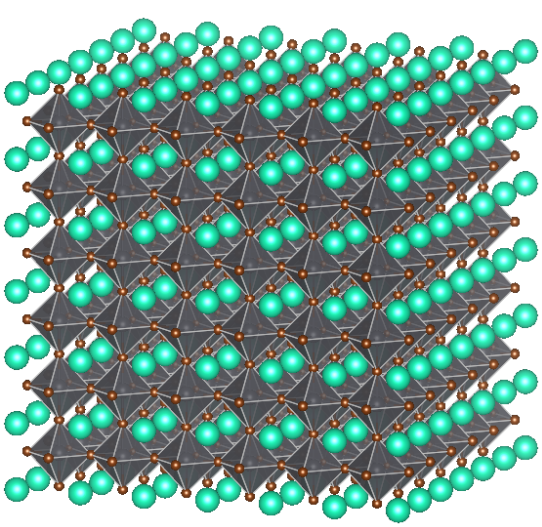

(a) 3D model of cubic $CsPbBr_3$ NC.

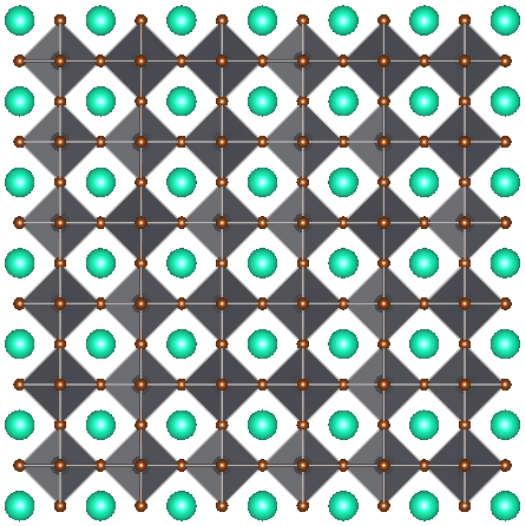

(b) Projection of cubic $CsPbBr_3$ perovskite along $\overrightarrow{a}$.

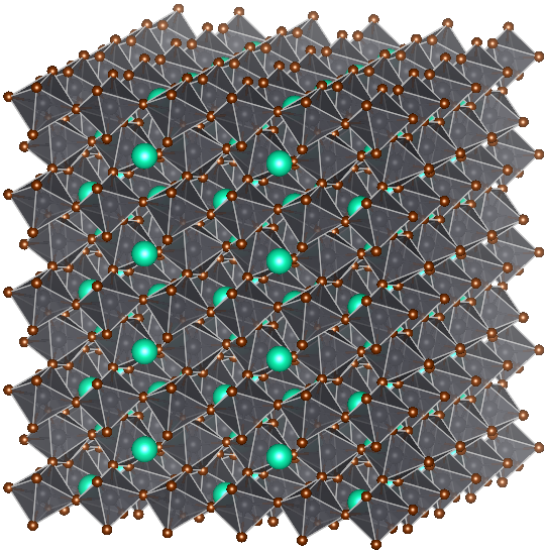

(c) 3D model of orthorhombic $CsPbBr_3$ NC.

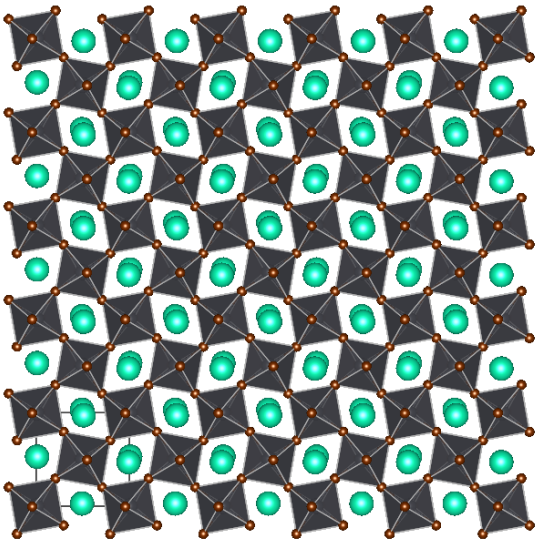

(d) Projection of orthorhombic $CsPbBr_3$ perovskite along $\overrightarrow{b}$.

Figure 4.3 – Models of cubic $Pm\overline{3}m$ and orthorhombic $Pnma$ $CsPbBr_3$ (Cs is represented in green, Pb grey and in the centre of octahedra, Br brown).

Glazer [152] divided the overall tilts according to the three main axes [1 0 0], [0 1 0], [0 0 1] and three letters were chosen to indicate the magnitude of tilting along each of the axes. Superscripts + and − indicate if the successive octahedron tilts in the same direction (+) or in the opposite direction (−), superscript 0 is used if there is no tilt about the axis. Same tilts are indicated with the same letter, and unequal tilts by different letters. For instance, $a^0b^+c^-$ indicates unequal tilts occurring along [0 1 0] and [0 0 1] axes and no tilt along [1 0 0]. The octahedral pairs along [0 1 0] are tilted in the same direction, whereas along [0 0 1] they are tilted in the opposite ways.

In the case of the reported orthorhombic structure for $CsPbBr_3$, the space group *Pnma* results in a representative tilt system $a^+b^-b^-$ [153]. The projections over the [1 0 0], [0 1 0] and [0 0 1] of the pseudocubic unit cell are shown in figure 4.4.

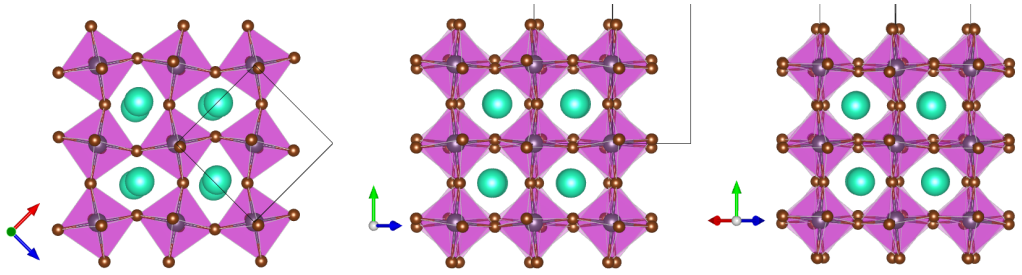

(a) 0 1 0 (b) $\bar{1}$ 0 1 (c) 1 0 1

Figure 4.4 – Projection of the *Pnma* $CsPbBr_3$ structure along (a) [0 1 0], (b) [$\bar{1}$ 0 1] and (c) [1 0 1] zone axes. The red, green and blue arrows in the compasses correspond to $\vec{a}$, $\vec{b}$ and $\vec{c}$ respectively for the orthorhombic unit cell. (a), (b) and (c) show the [1 0 0], [0 1 0] and [0 0 1] zone axes in the pseudo-cubic system, respectively. Cs atoms are represented in light green, Pb atoms are grey and in the centre of the octahedra, Br atoms are brown and in the vertices of the octahedra.

In the cubic structure, atoms of the same species are perfectly aligned along the a, b and c axis, whereas in the orthorhombic structure, lateral displacements of some atoms are present in some particular projections. In the orthorhombic structure, the lighter atoms in the structure have the greatest displacements whereas Pb, the heaviest element, does not show any displacements. For instance, the following lists give for two particular directions of observation, i.e. in 2 particular projections, the displacement or distance between 2 atoms of the same type that are superposed in the projection of the cubic structure.

- Along the orthorhombic [0 1 0] zone axis:
  - Cs-Cs atoms have a lateral displacement in the projection equal to 6 pm;
  - Pb-Pb atoms no lateral displacements, they are aligned as in the cubic structure
  - Br-Br atoms in the pure Br columns have no lateral displacement;

  - Br-Br atoms in the mixed Pb-Br columns have a lateral displacement of 9 pm.

- Along the orthorhombic [1 0 1] zone axis:
  - Cs-Cs atoms have a lateral displacement of 1.2 pm;
  - Pb-Pb atoms have no lateral displacement;
  - Br-Br atoms in the pure Br columns have a displacement along $[\bar{1}\,0\,1]$ equal to 6 pm;
  - Br-Br atoms in the mixed Pb-Br columns have a lateral displacement of 1.2 pm.

In the orthorhombic structure, the Pb atoms have no lateral displacement; however the Pb form a Pb-sublattice that is different from the cubic Pb-sublattice. In the cubic structure, the Pb-sublattice is cubic with a lattice parameter of 0.584 45 nm. In the orthorhombic structure, the Pb-sublattice is a deformed cube with lattice parameters $a_{\mathrm{Pb}} = [1\,0\,1]$, $b_{\mathrm{Pb}} = [1\,0\,\bar{1}]$, $c_{\mathrm{Pb}} = \frac{1}{2}[0\,1\,0]$, $\alpha_{\mathrm{Pb}} = 90°$, $\beta_{\mathrm{Pb}} = 90°$ and $\gamma_{\mathrm{Pb}} = 89.66°$. Of course, these lattice variations of the Pb-sublattice are very small and are difficult to see in High Resolution images or even in diffraction as we will discuss below.

In the experimental results, the displacements of light atoms will be shown on some High-Resolution images. However, in fact, the easiest way to differentiate the two structures is to measure the lattice plane distances, either directly in diffraction experiments or indirectly by taking a Fourier Transform of a High-Resolution image. Indeed, as it is illustrated in figure 4.28 and in section I.2, the displacements of lighter atoms in the structure introduces larger periods distances when going from the cubic to the orthorhombic structure. These larger periods introduce additional spots in the reciprocal space.

In figure 4.5 the additional spots of the orthorhombic structure have been underlined in red. We recall that in the orthorombic structure the zone axis that have to be compared to a $\langle 0\,0\,1\rangle$ cubic are the [0 1 0], [1 0 1] and $[1\,0\,\bar{1}]$ directions. As the last two ones are equivalent, in figure 4.5, only the first two ones of the orthorhombic case are shown. In these two orientations, one can notice that the additional spots introduce additional rows of spots. The diffraction spots that are similar in the three diffraction patterns have minimal differences: difference of 2 pm in the distances and 0.3° in the angles at most. With a reference of pseudo-cubic [0 0 1] diffractogram, additional spots are at $(h + \frac{1}{2},\, k + \frac{1}{2},\, 0)$ in case of an orthorhombic [0 1 0] zone axis and at $(h + \frac{1}{2},\, k,\, 0)$ in case of an orthorhombic [1 0 1] zone axis. The additional spots of the othorhombic structure have low relative intensities: their simulated structure factors F_{hkl} are approximately nine times smaller than the spots visible in the cubic structure. Complete F_{hkl} values from cubic and orthorhombic structure are listed in the dedicated appendix at tables I.1 and I.2, respectively. Consequently these additional spots could easily be unnoticed in noisy diffractograms.

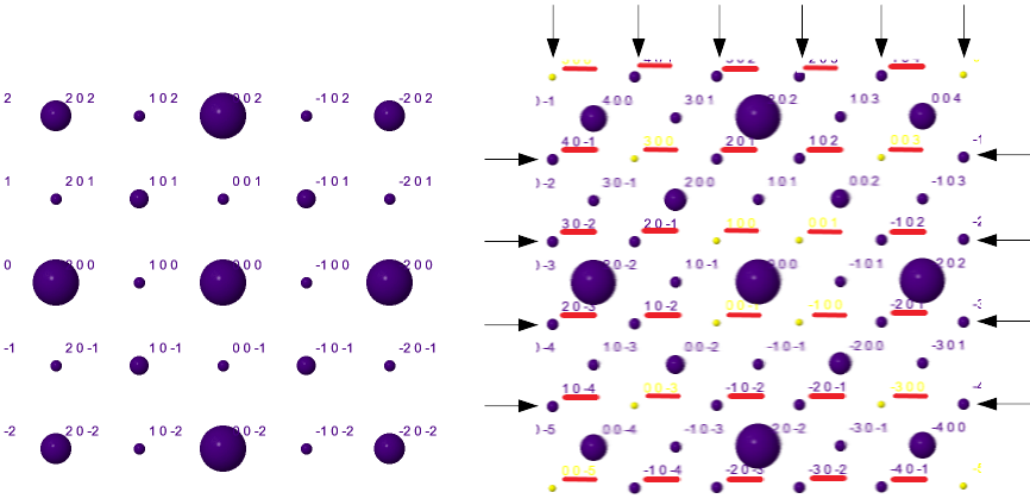

(a) Cubic $Pm\bar{3}m$ $CsPbBr_3$, zone axis $\langle 0\,0\,1 \rangle$

(b) Orthorhombic $Pnma$ $CsPbBr_3$, zone axis $\langle 0\,1\,0 \rangle$

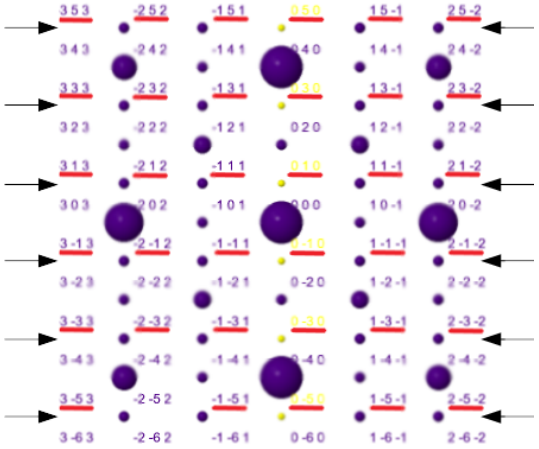

(c) Orthorhombic $Pnma$ $CsPbBr_3$, zone axis $\langle 1\,0\,1 \rangle$

Figure 4.5 – Simulated diffraction patterns for $CsPbBr_3$ performed on the UCA Cadiz server [154]. The extra reflections, whose indices are underlined in red, lay on lines (indicated by arrows). These extra reflections are caused by the the octahedra distortions and rotations in the orthorhombic structure.

4.4 Structural analyses of $CsPbBr_3$ nanocrystals in the literature

In this section, some studies investigating the crystal structure of $CsPbBr_3$ synthesized by colloidal methods and of similar morphology to ours are presented.

Cottingham studied two monodisperse samples having an average size of 6.5 and 12.5 nm, respectively. X-ray powder diffraction was performed at room temperature using synchrotron radiation. Rietveld refinement of orthorhombic structure fits substantially better on the 12.5 nm QDs. Pair distribution function (PDF)[2] analysis of total X-ray scattering showed that the orthorhombic distortion (favourable in bulk samples) is also present when the material is in the form of colloidal NCs[3] [67]. For the smaller NCs, the larger width of the peaks does not allow a reliable fit with Rietveld refinement, but some of the Bragg reflections can be exclusively fit by the orthorhombic model.

Another strategy to investigate the structure of $CsPbBr_3$ consists in observing the diffractogram of the sample cooled at a low temperature. The different thermal expansion coefficients of the $CsPbBr_3$ material were studied by powder X-ray diffraction in the range 12-300 K in Desy synchrotron lab [155]. The determined space group is orthorhombic ($Pbnm$) in the whole investigated temperature range. Neither splitting of reflections due to symmetry changes nor broadening was observed. Strong anisotropic behaviour of lattice parameters is shown in figure 4.6: a and c parameters increase from about 40 K to 300 K (the lattice expands along a direction stronger than along c axis), whereas b parameter decreases in the same temperature range. Inspired by this report, Dang observed only cubic peaks in the diffractograms at room temperature while, at a lower temperature (153 K), characteristic peaks of orthorhombic structure appeared [156]. The authors did not explain this behaviour by a phase transition, preferring instead focusing on the different thermal expansion of the three lattice parameters. They comment that the lattice parameters a', b', c' recalculated with respect to the ideal perovskite (a, b, $c/2$) for bulk orthorhombic $CsPbBr_3$ are very similar at room temperature (298 K) and further decreasing of temperature below the transition temperature 361 K increases the discrepancy between them. They performed HRTEM and SAED study for $CsPbBr_3$ NCs at various lower temperatures (figure 4.7). Their results have shown that the spacing among closely spaced peaks (298 K) increases at low temperature (153 K), indicating a

[2]The PDF describes the probability of finding any two atoms at a given distance r. Applying PDF analysis to crystalline materials, it is possible to obtain information on a medium-range of inter-atomic distances. This approach is complementary to the Rietveld method. A PDF can discriminate between short-range order (finite non-random displacement of the atoms) and random displacements of the atoms. The experimental PDF $G(r)$ or the radial distribution function $4\pi r^2 G(r)$ are obtained from the diffraction data by Fourier transforming the normalised total structure factor $S(Q)$ with $Q = 4\pi \frac{\sin\theta}{\lambda}$. $S(Q)$ is the measured intensity corrected for background, Compton and multiple scattering, absorption, geometric and other factors.

[3]Orthorhombic distortion splits Br positions into two crystallographically distinct sites, giving rise to a substantial reduction in the isotropic thermal displacement parameter for Br. For the smaller NCs, the large width of the peaks does not allow a reliable fit with Rietveld refinement, but some of the Bragg reflections can be fit exclusively by the orthorhombic model. PDF was generated using the X-ray total scattering data and fit with the same cubic and orthorhombic space groups. The best fit is observed with orthorhombic structure, particularly in the range between 5 Å to 7 Å (corresponding also to the Br-Br distance). The local Pb^{2+} off-centring resulted minimal.

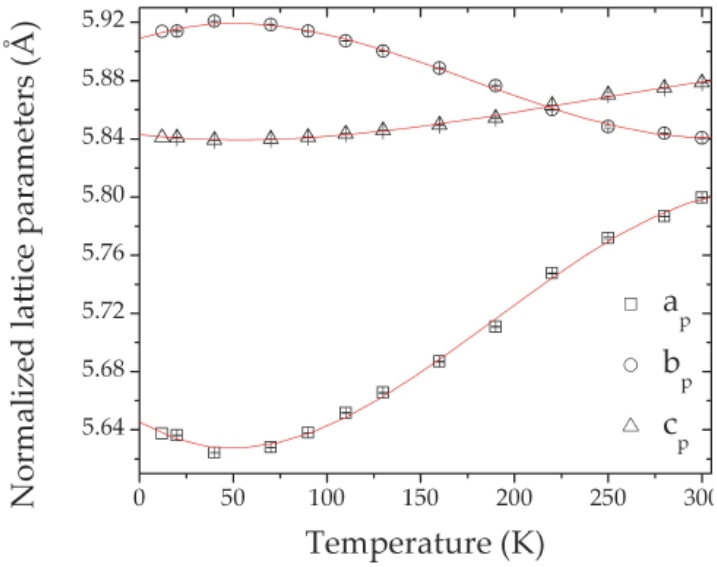

Figure 4.6 – Temperature evolution of normalized cell parameters in $CsPbBr_3$ $a_p = \frac{a}{\sqrt{2}}$, $b_p = \frac{b}{\sqrt{2}}$, $c_p = \frac{c}{2}$ where a, b, c are cell dimensions of orthorhombic $Pbnm$ $CsPbBr_3$. Lines are guides for the eyes. Reproduced from [155].

larger discrepancy among the lattice parameters [156].

In our opinion, this approach needs precautions. Crystal structure of bulk materials determined at low temperature should not be directly extrapolated to NCs at ambient temperature. The absence of phase transition must be demonstrated in the whole temperature range by Differential Scanning Calorimetry (DSC) (not carried out in the cited works). DSC is relatively easy to apply to bulk materials. Nevertheless, it can be difficult for colloidal NCs in solution, as the contribution from the NCs must be separated from surface ligands and organic molecule influence. Moreover, phase transition temperatures in bulk cannot be directly compared to phase transitions in nanomaterials. The surface-to-volume ratio is higher for smaller NCs and, therefore, variations in phase transition temperature depend on the NC size. Besides, the information from powder diffraction experiments is averaged over thousands of NCs and does not provide any contribution to establishing the structural homogeneity in the sample population.

After the realisation of our experiments in February 2016, new findings using HRTEM were reported by Yu, Zhang, Bertolotti and Brennan [69, 157–159], confirming the complex nature of these nanoparticles. Here, we summarise these works to provide an overview of the state-of-the-art in $CsPbBr_3$ NCs. With respect to the precedent works, electron microscopy provides a deep insight into the structure of single QDs. The structure can be observed for a great range of NC sizes, from the unit cell size to some tens of nanometers, while peak broadening and background signal are limiting factors for X-ray diffraction of small QDs.

The existence of polymorphism in $CsPbBr_3$ nanomaterials was reported by Yu [69]

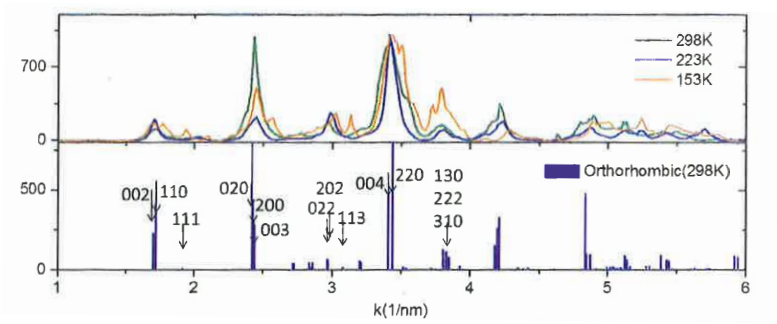

Figure 4.7 – Azimuthal integration of the SAED patterns taken for NCs at various temperatures and comparison with the powder XRD data for reference orthorhombic phase. Printed from [156].

in $CsPbBr_3$ nanosheets. Cubic and orthorhombic structures were found to be present in the same sheet (see figure 4.8); their finding was confirmed by focal series reconstruction from 70 low-dose AC-HRTEM images. The low-dose strategy was applied to avoid the alterations due to electron irradiation. The position of all the atoms in the sheet was determined, and in particular, a map of the octahedra tilting and of octahedra rotation was created. Accelerating voltages of 80 keV and 300 keV were used but 80 keV was preferred.

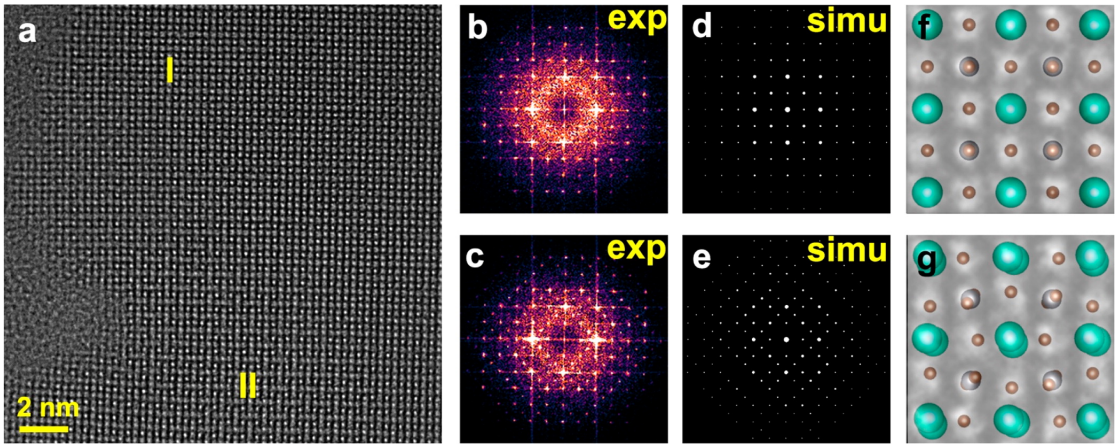

Figure 4.8 – Coexistence of cubic and orthorhombic $CsPbBr_3$ within single AC-HRTEM image from $CsPbBr_3$ nanosheets. (a) Experimental AC-HRTEM image with two regions denoted as I and II. (b,c) Experimental Fourier transforms from region I (b) and II (c). (d,e) Simulated electron diffraction of cubic (d) and orthorhombic (e) $CsPbBr_3$. (f,g) Enlarged images from region I (f) and II (g). The cubic and orthorhombic structure models are overlaid on (f) and (g), respectively. Reprinted from [69].

Zhang [157] investigated single crystal $CsPbBr_3$ by single crystal XRD, powder XRD, and SAED. Weak spots, unique for the orthorhombic phase and missing in the cubic

and tetragonal phases, were observed at room temperature. Powder XRD showed phase transition from orthorhombic $Pbnm$, equivalent to $Pnma$, to tetragonal $P4/mbm$ at 88 °C and a successive phase transition to cubic $Pm\bar{3}m$ at 130 °C.

Bertolotti [158] affirms that high-temperature phases of inorganic halide perovskites are highly dynamic, and appear cubic while fluctuating among locally non-cubic structures, underlining that atomic arrangement is not trivial to solve. With the support of high-resolution synchrotron X-ray total scattering data and an advanced modelling performed through the Debye scattering equation, they proposed a high defectiveness and in particular the formation of orthorhombic subdomains. In particular, in the case for $CsPbBr_3$, they underlined that the most intense peaks match the nominal Bragg positions for the cubic structure; a few weak superstructure peaks appeared, providing a fingerprint for $PbBr_6$ octahedral tilts at room temperature. The proposed generalised model is that orthorhombic subdomains are separated by a network of twin boundaries, denser at high temperature and maintaining fixed Pb locations. Their mutual orientation leads to an apparent higher symmetry structure on average while keeping the tilted orthorhombic arrangement of $PbBr_6$ at the length scale of subdomains. Nevertheless, HRTEM images did not show rotation-induced halide offset at the domain interface. They underline that the disappearance/appearance of weak superstructure peaks upon heating-cooling further suggests the dynamic processes within twin-boundary modifications.

Brennan [159] reported TEM analysis of $CsPbBr_3$ nano-cubes, combining different techniques including low temperature and *in situ* TEM observations. Their XRD patterns indicate a cubic symmetry for nano-cubes, whereas nanosheets adopt orthorhombic symmetry. FFTs of HRTEM images acquired at room temperature evidence their difference in structure.

4.5 Experimental results and analysis

In this section, the main experimental results obtained on the $CsPbBr_3$ NCs are presented in a kind of chronological order to outline the different tests and observations that have been done.

4.5.1 Standard HRTEM

After sample preparation, a quick look at the sample is needed to check if the preparation worked well and see quickly what the sample looks like. In our laboratory, this sample check is generally performed on either SEMs or older TEMs. For this study, the JEOL 3010 of the LEMMA group[4] was used.

Figure 4.9 shows typical HRTEM image of the NCs. Atomic columns and planes can be seen in most of the NCs, thanks to the cuboid shape and the self-organisation of the NCs on the membrane: unlike spherical or irregular nanoparticles, the crystallographic direction of crystalline cuboids is not randomly oriented. A crystalline cube deposited

[4]Characteristics of the JEOL 3010: accelerating voltage 300 kV, C_c 1.2 mm, C_s 0.7 mm.

on a planar surface will have a (0 0 1) plane parallel to the surface: an electron beam hitting perpendicular to the surface plane will be parallel to a [0 0 1] direction. However, the alignments of the NCs are not perfect, as perfect atomic columns are only seen in few NCs. This misalignment can come from the deformation of the supporting film or from the organic shell surrounding the NCs. To obtain nice on-axis images, two strategies are possible: a given NC is selected and oriented to have its low index zone axis parallel to the electron beam; alternatively, one can browse between the many NCs to find the ones with a proper orientation. The second option is generally faster, and this was preferred in this work. To avoid a possibility of selecting a particular type of NCs, from time to time the goniometer stage was tilted randomly by a few degrees and a new oriented NC was selected.

These images allow computing the lateral size of the particles. The comparison with image simulations may provide an estimate of the NC thickness, as attempted in the following.

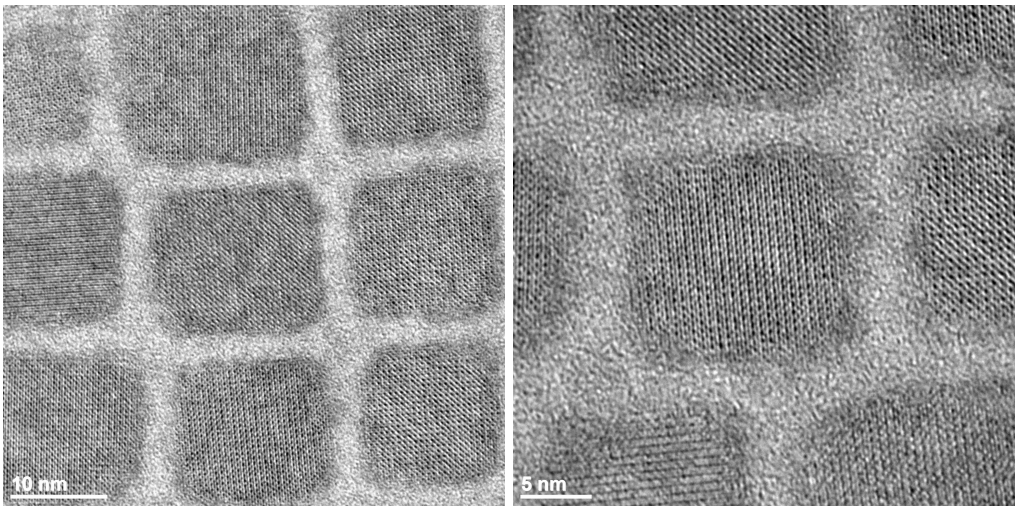

(a) (b)

Figure 4.9 – $CsPbBr_3$ NCs observed with a (a) 200 kx magnification and at (b) 300 kx magnification.

Figure 4.10 shows a defocus-thickness map of simulated HRTEM images of a cubic $CsPbBr_3$ crystal observed along a $\langle 0\,0\,1 \rangle$ direction with a JEOL 3010 microscope at 300 kV. This map has been calculated with the JEMS software. Large defocus and thickness range has been taken to outline the general trends. Two large domains can be seen. In these two domains, the HRTEM image looks like a simple cubic lattice visualising the Pb atomic columns. In the left domain extending roughly over 20 nm to 95 nm thickness and −70 nm to 40 nm defocus (surrounded by dotted blue in the figure), white spots overlap with Cs column positions. In the right domain extending roughly over 20 nm to 95 nm thickness and 70 nm to 160 nm defocus (surrounded by green lines),

Pb atomic column are white. These simple contrasts originate from the strong $\{0\,0\,2\}$ diffracted beams. Of course, it is impossible to estimate the sample thickness from the contrast in these different domains which are too wide. In between these two big domains, there is another one (thickness ranging from 22 nm to 27 nm, defocus varying between 50 nm to 79 nm), where the white dots are positioned at the Cs and Br atomic columns.

Figure 4.11 shows a similar map of the orthorhombic structure observed along $[0\,1\,0]$[5] and $[1\,0\,1]$ zone axes. Similar trends are observed although more variations are present.

As it is likely that the NCs have a cuboid shape and so that thickness values range from 5 nm to 15 nm, a zoom of the initial overview maps are performed for defocus values varying from -35 nm to 35 nm with a 5 nm step. For these thickness values, the contrast is smaller and the interpretation of the image feature are more complex. $PbBr_6$ octahedra are rotated in the orthorhombic structure with respect to the cubic structures. Nevertheless we observe in figure 4.12 that in some cases the bright peaks corresponding to pure Br atoms (in brown) are shifted from the real atom positions, and therefore the symmetry in the image is extremely similar to the cubic case (figure 4.12a) making the differentiation of the 2 phases very difficult. At the same time, the splitting of the position of the Br atoms in the mixed Pb-Br columns and the splitting in the pure Cs atoms does not correspond to an image elongation in the bright peaks. This fact is rather surprising because the main differences between cubic and ortho comes from low frequencies that are not cut by the transfer function. In 4.12, the diffractograms of the simulated images are displayed and indeed the additional peaks of the orthorhombic structure are not visible in this diffractogram. Visible elements of elongations and lack of symmetries are present for defocus values higher than -5 nm and do not correspond directly to the position of the atoms. In the considered range, generally for negative defocus values white atom regime is observed; on the contrary, at defocus values higher than 25 nm atoms result black. Additional difficulties in the comparison between experimental and simulated HRTEM images are the small angular deviations from the zone axis, and the influence of the background from the amorphous support.

[5] $[0\,1\,0]$ simulations are rotated of $45°$ for direct comparison.

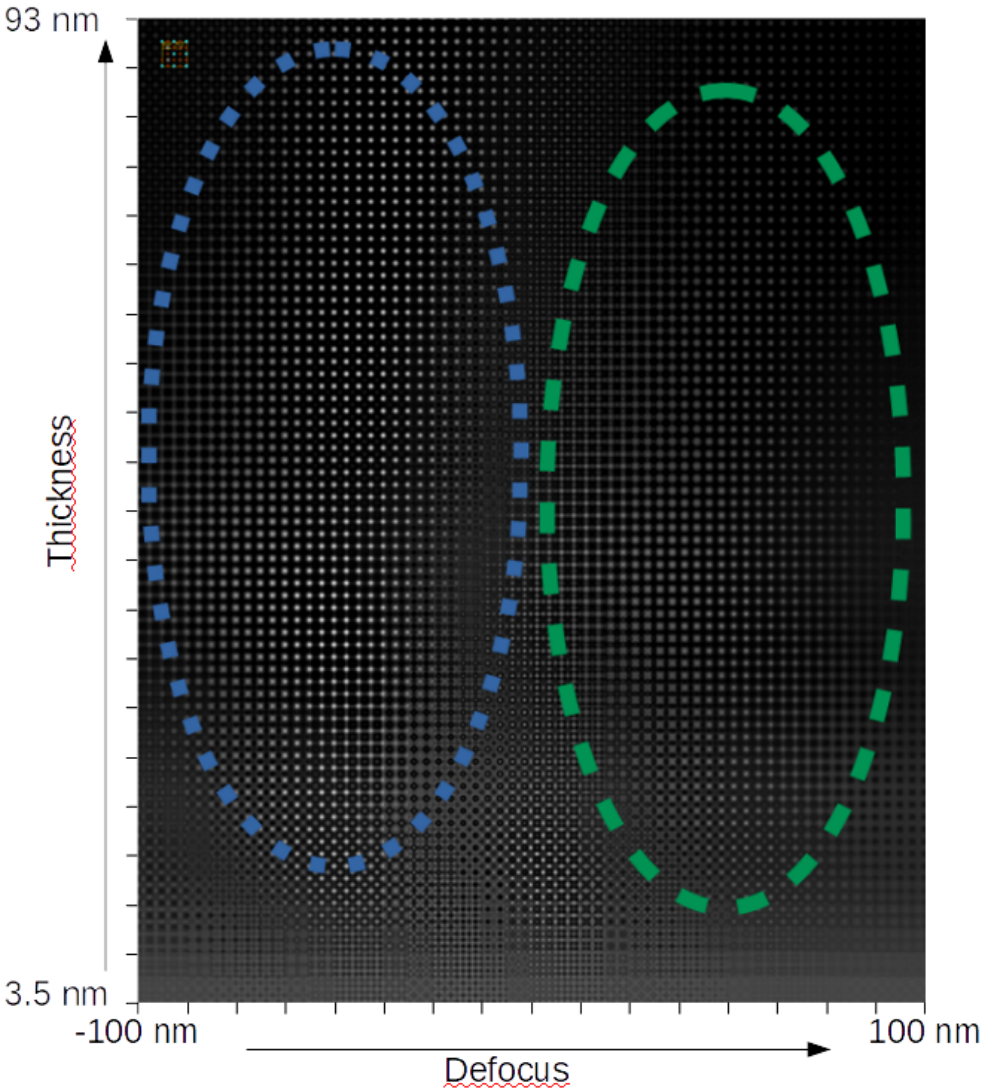

Figure 4.10 – Defocus-thickness HRTEM map of a cubic $CsPbBr_3$ crystal observed along a $\langle 0\,0\,1 \rangle$ direction with a JEOL 3010 microscope operated at 300 kV. $C_s = 0.7$ mm. 32 defocus values, with lowest defocus -100 nm and defocus step 10 nm. 40 different thickness, starting at 3.5 nm, with a thickness step of $4 \times a_{cubic} = 2.3378$ nm.

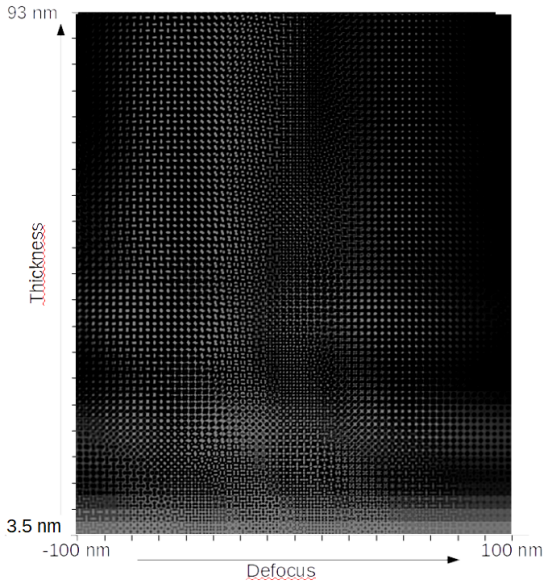

(a)

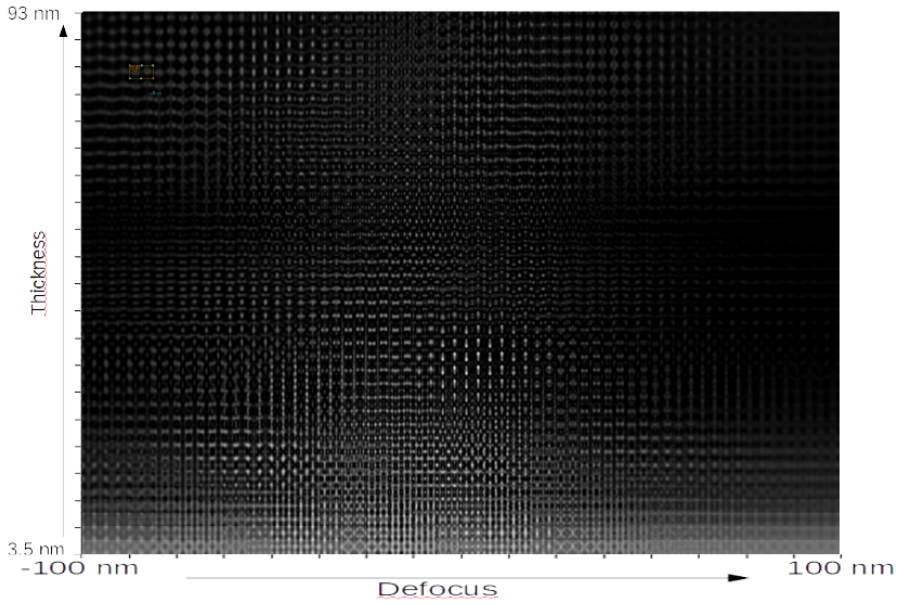

(b)

Figure 4.11 – Defocus-thickness HRTEM map of a orthorhombic $CsPbBr_3$ crystal observed (a) along [0 1 0] and (b) along [1 0 1] direction with a JEOL 3010 microscope operated at 300 kV. $C_s = 0.7$ mm. 32 defocus values, with lowest defocus -100 nm and defocus step 10 nm. 40 different thickness, starting at 3.5 nm, with thickness step of $2 \times b_{ortho} = 2.3378$ nm.

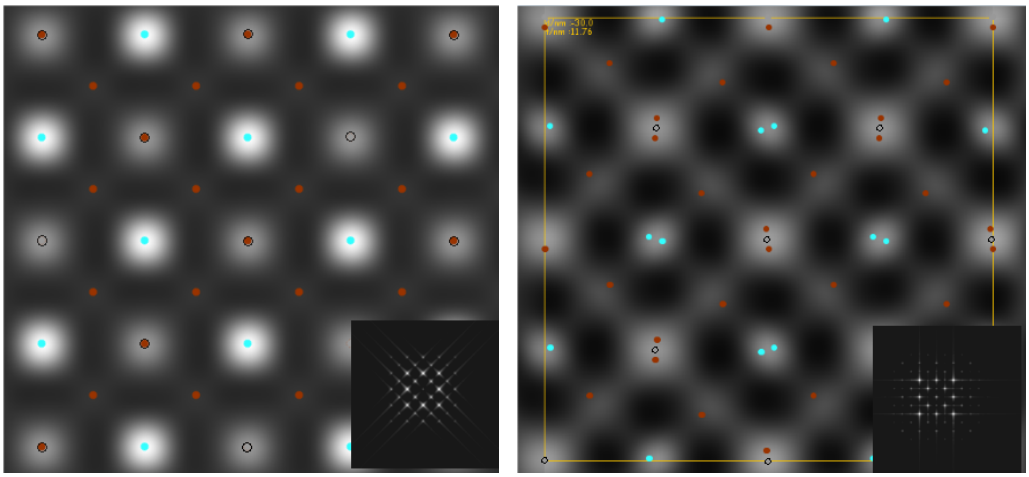

(a) $Pm\bar{3}m$ (b) $Pnma$

Figure 4.12 – Simulation of cubic and orthorhombic structure, zone axis [0 1 0], Jeol 3010 300 kV, defocus −30 nm, thickness 11.76 nm. Model: Cs blue, Pb grey, Br brown.

A detail of a HRTEM image obtained in Jeol 3010 is shown in figure 4.13. The FFT of the image does not provide any visible additional spot with respect to the cubic diffractogram. Nevertheless, in is clear the anisotropy of the features, such as the alternating vertical black and white strips. By comparing with the simulations in figure 4.12, we observe the same features of the orthorhombic structures in [1 0 1]zone axis, with a crystal thickness of 10 nm at a defocus value of 35 nm. The corresponding simulation is shown in the inset.

31 FFTs from single NCs have been calculated from the HRTEM micrographs obtained by the JEOL 3010, such as the ones in figure 4.9. Most of the NCs show the cubic structure pattern as in figure 4.14a. Nevertheless, some low-intensity peaks due to the breaking of the cubic symmetry can be observed in some of the FFTs. One of them is shown in figure 4.14b. Only 6 of the 31 calculated FFT show additional diffraction peaks with respect to $Pm\bar{3}m$ cubic pattern. The totality of the calculated patterns and the selected digital diffraction patterns are shown in appendix I.1 in figure I.-2. All the digital diffraction pattern showing additional peaks with respect to the cubic structure are presented in figure I.-1. These additional peaks correspond to [0 1 0] or [1 0 1] orthorhombic projections. Even though all the peaks can be indexed, not all reflections simulated for orthorhombic *Pnma* structure are visible in the digital diffraction patterns, probably because of small tilts of these NCs from the exact zone axis. Figure 4.14b is indexed according to the orthorhombic phase in zone axis [1 0 1], as the one in figure 4.5c. Only the peaks $(1\,1\,\bar{1})$ and $(2\,1\,\bar{2})$ can be observed, whereas others are missing or under the noise level.

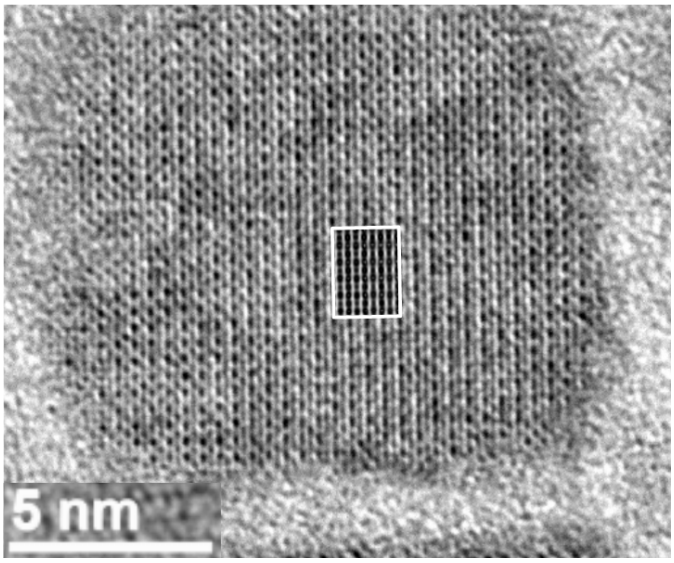

Figure 4.13 – Detail of $CsPbBr_3$ NC, obtain with the Jeol 3010 microscope. The inset simulation corresponds to a thickness of 10 nm at a defocus value of 35 nm.

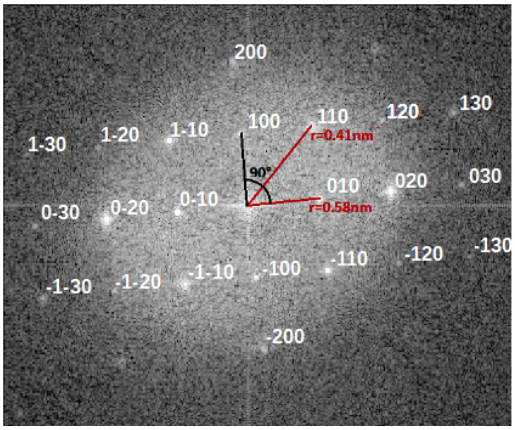

(a) Typical digital diffraction pattern of cubic $CsPbBr_3$ NCs.

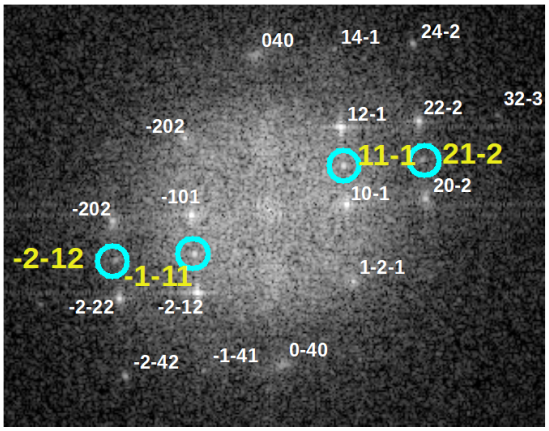

(b) One of the digital diffraction pattern of $CsPbBr_3$ NCs which show more reflections (surrounded in light blue).

Figure 4.14 – Some peculiar FFTs calculated over HRTEM images of single $CsPbBr_3$ NCs.

4.5.2 C_s-corrected HRTEM

Some observations were also performed by aberration-corrected FEI Titan Ultimate, for more resolution and better stability. Some well-oriented NCs were observed at different defocus values; these experimental images are compared to some simulations performed by JEMS. Only in some cases a good match between experimental image and simulation is possible. This is one of the drawbacks of conventional HRTEM, compared to the straightforward interpretation of STEM-HAADF, where every bright spot corresponds to an atomic column. The interpretation of HRTEM is more complex, as there is no direct correspondence between the white spots and the atomic column. In a simple crystal composed of one or two atom types, like in Au, Si or ZnTe crystals, one can determine experimental conditions where atomic columns are either black or white. In a more complex crystal like $CsPbBr_3$, some atomic columns can appear black and other grey or white at the same time.

Figure 4.15 presents the analysis over a single NC. Reflections in the digital Fourier Transform (figure 4.15b) ensure the orientation of the crystal, namely [0 1 0]. Simulations are compared with the real experiment image at different defocus values. Thanks to the simulations, the thickness is identified to be approximately 18 nm. As the NC has lateral size of 14 and 16 nm the NC looks like more than a cube than a platelet. In the image corresponding to the defocus value −80 nm (figure 4.15c), some elongated and alternating cross features are identified. Defocus value −60 nm (figure 4.15c) properly compares the position and the shape of the white features. Finally, at a defocus value of 20 nm (figure 4.15e) the symmetry of black zones in the image is clearly respected. Nevertheless, it is not easy to compare the simulations with the real micrographs acquired at different defocus values.

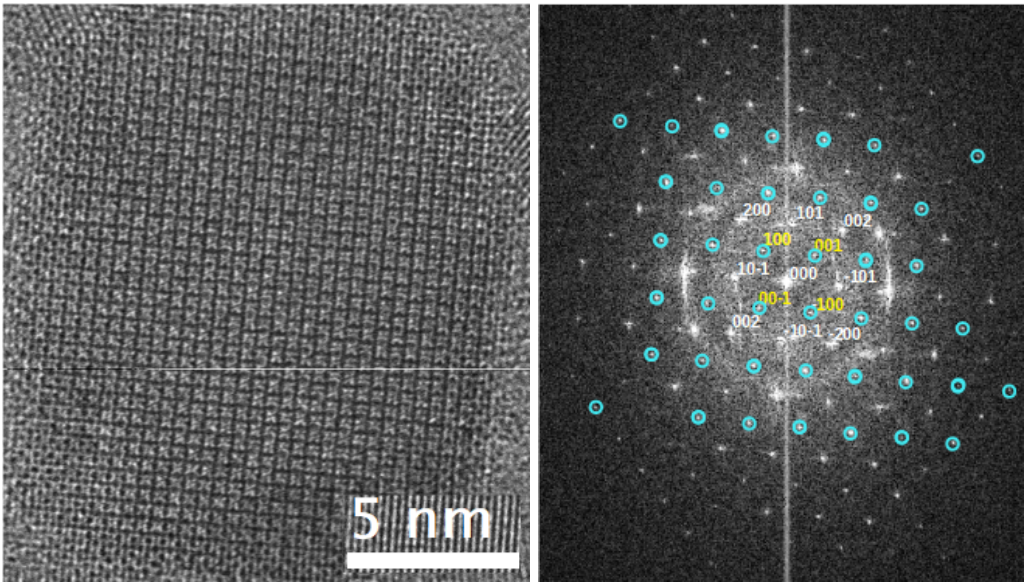

(a) General plan (b) FT

(c) $\Delta f = -80\,\text{nm}$ (d) $\Delta f = -60\,\text{nm}$ (e) $\Delta f = 20\,\text{nm}$

Figure 4.15 – AC-HRTEM image $CsPbBr_3$ NC, zone axis [0 1 0].

4.5.3 HRSTEM

As the samples were of good qualities, we decided to use a better microscope to perform both HR-STEM and EDS experiments, so we chose the FEI-Titan Themis, microscope equipped with a probe C_s-corrector and four EDS detectors. Fearing beam damage, NCs were observed firstly at 80 kV. EDS analysis will be presented below. As far as HR-STEM is concerned, we mainly used the Fischione HAADF detector and acquired two types of images. Either classical single image or series of images were acquired. In the last years it has been shown that by registering, aligning and averaging series of short-acquisition time STEM images [143,144,160], one can reduce significantly scanning error artefacts, which are inherent to all scanning acquisitions, and improve drastically the signal-to-noise ratio. In this work, the Statistically Determined Spatial Drift (SDSD) program [161] was used to align the acquired stacks. This program was initially developed for energy-filtering TEM (EFTEM) but is now widely used in material science. The SDSD correction program involves a three-step approach:

1. a set of digital filters is used to enhance the relevant information (such as edges, features) while noise is reduced. Therefore, the images become suitable for a cross-correlation algorithm;

2. the user selects the best region in the image for drift correction;

3. then the algorithm increases its robustness by correlating all image pairs with each other, and the obtained information is evaluated statistically. Outliers, which are the pixels which are not contained in all the images from the series, can thus be identified and excluded, resulting in a more accurate drift determination with even sub-pixel precision.

Some excellent images were reconstructed at 80kV. Well oriented NCs (NCs with a diffraction pattern with many symmetrical spots, indicating that the NC is oriented along a low index axis) were selected. Eventually, the orientation was slightly adjusted with the tilts of the microscope. For a NC, this beam orientation is somewhat tedious as the stage is not eucentric and consequently a little mechanical tilt of the sample always introduce a not negligible shift of sample. For instance, a tilt of 0.3° can quickly shift the sample by 100 nm. This sample reorientation is easier in the STEM mode than in the TEM mode. Indeed in the STEM mode, one can have a scanned image on the computer screen and a local diffraction pattern on the fluorescent screen: one can select with the mouse on the computer screen the area where the local live diffraction pattern is taken. Figure 4.16 shows the registration and average of 45 images. HAADF images are much easier to analyse than HRTEM images as there is no contrast reversal, i.e. atomic columns always appear as white spots and the brighest spots generally correspond to the atomic columns with the heaviest atoms. So, in figure 4.16, the brightest atomic columns correspond to the columns containing Pb and the least bright spots are the pure Cs columns.

Unfortunately, the pure Br columns which form the corners of the perovskite octahedra are in the noise level and are hardly recognisable. Therefore, the tilting of the

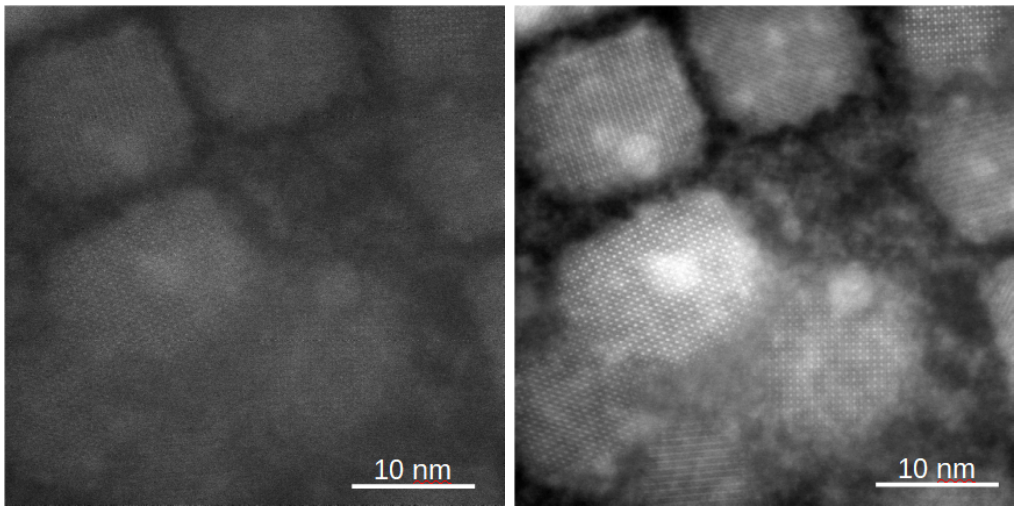

(a) single image (b) sum of aligned stack

Figure 4.16 – Improvement of the image quality and suppression of the noise thanks to acquisition of series of 45 sequential images, aligned by SDSD plugin for Digital Micrograph.

octahedra is not directly visible. Nevertheless, the elongation observed in the simulated data from orthorhombic space group (figure 4.23e) is never observed in any acquired images (figure 4.17). This lack tends to reject the orthorhombic structure hypothesis.

Nevertheless, some additional experiments were performed on the aberration-corrected FEI Themis operated at 200 kV. At higher tension, more resolution is expected unless the NCs are damaged by the electron beam. In addition to the Fischione HAADF detector, the FEI bright field (BF) and annular dark field (ADF) detectors were used. By tuning the camera length and the convergence angle correctly and using two ADF detectors, ABF images which are particularly sensitive to light elements [74] have been acquired.

As done at 80kV, image series were also acquired. Since this acquisition was performed more than four years after the starting of this PhD, the software of the microscope evolved: the image series were not recorded with an additional script but with the FEI new software. The advantage of this new acquisition set-up is that it is easier to use as incorporated in the standard software. The drawback it is that the images are saved in a proprietary format that was not possible to read by another software. So we had to rely on the FEI software to align the images. The software succeeded, but as it is a result of a black box process, we obtained no measure of uncertainty and therefore it is difficult to estimate its accuracy.

Figure 4.18 shows the average of one series containing 100 images acquired every 0.3 s. The quality of the image is exceptional. One can see all the atomic columns and the displacement of some atomic columns. The digital diffraction pattern in the inset

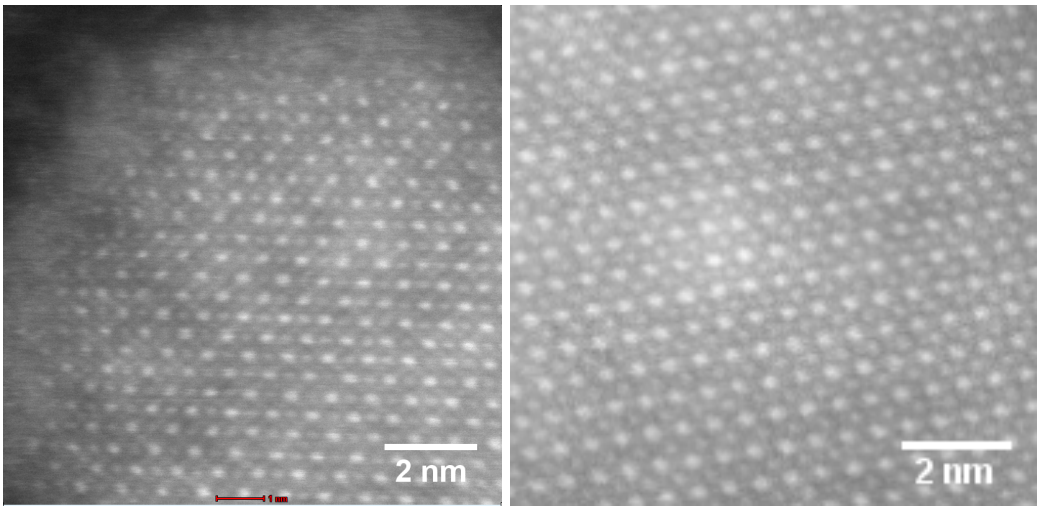

Figure 4.17 – Experimental STEM-HAADF images showing the patterns from ordered $CsPbBr_3$ crystal structure in NCs.

shows clearly that the biggest NC exposes the orthorhombic [1 0 1] zone axis.

Figure 4.19 shows BF, ABF and HAADF obtained on the same NC. One can see the correspondence between the three images. BF image resembles a conventional TEM micrograph and requires deep investigations to solve it. Atomic columns are white in the HAADF image, whereas they are dark in the ABF images. The lighter Br columns are visible in the ABF image and one can observe some atomic column displacements specific to the orthorhombic structure in the three imaging modes.

In the same ABF acquisitions, we observed that the average position of Br columns are in general not in the equilibrium position as expected from the atomic structure, but their centre is shifted towards one of the Cs atoms. Some arrows in figure 4.20 indicate this phenomenon. It is likely that the position of Br atoms is modified by the electron beam: in fact, most of the shifts of Br atoms lay on the [1 0 0] direction. Direction [1 0 0] is approximately 20° from the horizontal scanning direction of the STEM probe.

In particular, in some of the images, periodic oscillations of some atom column are observed. The top image of figure 4.21 represents the general plan of a STEM-HAADF acquisition at 10 Mx magnification. The colored rectangles indicate the 1×4 arrays of pseudocubic unit cell. These rectangular selections have been aligned by cross-correlation and averaged. The central image in figure 4.21 is a zoom in the image and demonstrates the displacement of the Cs atoms. The yellow horizontal line is drawn as a visual aid; yellow arrows indicate the displacement direction of the Cs columns. These columns alternatively displace up and down with respect to Pb atoms (the brightest in the image) in the horizontal lines; they displace in the same direction in the vertical lines. The arrows evidence this shift in position in the atomic model ([1 0 1] zone axis) as well. The same behaviour is observed in the structural model.

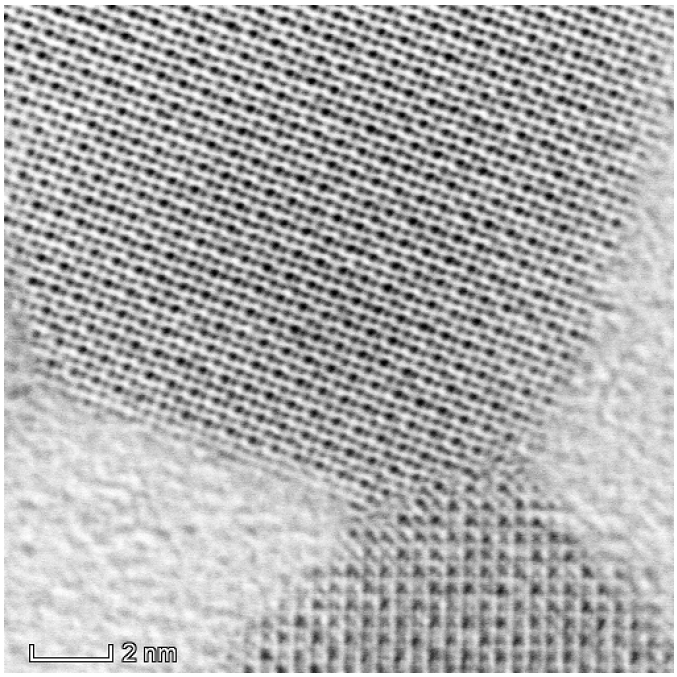

(a) ABF

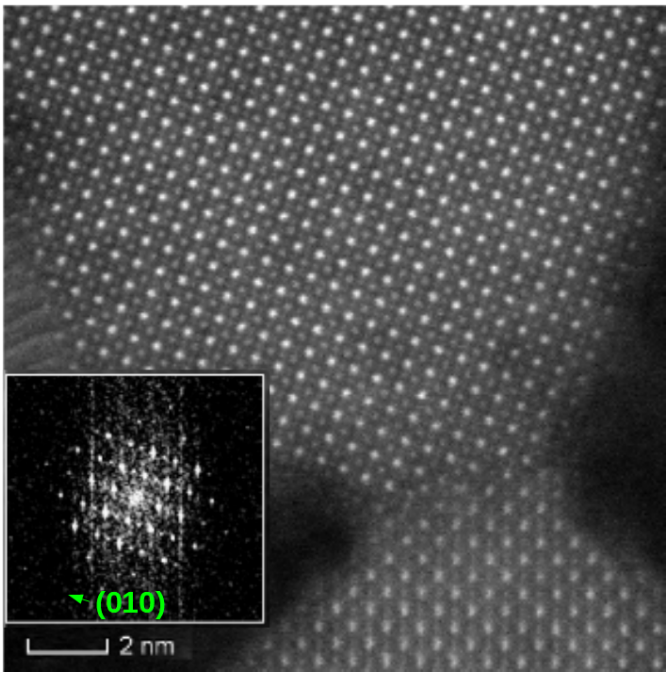

(b) HAADF

Figure 4.18 – Averaged STEM image of $CsPbBr_3$ NCs.

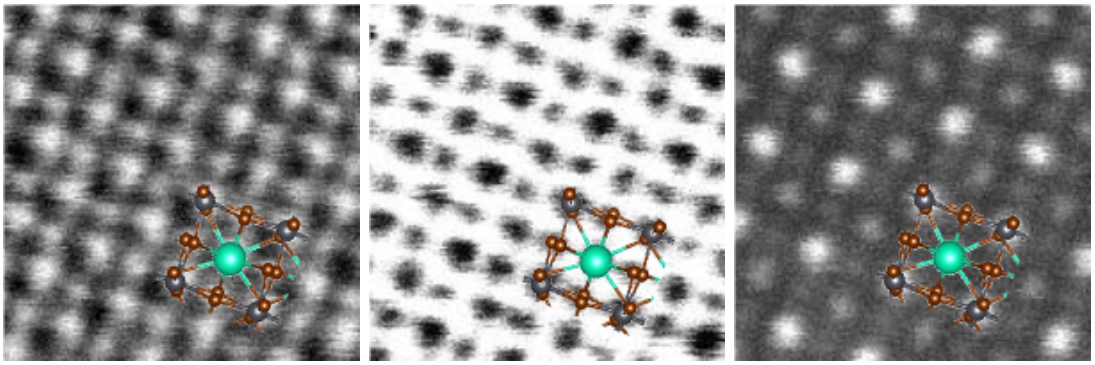

(a) BF (b) ABF (c) HAADF

Figure 4.19 – Detail of multidetector acquisition for STEM; each detector collects a different angular range of scattered electrons.

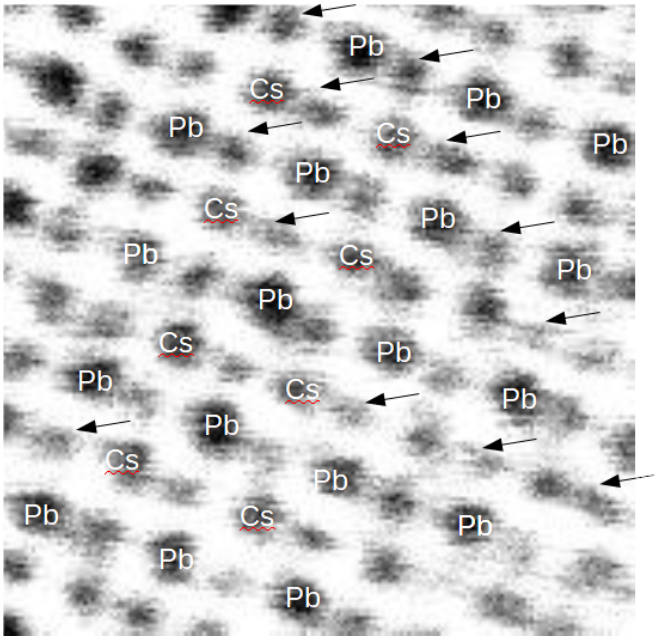

Figure 4.20 – Detail from image 4.18a. Arrows indicate the positions where the Br columns are displaced from the equilibrium positions. Cs and Pb are labeled, whereas the Cs are not.

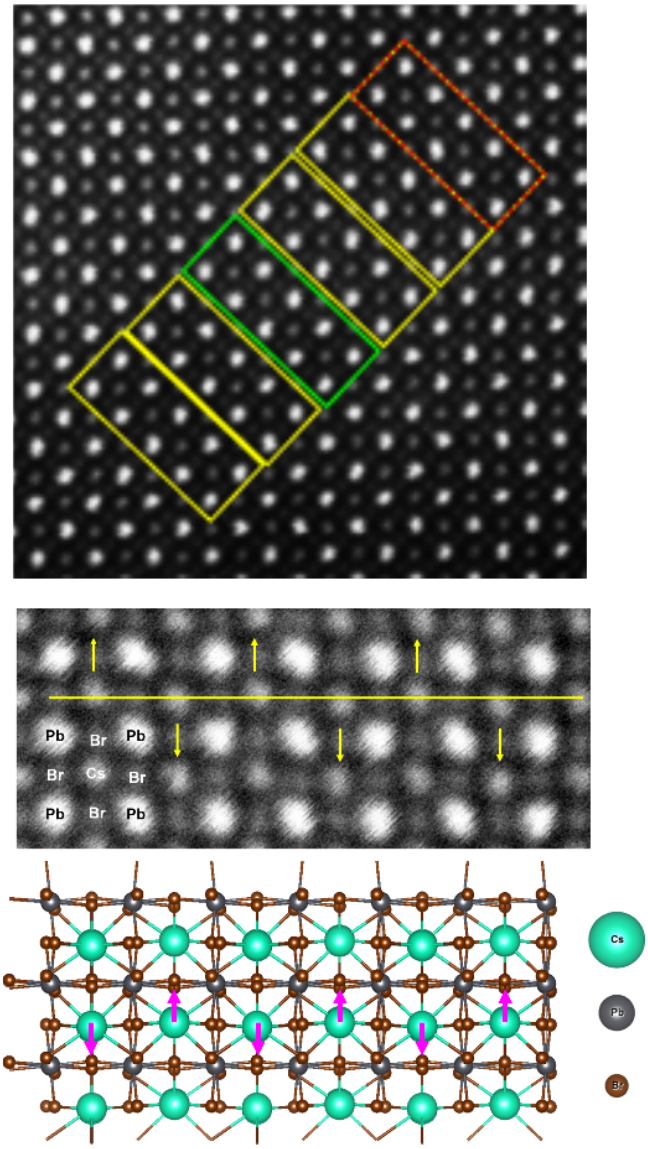

Figure 4.21 – STEM-ADF image acquired at 10 Mx magnification and atomic model of $CsPbBr_3$ (zone axis [1 0 1]). Arrows indicate the displacement of Cs columns. The yellow horizontal line is provided for visual aid.

Figure 4.22a represents the average of the selected five 1×4 array of unit cells, after alignment. The Cs columns are in red. The intensity maximum of the Cs columns have been determined: the difference in the vertical line between the up and down positions is 4.5 pixels, corresponding to 38 pm (6.42% of the cubic unit cell parameter). The unit cells with common configuration have been aligned by cross-correlation and averaged. Figure 4.22b represents the average image of Cs-down configuration (red), while figure 4.22c indicates the average of the Cs-up configuration (green). These two configurations are summed in figure 4.22d, by fixing the position of the Cs columns in the centre of the image. If the Cs column is forced in the centre of the image, we create a new reference system where the Cs columns are in the centre of the image; the original displacement in the Cs column is not therefore visible but it is transposed on the Pb atoms in this new reference system. When Cs atom is forced to the centre of the image, relative Pb displacements are observed by the change in the colour around the Pb atoms. This image helps to visualise the effect of the orthorhombic distortion.

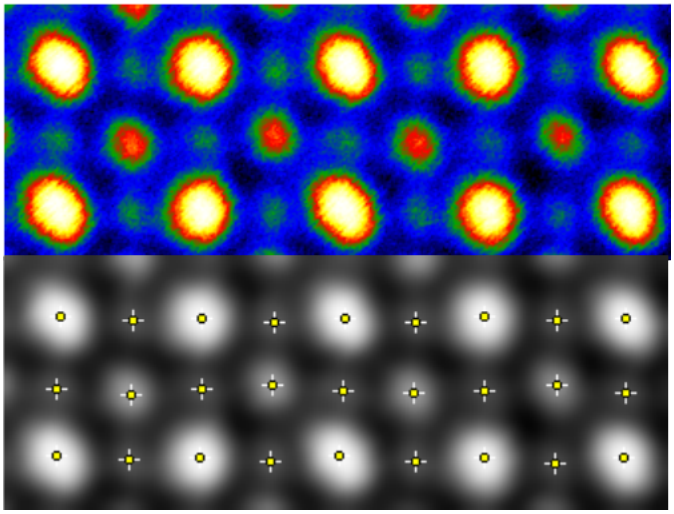

(a) Averaged image and intensity maxima

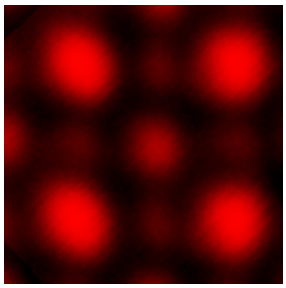

(b) Cs-down

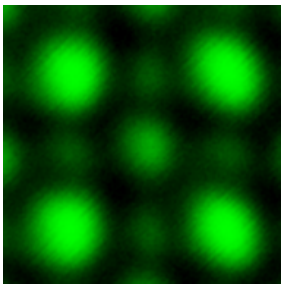

(c) Cs-up

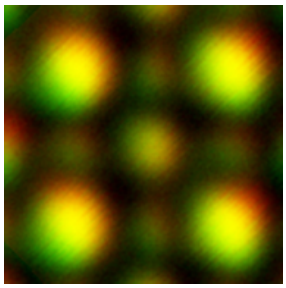

(d) Sum of Cs-down and Cs-up

Figure 4.22 – Displacement of the Cs columns.

4.5.4 STEM simulations

Simulation of the STEM images has been performed with the autostem program coded by Kirkland [85]. The parameters were chosen to be consistent with the experimental images. Supercells were built by using the TEM UCA server from Cadiz University [154] and their sizes are 2.3378 nm × 2.3378 nm × 11.689 nm. The zone axes chosen for the simulations are the [0 0 1] for cubic structure and the [0 1 0] for the orthorhombic crystal structure. Thickness is chosen according to an integer multiple of the unit cell parameter and to be close to a typical size of a nanocrystal[6].

These are the parameters for the simulations.

- $V_0 = 80\,\text{kV}$, $C_s = 0.001\,\text{mm}$, $C_5 = 0.05\,\text{mm}$;
- Multislice approach, slice thickness 0.292 25 nm (one atomic layer per slice);
- Convergence angle: 18.6 mrad;
- Probe size: 0.07 nm;
- Camera length:
  - 110 mm (minimum and maximum angles for ADF: 75-359 mrad, minimum and maximum angles for BF: 0-43 mrad);
  - 135 mm (minimum and maximum angles for ADF: 61-297 mrad, minimum and maximum angles for BF: 0-35 mrad);
- TDS (Thermal Diffused Scattering): 10 configurations at 300 K;
- Crystal thickness: 5 nm, 10 nm, 11.689 nm;

In figure 4.23 the simulation performed with a sample thickness of 11.689 nm acquired with a camera length of 135 mm are presented. The thickness is the most similar to the real sample thickness. The difference with 110 mm camera length is minimal. Good chemical contrast is visible in the HAADF imaging mode.

The projections of models presented in figures 4.23a and 4.23d demonstrate an evident tilting of the octahedra in the orthorhombic structure. In figure 4.23e the most important feature is the elongation of some atomic columns. In fact, the atomic columns are not perfectly in the same x-y projection but are piled up on two different positions. This fact gives rise to elongation in these atomic columns, particularly visible for the brightest columns in STEM-HAADF (mixed of Pb and Br). The elongation is also visible in pure Br columns.

[6]By assuming a cuboid shape, thickness determination is straightforward: thickness is corresponding to the edge of the square facets visible in the microscopy images.

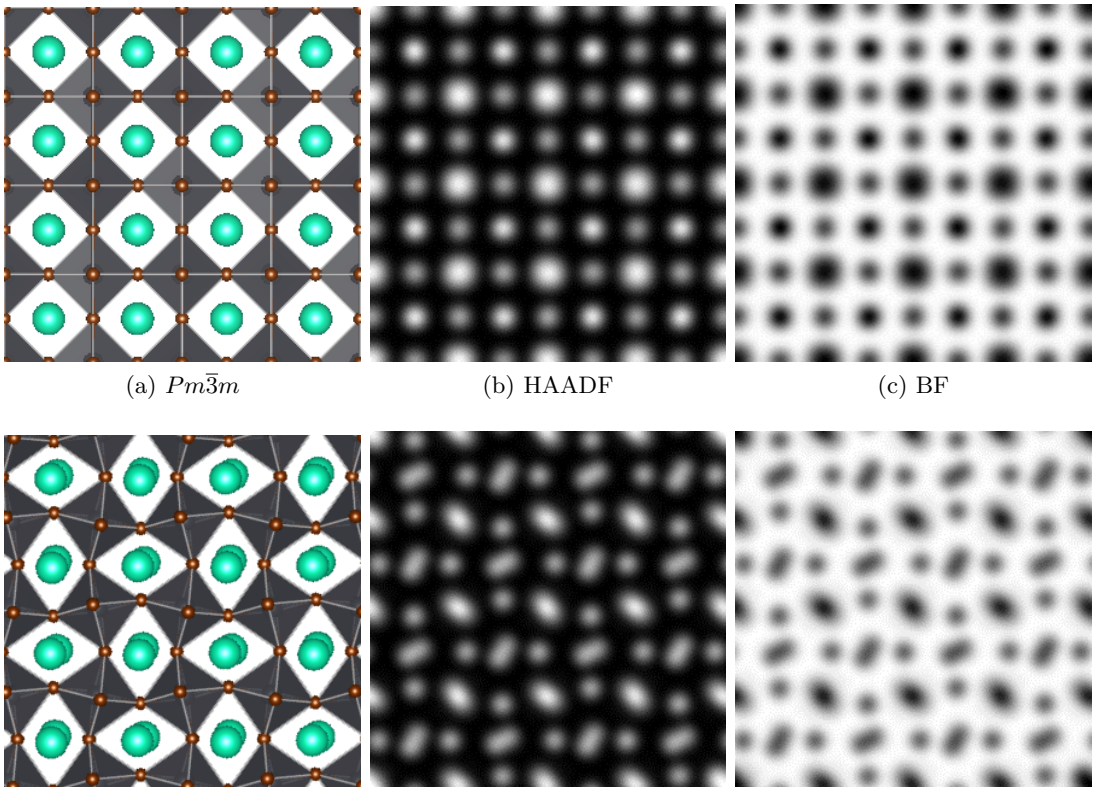

(a) $Pm\bar{3}m$ (b) HAADF (c) BF

(d) $Pnma$ (e) HAADF (f) BF

Figure 4.23 – STEM-HAADF and STEM-BF simulations performed on [0 0 1] cubic structure (a) (b) (c) and on [0 1 0] orthorhombic structure (d) (e) (f). Cs atoms are represented in green, Pb are in grey and in the centre of octahedra, Br in brown.

4.5.5 SAED

SAED was acquired to obtain further information about the structure of this nanomaterials. FEI Themis operated at 200 kV was used for this complementary experiment. A camera length of 255 mm was chosen, and the diffraction pattern was acquired using a FEI CETA camera. The acquired diffractogram was exploited by using CrisTBox (crystallographic toolbox) [162]. In particular, the ringGUI tool is dedicated for automated analysis of electron diffraction patterns: the beam stopper is detected, the centre localised, the background is extracted, and the peaks are identified. Figure 4.24 shows one experimental SAED acquired over several $CsPbBr_3$ NCs after beam stopper and background removal. It can be seen that both structures can index the most intense diffraction rings. Nevertheless, low-intensity rings (sometimes composed by less than ten spots) are better described by the orthorhombic structure, which possesses low-intensity reflections.

An additional SAED experiment was performed on FEI Titan Ultimate operated at 200 kV. A 30 µm aperture forms a convergent beam which impinges a 9 nm diameter circle of the NC[7]. The illuminated area can be observed in direct space, together with the corresponding diffraction pattern (figure 4.25). In this particular case, there is direct evidence of the observation of the superstructure diffraction spots, with the breaking of cubic symmetry: the diffraction pattern corresponds to [1 0 1] orthorhombic structure. Speckles around the most intense peaks can be observed: this is due to the finite and small size of the aperture which forms the beam, which implies a cardinal sine function convolution in the diffraction domain. In principle, this kind of diffractogram could be used in a Coherent Diffraction Imaging (CDI) routine to retrieve amplitude and phase of the wave function. The missing phase can be retrieved ab initio from diffraction intensities by an iterative procedure. This approach was tested on carbon nanotubes by Zuo [163] and could be applied to these kinds of samples for high-resolution imaging.

[7]The aperture was manifactured in-house on a Mo plate by FIB, during the visit of professor Jian Min Zuo (University of Illinois) in the contest of his Chair of Excellence by Nanosciences Foundation, to develop electron diffraction over small volumes of sample.

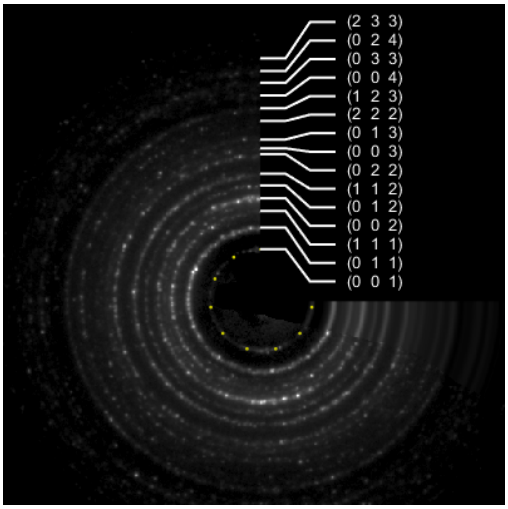

(a) Cubic

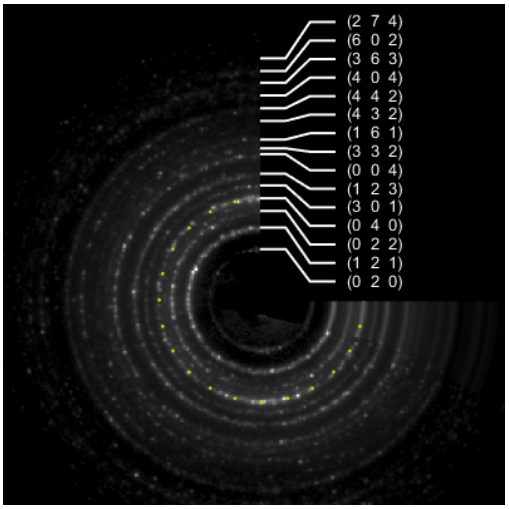

(b) Orthorhombic

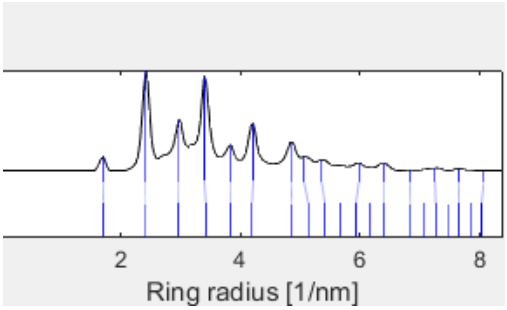

(c) Cubic

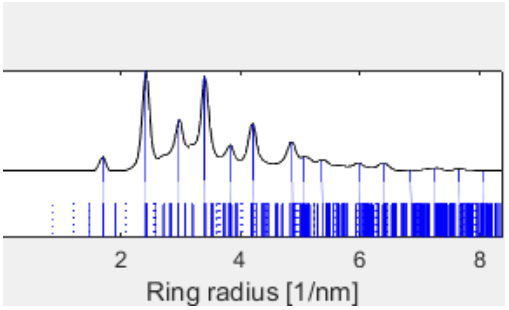

(d) Orthorhombic

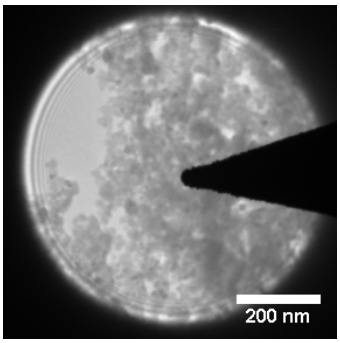

(e)

Figure 4.24 – Indexed experimental SAED from $CsPbBr_3$ NCs and radial profiles after background removal. Peaks are labeled as both cubic structure reflections (a), (c) and orthorhombic structure reflections (b), (d). TEM image of $CsPbBr_3$ NCs producing the presented DP (e).

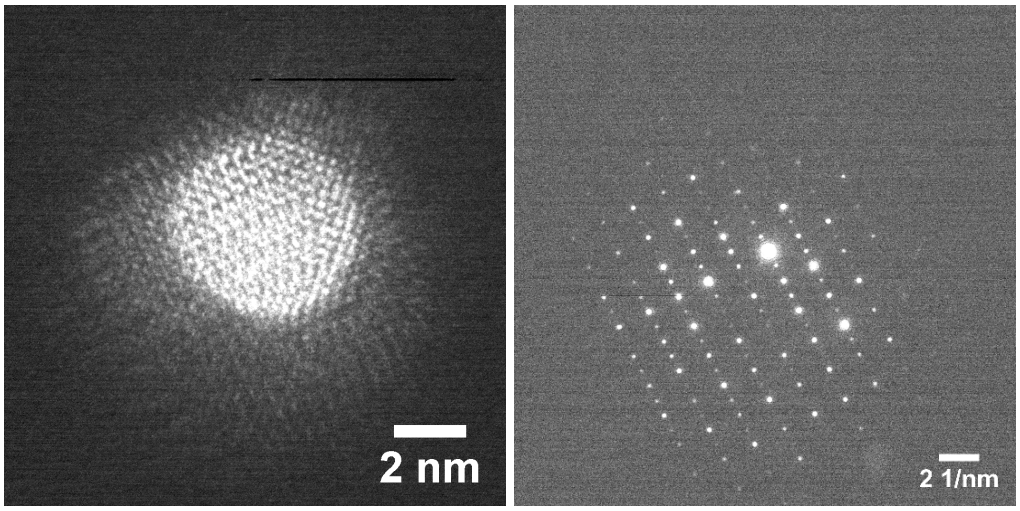

(a) Image (b) Diffraction

Figure 4.25 – Image and diffraction pattern from SAED from a single $CsPbBr_3$ NC.

4.5.6 STEM-EDS

Figure 4.26 shows a small dark stain on most of the NC. They are present on most of the nanocrystals, and they are not particularly induced or enhanced by the electron beam. The composition of these objects has not been identified. Since this stain is only observed in HRTEM and less noticeable in STEM imaging, the stain is attributed to the oxidation of NCs or degradation of their surface ligands, forming an amorphous entity. No crystalline features have been identified in any of these stains. Dang identified these stains as Pb NCs formed by electron beam irradiation, with very visible crystalline structure [164, 165]. In separate studies, they focused on the effect of irradiation on $CsPbX_3$ nanocrystals. Severe modifications were observed: together with halogen desorption, principally Pb^{2+} were found to reduce to Pb^0 and form lead nanoparticles at temperatures higher than $-40\,°C$. At lower temperature, irradiation induces the nucleation of randomly oriented CsBr, CsPb and $PbBr_2$ crystalline domains. Br is also desorbed, involving the creation of voids. The NCs are therefore unstable even at a temperature lower than $-40\,°C$, despite inhibition of lead NC growth.

Our STEM-HAADF and STEM-EDS experiments performed on these stains do not provide solid evidence of such Pb segregation. Figure 4.16b shows brighter spots on the NCs, which does not exhibit any crystalline feature. STEM-EDS maps, such as the one presented in figure 4.27, does not show any particular Pb segregation in the acquired elemental maps. However, the 10 minutes acquisition time strongly deteriorates the sample structure; therefore, these data are not shown here, and we do not present any conclusion over the compositional homogeneity in the $CsPbBr_3$ NC population. If Pb were present in the form of crystallites on the surface of the NCs and the perovskite lying under the Pb stain is Pb-poor, the STEM-EDS acquisition would give a homogeneous

elemental distribution. Therefore, the nature of this contrast is still open to debate.

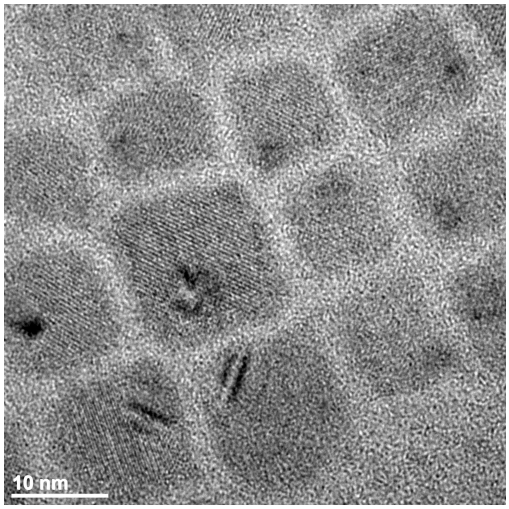

Figure 4.26 – HRTEM showing an amorphous stain on the surface of each $CsPbBr_3$ NC.

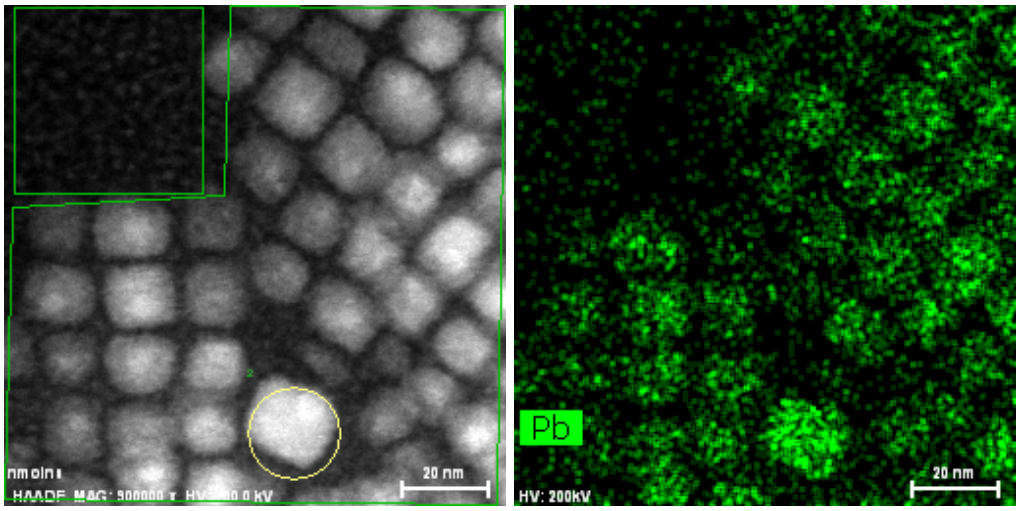

(a) General plan (b) Pb elemental map

Figure 4.27 – (a) General plan of $CsPbBr_3$ NCs with bright spots and (b) qualitative Pb elemental map acquired at 200 keV.

4.5.7 X-ray powder diffraction

X-ray powder diffraction was performed on the synthesized $CsPbBr_3$ NCs. The diffractogram is presented in figure 4.28a. The peaks correspond to an orthorhombic *Pnma* space group (ICDD 04-014-9676). In particular, the peaks observed at approximately 24.1°, 25.1° and 28.5° are described in the orthorhombic model (corresponding respectively to (2 0 1) and (1 0 2), (0 3 1), and (2 2 1)) and not in the cubic model. Lebail refinement provides lattice parameters $a = 8.272$ Å, $b = 11.763$ Å and $c = 8.222$ Å. With the same refinement, the average size is estimated at approximately 20 nm[8]. Cubic and orthorhombic simulated diffraction patterns are shown in figure 4.28b.

[8] 20 nm is a rough estimate of the NC size, and may derive form the preferential orientation of the NCs. Measures from TEM are more accurate.

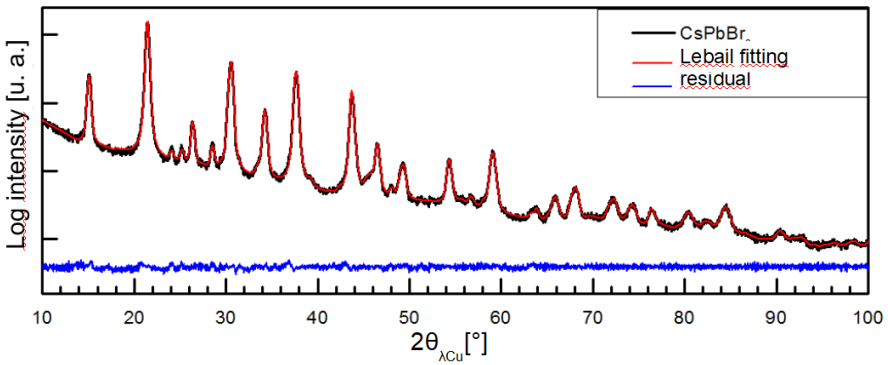

(a) Diffractogram and Lebail refinement

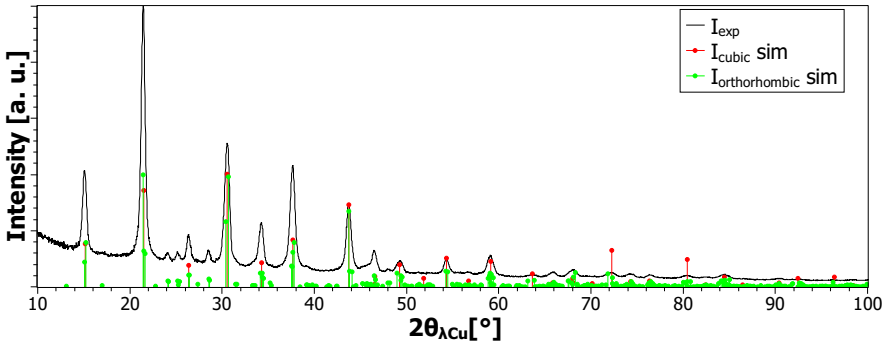

(b) Experimental (black) and simulated diffractograms for cubic (red) and orthorhombic (green) structures.

Figure 4.28 – Diffraction pattern of $CsPbBr_3$ NCs.

4.6 Conclusion

In this study, we showed an in-depth structural characterisation of cuboid-shaped and self-organised NCs of $CsPbBr_3$ by HRTEM and HRSTEM techniques. The samples studied are polydisperse; domains of aggregates of NCs of the same size tend to form. In particular, we showed domains of NCs having a lateral size of 8.6 nm, in contact with domains formed by 12.8 nm size NCs.

Literature reports indicate conflicting crystal structures (cubic, orthorhombic and polymorph). In particular, by X-ray diffraction, the characterisation of small NCs ($<$ 6.5 nm) is very difficult due to peak broadening. In this work, we studied the crystal structure by STEM-HAADF technique coupled with simulations. STEM-HAADF simulations of both structures were calculated to observe the differences. Anistropy, particularly an elongation, was perceived in atomic columns for the orthorhombic simulations, allowing the discrimination between two crystal structures.

High-resolution STEM-BF and STEM-HAADF were performed by acquiring a fast series of images to improve signal-to-noise ratio and to minimise the distortions from scanning: we showed that the orthorhombic structure fits better to the experimental images. In particular we directly observe the alternating displacement of Cs columns typical of [1 0 1] projection.

HRTEM analysis was also performed on the same sample. The experimental images have been compared with simulations to guess the thickness and the structure. Several images were acquired, and the FFT of single crystals have been calculated. Only in some individual nanocrystals, evidence of PbBr octahedra tilting was found. For those nanocrystals, the digital diffractogram showed the low-intensity additional spots, which indicate a decrease in symmetry with respect to the cubic structure. These spots fitted well to an orthorhombic structure in [1 0 1] zone axis or [0 1 0] zone axis. This study may suggest the possibility of polymorphism in $CsPbBr_3$ nanocubes, which has been previously observed in $CsPbBr_3$ nanosheets. From the first TEM experience, approximately 19% of the NCs show orthorhombic structure among cubic structure NCs. We underline that experimental techniques which give average information over a high number of nanocrystals will result in an exclusive identification of the orthorhombic structure.

Moreover, we presented a powder-like electron diffraction experiment, which confirms the lowering of symmetry due to the orthorhombic distortion. Also, a local SAED experiment was able to probe the [1 0 1] projection over an illuminated area with a diameter of 9 nm. Furthermore, HRTEM showed an amorphous stain on the surface of each NC. We speculate that this is an initial degradation process in the crystals.

Chapter 5

Conclusions and perspectives

5.1 Conclusions

This thesis shows the potentials, but also the difficulties, of advanced transmission electron microscopy to probe the local structure and morphology of the solution-processed semiconductor nanocrystals (NCs). Several TEM imaging and spectroscopy techniques were explored in the frame of this work: high-resolution TEM, scanning transmission electron microscopy (STEM), energy dispersive X-ray spectroscopy (EDS), electron energy-loss spectroscopy (EELS), Nanobeam Precession Electron Diffraction (NPED).

Most of our efforts focused on the synthesis and sample preparation methods, as the validity and performance of these techniques strongly rely on them. After that, TEM techniques were applied to several NCs synthesised by wet chemical methods. In particular, three types of samples were examined in more detail. Concerning the sample preparation and purification (chapter 2), several classical physico-chemical methods for colloidal NCs were tested: solvent-antisolvent dispersion cycles, heating up the sample and plasma cleaning. These methods were proven to be insufficient for TEM imaging: bad reproducibility and sample damage (due to exposure time to plasma or excessive temperature) posed many difficulties for TEM examination. Two strategies, previously reported for different materials or applications, were proposed. *Fast thermal annealing* was inspired by a procedure applied in catalysis to activate the surface sites of metallic NCs. The sample was heated up at high temperature (700 °C) for a short time (30 s). The tests were unsuccessful. In fact, the treatment induced significant damage to the grid and the amorphous carbon film, when applied directly on the support TEM grid; when the treatment is applied to the dried solution, agglomeration and a significant change in the size of NCs were observed. The concentrated electron beam still induced dark halos. For the *acid treatment*, purification by acetic acid solution as an antisolvent in solvent-antisolvent cycles was previously tested on $CuInS_2$ [113] and on PbS NCs [114]. It was proposed as a good solution to remove excess ligands and a substitutional ligand (in the case of oleic acid ligands). Particularly, we have chosen Akdaş's purification procedure [113] to Cu_2ZnSnS_4 NCs. A great improvement in image quality allowed us to study the reaction steps during the synthesis, as well as to achieve an unprecedented structural

characterisation on this kind of nanomaterials. For the sample support, graphene was preferred to ultra-thin amorphous carbon film for the unique level of contrast in TEM imaging. It also allows direct visualisation of the ligand shell surrounding the NCs. Moreover, the observation of the contamination deposited on the clean graphene provides an empirical measure of the efficiency of the cleaning procedures previously tested.

After the sample purification and preparation methods, the growth of CZTS NCs was investigated by coupling STEM-HAADF, STEM-EDS, SAXS and WAXS techniques (chapter 3). The NCs were synthesised by Steinhagen method, and seven samples were extracted at different times to study the growth mechanism at different stages of the reaction. In sample 1, only one type of NC containing Cu and S was observed. In sample 2, CZTS NCs of different morphologies (large NCs, small NCs and platelet-like NCs) with different stoichiometry were formed. After this stage, platelets disappeared (sample 3), and small NCs merged (sample 4) and only large NCs were left. After this stage, while Cu amount decreased, Zn and Sn amounts remained approximately constant. The stoichiometry of the final sample (sample 7) was similar to the model stoichiometric Cu_2ZnSnS_4. A similar investigation on CZTS NCs synthesised and prepared in the same way was conducted using synchrotron diffraction techniques: Wide Angle X-ray Scattering (WAXS) and Small Angle X-ray Scattering (SAXS). Although the diffraction techniques provided the information on the morphology and the crystal structures averaged over the whole sample, it was found to be complementary to our results. Both morphology and crystal structures of samples in corresponding reaction steps were comparable to the samples characterised by TEM, confirming the validity of our growth model. The detailed structural characterisation was performed on the final CZTS sample (sample 7). CZTS can be found in the form of kesterite, stannite or pre-mixed Cu-Au (PMCA) structures. Nanobeam Precession Electron Diffraction (NPED) technique was used to characterise several NCs on a large field of view. When multiplying the result of the phase mapping with the reliability value, the PMCA structure appeared to be the dominant one for all the observed NCs. To the best of our knowledge, it was the first time that PMCA structure was identified experimentally for a Cu_2ZnSnS_4 NCs. High-resolution multislice simulations of STEM-HAADF images have shown that kesterite-stannite and PMCA structures could be distinguished thanks to a peculiar brightness motif due to typical position of the heavier atoms inside the compound (Sn). However, the discrimination can be done exclusively when some particular zone axes are perpendicular to the incident electron beam: therefore, the number of analysed NCs was relatively low. Nevertheless, the well-oriented NCs clearly showed patterns specific to the PMCA structure, even though it coexists with smaller kesterite-stannite domains. This results showed that the cation order was more complex than expected in this chalcogenide material.

In chapter 4, we showed an in-depth structural characterisation of cuboid-shaped, self-organized $CsPbBr_3$ NCs by HRTEM and HRSTEM techniques. This material is very promising for photovoltaic applications; however, it has low stability. The samples studied are polydisperse; domains of aggregates of NCs of the same size tend to form. In particular, we showed domains of NCs having a lateral size of 8.6 nm, in contact with

domains formed by 12.8 nm size NCs. Literature reports indicate conflicting crystal structures (cubic, orthorhombic and polymorph). In particular, by X-ray diffraction, the characterisation of small NCs (< 6.5 nm) is very difficult due to peak broadening. In this work, we studied the crystal structure by STEM-HAADF technique coupled with simulations. STEM-HAADF simulations of both structures were calculated to observe the differences. Anistropy, particularly an elongation, was perceived in atomic columns for the orthorhombic simulations, allowing the discrimination between two crystal structures. High-resolution STEM-BF and STEM-HAADF were performed by acquiring a fast series of images to improve signal-to-noise ratio and to minimise the distortions from scanning: we showed that the orthorhombic structure fits better to the experimental images. In particular we directly observe the alternating displacement of Cs columns typical of [1 0 1] projection. HRTEM analysis was also performed on the same sample. The experimental images have been compared with simulations to guess the thickness and the structure. Several images were acquired, and the FFT of single crystals have been calculated. Only in some individual nanocrystals, evidence of PbBr octahedra tilting was found. For those nanocrystals, the digital diffractogram showed the low-intensity additional spots, which indicate a decrease in symmetry with respect to the cubic structure. These spots fitted well to an orthorhombic structure in [1 0 1] zone axis or [0 1 0] zone axis. This study may suggest the possibility of polymorphism in $CsPbBr_3$ nanocubes, which has been previously observed in $CsPbBr_3$ nanosheets. From the first TEM experience, approximately 19% of the NCs show orthorhombic structure among cubic structure NCs. We underline that experimental techniques which give average information over a high number of nanocrystals will result in an exclusive identification of the orthorhombic structure. Moreover, we presented a powder-like electron diffraction experiment, which confirms the lowering of symmetry due to the orthorhombic distortion. Also, a local SAED experiment was able to probe the [1 0 1] projection over an illuminated area with a diameter of 9 nm. Furthermore, HRTEM showed an amorphous stain on the surface of each NC. We speculate that this is an initial degradation process in the crystals.

Finally, in appendix J an inexpensive and efficient $CuFeS_2$ NCs were studied. These NCs have a potential for thermoelectric applications. Two synthesis methods (hot-injection and heat-up methods) were developed to obtain nanosized $CuFeS_2$. Both procedures provided NCs which were small enough to reduce the thermal conductivity due to nanostructuration. *Hot-injection method* led to strongly anisotropic NCs with a shape of hexagonal platelets, with a lateral size varying from some tens to some hundreds of nanometers. The structure was evaluated from the digital Fourier transform of HRTEM images containing several NCs. Its radial profile can be indexed from the chalcopyrite structure, excluding wurtzite. This result is in agreement with X-ray powder diffraction analysis. Despite the inhomogeneity in size, all the hexagonal facets exhibited the same [1 1 0] zone axis, and the set of planes of the lateral facets were the same for all NCs. This information allowed the construction of a simple 3D atomistic model, which can be used as an input for first-principle simulations of electronic structure or phonon dispersion. Moreover, this model explained the anisotropic shape: the selectivity of the ligands

prevented the growth of the larger facets. *Heat-up method* led to polydisperse NCs with an average size of 20 nm and an irregular shape. Their large dispersion in size and the irregular shape were explained by the low reactivity of the metal precursors with thiols. The heat-up method was favoured for the following pellet elaboration because of an easier scaling up (approximately 1 g NCs per synthesis). Thermoelectric properties were measured in hot pressed pellets. Pure $CuFeS_2$ pellets presented a ZT of 0.10 at most. To increase this value, metallic NCs were added and mixed with $CuFeS_2$ NCs. Several metals have been tested (Ag, Cu, Sn). TEM was performed only on the best composite material, obtained with $CuFeS_2$ NCs from heat-up process and 4% mol Sn NCs (12 ± 2 nm). An exploratory STEM-EDS experiment of the composite was performed to obtain first information about the microstructure. As expected, some empty space appeared between the grains. Cu, Fe and S mappings were superimposed, as they were present in the same position. Sn was not evenly distributed in the material, and it remained confined in the original NC positions. No evidence of the formation of a percolation network was found. Iodine was also observed for the first time in this material. It originated from CuI precursor. Further studies are necessary to understand the position of iodine in the structure and its influence on the properties of this material.

5.2 Perspectives

The optimisation of sample preparation and the variety of advanced TEM techniques open doors to new solutions in the structure and methods to study the morphology of semiconductor NCs.

Ligand removal by acetic acid was proven to be an efficient method, as no substantial changes in the semiconductor NCs and the surface status were observed. Nevertheless, in different systems, the bonds between the surface and organic compounds involve different ions and organic groups. Therefore, a deeper understanding of the interaction between ligands and surface is vital to improve the purification techniques and to use appropriate and selective acid solutions.

The issue of irradiation damage and induced diffusion is common in electron microscopy. Using graphene sandwich would be very useful for the community interested in volatile and beam-sensitive nanomaterials. In section 2.5, the use of graphene as support for TEM imaging of CZTS NCs are shown. It can be applied to other colloidal NCs in a "sandwich" formed by two graphene walls, e.g. small InP NCs, which are often very difficult to observe in TEM due to the excess of organic compounds in solution and on the NC surface. This technique may help avoid the diffusion and sublimation of volatile indium and iodine atoms. Indeed, it was shown in section J.5.2 that $CuFeS_2$ NCs grown from CuI precursor incorporates a non negligible quantity of iodine. Some discrepancies could appear in the properties of pure and iodine-doped $CuFeS_2$ NCs. Preliminary tests on the quantification of iodine in $CuInS_2$ and $CuFeS_2$ NCs were conducted in a simple sandwich configuration (drop casting of NC solution on monolayer graphene) by STEM-EDS. The results indicate that iodine content is stable during acquisition. Two possibilities may explain this behaviour:

1. iodine is strongly incorporated in the structure;

2. the sublimation of most iodine occurs in the very first stages of the acquisition, up to stabilisation of its content in the NC.

By sandwiching the iodine-doped NCs between two graphene layers, transparency to the electron beam is still ensured, as the two layers of graphene are one monolayer thick. Spectroscopy acquisition times could thus be longer in order to quantify elemental ratio and distribution precisely. Technologically, the deposition of a monolayer of graphene is relatively easy[1]. However, the results should be interpreted with caution, as it is difficult to determine whether a NC is sandwiched between two graphene layers, or it just lies on a graphene film: *by TEM* the diffraction patterns of two misaligned superposed graphene layers can typically be observed. However, in this case, the diffraction pattern is almost entirely dominated by the semiconductor NCs. *Micro Raman spectroscopy* is a standard technique to distinguish monolayer graphene from carbon multilayers. However, the sample transfer from the Raman to the TEM apparatus is complicated. Moreover, organic molecules and the NC would give additional spurious signals. Without certitude of confinement of NCs, a meaningful test cannot be carried out. A dedicated study needs to be conducted to sort this issue out.

Concerning Cu_2ZnSnS_4 NCs, the presence of defects must be analysed in detail. Cation disorder needs to be further understood. In the present study, we show that more phases may coexist in single NCs. The ordering of Sn cations was confirmed by studying atomic column intensity in STEM-HAADF images: a confirmation on the nature of the cations by atomic-resolution EELS would not only allow determining Sn cation positions, but also to distinguish the almost isoelectronic Cu and Zn, and therefore kesterite and stannite structure. Obtaining atomic resolution of CZTS NCs by STEM-EELS has been attempted many times during this thesis. Unfortunately, it was never successful. The points that need to be optimized are: the sample preparation (carbon contamination), the ratio between signal and exposure time[2], the exact determination of the lateral size of the matter interacting with the beam (which must be smaller than an atomic column), strategies for beam-damage reduction and advanced data analysis tools for noise reduction (e.g. principal component analysis). Spectroscopy-dedicated electron microscopes could be apt to solve the issue.

The study of the self-organisation of $CsPbBr_3$ NCs could be completed by observing the drying process in an *in situ* experiment by a liquid cell sample holder. Preliminary tests were conducted using a Protochip Poseidon liquid microscopy cell; however the imaging was problematic. The choice of the solvent and the window material must be optimised. Conditions in the liquid cell must be comparable to the drying process in the air.

[1]It involves a deposition of the sample by drop casting on prepared graphene grid; deposition of graphene - PMMA (no harm on the sample, as the deposition occurs in water, and the sample is hydrophobic); and elimination of PMMA in 1 hour in acetone (which is an antisolvent for the semiconductor NC).

[2]In the order of hundreds millisecond, hardly sustainable by such NCs

A NPED experiment was attempted to analyse the structure of $CsPbBr_3$ NCs with higher precision (not shown in this manuscript). In particular, NPED might detect a difference of a, b and c lattice parameters, typical of the orthorhombic structure. NPED is complementary to STEM-HAADF imaging, as shown in the CZTS study. Nevertheless, even after careful storage under vacuum, the sample underwent a significant degradation. NCs are more prone to the contamination under the electron beam, and a proper acquisition is thus impossible. Advanced microscopy characterisation should be carried out right after synthesis.

Degradation is a major drawback for $CsPbBr_3$. It is very a promising material, but, unfortunately, it degrades very fast. An understanding of the degradation process could contribute to addressing the problems related to the limited stability of perovskite solar cells and to the substitution of toxic lead in their composition. These points will be evaluated in a PhD thesis starting in October 2017 in SyMMES laboratory.

The study on the $CuFeS_2$/Sn composite pellet allows building a qualitative description of the system. FIB-SEM equipped with EDS detector would be suitable to obtain 3D information on the morphology of the composite, in particular with the recent advances in spatial resolution in this particular technique. Other 3D-reconstruction methods such as STEM-EDS tomography or atom probe tomography could provide complementary information. Reconstruction of a large volume provides further information on the homogeneity of the pellet. A proper quantitative STEM-EDS of the composite material is also suggested, after the preparation of a thin foil by FIB. The limitations of such a preparation originate from the presence of voids in the microstructure, and ions may interact differently with the two components (a typical issue for heterogeneous materials).

As a conclusion, electron microscopy provides vast possibilities for NCs characterisation. However, it also needs high caution before and during imaging. Most of these points have been addressed in this work; some issues have been solved, while some still need to be thoroughly investigated. Nevertheless, this thesis covers all the attempts (whether or not successful) for a solution and thus aims to contribute to future research.

Appendix A

Synchrotron and laboratory WAXS and SAXS studies for CZTS NC growth

An introduction to the analysis techniques used here can be found in appendix B.

A.1 Experimental methods

This complementary study has been performed to study the structure and size of CZTS NCs during synthesis stages of the Steinhagen procedure, as described in chapter 3. X-ray diffraction measurements were performed in the ID01 beamline at the European Synchrotron Radiation Facility (ESRF). The chosen incident wavelength was $\lambda = 0.774\,\text{Å}$ (incident energy 16 eV) and a 512×512 pixels Maxipix detector was used (1 pixel corresponds to approximately 0.006° in 2θ). The experiment was optimized for Wide Angle X-ray Scattering (WAXS) measurements ($1\,\text{Å}^{-1}$ to $6\,\text{Å}^{-1}$) but SAXS data were also recorded from $0.05\,\text{Å}^{-1}$ to $1\,\text{Å}^{-1}$. The prepared solutions were placed in borosilicate glass capillaries (Lindemann capillaries), with 1 mm internal diameter and 0.01 mm wall thickness. The measure is done in transmission mode, in Scherrer geometry. Samples were placed in a Linkham heating stage allowing temperature control with a $\pm$ 1 °C precision and a maximal temperature of 600 °C (figure A.1). Additional WAXS and SAXS measurements were also performed in the laboratory instruments. A Panalytical X'Pert diffractometer in Bragg-Brentano geometry, equipped with a linear X'Celerator detector was used with Cu K_α radiation ($\lambda_{K_{\alpha_1}}$ =1.540 56 Å). The divergence slit was automatically driven to keep a constant 8 mm irradiated length along the $\theta/2\theta$ scan and a set of anti-scattering slits was used before and after the sample. Axial divergence was limited by 0.02 rad Soller slits. SAXS measurements were performed with an in-house point collimation SAXS Camera equipped with a rotating anode generator (FR591 Nonius) operating with a copper target and a point focus source of 200 µm size. The X-ray beam was K_α/K_β filtered (λ =1.5418 Å) by total reflection from two curved Ni-coated Franks mirrors and by transmission through a thin 10 µm Ni foil. The detector is a multi-wire gas-filled proportional counter with a large $17\times17\,\text{cm}^2$ active area. It was

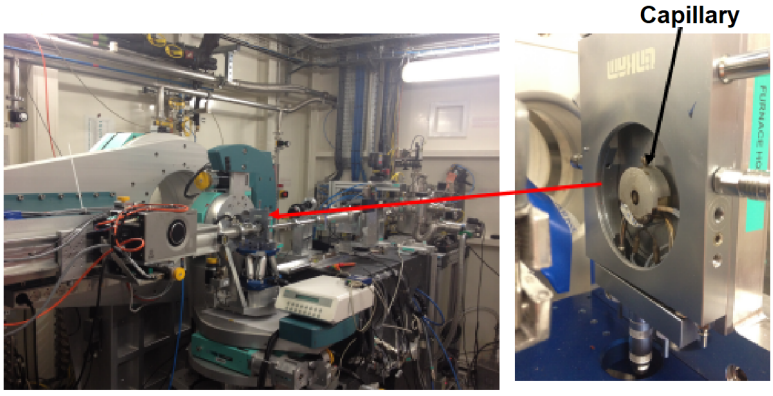

Figure A.1 – Left: A photograph of the experimental setup in ID01 beamline at ESRF. The red arrow points at the heating stage, in which the sample lies. The right image is the focus-up of the heating stage. The black arrow indicates the capillary containing the analysed solution.

successively positioned at 50 cm and 150 cm, thus allowing to cover a 0.01 $Å^{-1}$-4 $Å^{-1}$ q-range. The SAXS patterns were obtained by reduction of the two-dimensional data by radial integration of intensities.

A.2 *In situ* synchrotron WAXS and SAXS

The studied samples were all pre-heated at 110 °C before capillary filling[1]. WAXS and SAXS spectra were then recorded at 110 °C and after 10 minutes heating at 280 °C.

The WAXS data recorded at a wide range of 2θ is shown in figure A.2. Considering the ICDD-PDF data of kesterite Cu_2ZnSnS_4 phase and CuS phase, an apparent shift in the position of the highest intensity peak located at approximately 23.6° is observed.

To get a clearer view, we focus on the diffraction pattern around 23.6° as shown in figure A.3a and this time, we follow the evolution of the CuS characteristic peak at 280 °C with time (from 80 s to 1280 s).

During the reaction, we notice a slow shift towards smaller angular values. At the end of the synthesis, the observed peak is shifted to $2\theta = 23.25°$ (peak corresponding to kesterite CZTS, $d_{220} = 1.9$ Å). The evolution of the peak position as a function of heating time at 280 °C (table A.1) is plotted in figure A.3b. It linearly decreases in the first stages; at approximately 600 s an abrupt shift is observed, due to a phase transition from CuS-like phase to kesterite-like CZTS phase; then it continues decreasing linearly. This behaviour indicates a crystalline phase transition after 10 minutes of heating at 280 °C. The diffractograms measured before the transition give indications of the presence of several crystalline phases but which couldn't be reliably identified; the

[1]Capillaries are necessary for *in situ* experiments; temperature can be controlled; nevertheless the conditions of the process are slightly different with respect to the reaction performed in three-neck round-bottom flasks.

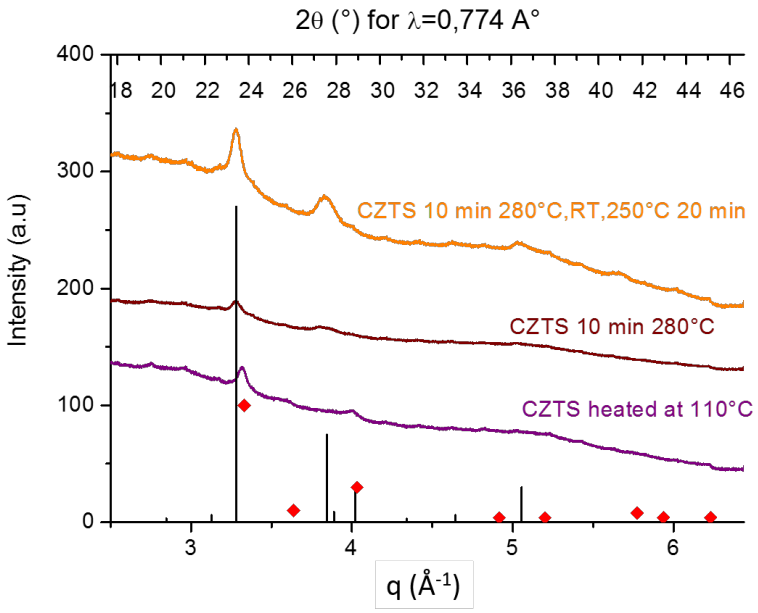

Figure A.2 – WAXS diffraction patterns at 110 °C (violet colour) and after heating at 280 °C (brown and orange colours). Black vertical lines correspond to the ICDD-PDF 26-0575 data for kesterite phase of Cu_2ZnSnS_4; the red squares correspond to ICDD-PDF data for CuS.

crystalline phase after 10 minutes is compatible with a tetragonal kesterite-like structure. This trend is in agreement with the microscopy data, as the first quasi-stoichiometric CZTS NCs were observed after 10 minutes at 280 °C. Some low-intensity peaks appear at slightly lower 2θ angles (22.3°) after heating for 680 s. These peaks do not have a physical meaning, but they are due to artefacts from the detector. The same is true from the obvious discontinuity at approximately 22.8 nm, due to the integration of the signal from different segments of the detector. For this reason, we focus our attention on the position of the peak, and we provide only qualitative information about peak width.

The splitting between (0 0 4) and (2 2 0) peaks, caused by the fact that $a \neq 2c$, could be used to differentiate between kesterite-stannite and PMCA structures[2]. Nevertheless, this difference is in the order of 0.02°: this quantity is inappreciable due to the peak broadening.

Heating time at 280 °C (s)	Peak position 2θ (°)	FWHM (°)	Crystallite size (nm)
80	23.58	0.444	10.21
180	23.54	0.477	9.50
280	23.50	0.533	8.50
380	23.51	0.529	8.57
480	23.49	0.527	8.60
580	23.46	0.443	10.23
680	23.33	0.431	10.51
980	23.27	0.376	12.05
1230	23.25	0.463	9.78

Table A.1 – Shift of diffraction peak at 280 °C from WAXS.

SAXS data recorded at room temperature (figure A.4) put in evidence two peaks centred at $q_1 = 0.034\,\text{Å}^{-1}$ and $q_2 = 0.076\,\text{Å}^{-1}$, corresponding to correlation distances of about 18 nm and 8 nm respectively. This indicates a double population. Upon heating up, low q intensity increases and the peak centred at q_1 becomes hardly discernible. The position of the second peak remains mainly unchanged, while its intensity decreases.

These *in situ* measurements were complemented with *ex situ* experiments performed on four samples extracted at different stages of the process.

[2]Clarification about the nomenclature and structure characterisation can be found in chapter 3.

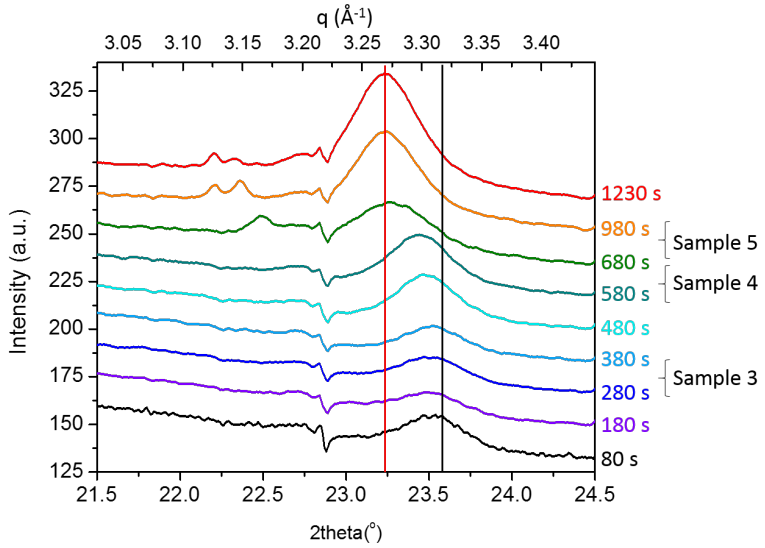

(a) Evolution of diffractogram as a function of time. The red vertical line at $2\theta = 23.25°$ corresponds to a characteristic peak of kesterite Cu_2ZnSnS_4 phase. The black vertical line at $2\theta = 23.6°$ corresponds to a characteristic peak of CuS.

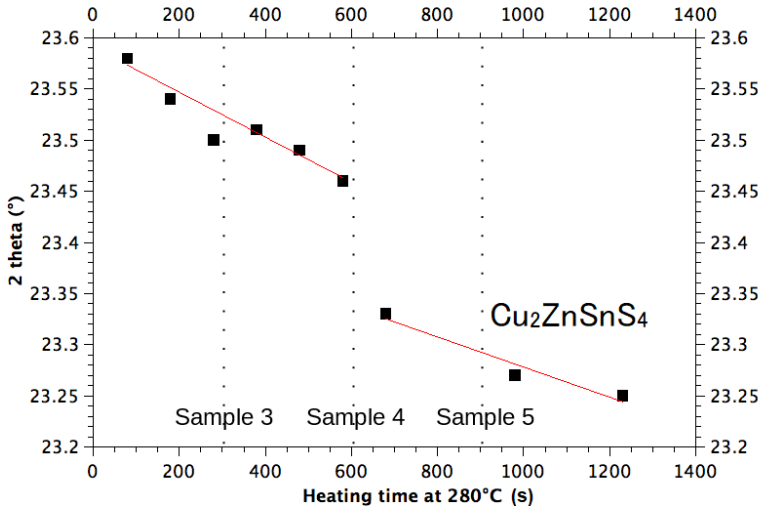

(b) Evolution of peak position as a function of time.

Figure A.3 – WAXS analysis at 280 °C.

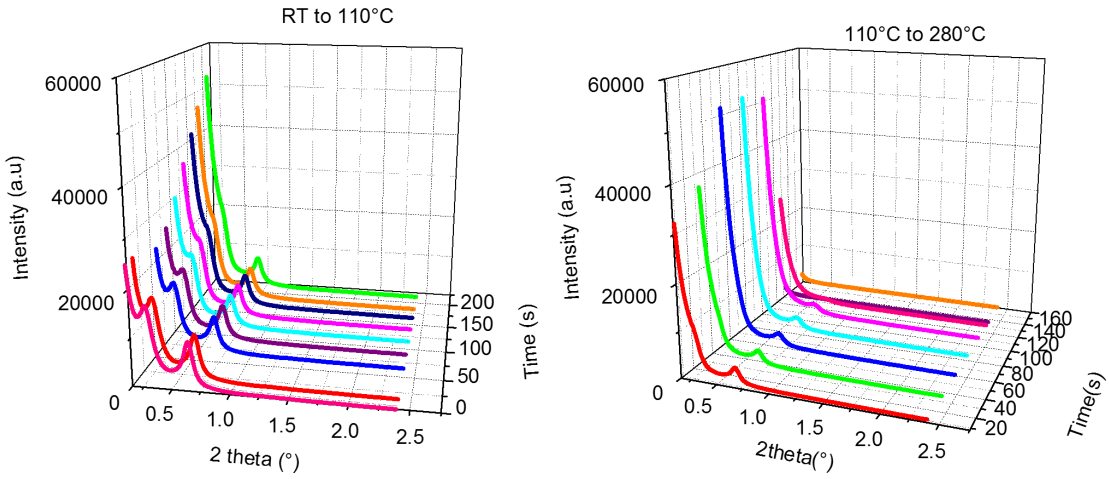

Figure A.4 – Evolution of SAXS spectra from room temperature to 280 °C.

A.3 *Ex situ* laboratory WAXS and SAXS

A.3.1 First stage: 110 °C pre-heating of the precursors in oleylamine

Laboratory WAXS measurements performed on sample 2 indicate the presence of two sets of diffraction peaks, the widths of which correspond to crystalline particles of approximately 9 and 4 nm. The associated crystalline phases cannot be unequivocally determined, as several Zn-S and Cu-S binary or Cu-Zn-S ternary phases could give satisfactory agreement. No phase containing Sn was found to correspond to the measured peaks. This result is coherent with the mean stoichiometry $Cu_{3.13}Zn_{1.5}Sn_{0.1}S_4$, determined by SEM-EDS.

The sample prepared for SAXS measurements, which consisted of a 1 mm diameter capillary filled with a solution of precursors and oleylamine previously heated at 110 °C rapidly appeared to decant. Therefore, the data were recorded with the beam centred on the precipitate and successively on the supernatant (figure A.5). The diagram obtained with the precipitate provides, in the 1-4 $Å^{-1}$ q-range, crystalline peaks similar to the ones obtained in WAXS. In agreement with the synchrotron data, a bump and a peak are present at lower q values, the positions of which respectively correspond to correlation distances of about 20 and 7 nm. Knowing that their width is inversely proportional to the standard deviation of the correlation distance implies that the larger distance correlations are less precisely defined. The identification of two correlation distances is coherent with the two crystallite sizes determined from WAXS results. The discrepancies between the values deduced from the two techniques can be explained by the fact that a particle might be formed of several crystallites. They can also be due to the presence of oleylamine surrounding the particles. This solvent, which acts as the surface stabiliser, might have different affinities with the different crystallographic phases corresponding to the two sets of crystallites. This affirmation is justified by the observation of the

different size populations by TEM.

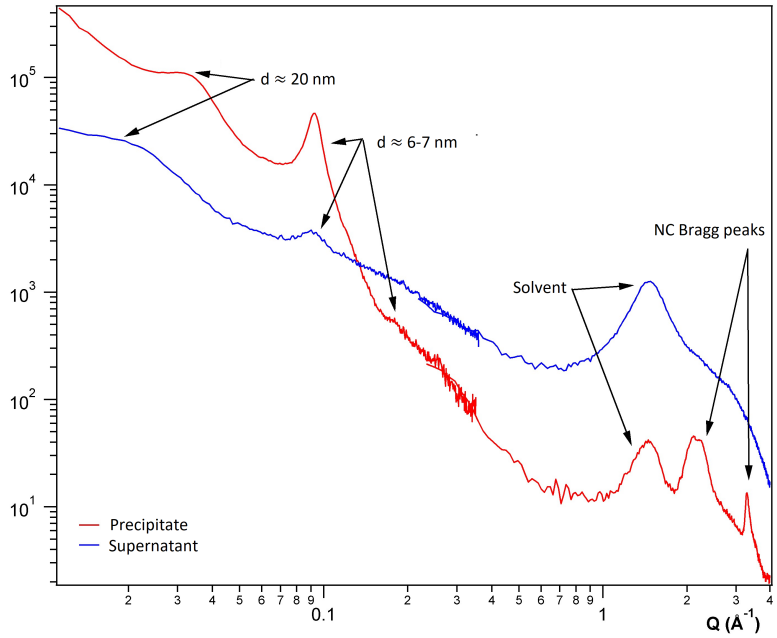

Figure A.5 – SAXS performed in supernatant and precipitate in sample 2, after 30 minutes at 110 °C

A.3.2 Following stages: 280 °C heating

Laboratory WAXS measurements performed on sample 3 evidence a dominant set of diffraction peaks corresponding to crystallites of 8-9 nm. The peak positions are compatible with the tetragonal CZTS crystalline phase, but the relative intensities indicate a non-nominal composition. The latter is modified between 5 and 15 minutes spent at 280 °C but remain almost unchanged above 15 minutes. SEM-EDS measurements give the following mean composition for samples 6 and 7: $Cu_{2.1}Zn_{1.1}Sn_1S_4$. The crystallite size calculated with Scherrer's formula moderately increases to 10 ± 2 nm for sample 7. The herein described WAXS studies from *ex situ* experiments are plot in figure A.6.

The final sample was also drop cast onto a disordered silicon substrate, and X-ray diffraction was performed on a PHILIPS X'PERT powder diffractometer, with a copper anode X-ray source ($\lambda = 1.541$ Å). The diffraction pattern is shown in figure A.7. 16 of the 17 identified diffraction peaks can be attributed to tetragonal-like phase of bulk Cu_2ZnSnS_4 and compatible with kesterite structure (ICDD 04-015-7542, space group $I\bar{4}$), with lattice parameters $a = 5.439(3)$ Å and $c = 10.854(5)$ Å (tetragonal lattice distortion $\eta = \frac{c}{2a} = 0.9978$). Also, a Rietveld refinement was performed by imposing PMCA Cu_2ZnSnS_4 structure. Neither the refinement performed with the kesterite nor with the PMCA structures provide a full matching of the diffractogram. This low matching

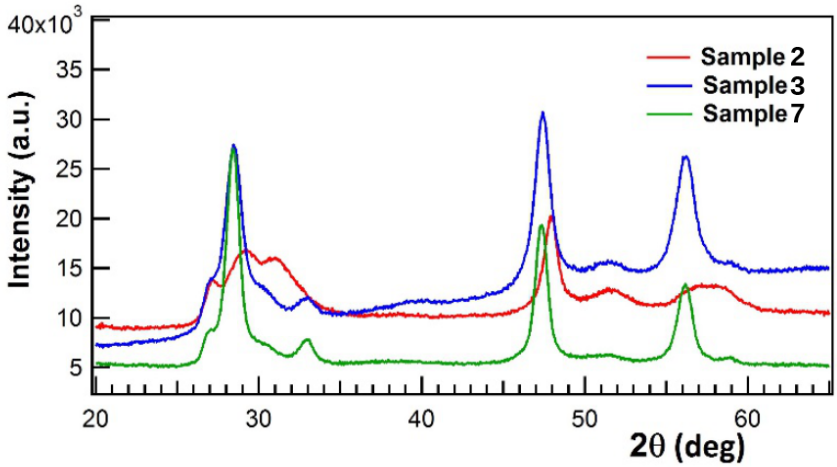

Figure A.6 – WAXS data measured with samples 2, 3 and 7. Zoom on a reduced 2θ range to illustrate the phase transition induced by heating at 280 °C.

can be explained by the presence of more phases inside the NCs (see section 3.6 and following).

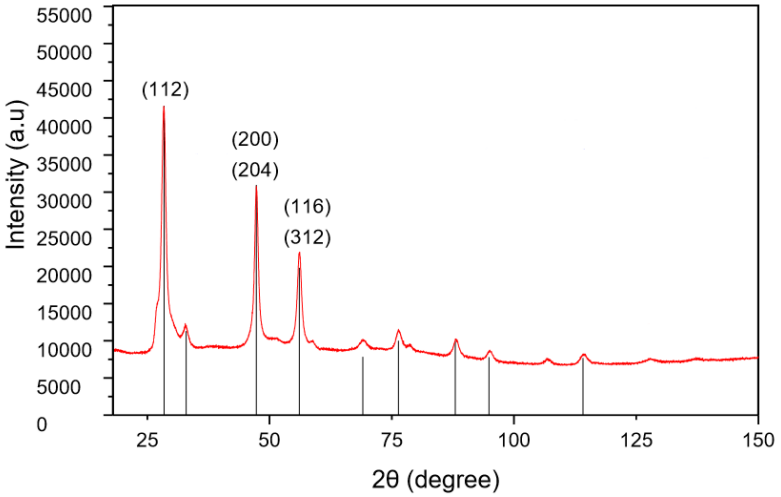

Figure A.7 – Diffraction pattern of CZTS NCs obtained by Steinhagen procedure. Black lines indicate the peaks corresponding to bulk CZTS in the kesterite phase reference pattern (ICDD 04-015-7542).

Appendix B

Selection of X-ray techniques: nanocrystals growth studied by *in situ* methods

The control in size, shape and composition of NCs through design and optimisation of synthetic methods can be done by monitoring the nucleation and the growth. The growth mechanism influences the morphology of the initial crystalline nucleus and therefore of the final NC [166]. In such monitoring, the acquisition time must be fast, as the initial growth kinetics take place in seconds; the method must be compatible with the specific reaction conditions, such as temperature and atmospheric composition. Moreover, the measurement must not disturb the reaction itself, which is a problematic task when using highly energetic X-rays or electrons.

The first attempts of *in situ* observation of metallic NC growth using electron microscopy in liquids [96] was obtained by placing the precursor solution in a particular sample holder, containing silicon nitride or graphene windows. Those gave access to the kinetics of size and shape evolution with reaction time [97]. To minimise beam-induced NC growth and other effects, STEM techniques at relatively low doses have to be applied [167]. Nevertheless, mixing and injection of precursors inside the sample holder are difficult to realise, and the nucleation and growth could be triggered by the electron beam or by supplying thermal energy. In the case of semiconductor NCs, the size-dependent optical properties can be exploited through *in situ* UV-vis absorption measurement to determine NC growth kinetics [27]. An advantage of this method is its high temporal resolution, which is on the order of microseconds. Nevertheless, this method needs a strong colour change or a gradual change in optical density of the reaction medium during growth. It can also be used in combination with *ex situ* NMR spectroscopy or *ex situ* TEM studies.

In situ X-ray diffraction experiments provide a powerful tool for describing NC nucleation and growth kinetics. High-energy synchrotron radiation is often necessary for obtaining sufficient signal intensity during *in situ* X-ray studies on solutions enclosed into or flown through thin glass capillaries. Sample damage is limited by using beam shutter and short acquisition times (tens of milliseconds for SAXS, seconds for WAXS).

Small-angle X-ray scattering (SAXS) is a small-angle scattering (SAS) technique

where X-rays (wavelength 0.1 nm to 0.2 nm) are elastically scattered by a sample which has inhomogeneities in the nanometer range. SAXS can give access to prenucleation stages, the precursor organisation, and the mean size and auto-assembly during post-nucleation stages. It is recorded at very low angles (typically 0.1 nm to 10 nm). This angular range contains information about the shape and the size of macromolecules, characteristic distances of partially ordered materials, pore sizes, and other data. SAXS is capable of delivering structural information of macromolecules between 5 and 25 nm, of repeat distances in partially ordered systems of up to 150 nm [168]. USAXS (ultra-small angle X-ray scattering) is able to resolve even larger dimensions. SAXS and USAXS are part of X-ray scattering techniques that are used in material characterisation; also, non-crystalline samples such as biological macromolecules can be analysed.

Wide-angle X-ray scattering (WAXS) is a diffraction technique used to identify the crystalline structure. This technique refers to the analysis of Bragg peaks scattered to wide angles. Such reflections, obeying the Bragg's law, probe the crystalline structures having sizes comparable to the incident wavelength (for X-rays, under the nanometer range, such as interplanar distances). A WAXS setup is similar to SAXS. However, the detector is closer to the sample holder: therefore diffraction is observed at larger angles. Some instruments can perform both WAXS and SAXS at the same time. The acquired diffraction pattern allows the determination of the crystalline structure of the formed NCs, of the crystallite sizes, and the lattice parameter of the observed crystalline structure. The sample is scanned in a wide-angle X-ray goniometer, and the scattering intensity is plotted as a function of the 2θ angle.

The first studies were performed on nucleation and growth of gold NCs employing a combined SAXS/WAXS and UV-vis study [169]. Also, extended X-ray absorption fine structure measurements have been used to study the nucleation of CdSe NCs [170]. The study presented in chapter 3 is one of the first studies on multinary semiconductor NCs, which couples *in situ* SAXS and WAXS with *ex situ* STEM-EDS of the first reaction steps.

Appendix C

Surface science of NCs

The surface of the NC is a dominant player in many physical and chemical processes due to the large surface-to-volume ratio. The molecules binding to the surface are called surface ligands and are essential components of nanomaterial synthesis, processing and application. By diminishing the size of the NCs, the role of the surface atoms increases as the number of dangling chemical bonds . At the nanoscale, surfaces can alter properties (solubility, luminescence) and generate new effects such as surface plasmon resonance or size-dependent band gap. Traditional surface science states that dangling bonds can introduce new electronic states [171], and foreign molecules (adsorbates or surfactants) alter energy and reactivity of the crystal surface [172]. These effects also apply to NCs. Nevertheless, the small facet size and the abundance of edge and corner sites complexify a quantitative description. The chemical bond between a NC superficial atom and a surfactant atom is similar to a coordination complex formed by a metallic ion and a ligand. The ensemble of ligands on a NC forms a capping layer which saturates dangling bonds. Ligands protect the particle from the external environment; this layer is crucial during the synthesis when nucleation and growth are controlled and stabilised [173]. Ligands influence optoelectronic properties and provide steric and electrostatic stabilisation. NC with an immaculate surface would agglomerate and precipitate.

Ligands can be exchanged, providing great versatility for applications: ligands can be targeted for applications, applying organic chains or inorganic ions [174,175], clusters [176] or polymers [177]. NCs are therefore functionalised to be grafted to biomolecules and molecular objects.

C.1 Structure and bonding at the inorganic-organic interface

NCs are structures composed of hundreds to thousands of atoms, usually synthesised in a solution containing surface ligands with an anchoring group tethered to the semiconductor surface, and a hydrocarbon tail directed to the outside. The shape of a NC in equilibrium minimises the energy of the exposed surface area and the energy of dangling bonds, which are specific to the index of the facet. Typical core shapes are polyhedral, exposing facets with high-coordination surface atoms. In this case, the exposed area is

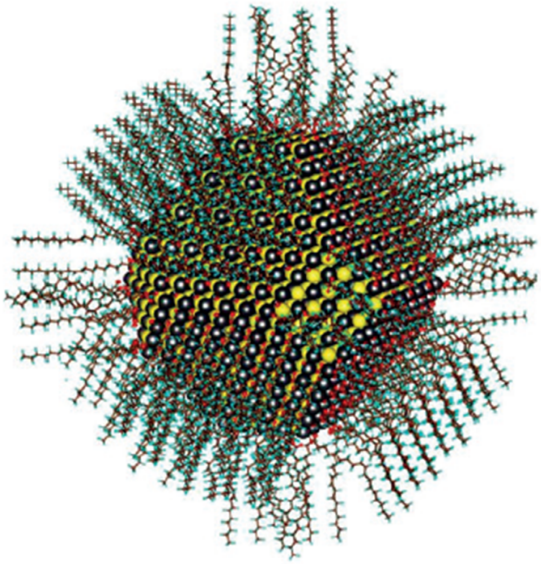

Figure C.1 – Calculated capping-layer structure of 5-nm diameter PbS NC capped with oleic acid. PbS (1 1 1) surfaces are terminated by oleate and hydroxide ions, PbS (1 0 0) by oleic acid. Retrieved by [178].

only slightly larger than in a sphere. If surface ligands bind selectively to certain facets of a growing NC, the surface energy is reduced relative to the others. Ligands can also block delivery of new reagents to the facets: both kinetic and thermodynamic factors are used during the synthesis of anisotropic shapes, such as platelets [179] and rods [180].

The capping layer can be considered as a miniature self-assembled monolayer [181]. Binding between the surface metal atoms and ligands can be comparably strong. As an example, the bond dissociation energies for Pb-S and Pb-O, which occur in thiolate or carboxylate capped PbS NCs, are 346 and 378 kJmol^{-1} respectively [182]. The strong interaction between metal atoms and sulfur atoms pushes the free ligands still present in the solution to bind tightly to the metal surface. Hydrocarbon tails attract by weak van der Waals interactions (interaction energy of some tens of meV [182]), which induce a dense packing in the organic overlayer. On a flat surface and at equilibrium, a crystalline arrangement of surfactant molecules is expected. The grafting density of the self-assembled monolayer is limited by the size of organic tails, which are densely packed. Nevertheless, NCs do not have flat surfaces but contain several vertex and edge sites, which give more volume to the tails to stay. As a result, the capping layer density is usually higher than on flat surfaces [183]. Open spaces in the NC capping layer allows penetration of solvent molecules or ligand chains from neighbouring NCs. The nanometric dimensions and the heterogeneity of the objects (each NC exposing facets with different patterns of surface atoms) make the experimental study of NC surfaces challenging. At the moment, no atomic-level reconstruction of the capping layer is possible with current characterisation techniques. Instead, a series of complementary methods

should be applied to obtain information about the NC-ligand bonding, the structure of the capping layer and the interactions between surface and the surrounding environment.

C.2 Characterisation of the nanocrystal surface

Several imaging, scattering, spectroscopic and computational techniques are used to characterise NC surfaces successfully. Each of these methods provides complementary information about the interface:

1. chemical bonds between core and surface ligands;
2. composition and structure of ligand molecules;
3. effective properties of the whole capping layer.

In the following, some useful techniques are cited.

- Fourier transform infrared spectroscopy (FTIR) probes the NC surface, providing information on the structure of ligand molecules. NC capped with organic ligands show strong infrared absorption bands around $3000\,\mathrm{cm}^{-1}$ and $1500\,\mathrm{cm}^{-1}$, corresponding to the C−H stretching and bending modes of surface-bound hydrocarbon molecules [183]. Chain conformations and molecular order of the capping layer can be investigated from width and position of infrared resonances [184].
- Raman spectroscopy is used to monitor the inorganic ligands with heavy atoms vibrating at low frequencies [176, 185].
- Nuclear magnetic resonance (NMR) spectroscopy can be used to characterise the capping layer of NCs, following fingerprints of spin-active nuclei such as ^{1}H, ^{13}C, ^{31}P [186]. NMR peaks show significant broadening from dipolar coupling effects in surface-tethered ligands. Diffusion-ordered spectroscopy (DOSY) links a diffusion coefficient D to each resonance, allowing the separation of signals from surface-bound and free ligand molecules [187].
- Small-angle X-ray scattering (SAXS) and dynamic light scattering (DLS) are used to study the effective thickness of the NC capping layer, and the contribution to overall dynamic radius [174, 188, 189].
- Transmission electron (TEM) and scanning probe (scanning tunnelling and atomic force) microscopes allow real-space imaging of the NCs and in some cases the surface ligands. Microscopic techniques analyse single objects, allowing the analysis of features in the systems which could be hidden in the averaged ensemble [111]. An example can be seen in figure 2.11.
- Density functional theory (DFT) and molecular dynamics (MD) can overcome the difficulties linked to the experimental determination of experimental probing. DFT is useful to model electronic interactions between NC facets and binding

molecules. A combination of *ab initio* electronic structure and MD calculations can reconstruct a NC completely, with the structure of the inorganic part and the confirmation of the organic ligand shell. These tools help in the interpretation of experimental results [178, 190].

C.3 Effect of ligands on the electronic structure

The organic shell covering the semiconductor core can drastically influence electrical, optical, catalytic and magnetic properties of the NCs. Due to quantum confinement, valence and conduction bands are not continuous but split into discrete quantum-confined energy levels. This effect gives rise to size-tunable luminescence [13]. Nonetheless, uncoordinated atoms on the surface which expose dangling bones may contribute to building novel electronic states lying between the highest occupied and the lowest unoccupied quantum-confined orbitals of the nano-object; these new electronic states can form a trap for charge carriers, quenching luminescence and generally lowering the performance of a final device [191].

Bonding between surface semiconductor atoms in proximity with organic ligand orbitals forms a new molecular orbital set, which can be described by using the terminology of crystal field theory. Bonding orbitals σ are energetically stabilised with respect to the non-interacting surface atom and ligands, while antibonding orbitals $\sigma^\star$ have higher energies. Forming a strong covalent bond between surface atoms and ligands shifts the energies of σ and $\sigma^\star$ orbitals out of the band gap, cleaning from trap states responsible for non-radiative recombination [192]. To preserve NC luminescence and absorption, mid-gap trap states must be eliminated. Nevertheless, the link between NC surface structure and optical properties remains an open question and varies from materials and ligand species. It has been reported that some ligands introduce mid-gap electronic states, increasing the rate of non-radiative relaxation and quenching luminescence [193]. Some ligands can shift the absolute energy of electronic states with a variation of band energies. This effect has an electrostatic origin: a surface-bound molecule generates an electric dipole as the tethered molecules are oriented and point towards the centre. Electric field potential shifts all the levels [194]. Two contributions determine the direction and the intensity of the dipole:

- the interfacial dipole formed between surface atoms and ligand heads;
- any intrinsic dipole associated with the ligand molecular structure.

As all energy levels in the system are shifted by the same energy and with the same tendency, these changes are not observable from absorption or luminescence spectra. Nevertheless, it is crucial to control absolute energies of lowest occupied and highest unoccupied levels in band gap engineering of devices, e.g. light-emitting diodes, single and multi-junction solar cells [195]. For semiconductor NCs, practically every physical properties can be adjusted by surface ligands, including band gap, ionisation potential and affinity, and luminescence.

C.4 Ligands for synthesis, ligands for applications

The transformation of precursors to NC with desired size, shape and composition is optimised and controlled by the kind of ligands employed. Organic surfactants such as oleic acid and oleylamine [173, 188] are among the leading solvents and ligands. These "pristine" ligands are also indicated for dispersing NCs in ordered superlattices [188,196]; when mixed with polymers, they can generate interesting composite materials [197]. Nevertheless, some applications need different capping layers that are modified during a post-synthetic treatment: this is usually called ligand exchange. Depending on the desired application, electrical conductivity or solubility in water can be regulated.

NC solutions can be processed to produce thin-film field-effect transistors, solar cells, photodetectors, light-emitting diodes [176,198,199]. These applications need an efficient transport of charge carriers between NCs, and ligands must be good conductors. The ligands employed during the synthesis contain long aliphatic chains (C_8 - C_{18}). While they may prevent charging, they do not allow an efficient electron transport. Therefore, they are detrimental to device performance. The exchange of insulating organic ligands with small or conducting molecules (such as hydrazine) is a critical factor for increasing the conductivity of a deposited thin film (even 10^{10} fold) [200]. Two strategies are used for the exchange of the original ligands:

1. solution exchange: even the ligand-exchanged NCs retain colloidal stability. This factor is necessary to produce uniform films with easier device manufacturability. Great improvements have been linked to the development of charged inorganic ligands which, once bound to NC surface, provide electrostatic stabilisation in polar solvents;

2. solid-state exchange: the treatment is applied on a NC film; the molecular species displace the original ligands but do not disperse NCs in the solvent. A broad choice of solid-state ligand exchange reaction is available, using for example short dithiols (1,2-ethanedithiol, 1,3-benzenedithiol) or diamines. However, they often lead to cracks in the film due to the volume contraction from the substitution of bulky original ligands with smaller molecules [201]. To avoid this problem, the films can be formed in a layer-by-layer manner, applying after each spin-coating step a ligand exchange step, which crosslinks and hence stabilised the deposited layer.

The substitution with compact and electronic transparent ligands allows achieving mobilities among the highest measured for solution-processed semiconductors [202], permitting the integration in circuits and transistors [203]. Also, inorganic ligands can promote the overlap of electronic wave functions of individual NCs, creating extended electronic states delocalized across several NCs [204] and therefore changing the transport behaviour. In a solar cell, competing processes are present. It is essential to understand the kinetics of charge kinetics and transport. Photogenerated excitons can be successfully separated at the junction and collected by electrodes, or inappropriately eliminated through a recombination event. Important factors are the carrier lifetime (limited by

recombination), temperature and mobility [198]. Incomplete surface passivation accelerates surface recombination that drains carriers from the solid and is the primary factor limiting the performance of NC solar cell. Trap concentration is reduced by using atomic ligands [205].

The combination of NCs with other materials can produce composites, where the surface ligands are the interface between the NC and the surroundings. Organic ligands promote the mixing in organic hosts, such as polymers [199]. On the contrary, inorganic ligands are needed for inorganic hosts matrices. NCs can be therefore integrated into chalcogenide glasses [206] and amorphous oxide layers [176]. Thermal annealing is used to transform films deposited from soluble NC precursors inks into larger crystallites, after sintering and grain growth. Surface ligands have impacts on the sintering behaviour: volatile ligands help sintering, providing final phases which are organic contaminants-free [191].

Appendix D

Inspiring ligand removal methods in literature

As the standard and routinely used purification methods do not show the expected success, a deep investigation of literature has been made to allow advanced microscopy. The investigated literature concerned:

1. samples similar to semiconductor NCs, which share the same drawbacks about surface contamination (metallic NCs, or bulk semiconductors);

2. fields where the control of surface properties plays a major role such as catalysis.

In the following, some works that inspired our strategies are reviewed.

D.1 Fast thermal annealing

In catalysis, the surface state is crucial. Active materials need to be scaled down to increase the surface-to-volume ratio and provide the maximum catalytic sites for a given amount of material, which is often based on expensive and rare elements. It has been shown (see subsection 2.3.2) that ligands are efficiently removed with thermal treatments performed at a minimum temperature of 300 °C, despite the fact that the slow heating ramps (associated with relatively long annealing times) lead to changes in morphology of the particles and a sintering restructuring of NCs on the support [100].

Cargnello et al. proposed an efficient thermal treatment to remove organic ligands from catalysts prepared by colloidal methods [112]. The uniformity of the particles is preserved, and the system is activated for catalytic reactions. Their approach was tested on metallic nanomaterials, such as Pd tetrahedral Pt NCs [1], and core-shell Au@Fe_xO_y structures [2]. The so-called "fast thermal annealing" consists of very rapid heating and cooling ramps of the order of several tens of degrees per second in air. The sample is

[1] Oleylamine and oleic acid were used in the synthetic and washing steps

[2] The Au core NCs are stabilised with dodecanethiol, while the shell is growth in an oleylamine-octadecene-oleic acid mixture [207]

introduced into a furnace, preheated at a specific and high temperature. After a certain time, the sample is quickly removed from the furnace and cooled down on a benchtop. Authors state that "with these high heating and cooling ramps, kinetic transformations are favoured over thermodynamics, preventing the system from relaxing to its lower energy state" [112]. In other words, being the process fast, the lowest energy configuration is not reached: there is no loss of high surface energy facets, or lowering of collective surface energy through sintering. The only effect from the treatment would be an expulsion of the ligands from the surface.

D.2 Purification by acetic acid

Here are briefly explained some works that inspired us for using acids for the purification of NCs.

D.2.1 Surface treatment by acetic acid on $CuInS_2$ NCs

Akdaş and collaborators performed a detailed investigation of the surface of $CuInS_2$ and analysed strategies to control the number of ligands on the surface [113]. $CuInS_2$ is synthesized with 1-dodecanethiol (1-DDT) having at the same time the roles of sulfur source and surfactant. The improvement of the purification of quantum dots was attempted while keeping in mind three particular factors: reduction and control of the amount and the nature of organics at the particle surface; effective purification with the least amount of solvent; minimum cycles of centrifugation. These factors enable the reduction of solvent consumption and therefore time and costs needed for the purification step [113]. To separate excess organic components from the inorganic part, or chains embedded in the ligand shell, three mixtures were used as antisolvents: acetone in pure form, acetone in combination with methanol (MeOH), or acetone in combination with acetic acid (HAc). MeOH is used to increase the polarity of the solvent/antisolvent mixture, while HAc is expected to promote desorption of weakly bound ligands from the surface. Purification of the reaction solution was performed by repeating 5 timed the cycle

1. addition of solvent $CHCl_3$;
2. flocculation by addition of antisolvent. Those are the ones tested:
   - 4 eq.s of acetone;
   - 1 eq. of methanol plus 3 eq.s of acetone (MeOH - acetone combination);
   - 1 eq.of acetic acid plus 3 eq.s of acetone (HAc - acetone combination);
3. centrifugation for 10 min at 8000 rpm;
4. discard of supernatant[3].

[3]The supernatant is defined as the precipitate-free liquid remaining above the solid after centrifugation.

The number of organics remaining on the surface after drying was measured by thermogravimetric analysis (TGA) and resulted in approximately 60 wt.% for using acetone as antisolvent; the remaining compound was oily. MeOH - acetone combination led to 50 wt.% organic left, and a waxy product; for both purifications, evaporation of organics started at 150 °C. The novel method with HAc - acetone resulted in only 40 wt.% organics in the sample, with an evaporation starting at 250 °C. Therefore, the loosely bound organics are more efficiently washed out with HAc - acetone antisolvent: calculation of the surface coverage results in approximately 77% of a monolayer, versus the bilayer of organics with simple acetone purification (approximately 205% of monolayer coverage) and roughly 125% of a monolayer for MeOH-acetone. The NCs treated by HAc - acetone procedure were found to be stable in solution. The ratio of S was also measured by inductively coupled plasma - optical emission spectrometry (ICP-OES), confirming the ability of removing excess ligands for HAc - acetone; from the Cu:In ratio, a moderate surface etching is suggested, as about 23% of the surface might be unprotected and free to react and dissociate from the surface. As a result, the authors state that acetone used as antisolvent leads to incomplete purification. MeOH - acetone combination removes residual indium salts but leaves organic chains attached to the NC. HAc - acetone removes organic compounds from the surface but seems to etch the surface as well slightly. The same results on the purification were confirmed on core/shell $CuInS_2$/ZnS NCs. In their study, also HRTEM images and Selected Area Electron Diffraction (SAED) investigations were performed. Washing NCs with acid resulted in a reduction of difficulties in visualisation, due to organic residuals and side products from the synthesis. It was also noticed that decreasing the electron dose[4] helped to prevent nanoparticle ripening to minimise their mobility. The authors conclude: "(...) the newly developed purification method leads to a substantially decreased amount of organics at the particle surface. This allows an easier characterisation of the small NCs by HRTEM and opens avenues to utilise these NCs in electronic devices. We are fairly confident that this purification procedure is adaptable to different materials, where strongly bound thiols are used as ligands and sulfur source simultaneously. Depending on ligand chain length and polarity, further acids, probably with lower acidity, may become interesting to purify NCs" [113].

D.2.2 Ligand exchange in PbS:P3HT

Seo developed a methodology for a versatile and facile ligand exchange by post-synthesis chemical treatment of PbS NC:poly(3-hexylthiophene) (P3HT) hybrid composite film [114]. PbS NCs where synthesised with octadecene serving as a solvent, and oleic acid serving as the surfactant. Hexamethyl disilathiane (HMD) was chosen as the sulfur precursor. An 80 nm P3HT:PbS (50:50 wt.%) blend film was spin coated on top of a PEDOT:PSS[5] using a chloroform solution; it was dried at 80 °C for 10 minutes. The film was successively immersed into an acetic acid solution (0.01 M) in acetonitrile; after

[4] A decrease in the electron dose could be obtained by reducing the acquisition time, and the beam current

[5] PEDOT:PSS or poly(3,4-ethylenedioxythiophene) polystyrene sulfonate is a polymer mixture of two ionomers

30 minutes under continuous stirring, the film was washed by excess acetonitrile and was dried at 150 °C for 10 minutes. The film was stable during the processing. FTIR spectroscopy showed that the oleic acid ligand disappears and the acetic acid ligand appears, following a replacement in the solid-state film of PbS [114].

Appendix E

Examples of clean graphene as sample support for other classes of materials

Some images acquire by monochromated beam by HRTEM operated at 80 kV are displayed here. The microscope alignment is the same of the images presented in subsubsection 2.5.3, as the ones presented here where acquired during the same session. The

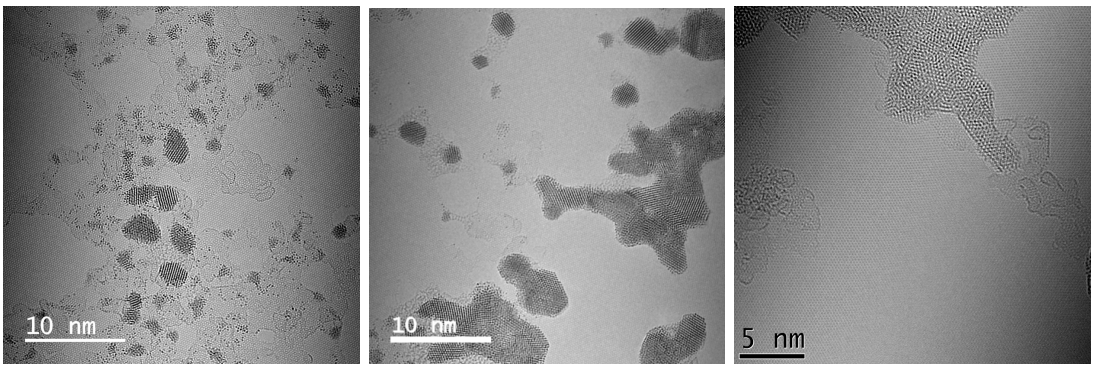

(a) (b) (c)

Figure E.1 – Pt metallic salts deposited on graphene (magnification 295 kx, 380 kx for figure E.1c). Courtesy Hanako Okuno.

.

sample consists in Pt salts which have been grown directly on the graphene, therefore there is no presence of organic ligands on their surface. Therefore, visualization of single atoms on graphene is possible and straightforward. Some adsorbates are partially covering graphene; the area covered by adsorbates is relatively smaller as compared with our deposition of semiconductor NCs in solution. Large areas of pristine graphene are present.

Appendix F

STEM-EELS

STEM-EELS applied to those kinds of semiconductor NCs has been tested on CZTS QD (sample 7 of chapterF 3). The goal of the study is trying to quantify the composition of atomic columns: it would be a further confirmation of the presence of PMCA structure, and distinguishing between kesterite and stannite would be feasible. Moreover, by using a monochromated microscope and a high-resolution spectrometer, it is possible to identify the oxidation state of cations.

The study was performed on an aberration-corrected FEI Titan STEM operating at 200 keV. The probe semi-convergence angle was 21 mrad. A Gatan Tridiem spectrometer with a 100 mrad semi-collection angle was used for the EELS measurement. The energy loss range of the EELS spectrum contains the Cu and Zn L-edges at energy loss of $\approx$ 931 and $\approx$ 1020 eV: hence, there is some overlap between the two L-edges. Sn M-edge and O K-edge have a lower energy loss (433 and 474 eV), but they can be included. A significant issue in this study is finding the ratio between maximising the beam current and avoiding destruction of NCs; at the same time, the signal is needed, with low noise, to detect the edge. This ratio is tough to find. In effect, it is very easy to create a hole in the Cu_2ZnSnS_4 NCs. The output of a STEM-EELS experiment consists in a spectrum map, and a corresponding DF image. In particular, we analysed well-oriented NCs which showed a contrast in the atomic columns to solve cation disorder (i.e. confirm that Sn is effectively in the bright columns, and analyse Cu and Sn distribution). Principal component analysis (PCA), non-negative matrix factorisation (NMF) and blind source separation (BSS) available in the multi-dimensional data analysis toolbox Hyperspy [208] were used to de-noise the spectra and find the principal independent components, corresponding to elemental signals.

Figure F.1 shows one of the best acquisitions. Figure F.1a shows the survey plan of a CZTS NC, showing a contrast in the atomic columns. Some holes were induced by previous acquisition with too long exposure time. Figure F.1b represents the DF signal, acquired alongside the EELS acquisition. The atomic column intensities are visible, with some variations presumably due to the Sn cations. Figure F.1c shows the spectrum image: the position of the atomic columns does not correspond to the intensity in any of the energy gaps. The EELS signal in figure F.1d is noisy, and the number

of electrons for each channel is low. Principal component analysis cannot recognise physically significant components which could indicate the signals from the elements: there is only one component with a high variance, which corresponds to the background, as shown in figure F.1e.

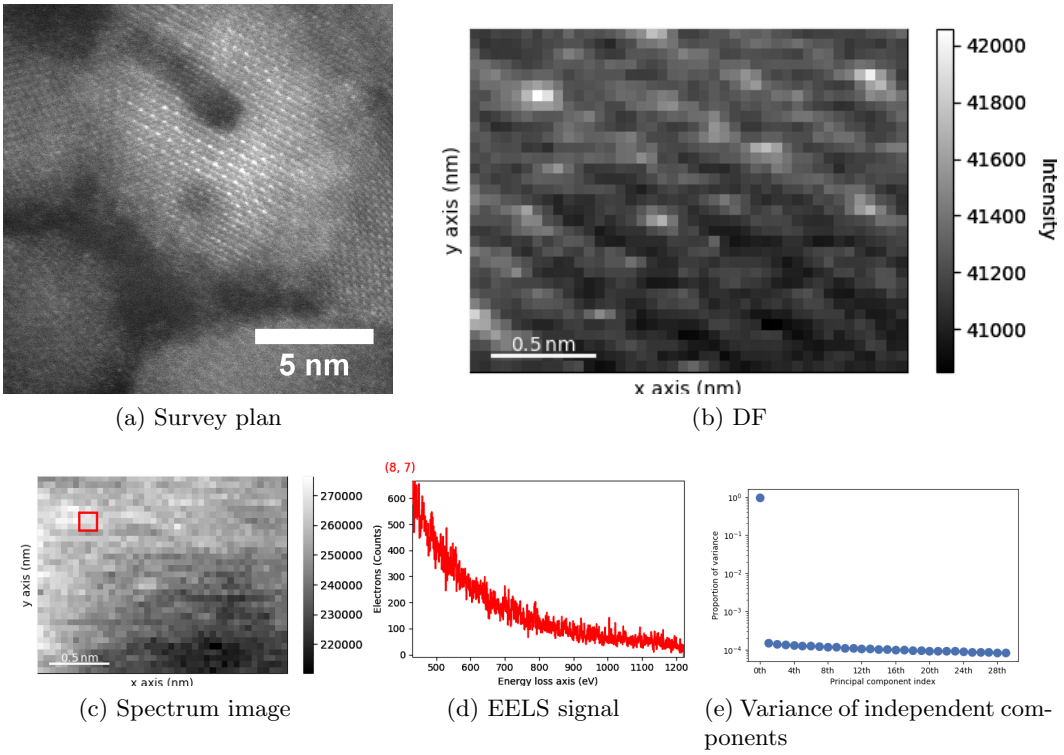

(a) Survey plan (b) DF

(c) Spectrum image (d) EELS signal (e) Variance of independent components

Figure F.1 – EELS experiment on CZTS NCs.

Several other STEM-EELS acquisitions were taken but are not shown here. When trying to push towards atomic columns resolution, a hole in the sample was created, or an insufficient signal was acquired. Tests performed at low resolution indicate that the acquisition time for one pixel in the spectral image should be in the order of one second, to obtain a good signal-to-noise ratio (SNR) at energies higher than 900 eV; this value is not compatible with fragile NCs.

Appendix G

Additional STEM-EDS acquisitions in CZTS synthesis

Sample 1

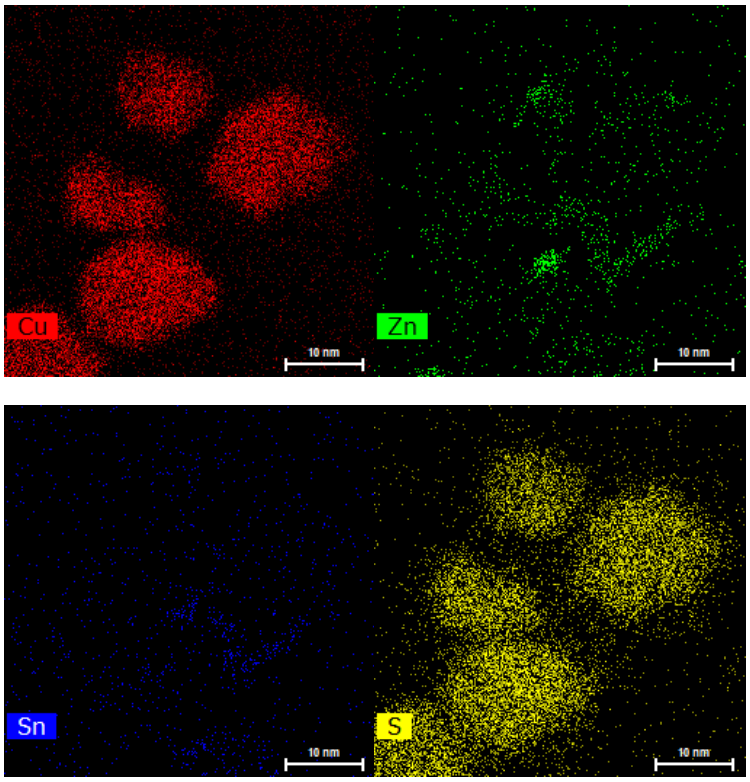

Figure G.1 – Elemental mapping (Cu-K_α, Zn-K_α, Sn-L_α and S-K_α) of sample 1.

Sample 4

Five NCs having a diameter around 10 nm are observed and a spectral STEM-EDS mapping acquired in figure G.2. The shape appears to be quite irregular. Qualitatively, NCs look homogeneous, with the exception of Zn distribution, where some inhomogeneities are present: some zones look richer in Zn.

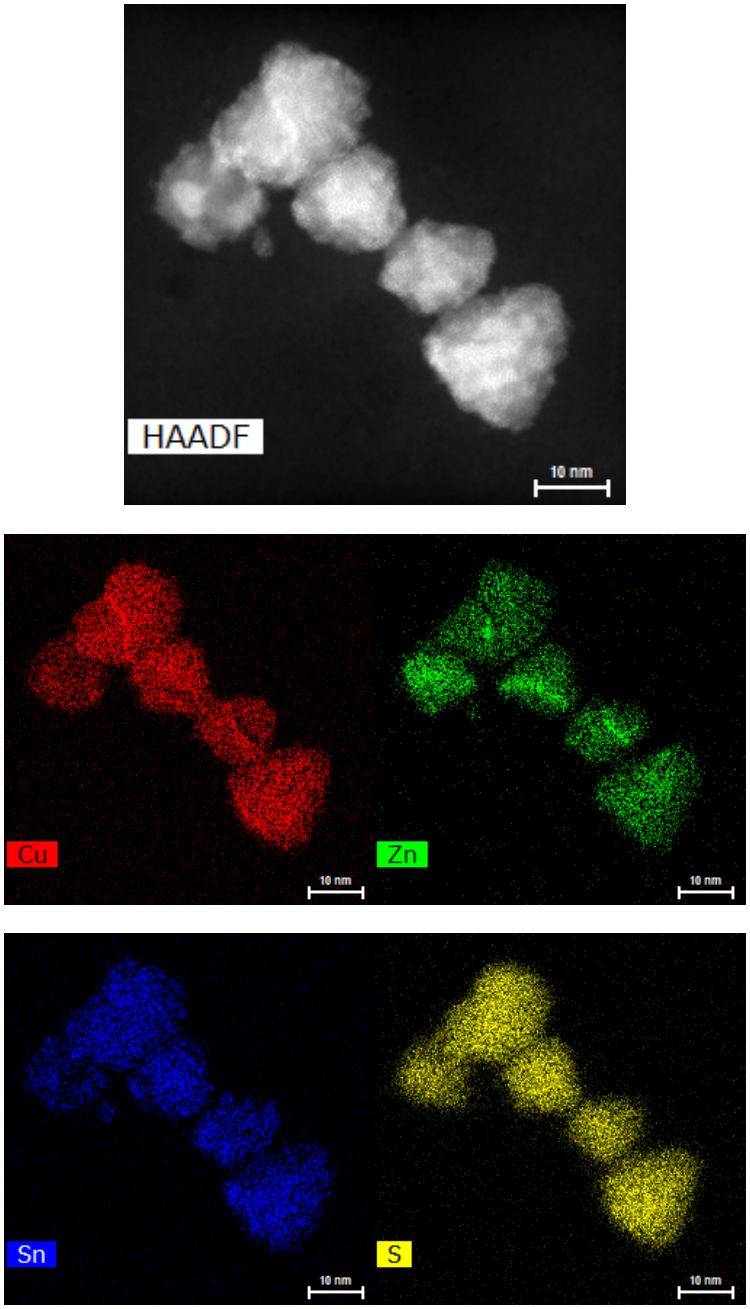

Figure G.2 – Five NCs and their elemental mapping (Cu-K_α, Zn-K_α, Sn-L_α and S-K_α).

Figure G.1 shows the quantification of the homogeneous NC, denominated "full NC centre", and the two NC which show chemical segregation (they are only partially included in the scanning area). The full NC centre is equivalent to $Cu_{2.27}Zn_{0.89}Sn_{1.16}S_4$; top left NC corresponds to $Cu_{2.20}Zn_{0.94}Sn_{1.24}S_4$, while top right NC corresponds to $Cu_{2.06}Zn_{0.84}Sn_{1.28}S_4$.

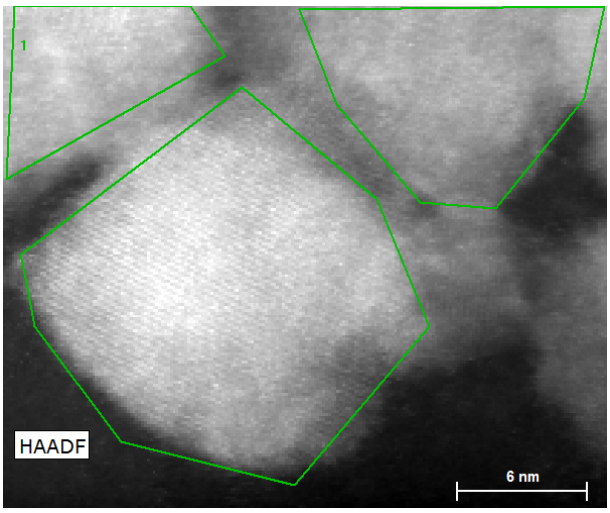

Atomic concentration [%]				
Label spectrum	Cu	Zn	Sn	S
Full NC centre	25.18	10.27	15.66	48.89
top left NC	27.26	10.72	13.98	48.05
top right NC	26.25	11.29	14.74	47.72

Table G.1 – Quantification of the homogeneous NC and of the two NC which show chemical segregation.

Sample 5

The NCs shown in figure G.3 are very close the one with each other, therefore only an overall quantification is presented (table G.2), equivalent to $Cu_{2.06}Zn_{0.84}Sn_{1.28}S_4$.

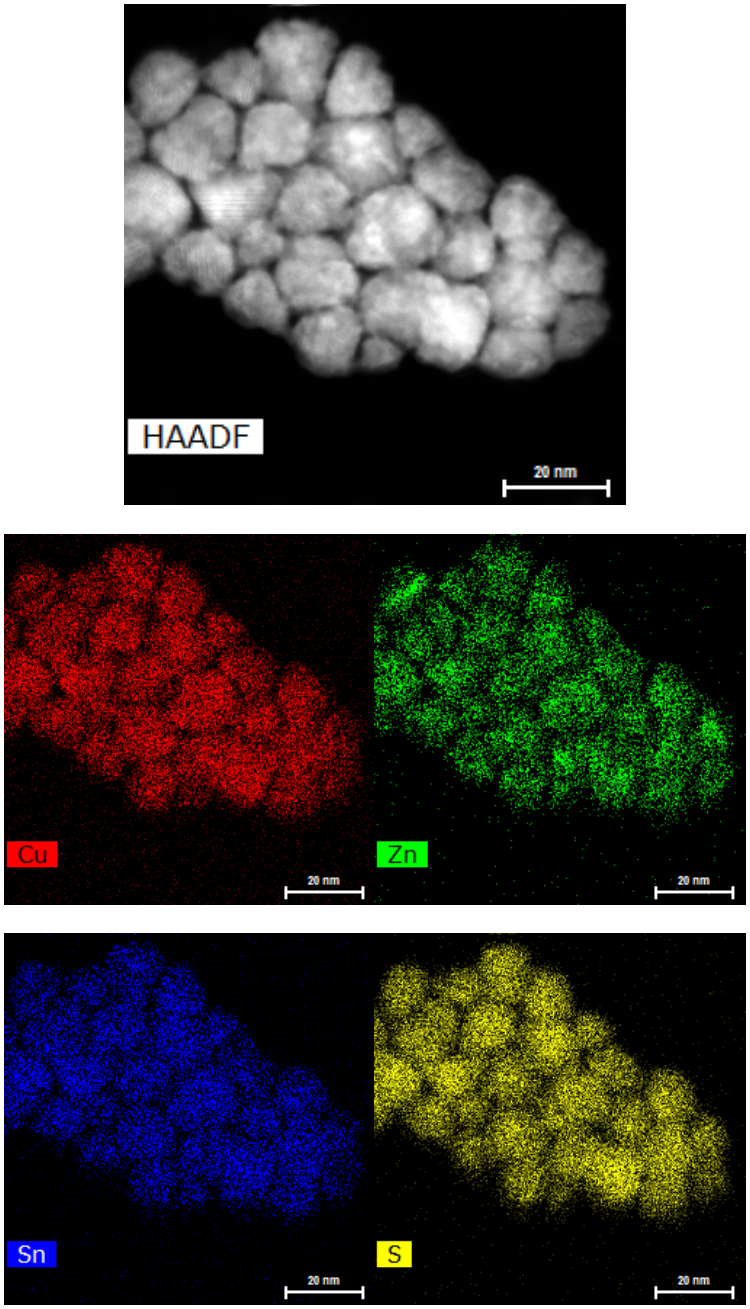

Figure G.3 – General plan and elemental mapping (Cu-K_α, Zn-K_α, Sn-L_α and S-K_α) for the intermediate reaction sample 5.

Overall composition		
Element	Atom C. [at %]	Rel. error (σ)
Cu	29.51	3.11
Zn	11.01	3.30
Sn	16.01	10.10
S	43.47	3.13

Table G.2 – Overall quantification.

Sample 7

A qualitative line profile of the crystal in the centre of the image is presented in figure G.4. It has a Zn-rich band in the middle.

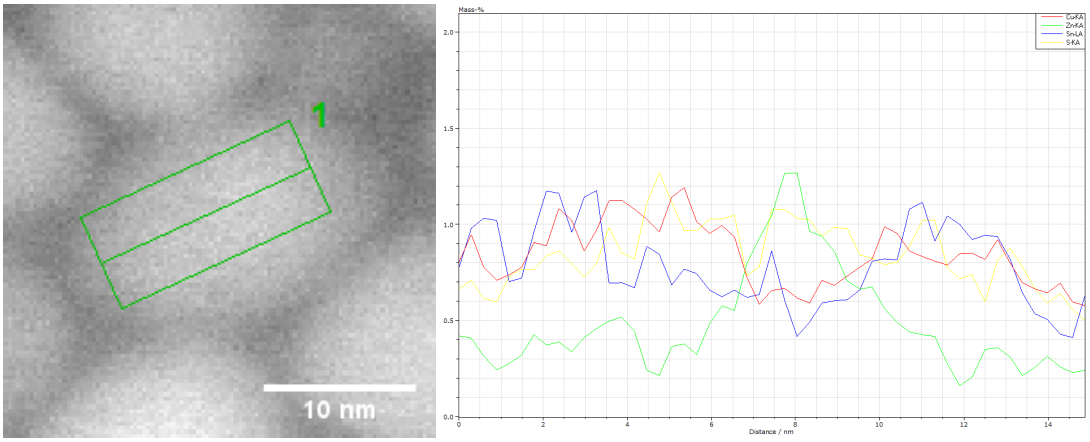

Figure G.4 – Line profile of the crystal in the centre of the image.

Appendix H

Additional STEM-HAADF simulations

Here we show additional STEM-HAADF simulations of kesterite and PMCA Cu_2ZnSnS_4 structures, with the microscope parameters reported in table 3.18. In particular, the presented micrographs investigate the influence of thickness over the possibility of visualizing the intensity pattern due to the heaviest atoms in the structure (in this case, Sn). We notice that in the considered range of thickness, the intensity pattern due to Sn atoms is always visible. The intensity is slightly increasing with the thickness.

Simulations have been performed for different values of camera length available in our equipment, both in DF and in HAADF mode. Camera lengths were selected between 46 mm to 460 mm. For 46 mm camera length, the DF ranges from 22.9 mrad to 52.0 mrad, and the HAADF detector ranges from 119.8 mrad to 148.5 mrad; for 460 mm camera length, DF detector ranges from 2.4 mrad to 5.4 mrad while HAADF detector ranges from 12.5 mrad to 58.3 mrad. The detector and the camera length chosen for the acquisition (HAADF, 115 mm; acquisition angles 51.3 mrad to 173.9 mrad) for the Cu_2ZnSnS_4 NCs is quite a standard one and ensures a good contrast between the Sn-rich atomic columns and the other columns.

Quantitative measurements and the reconstruction of the atom position from a single or from two STEM-HAADF images (discrete tomography) has been reported for metallic NCs, for binary NCs, and for core-shell structures [209–211]. In our case, this approach has not been attempted, as Cu and Zn are almost indistinguishable in imaging mode.

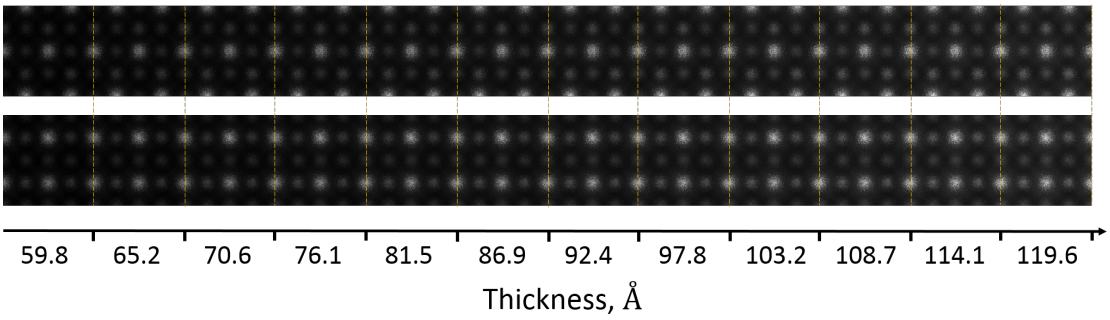

(a)

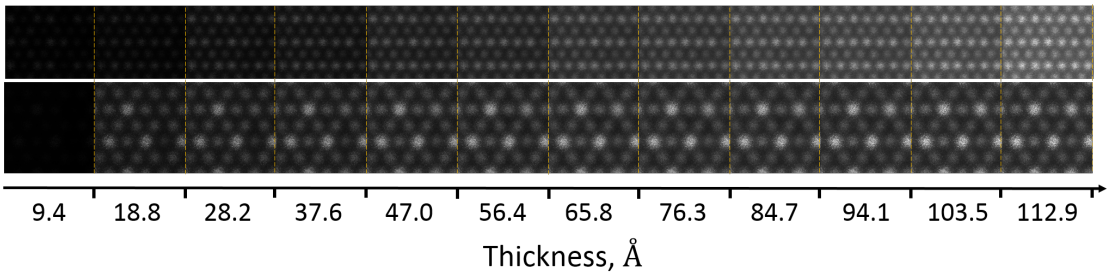

(b)

Figure H.1 – Influence of thickness in STEM-HAADF imaging of (a) [1 0 0] zone axis (top: kesterite, bottom: PMCA) and of (b) [2 2 1] zone axis (top: kesterite, bottom: PMCA; different scalebar).

Appendix I

Perovskite structure

Perovskite is a calcium titanium oxide mineral with chemical formula $CaTiO_3$. In crystallography this name is extended to the class of compounds which have the same type of crystal structure as $CaTiO_3$, with a general formula ABX_3. Many of these materials possess interesting properties such as ferroelectricity, piezoelectricity as well as non linear optical behaviour. In figure I.1 the basic perovskite cubic unit cell is displayed: it consists of corner-linked octahedra of X anions (usually oxygen or halogen atoms) with B cations at their centre and A atoms between them. The A cations are structural templates and their shape, size and charge distribution are essential for the stabilisation of the perovskite structure. The ideal structure here described is found in materials like

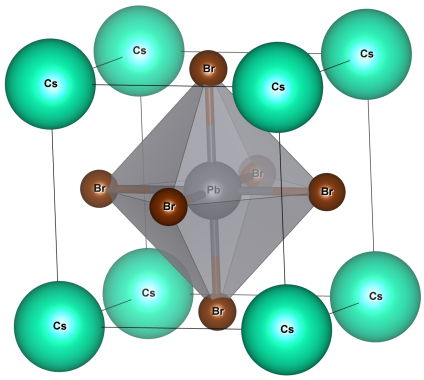

Figure I.1 – Structural model of a cubic perovskite.

$SrTiO_3$[1] at room temperature; the ideal structure can be modified by cation displace-

[1] $SrTiO_3$, a non-magnetic wide-band gap semiconductor, is a foundational material in the emerging field of complex oxide electronics. It is an excellent substrate for epitaxial growth of high-temperature superconductors and many oxide-based thin films

ment, as in $BaTiO_3$[2] or by the tilting of the octahedra as in $CaTiO_3$, or by a combination of the two as in $NaNbO_3$[3]. Cation displacements are directly linked with ferroelectricity and antiferroelectricity in these materials, and do not directly affect the lattice parameters except for a relatively small distortion of the octahedra. The various tilt systems and their effect on symmetry have been classified by Glazer [152].

The Goldschmidt tolerance factor is a parameter that can theoretically give indications about the final structure of a perovskite:

$$t = \frac{r_A + r_X}{\sqrt{r_M + r_X}} \tag{I.1}$$

where r_A, r_B and r_X are the radii of the respective ions in the AMX_3 formula. Various single charged organic or inorganic A cations ($CH_3NH_3^+$ or Cs^+), divalent B cations (Pb^{2+} or isoelectronic but oxidatively unstable Sn^{2+}) and single-valent anion X^- can be combined in this kind of structure as long as the Goldschmidt tolerance factor is in the range 0.8-1, below which 1D or 2D structures are more likely. With comparison to perovskite oxides, these materials show high ionic mobilities for halide ions and moderate mobilities for A cations, with low mobility for B cations, due to the lower charge of constituting elements. The melting point is lower, and they can be formed at a relatively low temperature. Nevertheless, only specific combinations of elements are allowed. Halide anions (Cl^-, Br^-, I^-) have a smaller negative charge than oxides, so only metal ions in lower oxidation state can compensate the charge. Moreover, halides are larger, so small metal cations do not incorporate in an octahedral geometry. Because of these restrictions B^{II} metal anion is selected between alkaline earths, bivalent rare earths and the heavier group 14 elements such as Ge^{2+}, Sn^{2+}, Pb^{2+}. Surprisingly, no transition metal can adopt the halide perovskite structure, except Mn. The only three A cations which stabilise perovskite halides are the organic methylammonium cation $CH_3NH_3^+$ and formamidinium cation $HC(NH_2)_2^+$, which are the constituents of the hybrid perovskite class. Cs^+ is the only elemental cation capable of stabilising a full-inorganic perovskite structure.

The band gap can be easily tuned by making solid solutions on the B or X sites, only if these two elements are immediate neighbours in the periodic table. The band gap is modified and seems to follow Vegard's law[4] in the case of a true $ABX'_{3-x}X_x$ solid solution. As an example:

$$E_{g,\mathrm{CsPb(Br_{1-x}I_x)_3}} = (1-x)E_{g,\mathrm{CsPbBr_3}} + xE_{g,\mathrm{CsPbI_3}} \tag{I.3}$$

[2] $BaTiO_3$ is a dielectric ceramic used for capacitors, and in the past used as piezoelectric material for microphones and transducers.

[3] $NaNbO_3$ is of technological importance due to applications in lead-free piezoelectric devices and high-temperature capacitors.

[4] Vegard's law is an empirical law which states that the lattice parameters of a solid solution are approximately equal to a rule of mixtures of the two constituent's lattice parameters at the same temperature:

$$a_{A_{1-x}B_x} = (1-x)a_A + xa_B \tag{I.2}$$

This simple linear relationship can be used for other crystal parameters, such as the band gap.

therefore, the band gap energies can be tuned over the whole visible spectrum by simply adjusting the ratio Cl/Br or Br/I. On the contrary, this control is not possible with chalcogenide NCs, where the band gap is tuned by the size of the crystals below the material-related exciton Bohr radius (quantum confinement effect) and their photoluminescence quantum yield enhanced by forming nanostructures such as core-shell structures.

I.1 FFTs from single NCs from HRTEM micrographs

Figure I.-2 shows all the FFTs obtained from HRTEM micrographs and calculated over single NCs. Most of them show a diffraction pattern typical of the $Pm\overline{3}m$ cubic structure, and approximately 19% show additional spots (in this case, the FFT is cased in green squares).

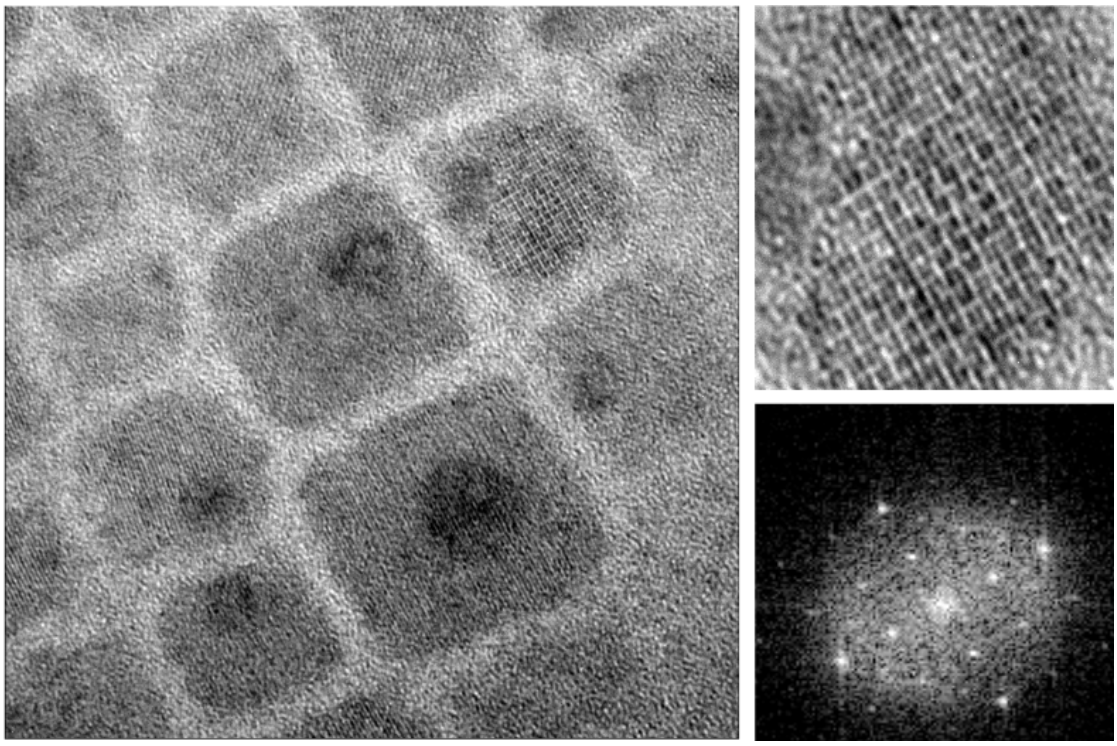

(a)

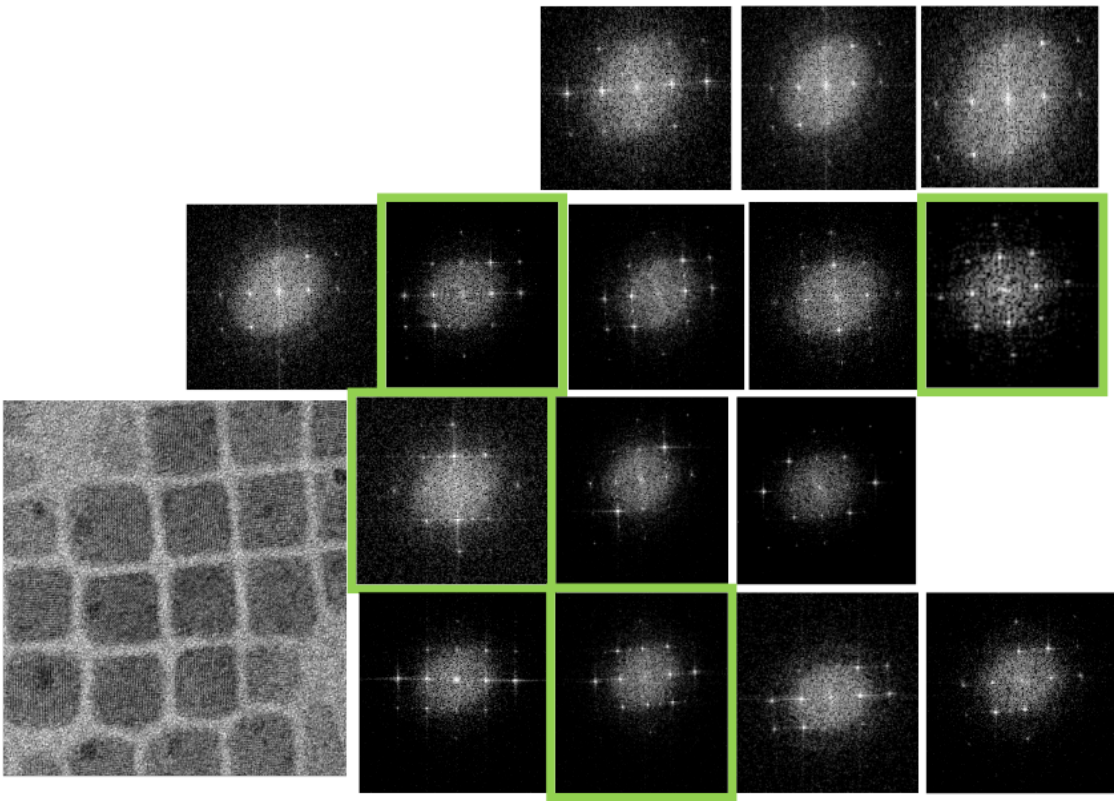

(b)

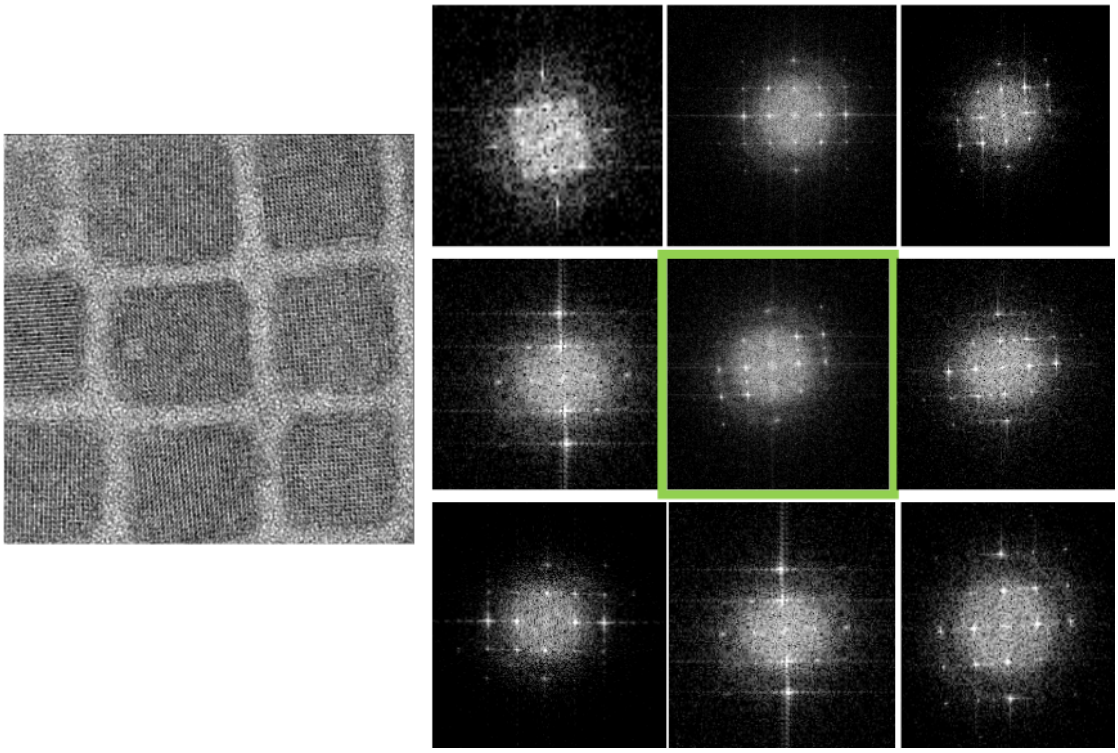

(c)

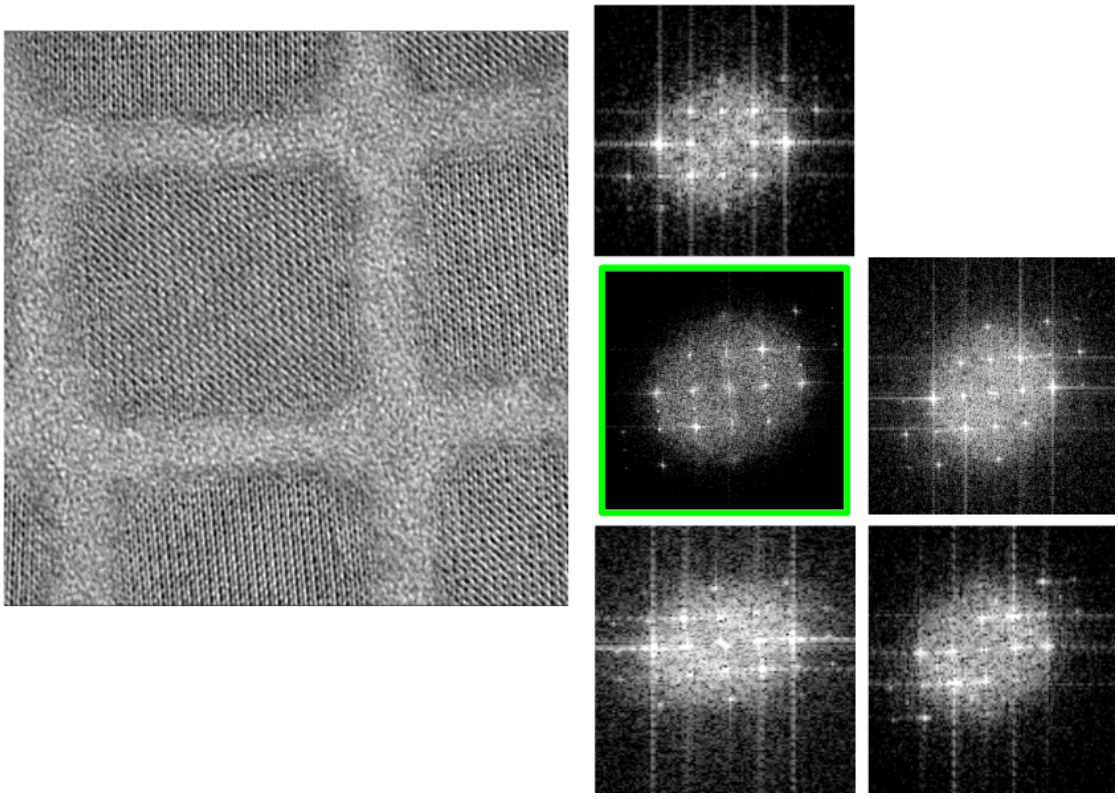

(d)

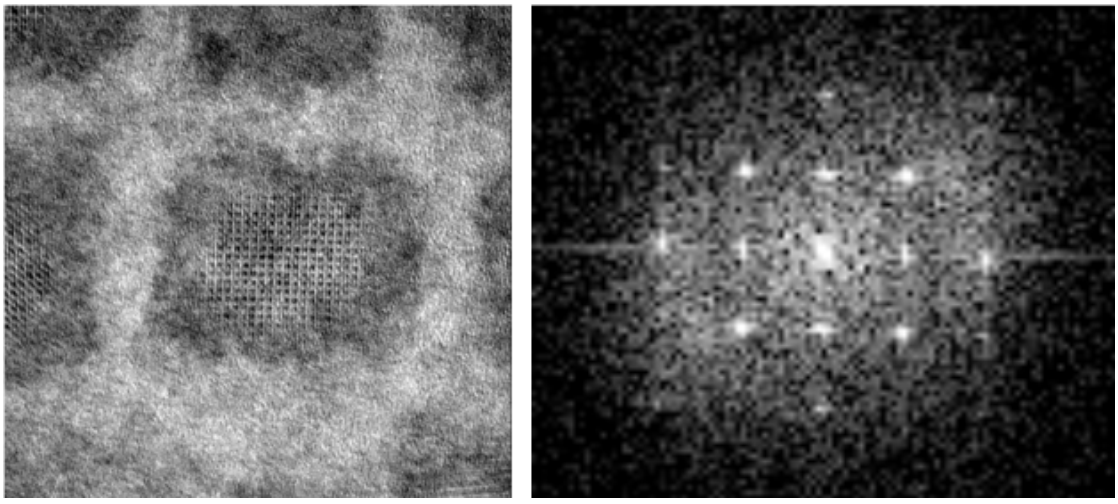

(e)

Figure I.-2 – HRTEM micrographs and calculated FFT from single NCs.

Figure I.-1 shows the FFT which have additional peaks due to the breaking of the cubic symmetry. The recognized additional spots are surrounded in light blue for clarity. Reflections are of the type $h + \frac{1}{2}$, k, 0, with a general extinction of the 0, $k + \frac{1}{2}$, 0. However, not all the reflections typical of the $Pnma$ orthorhombic structure (figure 4.5a) are observed in the same digital diffraction pattern.

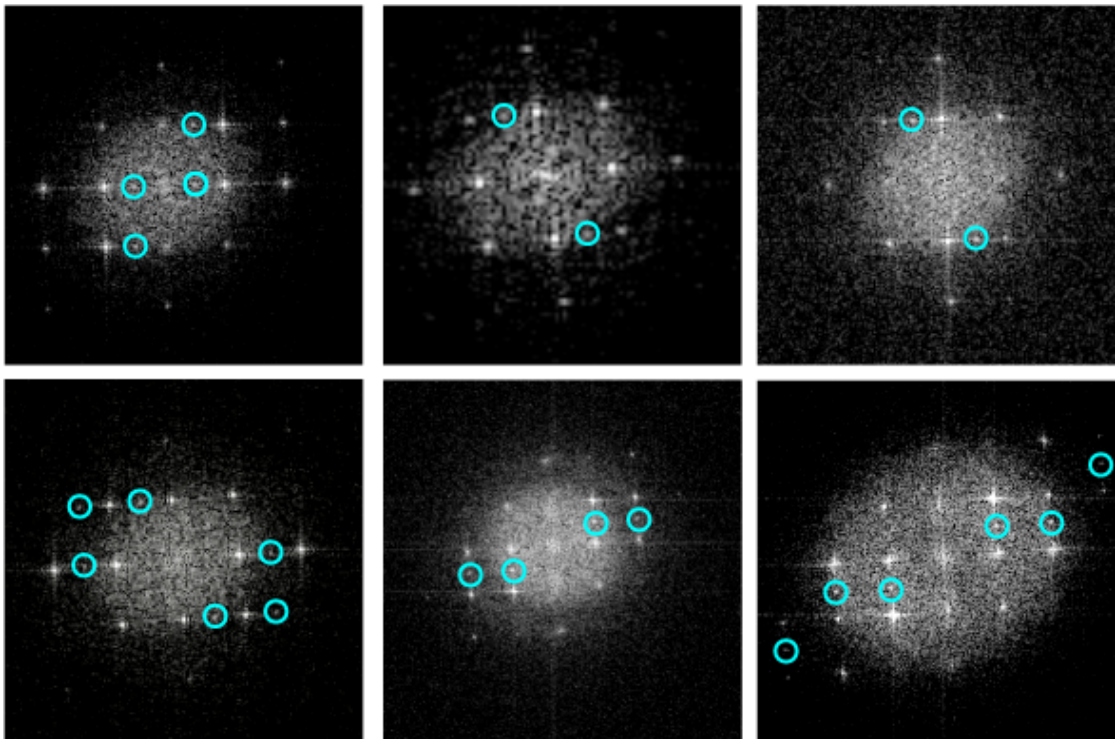

Figure I.-1 – HRTEM micrographs and calculated FFT from single NCs which show additional peaks with respect to the $Pm\overline{3}m$ cubic pattern.

I.2 Structure factors from cubic and orthorhombic $CsPbBr_3$

Here are listed the calculated structure factors for cubic $Pm\overline{3}m$ (table I.1) and for orthorhombic $Pnma$ $CsPbBr_3$ (table tab:OrthorhombicstructurefactorCsPbBr3).

h	k	l	d_{hkl} [Å]	F_{hkl} [Å]
1	0	0	5.8445	6.0960
1	1	0	4.1327	13.6127
1	1	1	3.3743	15.0693
2	0	0	2.9223	30.3293
2	1	0	2.6137	5.3095
2	1	1	2.3860	9.4510
2	2	0	2.0663	23.2160
3	0	0	1.9482	4.3264
2	2	1	1.9482	4.3264
1	3	0	1.8482	7.6646
1	3	1	1.7622	8.6134
2	2	2	1.6872	19.0770
3	2	0	1.6210	3.7191
2	1	3	1.5620	6.5594
4	0	0	1.4611	16.3533
2	2	3	1.4175	3.2971
4	1	0	1.4175	3.2971
4	1	1	1.3776	5.7819
3	3	0	1.3776	5.7819
1	4	1	1.3776	5.7819
0	3	3	1.3776	5.7819
1	3	3	1.3408	6.0805
4	2	0	1.3069	14.4008

Table I.1 – Structure factor for cubic $Pm\bar{3}m$ $CsPbBr_3$ structure.

h	k	l	d_{hkl} [Å]	F_{hkl} [Å]
0	1	0	11.7650	0.0000
1	0	0	8.2609	0.0000
0	0	1	8.2124	0.0000
1	1	0	6.7607	0.0000
0	1	1	6.7341	3.3053
0	2	0	5.8825	21.8350
1	0	1	5.8241	20.3040
1	1	1	5.2196	6.6017
1	2	0	4.7918	0.0000
0	2	1	4.7822	0.0000
1	2	1	4.1388	51.3309
2	0	0	4.1304	59.4001
0	3	0	3.9217	0.0000
2	1	0	3.8972	7.7527
0	1	2	3.8769	0.0000
2	0	1	3.6900	22.1387
1	0	2	3.6770	21.6165
1	3	0	3.5427	0.0000
0	3	1	3.5389	23.0586
2	1	1	3.5209	9.6756
1	1	2	3.5096	15.9673
2	2	0	3.3804	49.4717
0	2	2	3.3670	48.8697
1	3	1	3.2530	11.3922
2	2	1	3.1259	21.2044
1	2	2	3.1180	19.4284
0	4	0	2.9413	114.3471
2	0	2	2.9121	104.8446
2	3	0	2.8440	18.8442
0	3	2	2.8360	0.0000
2	1	2	2.8268	12.2054
1	4	0	2.7709	0.0000
0	4	1	2.7690	0.0000
3	0	0	2.7536	0.0000
0	0	3	2.7375	0.0000
2	3	1	2.6874	9.8216
1	3	2	2.6824	10.1818
3	1	0	2.6812	0.0000
0	1	3	2.6662	13.0024
1	4	1	2.6254	18.8375
3	0	1	2.6108	31.9778
2	2	2	2.6098	14.4376
1	0	3	2.5985	23.5170
3	1	1	2.5488	16.6829
1	1	3	2.5374	9.0963
3	2	0	2.4939	0.0000
0	2	3	2.4819	0.0000
2	4	0	2.3959	47.0817

h	k	l	d_{hkl} [Å]	F_{hkl} [Å]
0	4	2	2.3911	45.5945
3	2	1	2.3863	41.2982
1	2	3	2.3769	49.1419
0	5	0	2.3530	0.0000
2	3	2	2.3380	1.0927
2	4	1	2.3000	13.0843
1	4	2	2.2968	12.8832
3	0	2	2.2870	11.4555
2	0	3	2.2818	14.2072
1	5	0	2.2630	0.0000
0	5	1	2.2620	18.7735
3	3	0	2.2536	0.0000
3	1	2	2.2450	8.6292
0	3	3	2.2447	1.9168
2	1	3	2.2401	5.3366
1	5	1	2.1817	0.9204
3	3	1	2.1732	11.2872
1	3	3	2.1661	5.3011
3	2	2	2.1316	9.1919
2	2	3	2.1274	8.7262
2	4	2	2.0694	76.5536
4	0	0	2.0652	69.1749
0	0	4	2.0531	67.5900
2	5	0	2.0445	4.2587
0	5	2	2.0416	0.0000
4	1	0	2.0341	17.2718
0	1	4	2.0225	0.0000
3	4	0	2.0102	0.0000
0	4	3	2.0039	0.0000
4	0	1	2.0029	26.5707
1	0	4	1.9925	24.7568
2	5	1	1.9840	19.0716
1	5	2	1.9819	12.7992
3	3	2	1.9756	14.5732
4	1	1	1.9745	1.3020
2	3	3	1.9723	14.6110
1	1	4	1.9645	16.0217
0	6	0	1.9608	5.7177
3	4	1	1.9525	24.5899
4	2	0	1.9486	5.6188
1	4	3	1.9474	18.0095
3	0	3	1.9414	0.4064
0	2	4	1.9384	9.8335
3	1	3	1.9155	9.6770
1	6	0	1.9078	0.0000
0	6	1	1.9072	0.0000
4	2	1	1.8960	21.5929
1	2	4	1.8872	21.5127

h	k	l	d_{hkl} [Å]	F_{hkl} [Å]
1	6	1	1.8583	29.7604
4	0	2	1.8450	40.6090
3	2	3	1.8436	17.7549
2	0	4	1.8385	37.5736
2	5	2	1.8302	15.1478
4	3	0	1.8273	0.8542
4	1	2	1.8227	8.7135
0	3	4	1.8189	0.0000
2	1	4	1.8165	5.6004
3	4	2	1.8054	7.4757
2	4	3	1.8029	9.5005
3	5	0	1.7889	0.0000
0	5	3	1.7844	18.7100
4	3	1	1.7837	7.2053
1	3	4	1.7764	18.4269
2	6	0	1.7714	20.3977
0	6	2	1.7694	19.8967
4	2	2	1.7604	10.3666
2	2	4	1.7548	9.5568
3	5	1	1.7479	14.2316
1	5	3	1.7442	16.1199
3	3	3	1.7399	15.9844
2	6	1	1.7315	8.2031
1	6	2	1.7302	7.3791
4	4	0	1.6902	55.3073
0	4	4	1.6835	53.8383
0	7	0	1.6807	0.0000
4	3	2	1.6695	19.3366
2	3	4	1.6647	8.7441
4	4	1	1.6555	17.8185
5	0	0	1.6522	0.0000
1	4	4	1.6496	16.5028
4	0	3	1.6487	11.6058
1	7	0	1.6470	0.0000
3	0	4	1.6460	12.4306
0	0	5	1.6425	0.0000
3	5	2	1.6400	1.2039
2	5	3	1.6381	3.4276
5	1	0	1.6361	0.0000
4	1	3	1.6327	7.4424
3	1	4	1.6301	16.0460
0	1	5	1.6267	5.9745
2	6	2	1.6265	4.5227
3	4	3	1.6202	3.4347
5	0	1	1.6197	15.0462
1	7	1	1.6148	8.8565
1	0	5	1.6109	0.1561
5	1	1	1.6046	15.4450

h	k	l	d_{hkl} [Å]	F_{hkl} [Å]
3	6	0	1.5973	0.0000
1	1	5	1.5961	0.2181
0	6	3	1.5941	0.0000
5	2	0	1.5906	0.0000
4	2	3	1.5875	16.2251
3	2	4	1.5851	13.2100
0	2	5	1.5820	0.0000
3	6	1	1.5679	26.9557
1	6	3	1.5652	32.1678
4	4	2	1.5630	36.0405
5	2	1	1.5616	14.5024
2	4	4	1.5590	33.7054
2	7	0	1.5568	16.1084
0	7	2	1.5555	0.0000
1	2	5	1.5537	28.4724
4	5	0	1.5522	24.1253
0	5	4	1.5470	0.0000
5	0	2	1.5328	0.8650
2	7	1	1.5295	13.3450
1	7	2	1.5286	4.5780
2	0	5	1.5262	0.1210
4	5	1	1.5252	3.5861
5	3	0	1.5226	0.0000
1	5	4	1.5206	9.1860
5	1	2	1.5199	8.4006
4	3	3	1.5198	3.2837
3	3	4	1.5177	5.9148
0	3	5	1.5150	8.1082
2	1	5	1.5136	6.9886
3	5	3	1.4975	1.9561
5	3	1	1.4971	14.7076
1	3	5	1.4901	11.8290
3	6	2	1.4886	3.7314
2	6	3	1.4872	3.1405
5	2	2	1.4832	1.7490
2	2	5	1.4773	4.2975
0	8	0	1.4706	51.5730
4	0	4	1.4560	38.4901
2	7	2	1.4557	3.4463
4	5	2	1.4519	1.9373
2	5	4	1.4487	1.5852
1	8	0	1.4479	0.0000
0	8	1	1.4476	0.0000
4	1	4	1.4450	10.9216
5	4	0	1.4405	0.0000
4	4	3	1.4381	7.5108
3	4	4	1.4363	8.4127
3	7	0	1.4346	0.0000

h	k	l	d_{hkl} [Å]	F_{hkl} [Å]
0	4	5	1.4340	0.0000
0	7	3	1.4323	7.1519
5	3	2	1.4276	1.5143
1	8	1	1.4259	12.6794
2	3	5	1.4223	4.4648
4	6	0	1.4220	2.0858
5	4	1	1.4188	14.3871
0	6	4	1.4180	4.6503
5	0	3	1.4145	30.1508
4	2	4	1.4134	6.6471
3	7	1	1.4132	5.7152
1	4	5	1.4129	1.3721
1	7	3	1.4112	9.3589
3	0	5	1.4106	22.3503
5	1	3	1.4044	13.0473
4	6	1	1.4011	9.1518
3	1	5	1.4006	9.6291
1	6	4	1.3976	9.3518
2	8	0	1.3854	36.5572
0	8	2	1.3845	35.8903
3	6	3	1.3796	17.7853
6	0	0	1.3768	37.1290
5	2	3	1.3753	33.6029
3	2	5	1.3717	41.7617
0	0	6	1.3687	32.0493
6	1	0	1.3675	8.2662
2	8	1	1.3661	2.5818
1	8	2	1.3655	2.7366
4	3	4	1.3650	5.3795
0	1	6	1.3596	0.0000
5	4	2	1.3593	0.5196
6	0	1	1.3579	16.5959
2	4	5	1.3547	0.2898
3	7	2	1.3543	12.8574
2	7	3	1.3532	14.2622
5	5	0	1.3521	0.0000
1	0	6	1.3503	17.2312
4	5	3	1.3502	8.7571
6	1	1	1.3489	1.7034
3	5	4	1.3487	19.8294
0	5	5	1.3468	2.7360
4	6	2	1.3437	4.4299
1	1	6	1.3415	14.3791
2	6	4	1.3412	3.5899
6	2	0	1.3406	4.9336
5	5	1	1.3342	12.1221
0	2	6	1.3331	6.2602
5	3	3	1.3306	11.2230
1	5	5	1.3293	9.6194
3	3	5	1.3273	1.9715
6	2	1	1.3231	17.4911
1	2	6	1.3161	16.8851
2	8	2	1.3127	41.4600
0	9	0	1.3072	0.0000
6	0	2	1.3054	28.1063
4	4	4	1.3049	33.4910
4	7	0	1.3036	6.5022
0	7	4	1.3005	0.0000

Table I.2 – Structure factor for orthorhombic *Pnma* $CsPbBr_3$ structure.

Appendix J

Morphology and structural characterisation of $CuFeS_2$ nanocrystals and composite pellets

J.1 Introduction

Most of energy conversion mechanisms cause loss of thermal energy as high as 60% [212]. Thermoelectricity can transform this waste heat into electrical current. Thermoelectric modules can be used in several applications, such as heat recovery, cooling systems, or powering in nomad devices [213]. The efficiency of a thermoelectric device in generating electricity is described by η, defined as the ratio between the energy provided to the load and the heat energy absorbed at hot junction. Efficiency can be expressed as:

$$\eta = \frac{T_H - T_C}{T_H} \frac{\sqrt{1+\overline{ZT}} - 1}{\sqrt{1+\overline{ZT}} + \frac{T_C}{T_H}} = \eta_{Carnot} \frac{\sqrt{1+\overline{ZT}} - 1}{\sqrt{1+\overline{ZT}} + \frac{T_C}{T_H}} \tag{J.1}$$

where T_H and T_C represent the temperatures of hot and cold junctions. The ability of a given material to the efficient production of thermoelectric power is related to its dimensionless figure of merit ZT given by

$$ZT = \frac{\sigma S^2 T}{\kappa} \tag{J.2}$$

where S is the Seebeck coefficient, σ the electrical conductivity and κ the thermal conductivity. Consequently, to improve ZT, the materials must have a high electrical conductivity σ and a very low thermal conductivity κ. These quantities are usually related, as in conducting materials the charge carriers are also transporting a significant portion of heat. It is, therefore, challenging to select materials which are both excellent electrical conductors and poor thermal conductors.

In particular, chalcopyrite[1] $CuFeS_2$ has received a lot of attention for being abundant, cheap and chemically stable. Its band gap between 0.5 eV and 0.6 eV [214] is suitable

[1] Chalcopyrite designates both the class of material $CuMX_2$ and also more specifically the archetype

for thermoelectric conversion. Moreover, by adjusting the ratio of cations, the doping level of the material can be tuned: a *p*- or *n*-type material can be obtained for the same material class. Electrical conductivity and Seebeck coefficient depend strongly on the material and dopant concentrations.

Liang and Feng compared the thermoelectric properties of bulk and nanometer-sized $CuFeS_2$. The authors showed that the Seebeck coefficient of the material could be improved conspicuously by nanostructuration [215] (figure J.1). By reducing the size of $CuFeS_2$ NCs, the number of grain boundaries, which scatter phonons (their mean free path correspond to the distance between two grain boundaries), increases [216].

Previous examples in the literature show that stoichiometry of this nanomaterial must be controlled to maximise the Seebeck coefficient and the electrical conductivity (which are material properties). Stoichiometry control can be obtained by changing the reagent ratios during the synthesis to obtain non-stoichiometric chalcopyrite.

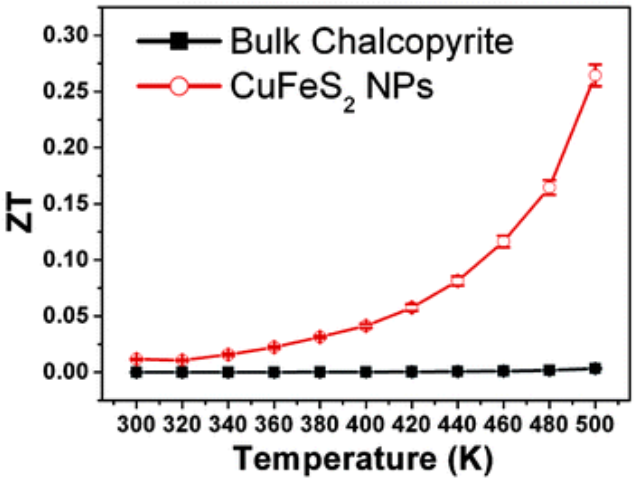

Figure J.1 – Temperature dependence of ZT of $CuFeS_2$ nanoparticles (red) and bulk chalcopyrite (black). Retrieved from [215]

The overall goal of this study is to synthesise and characterise nanostructured $CuFeS_2$, and to build a thermoelectric device. The final device must be stable and efficient at room temperature. Two colloidal synthetic procedure are presented in section J.2. TEM is used to describe the obtained morphology (section J.3) and the crystalline structure (section J.4). A significant amount of NCs are dried and hot pressed to build pellets to measure thermoelectric characteristics. A composite material is obtained by the addition of metallic NCs, resulting in improved thermoelectric properties. A test on the addition of Sn NCs to $CuFeS_2$ NCs is presented in J.5. An exploratory investigation by

mineral $CuFeS_2$. Chalcopyrite is a class of ternary materials containing one cation Cu^I and a second one which can be either Fe, Ga, In, Al. The anions providing charge stability are S, Se or Te. The general formula for a chalcopyrite is therefore $CuMX_2$, where M is a cation and X an halogenide (S^{2-}, Se^{2-}, Te^{2-}).

STEM-EDS allows the study of the distribution of Sn doping in $CuFeS_2$ material after sintering.

J.2 Synthesis and sample preparation

Several synthetic methods have been developed for $CuFeS_2$ NCs: hydrothermal methods [217] or in organic media [218, 219], some using oleylamine as solvent and ligand [71]. Generally, this material tends to form NCs with anisotropic nanostructures such as nanowires, nanorods, platelets, pyramids. Size and dispersion are challenging to control. The existing syntheses are not optimised for a large production, of several hundreds of milligrams of NCs: parameters are not mastered, and the resulting product features (size, shape) depend on the method used.

Two synthesis batches are developed by Louis Vaure during this study to obtain NCs of sizes between 30 and 50 nm with controlled stoichiometry [9].

Reactants are weighted in a glove box under Ar atmosphere, to protect against oxidation and humidity. The reaction is performed under vacuum or in an inert Ar atmosphere. The next two subsections briefly introduce these two methods.

J.2.1 Heat-up method

For the heat-up method, the metallic precursors are copper iodide (CuI) and iron acetylacetonate ($Fe(acac)_3$); the sulfur precursor is dodecanethiol (DDT) which also plays the role of ligand stabilizing the surface of NCs. DDT is co-solvent of the mixture, together with octadecene (ODE).

1 mmol of each cation precursor is introduced in a 50 mL three-neck round-bottom flask. 5 mL DDT and 5 mL ODE are added and mixed. The mixture is degassed under vacuum for 30 minutes, to eliminate oxygen from the reaction medium. Then the mixture is heated up at 100 °C under Ar to form metal-thiolate complexes which are the basis for crystal nucleation. After 1 h, vacuum is applied again to degas, then the mixture is rapidly warmed up at 230 °C under an Ar flux during 30 min. Afterwards the temperature is lowered down in order to quench crystal growth.

The synthesis yield from this procedure is 80%, with a product of approximately 200 mg NCs. The quantities of precursors and solvents can be scaled up to obtain up to 800 mg NCs in one synthesis.

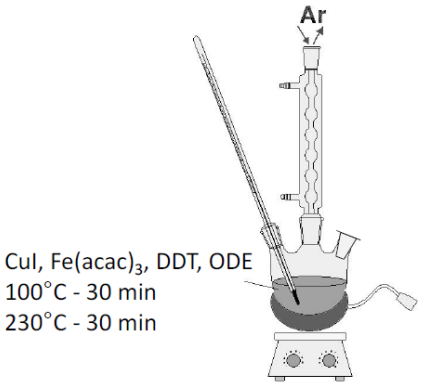

Figure J.2 – Setup for $CuFeS_2$ NCs synthesis by the heat-up method.

J.2.2 Hot-injection method

The second developed protocol is a hot-injection of the sulfur precursor, ammonium diethyldithiocarbamate, in a mixture of metal chlorides.

1 mmol $FeCl_3$ and of 1 mmol $CuCl_2$ are inserted in a three-neck round-bottom flask. Cu has an initial oxidation state Cu^{II} in the precursor form, and must be reduced during the process. Powders are dissolved in 18 mL DDT and 12 mL oleic acid. After an initial degassing under primary vacuum, the mixture is heated at 140 °C under Ar for one hour. After a fast degassing under vacuum, the sulfur precursors (1 mmol ammonium diethyldithiocarbamate dissolved in 6 mL DDT) is injected. Temperature is raised up at 280 °C for 15 min under Ar flux. Reaction is therefore quenched by fast cooling.

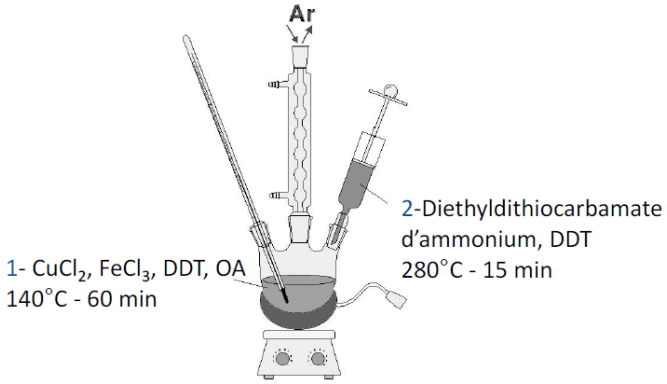

Figure J.3 – Setup for $CuFeS_2$ NCs synthesis by the hot-injection method.

The yield of this procedure is about 50% with up to 300 mg NCs obtained for each synthesis.

J.2.3 Purification

The washing of the NCs is the same for the two synthetic procedures. The solution is centrifuged at 8000 rpm for 5 min in the presence of methanol (5 mL:5 mL), to precipitate the NCs. The supernatant is eliminated, and NCs can be easily dispersed in chloroform or toluene. This process is repeated three times for eliminating ligands in excess and non-reacting species still present in the solution.

J.3 Morphology analysis of $CuFeS_2$ NCs by TEM

Two synthesis methods lead to NCs with different morphologies. Some NCs obtained by the heat-up method are displayed in figure J.4. The sample is polydisperse, with an average size > 20 nm. The large dispersion in size and the irregular shape of these

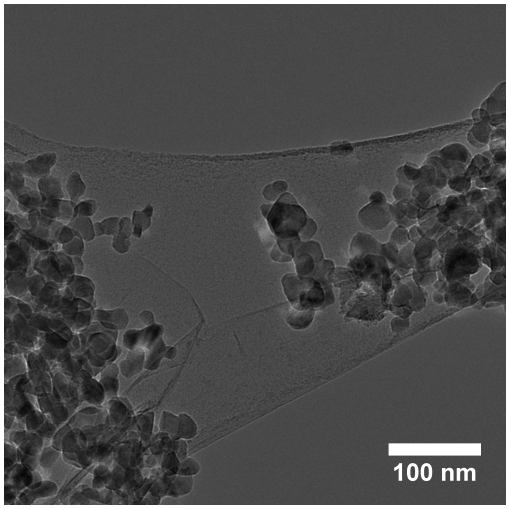

Figure J.4 – TEM-BF micrograph of $CuFeS_2$ NCs synthesized by heat-up method.

NCs can be explained by the low reactivity of the metal precursors with thiols. Also, the heating ramp to reach the highest temperature is not ideal, and heating is slower than desired. Smaller NCs are probably disappearing due to Ostwald ripening, a process where, because of thermodynamics reasons, the small particles dissolve, and their matter redeposit in favour of the growth of the larger NCs.

NCs obtained by the hot-injection method have a completely different morphology (figure J.5): their shape is well-defined; however the size dispersion is remarkably wide. These NCs are strongly anisotropic, shaped as quite regular hexagonal platelets. Their sizes vary from some tens to some hundreds of nanometers. It is possible to measure the thickness of these platelets, as they tend to pile up on the carbon support, as shown in figure J.5b. The ratio between thickness and lateral size is generally around $\frac{1}{5}$. The main interest of a hot-injection synthesis is to decouple nucleation and growth steps. Nevertheless, in this case, the advantage is minimal, as NCs are not monodispersed. The

separation between nucleation and growth steps would be more efficient if the change in temperature from 140 °C to 280 °C were faster.

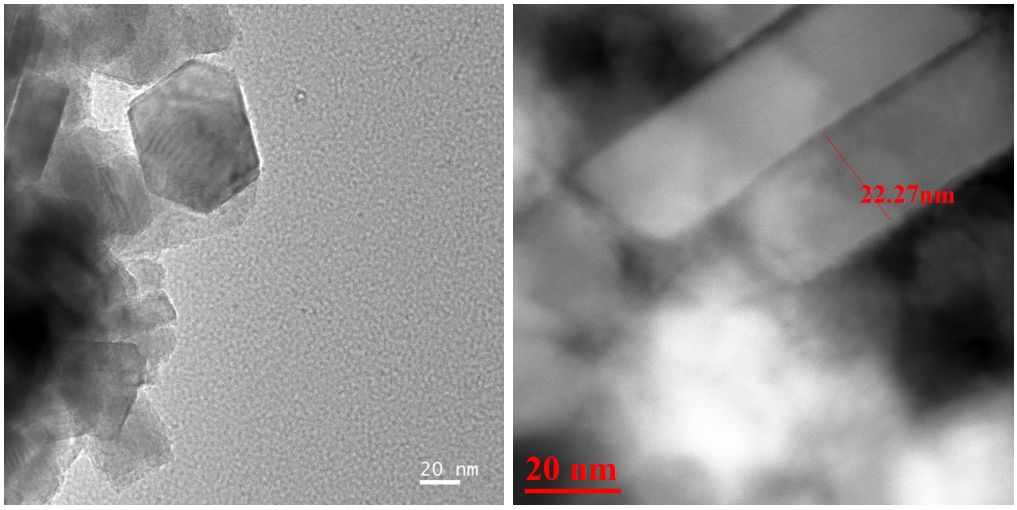

(a) HRTEM (b) STEM

Figure J.5 – (a) Top view and (b) lateral view of $CuFeS_2$ NCs synthesized by hot-injection method.

To summarise, the sizes of NCs prepared by both procedures are suitable for thermoelectric applications: they are small enough to reduce thermal conductivity through phonon scattering by grain boundaries. Their large size dispersion is not a drawback for this kind of applications. Nevertheless, the two processes have different scalability. The heat-up method provides gram-quantity of NCs. Therefore it is chosen to build pellets for thermoelectric devices, as presented in subsection J.5.1.

J.4 Structural analysis of $CuFeS_2$ nanocrystals by TEM

An extensive description of the structural characterisation performed on the products issued by the two synthesis paths of $CuFeS_2$ NCs can be found in [9]. X-ray powder diffraction, followed by Rietveld refinement, was used to determine the crystal structure. Predominantly, wurtzite structure is favoured for the heat-up method, whereas the tetragonal chalcopyrite is found in the hot-injection synthesis. After annealing, all the NCs show a tetragonal phase. As shown in figures J.4 and J.5, the NCs deposited on a TEM support grid strongly tend to agglomerate. It is rare to find isolated nanoparticles to perform an in-depth characterisation on single NCs.

The heat-up method leads to a population of irregular NCs. Morphological modelling is therefore not attractive, as each crystallite is very different from one another. On the other hand, the hot-injection method provides mostly platelets with a hexagonal shape and tetragonal chalcopyrite structure. A structural analysis is performed to identify the

crystalline facets of the NC. According to the facets which are favoured or inhibited in the growth, the anisotropy of the system can be explained. In the following, the different characterisations performed using TEM are presented.

J.4.1 Rotational average of FFT from several randomly oriented hot-injection NCs

By performing a digital Fourier Transform (FT) on an HRTEM image containing several NCs, several diffraction-like spots are obtained. By performing a rotational average of this FT, the result is comparable to the result of a powder diffraction experiment: some rings are therefore obtained. The radial profile of the obtained rings can be indexed as diffraction patterns from the chalcopyrite structure. Those are identified in a line profile from the rotational average of the FT in figure J.6.

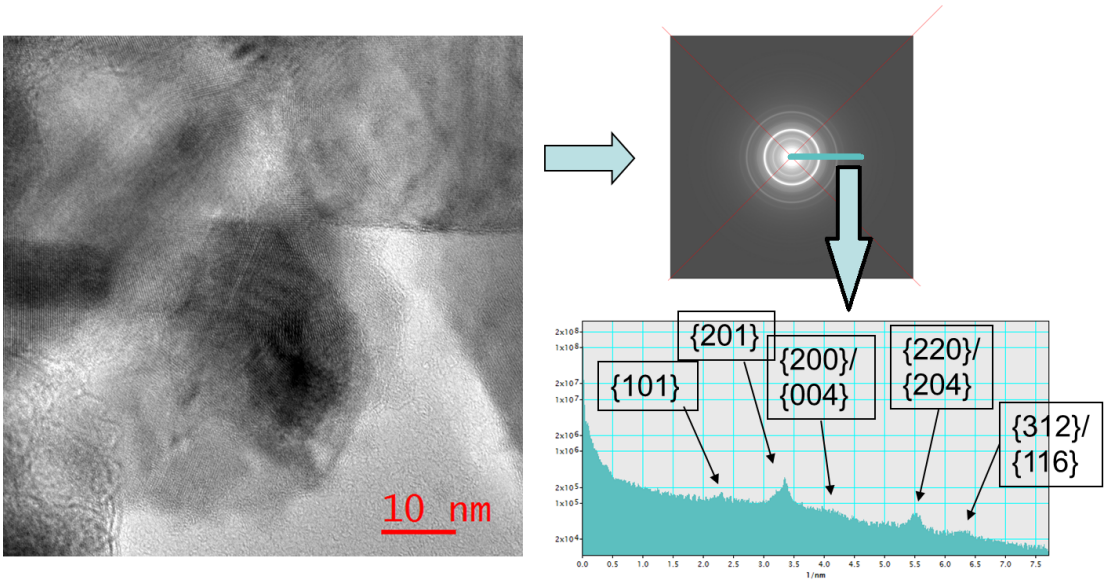

Figure J.6 – HRTEM image of several randomly-oriented NCs; rotationally averaged of FFT from the HRTEM image; radial profile of rotationally averaged FFT, with indexing from chalcopyrite structure.

Indexation of the diffraction-like rings corroborates the chalcopyrite structure for samples obtained by the hot-injection method, as demonstrated by powder X-ray diffraction [9]. In fact, simulated wurtzite $CuFeS_2$ reflections are not compatible with the experimental spacing of diffraction-like rings.

J.4.2 Modeling of hot-injection $CuFeS_2$ platelets

As seen in figure J.5a, $CuFeS_2$ platelets obtained by hot-injection tend to deposit with one of the hexagonal facet on the amorphous carbon ultrathin film. Despite the difference in size, all the observed hexagon-shaped platelet expose the same zone axis [1 1 0]. It is therefore straightforward to observe the diffraction pattern originated from this zone

axis and identify the lateral facets, in order to give a deeper insight in the homogeneous morphology of these platelets.

The hexagonal (wider) facets are parallel to (1 1 0) planes. The narrower lateral facets have been identified thanks to the angle between planes: {1 1 2}, {2 2 0} and {0 0 4} respectively. A simple 3D model is shown in figure J.7. This morphological information is useful as:

- it can provide an insight into how ligands interact differently on the crystallite surfaces during the growth. Ligands are indeed partially responsible for inhibiting the attachment of precursors, influencing a selectivity in the stability and growth of some facets. Therefore, this information is crucial for understanding nucleation and the influence of ligands during NC growth;

- the simple three-dimensional models can be used in simulations for electronic structure, or phonon dispersion: they can be used to optimise lateral size and thickness for obtaining the properties for efficient implementation in devices.

As a perspective, when monodisperse samples will be obtained, it would be interesting to perform a tomography experiment and to analyse the thickness of the hexagons by other techniques (quantitative STEM-EELS as an example).

The distance between hexagonal $CuFeS_2$ platelets is measured from the lateral projection of self-organised stacks of platelets (assuming that the hexagonal facets (1 1 0) of neighbour NCs are parallel). The NCs are covered by a layer of ligands. Therefore this distance is the combination of the interaction of two flat surfaces in a dry environment, and of the spacing by long-chain organic ligands. This distance is in the order of 2.6 nm, whereas the distance of a single molecule of oleylamine is approximately 1 nm [220].

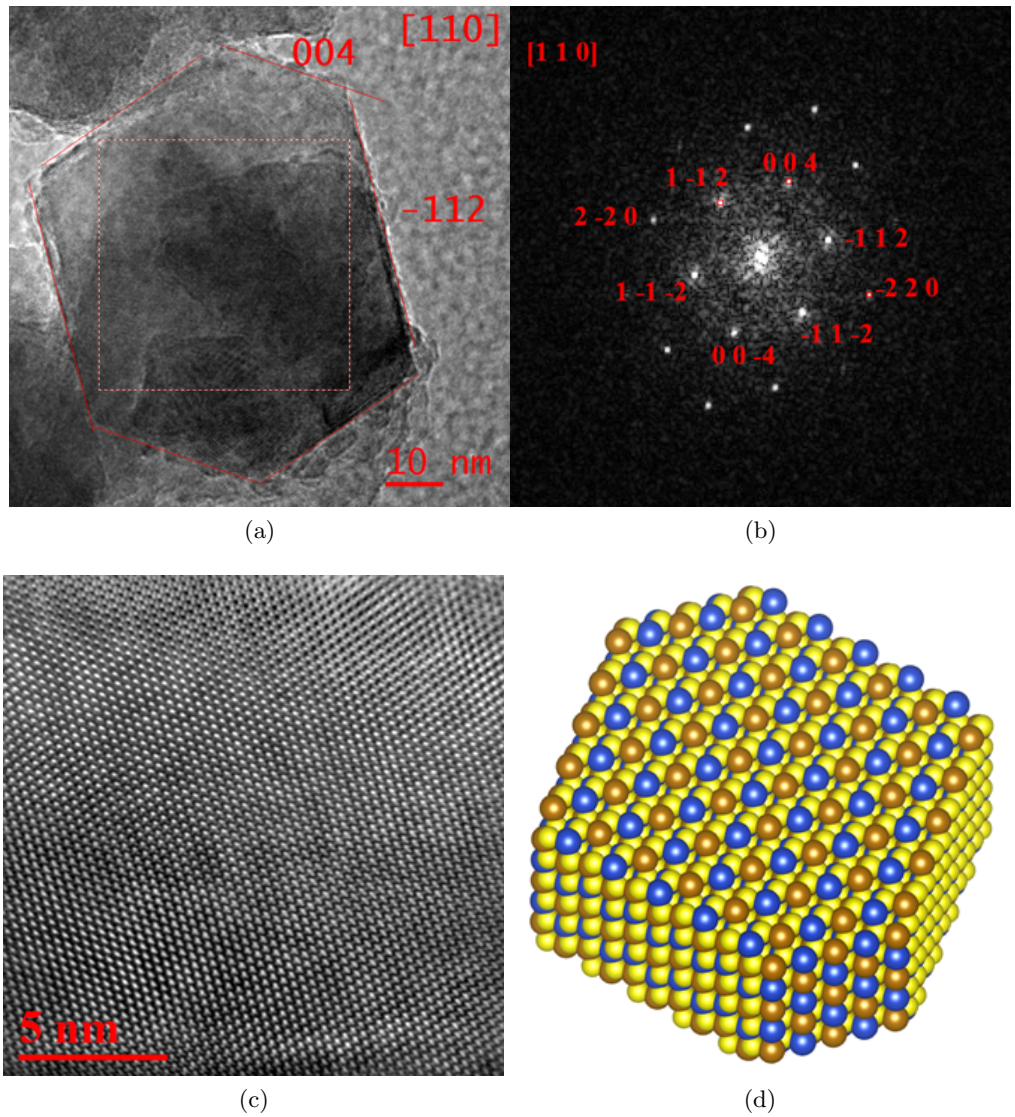

(a) (b)

(c) (d)

Figure J.7 – (a) HRTEM image of tetragonal chalcopyrite $CuFeS_2$ platelet obtained by the hot-injection method; (b) digital diffraction pattern and spot indexation; (c) detail of HRTEM micrograph of the bigger hexagon-shaped facet, oriented in the zone axis [1 1 0]; (d) 3D model of the platelet.

J.5 Nanocomposite materials

Pure $CuFeS_2$ pellets show a limited ZT of 0.10 at most, because of a too low electrical conductivity. It is, therefore, necessary to open new pathways for electrical conduction in the material, or to increase the number of charge carriers without diminishing their mobility. A recently proposed method consists in mixing metallic NCs with semiconductor NCs. By adding the right proportion of metal, new pathways are created in the nanocomposite material [221–223].

A possible drawback is the increase of heat transported by carriers and the global thermal conductivity in the material. Previous studies have been performed on smaller NCs, where the size of metal and semiconductor nanoparticles is comparable [221–223], while in this study $CuFeS_2$ the average size of the semiconductor is considerably larger than the added metallic NCs. Therefore, their effect needs to be studied.

The effect of the addition of Cu, Ag or Sn NCs in $CuFeS_2$ NCs was studied during Louis Vaure's PhD project [9]. Microscopy characterisation was performed only on the pellet most promising for its thermoelectric properties, which are only briefly described here. This pellet is a composite of $CuFeS_2$ and 4% mol of Sn NCs.

J.5.1 Fabrication of composite $CuFeS_2$/Sn pellet

The heat-up synthesis method for $CuFeS_2$ NCs described in subsection J.2.1 has been preferred as it provides a greater quantity of final product. Sn NCs were synthesised by collaborators in IREC Barcelona, following the protocol established by Kravchykv [224]. The diameter of the NCs is 12 ± 2 nm.

The organic ligand layer covering the surface of NCs represents a barrier for charge transfer, and therefore must be removed. NCs are precipitated by addition of an anti-solvent (methanol), dried under primary vacuum and introduced in a tubular oven at 400 °C[2] for 1 h under Ar flux. To form pellets, hot pressing is preferred, as it provides better mechanical stability (crystallite size increases under the effect of temperature and pressure). The density of the composite is 85% of the bulk material. NCs are introduced in the press and a pressure of $6000\,\mathrm{t\,m^{-2}}$ (0.5 t on a 10 mm diameter circle) is applied; temperature is increased to 400 °C and maintained for 5 minutes. Then the pressure is released, and the temperature lowered back to room temperature.

J.5.2 STEM-EDS of the pellet

Fragments of the pellet have been studied by STEM-EDS to observe the distribution of Sn NCs in the material. Melting temperature of bulk Sn is 232 °C[3], whereas bulk $CuFeS_2$ melts at approximately 950 °C: thus in the hot pressing procedure for pellet

[2] For T < 400 °C organic contamination still reduces the electrical conductivity; for T > 400 °C a non-negligible quantity of sulfur from the NC is eliminated because of the combined action of Ar flux and temperature.

[3] Moreover, usually melting temperature is reduced in nanosystems [225]

preparation, Sn NCs are expected to melt and its effect on composite microstructure needs to be observed[4].

The pellet was ground and the powder obtained was deposited on a holey amorphous carbon TEM grid. The obtained powders are irregular in shape, their thickness is not constant and is not known: therefore it is not possible to model the interaction of X-rays with the material for determining absorption. Quantitative composition information is therefore not obtained. Nevertheless, the qualitative information is sufficient to provide an insight into the composite appearance and to plan future studies.

In this section, a typical STEM-EDS acquisition obtained at high magnification is presented. The spectrum integrated on the region of the composite material is presented in figure J.8.

The elements identified from this EDS spectrum are:

- C and Ni, spurious signal from the sample supporting grid;
- Cu, Fe and S, from the matrix NCs;
- Sn, which is successfully incorporated as a filler in the composite material;
- I, which is conserved from the CuI precursor.

To the best of our knowledge, the detection of I in the composite has been reported for the first time. The presence of I is significant as it could influence the properties of $CuFeS_2$ NCs.

The STEM-HAADF image and the elemental map from STEM-EDS[5] of a grain of the composite pellet are presented in figure J.9. Even after hot pressing, some space remains between the grains. The maps of Cu, Fe and S, as well as I, can be readily superimposed, indicating a ternary material effectively. Most of Sn appears to be concentrated in some crystals of 12 nm to 30 nm. There is no clear evidence of the formation of a percolation network. Even though the STEM-EDS technique does not provide 3D information, the segregation of Sn is remarkable. Sn does not (or does in a very limited proportion) incorporates in $CuFeS_2$ NCs. From the integration of qualitative EDS measurement, Sn represents approximately $3.0 \pm 0.3\%$ mol with respect of $CuFeS_2$. Standard deviation is high, as Sn concentration (and therefore its fluorescence signal) is low in comparison to the signal of other major elements.

The detected iodine is approximatively 2% mol with respect to $CuFeS_2$. It does not form aggregates but appears evenly distributed in all the material. Further advanced studies (diffraction) would be interesting to determine whether iodine is incorporated in $CuFeS_2$ structure (as a substitution of the anion S^{2-}) or in interstitial sites. Also, it could merely represent non-reacted precursors which have not been removed during the purification of NCs from the reaction medium.

[4]FIB-SEM equipped with EDS detector would be perfect to obtain a 3D information about the composite material morphology. Proper observation of the composite material could also be possible after the preparation of a thin foil for STEM-EDS.

[5]The presented elemental maps have not been normalised, as the difference in relative composition between different elements is significant.

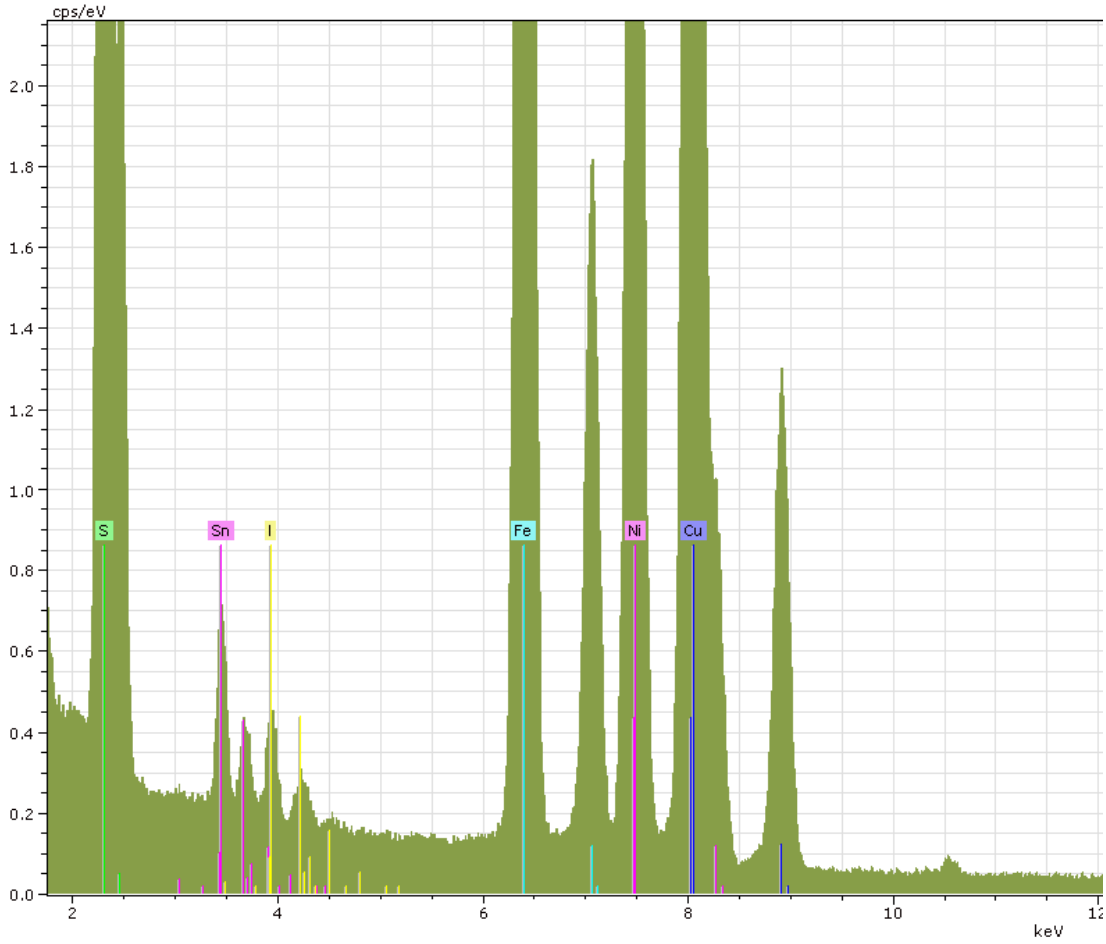

Figure J.8 – Spectrum integrated from the composite material $CuFeS_2$ with 4% mol tin NCs.

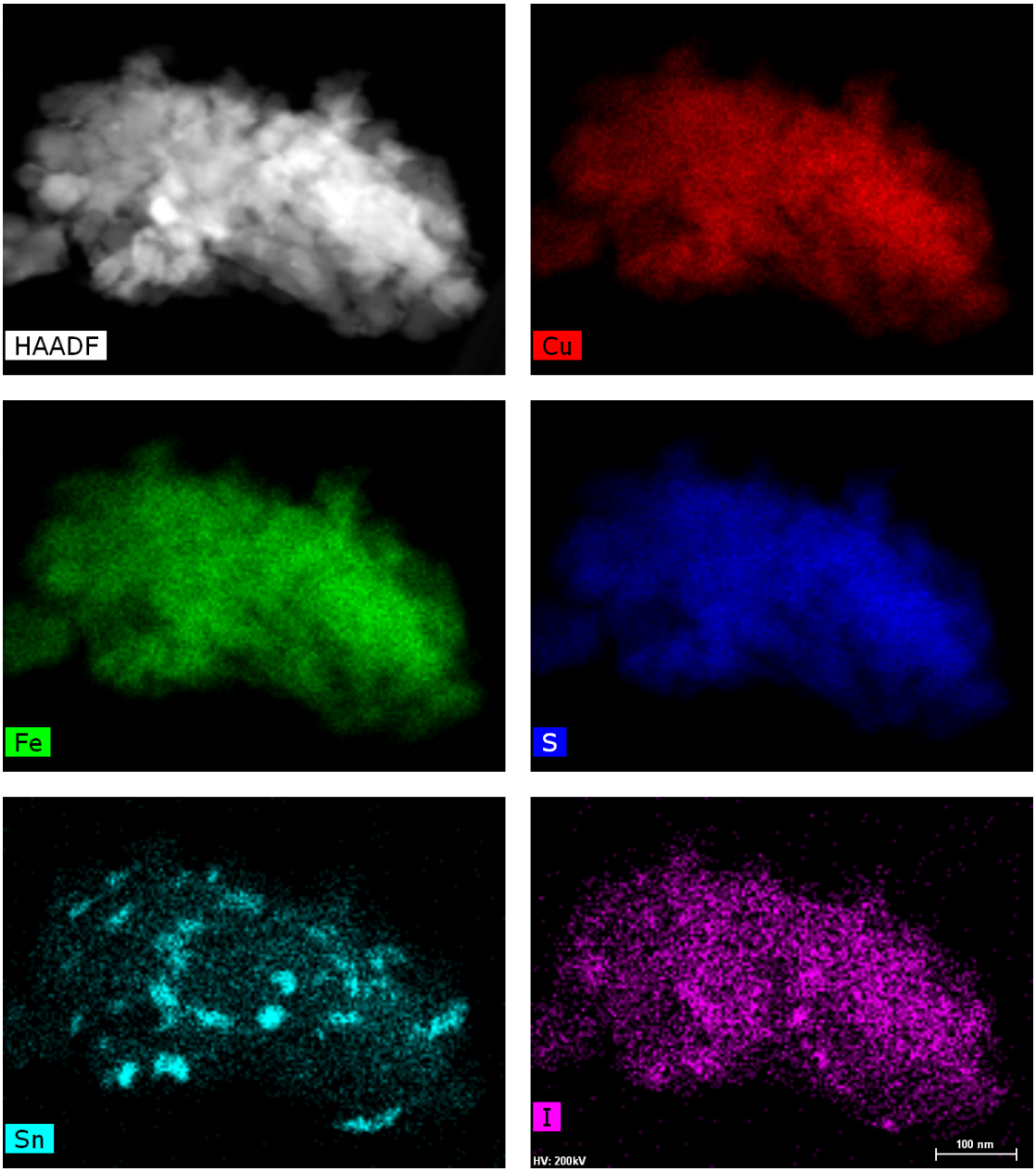

Figure J.9 – STEM-HAADF image and elemental mapping of the composite material. Scale bar 100 nm

J.6 Conclusion

Two synthesis methods (hot-injection and heat-up methods) are developed to obtain nano-sized $CuFeS_2$, which is an inexpensive and efficient material for thermoelectrics. Both procedures provide NCs which are small enough to reduce thermal conductivity by nanostructuration.

Hot-injection method leads to strongly anisotropic NCs: they are platelets, with a larger hexagon-shaped facet, and with a lateral size varying from some tens to some hundreds of nanometers. The structure is evaluated from the digital Fourier transform of HRTEM images which contain several NCs. Its radial profile can be indexed from the chalcopyrite structure, excluding the wurtzite. This result is in agreement with X-ray powder diffraction analysis. Despite the inhomogeneity in size, all the hexagon-shaped facets exhibit the same [1 1 0] zone axis, and the set of planes of the lateral facets are the same for all NCs. This information allows the construction of a simple 3D atomistic model, which can be used as input for first-principle electronic structure or phonon dispersion calculations. Moreover, this model explains the anisotropic shape: the selectivity of the ligands prevents the growth of the larger facets.

Heat-up method leads to polydisperse NCs with an average size of 20 nm and an irregular shape. Their large dispersion in size and the irregular shape are explained by the low reactivity of the metal precursors with thiols. This procedure is favoured for the following pellet elaboration because of better scalability (approximately 1 g per synthesis).

Thermoelectric properties are measured in hot pressed pellets. Pure $CuFeS_2$ pellets present a ZT of 0.10 at most. To increase this value, metallic NCs are added and mixed with $CuFeS_2$ NCs. Several metals have been tested (Ag, Cu, Sn). TEM was performed only on the best performance composite material, obtained with $CuFeS_2$ NCs from heat-up process in addition of 4% mol Sn NCs (having a diameter of 12 ± 2 nm).

An exploratory STEM-EDS experiment of the composite is performed to obtain first information about the microstructure. As expected, some space appears between the grains. Cu, Fe and S mappings can be superimposed, as they are present in the same position; Sn is not evenly distributed in the material, it remains confined in the original NC positions. There is no evidence of the formation of a percolation network.

Iodine is also observed in the material. It derives from CuI precursor. Further studies are necessary to understand the position of iodine in the structure and its influence on the properties of this material.

List of Figures

1.1 Calculated evolution of the band gap with size for various ternary I-III-VI_2 semiconductor NC. Reprinted from [22]. 20
1.2 Schematic representation of a nanocrystal which is capped by ligands. . . 22
1.3 The pseudoternary phase diagram to form CZTS phase and other secondary phases along with their crystal structures. Reprinted from [17]. . . 24
1.4 Structural relationships in ternary and quaternary metal chalcogenides. The typical zinc-blende binary structure (a) (space group $F\bar{4}3m$) transforms in chalcopyrite (b) ($I\bar{4}2d$) or in CuAu (c) ($P\bar{4}2m$) structures, after replacement of the single cation with two distinct cations. Kesterite (d) ($I\bar{4}$) is derived from the ordered chalcopyrite structure (b) ($I\bar{4}2d$), while stannite (e) ($I\bar{4}2m$) derives from the CuAu ordering (c). Both structures differ in the ordering of the Cu-Zn sublattice. The PMCA structure (f) (primitive mixed CuAu-like, $P\bar{4}2m$) derives from the CuAu ordering (c) too and features a 90° rotation of one of the II-IV layers with respect to stannite. 26
1.5 Monodisperse $CsPbX_3$ NCs and their structural characterisation. (a) Schematic of the cubic perovskite lattice; (b,c) typical transmission electron microscopy (TEM) images of $CsPbBr_3$ NCs; (d) colloidal solutions in toluene under UV lamp (λ = 365 nm); (e) representative PL spectra (λ_{exc} = 400 nm for all but 350 nm for $CsPbCl_3$ samples). Reprinted from [60]. 28
1.6 Schematics of the STEM electron beam-sample interaction and the different signals emerging from the sample. 31
1.7 Setup of STEM imaging. Retrieved from [82]. 33
1.8 (a) X-ray generation mechanism in the electron microscope, (b) an example of an EDS spectrum. Retrieved from [82]. 36
1.9 (a) FEI Titan Themis and (b) schematic of the EDS system design, including X-FEG high-brightness, Schottky electron source, and the Super-X geometry including four SDD detectors arranged symmetrically around the sample and the objective lens pole pieces (not to scale; retrieved from [90]). 41
1.10 Nano-beam Electron Diffraction from CZTS NCs (a) by classic conical illumination and by (b) 0.7° precessing beam 42

2.1 STEM-HAADF acquisition of NCs treated by O and H plasma. 47
2.2 TEM over the InPZn/ZnSe/ZnS core/shell/shell NCs after standard purification (sample A). The halo is produced by contaminants at higher exposure times. 53
2.3 TEM over the InPZn/ZnSe/ZnS core/shell/shell NCs after standard purification and fast thermal annealing at 700 °C for 30 s, performed on the grid (sample B). 54
2.4 TEM over the InPZn/ZnSe/ZnS core/shell/shell NCs after standard purification and fast thermal annealing at 700 °C for 30 s (sample C). 55
2.5 Comparison of the three baths proposed for Cu_2ZnSnS_4 NCs. 57
2.6 STEM-HAADF images from STEM-EDS acquisitions; 400 s, 1024×1024 px. CZTS NCs were poured in an acetone-HAc 3:1 bath. Shape and positions of NCs are clearly recognisable. 58
2.7 Comparison of purification performed in (a) solid state or in (b) solution. 59
2.8 Structure of the purchased graphene from Graphenea. 61
2.9 Comparison between (a) (b) the best HRTEM images obtained on CZTS NCs deposited onto a ultrathin amorphous carbon at 200 kV and (c) (d) images obtained by non-monochromated HRTEM at 80 kV of NCs deposited onto graphene, where the background contribution is minimized. All the NCs underwent the same purification process. Graphene allows the visualization of the remaining organic molecules on the surface of the semiconductor NCs. 63
2.10 (a) Image of CZTS NCs with monochromated 80 kV and details of (b) clean graphene in zone A, (c) NC in zone B, (d) the hard-soft interface in zone C. 65
2.11 Selected details of the hard-soft interface. 66

3.1 Temperature of the system as a function of time. Arrows indicate the moment of sample extraction (see also 3.2). 74
3.2 Sample 1 is the reactants solution extracted after mixing and degassing. . 77
3.3 General plan of acquisition area and elemental maps (Cu-K_α, Zn-K_α, Sn-L_α and S-K_α) in sample 1. Spectra from pixels delimited by green lines are integrated and used for elemental quantification in table 3.3. 78
3.4 EDS spectra of nanoparticles observed in figure 3.3. 80
3.5 (a) General plan of acquisition area and (b) Cu-K_α and Zn-K_α chemical mapping of the same area (sample 1). 81
3.6 STEM-HAADF general plan of acquisition area at a magnification of 640 kx of sample 1. 82
3.7 STEM-HAADF image of sample 2 acquired at a magnification of 320 kx. A) Spherical particles, B) 2D platelets, C) smaller particles with $d < 2$ nm 83
3.8 HAADF-STEM image and elemental mappings (Cu-K_α, Zn-K_α, Sn-L_α and S-K_α) of sample 2. 85
3.9 HAADF image of sample 2. Labelled areas are integrated for quantification. 86

3.10 Comparison of normalized EDS spectra in sample 2 between one isolated large NC (red) and a group of small NCs (green). 87
3.11 General plan of acquisition area at a magnification of 910 kx of sample 3, and elemental mapping (Cu-K_α, Zn-K_α, Sn-L_α and S-K_α) of the same zone. 88
3.12 General plan of acquisition area at a magnification of 1.8 Mx of sample 3. 89
3.13 HAADF image of sample 4. 90
3.14 General plan of acquisition area and elemental mapping (Cu-K_α, Zn-K_α, Sn-L_α and S-K_α) of sample 4. 92
3.15 Line profile of a compositional homogeneous NC and of a NC presenting a Zn-rich domain in sample 4. 93
3.16 HAADF images of NCs from sample 5, showing some atomic column contrast. 94
3.17 (a) HAADF image, (b) sum of Zn-K_α (green) and Sn-L_α (blue) and of (c) Cu-K_α (red) and Sn-K_α (blue) elemental maps. 94
3.18 General plan of acquisition area and elemental mapping (Cu-K_α, Zn-K_α, Sn-L_α and S-K_α) of sample 7. 96
3.19 General plan of acquisition area and elemental mapping of sample 7. . . . 98
3.20 The change in cation ratios for large NCs (black square), small NCs (red circle) and platelet NCs (blue triangle) as a function of time. The points correspond to samples 2, 3, 4, 5 and 7. The composition was determined using STEM-EDS. The average elemental composition is used for the calculation of cation ratios. The blue dashed line indicates the starting value for the precursor. After 3 hours degassing at room temperature (sample 1), only a binary Cu_xS specie is observed. Moreover, no sample could be observed by TEM at 30 minutes at 280 °C (sample 6). Therefore, the cation ratios for the two samples (sample 1 and 6) are excluded in the figure. 101
3.21 Scheme summing up the different steps of NC formation during Steinhagen's synthesis: from the precipitation of Cu_xS to the nucleation and growth of two populations of off-stoichiometric quaternary NCs to the final homogeneous CZTS NCs. 104
3.22 The almost-indistinguishable powder electron diffraction pattern for the three structures. 105
3.23 Lattice parameters vs. cation ratios of CZTS samples, with linear interpolation. Left: Cation ratio $\frac{Cu}{Zn+Sn}$. Right: Cation ratio $\frac{Zn}{Sn}$. Vertical black dotted lines represent the stoichiometric values for Cu_2ZnSnS_4 and vertical blue dashed lines represent the cation ratio measured experimentally on the synthesized CZTS NCs. Data retrieved from [149]. 111
3.24 Detail of the template matching at the two maxima. 113
3.25 Different filters applied on original diffraction patterns. 115

3.26 Digitally created images from NPED. Figure (b) is created by integrating the pixels inside the green circle in figure (a); figure (c) originates from the integration between the two red circles in figure (a); finally, the integration of the pixels outside the black circle in figure (a) originates figure (d). . . 115
3.27 NPED diffractograms from CZTS NCs. 116
3.28 Results from nanodiffraction experiment. 116
3.29 Results from nanodiffraction experiment. 117
3.30 Template matching with different phases from the template collection. . . 118
3.30 Comparison of the solution of the template matching (in the centre of the images) with 4 templates with the smallest misalignment. The index map plots the image correlation factor as a function of the direction. The indicated angles are the orientation of the simulated diffractogram following the Euler-Bunge notation. Q represents the image correlation factor. 119
3.31 Results from NPED experiment and template matching with different phases from the template collection. 120
3.32 Simulations and atomistic models for the direction [1 0 0]. Cu: brown, Zn: blue, Sn: fuchsia, S: yellow. 122
3.33 Simulations and atomistic models for the direction [2 2 1] ([1 1 1] in the case of PMCA structure). Cu: brown, Zn: blue, Sn: fuchsia, S: yellow. Sn atoms are artificially represented with an enlarged radius, to underline the heaviest atoms and explain the bright columns patterns in simulations. 124
3.34 A CZTS NC oriented in direction $\langle 1\,0\,0 \rangle$ 126
3.34 Details of a well-oriented CZTS NC and comparison of patterns and line profile between experimental image and PMCA structure simulation. . . . 129
3.35 Details of a well-oriented CZTS NC. PMCA structure is clearly recognised thanks to its intrinsic bright column pattern. 130

4.1 Typical STEM images of $CsPbBr_3$ NCs. 134
4.2 Particle analysis of two separated self-organized domains. Left and right images are binary images created from respectively the yellow and red boxed area of the central image. 135
4.3 Models of cubic $Pm\bar{3}m$ and orthorhombic *Pnma* $CsPbBr_3$ (Cs is represented in green, Pb grey and in the centre of octahedra, Br brown). 138
4.4 Projection of the *Pnma* $CsPbBr_3$ structure along (a) [0 1 0], (b) $[\bar{1}\,0\,1]$ and (c) [1 0 1] zone axes. The red, green and blue arrows in the compasses correspond to $\vec{a}$, $\vec{b}$ and $\vec{c}$ respectively for the orthorhombic unit cell. (a), (b) and (c) show the [1 0 0], [0 1 0] and [0 0 1] zone axes in the pseudo-cubic system, respectively. Cs atoms are represented in light green, Pb atoms are grey and in the centre of the octahedra, Br atoms are brown and in the vertices of the octahedra. 139

4.5 Simulated diffraction patterns for $CsPbBr_3$ performed on the UCA Cadiz server [154]. The extra reflections, whose indices are underlined in red, lay on lines (indicated by arrows). These extra reflections are caused by the the octahedra distortions and rotations in the orthorhombic structure. 141
4.6 Temperature evolution of normalized cell parameters in $CsPbBr_3$ $a_p = \frac{a}{\sqrt{2}}$, $b_p = \frac{b}{\sqrt{2}}$, $c_p = \frac{c}{2}$ where a, b, c are cell dimensions of orthorhombic $Pbnm$ $CsPbBr_3$. Lines are guides for the eyes. Reproduced from [155]. 143
4.7 Azimuthal integration of the SAED patterns taken for NCs at various temperatures and comparison with the powder XRD data for reference orthorhombic phase. Printed from [156]. 144
4.8 Coexistence of cubic and orthorhombic $CsPbBr_3$ within single AC-HRTEM image from $CsPbBr_3$ nanosheets. (a) Experimental AC-HRTEM image with two regions denoted as I and II. (b,c) Experimental Fourier transforms from region I (b) and II (c). (d,e) Simulated electron diffraction of cubic (d) and orthorhombic (e) $CsPbBr_3$. (f,g) Enlarged images from region I (f) and II (g). The cubic and orthorhombic structure models are overlaid on (f) and (g), respectively. Reprinted from [69]. 144
4.9 $CsPbBr_3$ NCs observed with a (a) 200 kx magnification and at (b) 300 kx magnification. 146
4.10 Defocus-thickness HRTEM map of a cubic $CsPbBr_3$ crystal observed along a $\langle 0\,0\,1 \rangle$ direction with a JEOL 3010 microscope operated at 300 kV. $C_s = 0.7$ mm. 32 defocus values, with lowest defocus -100 nm and defocus step 10 nm. 40 different thickness, starting at 3.5 nm, with a thickness step of $4 \times a_{cubic} = 2.3378$ nm. 148
4.11 Defocus-thickness HRTEM map of a orthorhombic $CsPbBr_3$ crystal observed (a) along [0 1 0] and (b) along [1 0 1] direction with a JEOL 3010 microscope operated at 300 kV. $C_s = 0.7$ mm. 32 defocus values, with lowest defocus -100 nm and defocus step 10 nm. 40 different thickness, starting at 3.5 nm, with thickness step of $2 \times b_{ortho} = 2.3378$ nm. 149
4.12 Simulation of cubic and orthorhombic structure, zone axis [0 1 0], Jeol 3010 300 kV, defocus -30 nm, thickness 11.76 nm. Model: Cs blue, Pb grey, Br brown. 150
4.13 Detail of $CsPbBr_3$ NC, obtain with the Jeol 3010 microscope. The inset simulation corresponds to a thickness of 10 nm at a defocus value of 35 nm. 151
4.14 Some peculiar FFTs calculated over HRTEM images of single $CsPbBr_3$ NCs. 151
4.15 AC-HRTEM image $CsPbBr_3$ NC, zone axis [0 1 0]. 153
4.16 Improvement of the image quality and suppression of the noise thanks to acquisition of series of 45 sequential images, aligned by SDSD plugin for Digital Micrograph. 155
4.17 Experimental STEM-HAADF images showing the patterns from ordered $CsPbBr_3$ crystal structure in NCs. 156
4.18 Averaged STEM image of $CsPbBr_3$ NCs. 157

4.19 Detail of multidetector acquisition for STEM; each detector collects a different angular range of scattered electrons. 158
4.20 Detail from image 4.18a. Arrows indicate the positions where the Br columns are displaced from the equilibrium positions. Cs and Pb are labeled, whereas the Cs are not. 158
4.21 STEM-ADF image acquired at 10 Mx magnification and atomic model of $CsPbBr_3$ (zone axis [1 0 1]). Arrows indicate the displacement of Cs columns. The yellow horizontal line is provided for visual aid. 159
4.22 Displacement of the Cs columns. 160
4.23 STEM-HAADF and STEM-BF simulations performed on [0 0 1] cubic structure (a) (b) (c) and on [0 1 0] orthorhombic structure (d) (e) (f). Cs atoms are represented in green, Pb are in grey and in the centre of octahedra, Br in brown. 162
4.24 Indexed experimental SAED from $CsPbBr_3$ NCs and radial profiles after background removal. Peaks are labeled as both cubic structure reflections (a), (c) and orthorhombic structure reflections (b), (d). TEM image of $CsPbBr_3$ NCs producing the presented DP (e). 164
4.25 Image and diffraction pattern from SAED from a single $CsPbBr_3$ NC. . . 165
4.26 HRTEM showing an amorphous stain on the surface of each $CsPbBr_3$ NC. 166
4.27 (a) General plan of $CsPbBr_3$ NCs with bright spots and (b) qualitative Pb elemental map acquired at 200 keV. 167
4.28 Diffraction pattern of $CsPbBr_3$ NCs. 168

A.1 Left: A photograph of the experimental setup in ID01 beamline at ESRF. The red arrow points at the heating stage, in which the sample lies. The right image is the focus-up of the heating stage. The black arrow indicates the capillary containing the analysed solution. 177
A.2 WAXS diffraction patterns at 110 °C (violet colour) and after heating at 280 °C (brown and orange colours). Black vertical lines correspond to the ICDD-PDF 26-0575 data for kesterite phase of Cu_2ZnSnS_4; the red squares correspond to ICDD-PDF data for CuS. 178
A.3 WAXS analysis at 280 °C. 180
A.4 Evolution of SAXS spectra from room temperature to 280 °C. 181
A.5 SAXS performed in supernatant and precipitate in sample 2, after 30 minutes at 110 °C 182
A.6 WAXS data measured with samples 2, 3 and 7. Zoom on a reduced 2θ range to illustrate the phase transition induced by heating at 280 °C. . . . 183
A.7 Diffraction pattern of CZTS NCs obtained by Steinhagen procedure. Black lines indicate the peaks corresponding to bulk CZTS in the kesterite phase reference pattern (ICDD 04-015-7542). 184

C.1 Calculated capping-layer structure of 5-nm diameter PbS NC capped with oleic acid. PbS (1 1 1) surfaces are terminated by oleate and hydroxide ions, PbS (1 0 0) by oleic acid. Retrieved by [178]. 188

E.1 Pt metallic salts deposited on graphene (magnification 295 kx, 380 kx for figure E.1c). Courtesy Hanako Okuno. 197

F.1 EELS experiment on CZTS NCs. 199

G.1 Elemental mapping (Cu-K_α, Zn-K_α, Sn-L_α and S-K_α) of sample 1. 200
G.2 Five NCs and their elemental mapping (Cu-K_α, Zn-K_α, Sn-L_α and S-K_α). 202
G.3 General plan and elemental mapping (Cu-K_α, Zn-K_α, Sn-L_α and S-K_α) for the intermediate reaction sample 5. 204
G.4 Line profile of the crystal in the centre of the image. 205

H.1 Influence of thickness in STEM-HAADF imaging of (a) [1 0 0] zone axis (top: kesterite, bottom: PMCA) and of (b) [2 2 1] zone axis (top: kesterite, bottom: PMCA; different scalebar). 207

I.1 Structural model of a cubic perovskite. 208
I.-2 HRTEM micrographs and calculated FFT from single NCs. 213
I.-1 HRTEM micrographs and calculated FFT from single NCs which show additional peaks with respect to the $Pm\bar{3}m$ cubic pattern. 214

J.1 Temperature dependence of ZT of $CuFeS_2$ nanoparticles (red) and bulk chalcopyrite (black). Retrieved from [215] 220
J.2 Setup for $CuFeS_2$ NCs synthesis by the heat-up method. 222
J.3 Setup for $CuFeS_2$ NCs synthesis by the hot-injection method. 222
J.4 TEM-BF micrograph of $CuFeS_2$ NCs synthesized by heat-up method. . . 223
J.5 (a) Top view and (b) lateral view of $CuFeS_2$ NCs synthesized by hot-injection method. 224
J.6 HRTEM image of several randomly-oriented NCs; rotationally averaged of FFT from the HRTEM image; radial profile of rotationally averaged FFT, with indexing from chalcopyrite structure. 225
J.7 (a) HRTEM image of tetragonal chalcopyrite $CuFeS_2$ platelet obtained by the hot-injection method; (b) digital diffraction pattern and spot indexation; (c) detail of HRTEM micrograph of the bigger hexagon-shaped facet, oriented in the zone axis [1 1 0]; (d) 3D model of the platelet. 227
J.8 Spectrum integrated from the composite material $CuFeS_2$ with 4% mol tin NCs. 230
J.9 STEM-HAADF image and elemental mapping of the composite material. Scale bar 100 nm 231

List of Tables

1 Abbreviations 12

1.1 Calculated lattice constant a, tetragonal distortion parameter $\eta = \frac{c}{2a}$, crystal field splitting Δ_{CF}, energy difference per atom relative to the lowest-energy structure Δ_E, and direct band gap E_g. Adapted from [50]. . 27

2.1 Solvent and antisolvent used for the materials analysed. 46

3.1 Precursors and solvent used in the synthesis of CZTS NCs. 73
3.2 Samples and reaction steps. 75
3.3 Elemental quantification of sample 1 in the zones labelled "single NC" and "bunch of NCs" in figure 3.3. 81
3.4 Elemental quantification of sample 1 from spectra integrated from labelled zones in figure 3.6. 82
3.5 Elemental quantification of sample 2 for all the particles in figure 3.7. . . 84
3.6 Elemental quantification of sample 2 of smaller and larger particles. . . . 86
3.7 Elemental quantification of sample 2 for different objects. 86
3.8 Elemental quantification (Cu-K_α, Zn-K_α, Sn-L_α and S-K_α) of sample 3 from figure 3.11. 89
3.9 Elemental quantification of sample 3 for three NCs from image 3.12. . . . 90
3.10 Elemental quantification of sample 4 from 5 NCs from figure 3.13. 91
3.11 Elemental quantification of sample 7 from figure 3.18. 95
3.12 Elemental quantification of most of the NCs of sample 7 in figure 3.19. . . 99
3.13 Summary of composition measurements on larger and smaller NCs by STEM-EDS. 100
3.14 Summary of composition measurements on larger and smaller NCs by STEM-EDS and SEM-EDS. 101
3.15 Calculated lattice parameters and tetragonal distortion parameters of the three structures [50]. 107
3.16 Relative differences between a and c lattice parameters and tetragonal distortion η for the kesterite (KS), stannite (ST) and pre-mixed Cu-Au (PMCA) structures. 107
3.17 Table representing the interpolation for cation ratios $\frac{\text{Cu}}{\text{Zn+Sn}}$ 110
3.18 Overview of simulation parameters 121

4.1 Unit cell parameters and atomic positions for $CsPbBr_3$ perovskites with $Pm\bar{3}m$ (221) and with *Pnma* space groups (62). 137
4.2 Atomic number and atomic radius of Cs, Pb and Br 137

A.1 Shift of diffraction peak at 280 °C from WAXS. 179

G.1 Quantification of the homogeneous NC and of the two NC which show chemical segregation. 203
G.2 Overall quantification. 205

I.1 Structure factor for cubic $Pm\bar{3}m$ $CsPbBr_3$ structure. 215
I.2 Structure factor for orthorhombic *Pnma* $CsPbBr_3$ structure. 218

Bibliography

[1] Grzegorz Gabka, Piotr Bujak, Maciej Gryszel, Andrzej Ostrowski, Karolina Malinowska, Grazyna Z Zukowska, Fabio Agnese, Adam Pron, and Peter Reiss. Synthesis and surface chemistry of high quality wurtzite and kesterite Cu_2ZnSnS_4 nanocrystals using tin(ii) 2-ethylhexanoate as a new tin source. *Chemical communications*, 51:12985–12988, 2015.

[2] Jennifer K Molloy, Christophe Lincheneau, Maria Moula Karimdjy, Fabio Agnese, Lucia Mattera, Christelle Gateau, Peter Reiss, Daniel Imbert, and Marinella Mazzanti. Sensitisation of visible and NIR lanthanide emission by InPZnS quantum dots in bi-luminescent hybrids. *Chemical Communications*, 52(24):4577–4580, 2016.

[3] Lucia Mattera, Shashi Bhuckory, K. David Wegner, Xue Qiu, Fabio Agnese, Christophe Lincheneau, Tim Senden, David Djurado, Loïc J. Charbonnière, Niko Hildebrandt, and Peter Reiss. Compact quantum dot–antibody conjugates for FRET immunoassays with subnanomolar detection limits. *Nanoscale*, 8(21):11275–11283, 2016.

[4] Susana Trasobares, Miguel Lõpez-Haro, Mathieu Kociak, Katia March, Francisco De La Peña, Jose A. Perez-Omil, Jose J. Calvino, Nathan R. Lugg, Adrian J. D'Alfonso, Leslie J. Allen, and Christian Colliex. Chemical imaging at atomic resolution as a technique to refine the local structure of nanocrystals. *Angewandte Chemie - International Edition*, 50(4):868–872, 2011.

[5] W.M.J. Coene, a. Thust, M. Op de Beeck, and D. Van Dyck. Maximum-likelihood method for focus-variation image reconstruction in high resolution transmission electron microscopy. *Ultramicroscopy*, 64(1-4):109–135, aug 1996.

[6] A. Thust, W.M.J. Coene, M. Op de Beeck, and D. Van Dyck. Focal-series reconstruction in HRTEM: simulation studies on non-periodic objects. *Ultramicroscopy*, 64(1-4):211–230, aug 1996.

[7] Dirk Van Dyck, Joerg R Jinschek, and Fu-Rong Chen. 'Big Bang' tomography as a new route to atomic-resolution electron tomography. *Nature*, 486(7402):243–6, jun 2012.

[8] G Brunetti, D Robert, P Bayle-Guillemaud, J L Rouviére, E F Rauch, J F Martin, J F Colin, F Bertin, and C Cayron. Confirmation of the Domino-Cascade Model by $LiFePO_4$ / $FePO_4$ Precession Electron Diffraction. *Chem. Mater.*, 23:4515–4524, 2011.

[9] Louis Vaure. *Matériaux à base de nanocristaux semi-conducteurs de chalcopyrite pour la conversion thermoélectrique*. PhD thesis, Université Grenoble Alpes, 2017.

[10] William Shockley, Hans Queisser, and Hans J Queisser. The Shockley-Queisser limit. *Journal of Applied Physics*, 32:510–519, 1961.

[11] Ekimov A.A.Onushchenko. Quantum size effect in three-dimensional microscopic semiconductor crystals. *Jetp Letters*, 34:345–349, 1981.

[12] Z Alfassi, D Bahnemann, and A Henglein. Photochemistry of Colloidal Sulfides. 3. Photoelectron Emission from CdS and CdS-ZnS Co-Colloids. *Journal of Physical Chemistry*, 86(6):4656–4657, 1982.

[13] Louis Brus. Electronic wave functions in semiconductor clusters: experiment and theory. *The Journal of Physical Chemistry*, 90(12):2555–2560, 1986.

[14] A. P. Alivisatos. Semiconductor Clusters, Nanocrystals, and Quantum Dots. *Science*, 271(5251):933–937, 1996.

[15] Dmitry Aldakov, Aurélie Lefrançois, and Peter Reiss. Ternary and quaternary metal chalcogenide nanocrystals: synthesis, properties and applications. *Journal of Materials Chemistry C*, 1(24):3756, 2013.

[16] Benjamin Abécassis, Cécile Bouet, Cyril Garnero, Doru Constantin, Nicolas Lequeux, Sandrine Ithurria, Benoit Dubertret, Brian Richard Pauw, and Diego Pontoni. Real-Time in Situ Probing of High-Temperature Quantum Dots Solution Synthesis. *Nano Letters*, 15(4):2620–2626, 2015.

[17] Mukesh Kumar, Ashish Dubey, Nirmal Adhikari, Swaminathan Venkatesan, and Qiquan Qiao. Strategic review of secondary phases, defects and defect-complexes in kesterite CZTS-Se solar cells. *Energy Environ. Sci.*, 8(11):3134–3159, 2015.

[18] Susan Schorr. The crystal structure of kesterite type compounds: A neutron and X-ray diffraction study. *Solar Energy Materials and Solar Cells*, 95(6):1482–1488, jun 2011.

[19] Anthony S. R. Chesman, Noel W. Duffy, Steve Peacock, Lynne Waddington, Nathan A. S. Webster, and Jacek J. Jasieniak. Non-injection synthesis of Cu_2ZnSnS_4 nanocrystals using a binary precursor and ligand approach. *RSC Adv.*, 3(4):1017–1020, 2013.

[20] Arnim Henglein. Small-particle research: physicochemical properties of extremely small colloidal metal and semiconductor particles. *Chemical Reviews*, 89(8):1861–1873, 1989.

[21] C. B. Murray, D. J. Norris, and M. G. Bawendi. Synthesis and characterization of nearly monodisperse CdE (E = sulfur, selenium, tellurium) semiconductor nanocrystallites. *Journal of the American Chemical Society*, 115(19):8706–8715, 1993.

[22] Takahisa Omata, Katsuhiro Nose, and Shinya Otsuka-Yao-Matsuo. Size dependent optical band gap of ternary I-III-VI_2 semiconductor nanocrystals. *Journal of Applied Physics*, 105(7):073106, 2009.

[23] Bernard Van Eerdenbrugh, Guy Van den Mooter, and Patrick Augustijns. Top-down production of drug nanocrystals: Nanosuspension stabilization, miniaturization and transformation into solid products. *International Journal of Pharmaceutics*, 364(1):64 – 75, 2008.

[24] Victor K. Lamer and Robert H. Dinegar. Theory, Production and Mechanism of Formation of Monodispersed Hydrosols. *Journal of the American Chemical Society*, 72(11):4847–4854, 1950.

[25] Gu Kwon Soon, Yuanzhe Piao, Jongnam Park, Subramanian Angappane, Younghun Jo, Nong Moon Hwang, Je Geun Park, and Taeghwan Hyeon. Kinetics of monodisperse iron oxide nanocrystal formation by "heating-up" process. *Journal of the American Chemical Society*, 129(41):12571–12584, 2007.

[26] Howard Reiss. The Growth of Uniform Colloidal Dispersions. *The Journal of Chemical Physics*, 19(4):482–487, 1951.

[27] Xiaogang Peng, J Wickham, and A P Alivisatos. Kinetics of II-VI and III-V Colloidal Semiconductor Nanocrystal Growth : "Focusing" of Size Distributions. *Journal of the American Chemical Society*, 120(21):5343–5344, 1998.

[28] James R. McBride, Andrew R. Lupini, Michael A. Schreuder, Nathanael J. Smith, Stephen J. Pennycook, and Sandra J. Rosenthal. Few-layer graphene as a support film for transmission electron microscopy imaging of nanoparticles. *ACS Applied Materials and Interfaces*, 1(12):2886–2892, 2009.

[29] Chien-Chun Chen, Chun Zhu, Edward R White, Chin-Yi Chiu, M C Scott, B C Regan, Laurence D Marks, Yu Huang, and Jianwei Miao. Three-dimensional imaging of dislocations in a nanoparticle at atomic resolution. *Nature*, 496(7443):74–7, apr 2013.

[30] Sara Bals, Bart Goris, Luis M Liz-Marzán, and Gustaaf Van Tendeloo. Three-Dimensional Characterization of Noble-Metal Nanoparticles and their Assemblies by Electron Tomography. *Angewandte Chemie (International ed. in English)*, pages 10600–10610, aug 2014.

[31] Bart Goris, Annick De Backer, Sandra Van Aert, Sergio Gómez-Graña, Luis M Liz-Marzán, Gustaaf Van Tendeloo, and Sara Bals. Three-dimensional elemental

mapping at the atomic scale in bimetallic nanocrystals. *Nano letters*, 13(9):4236–41, 2013.

[32] Laurent D. Menard, Fengting Xu, Ralph G. Nuzzo, and Judith C. Yang. Preparation of TiO_2-supported Au nanoparticle catalysts from a Au_{13} cluster precursor: Ligand removal using ozone exposure versus a rapid thermal treatment. *Journal of Catalysis*, 243(1):64–73, 2006.

[33] Guicen Ma, Andrew Binder, Miaofang Chi, Chao Liu, Rongchao Jin, De-en Jiang, Jie Fan, and Sheng Dai. Stabilizing gold clusters by heterostructured transition-metal oxide-mesoporous silica supports for enhanced catalytic activities for CO oxidation. *Chemical Communications*, 48(93):11413, 2012.

[34] Jose A Lopez-Sanchez, Nikolaos Dimitratos, Ceri Hammond, Gemma L Brett, Lokesh Kesavan, Saul White, Peter Miedziak, Ramchandra Tiruvalam, Robert L Jenkins, Albert F Carley, David Knight, Christopher J Kiely, and Graham J Hutchings. Facile removal of stabilizer-ligands from supported gold nanoparticles. *Nature chemistry*, 3(7):551–556, 2011.

[35] John Kilmartin, Rozie Sarip, Ricardo Grau-Crespo, Devis Di Tommaso, Graeme Hogarth, Carmelo Prestipino, and Gopinathan Sankar. Following the creation of active gold nanocatalysts from phosphine-stabilized molecular clusters. *ACS Catalysis*, 2(6):957–963, 2012.

[36] Ludovico Cademartiri, Arya Ghadimi, and Geoffrey A. Ozin. Nanocrystal plasma polymerization: From colloidal nanocrystals to inorganic architectures. *Accounts of Chemical Research*, 41(12):1820–1830, 2008.

[37] Cesar Aliaga, Jeong Y. Park, Yusuke Yamada, Hyun Sook Lee, Chia Kuang Tsung, Peidong Yang, and Gabor A. Somorjai. Sum frequency generation and catalytic reaction studies of the removal of organic capping agents from Pt nanoparticles by UV-Ozone treatment. *Journal of Physical Chemistry C*, 113(15):6150–6155, 2009.

[38] Chunya Li, Enna Ha, Wing-Leung Wong, Cuiling Li, Kam-Piu Ho, and Kwok-Yin Wong. A facile arrested precipitation method for synthesis of pure wurtzite Cu_2ZnSnS_4 nanocrystals using thiourea as a sulfur source. *Materials Research Bulletin*, 47(11):3201–3205, nov 2012.

[39] Mingjian Yuan, Mengxia Liu, and Edward H. Sargent. Colloidal quantum dot solids for solution-processed solar cells. *Nature Energy*, 1(3):16016, 2016.

[40] Martina Sandroni, K. David Wegner, Dmitry Aldakov, and Peter Reiss. Prospects of Chalcopyrite-Type Nanocrystals for Energy Applications. *ACS Energy Letters*, pages 1076–1088, 2017.

[41] Maria Ibáñez, Reza Zamani, Wenhua Li, Alexey Shavel, Jordi Arbiol, Joan Ramon Morante, and Andreu Cabot. Extending the Nanocrystal Synthesis Control to Quaternary Compositions. *Crystal Growth & Design*, 12(3):1085–1090, mar 2012.

[42] Maksym V Kovalenko, Liberato Manna, Andreu Cabot, Zeger Hens, Dmitri V Talapin, Cherie R Kagan, X Victor I Klimov, Andrey L Rogach, Peter Reiss, Delia J Milliron, Philippe Guyot-sionnnest, Gerasimos Konstantatos, Wolfgang J Parak, Taeghwan Hyeon, Brian A Korgel, Christopher B Murray, and Wolfgang Heiss. Prospects of Nanoscience with Nanocrystals . *ACS Nano*, 9(2):1012–1057, 2015.

[43] Enrico Dilena, Yi Xie, Rosaria Brescia, Mirko Prato, Lorenzo Maserati, Roman Krahne, Andrea Paolella, Giovanni Bertoni, Mauro Povia, Iwan Moreels, and Liberato Manna. $CuIn_xGa_{1-x}S_2$ Nanocrystals with Tunable Composition and Band Gap Synthesized via a Phosphine-Free and Scalable Procedure. *Chemistry of Materials*, 25(15):3180–3187, 2013.

[44] Feng-Jia Fan, Liang Wu, and Shu-Hong Yu. Energetic I-III-VI_2 and I_2-II-IV-VI_4 nanocrystals: synthesis, photovoltaic and thermoelectric applications. *Energy & Environmental Science*, 7(1):190, 2014.

[45] Huanping Zhou, Wan-Ching Hsu, Hsin-Sheng Duan, Brion Bob, Wenbing Yang, Tze-Bin Song, Chia-Jung Hsu, and Yang Yang. CZTS nanocrystals: a promising approach for next generation thin film photovoltaics. *Energy & Environmental Science*, 6(10):2822–2838, 2013.

[46] Jiaxiong Xu. Investigation of Cu_2ZnSnS_4 thin-film solar cells with carrier concentration gradient. *Journal of Physics and Chemistry of Solids*, 98:32–37, 2016.

[47] Claudia Coughlan, Maria Ibáñez, Oleksandr Dobrozhan, Ajay Singh, Andreu Cabot, and Kevin M. Ryan. Compound Copper Chalcogenide Nanocrystals. *Chemical Reviews*, page acs.chemrev.6b00376, 2017.

[48] Aron Walsh, Shiyou Chen, X. G. Gong, and Su Huai Wei. Crystal structure and defect reactions in the kesterite solar cell absorber Cu_2ZnSnS_4 (CZTS): Theoretical insights. In *AIP Conference Proceedings*, volume 1399, pages 63–64, 2011.

[49] Shiyou Chen, Aron Walsh, Xin-Gao Gong, and Su-Huai Wei. Classification of lattice defects in the kesterite Cu_2ZnSnS_4 and $Cu_2ZnSnSe_4$ earth-abundant solar cell absorbers. *Advanced materials*, 25(11):1522–39, mar 2013.

[50] Shiyou Chen, X. G. Gong, Aron Walsh, and Su-Huai Wei. Crystal and electronic band structure of Cu_2ZnSnX_4 (X=S and Se) photovoltaic absorbers: First-principles insights. *Applied Physics Letters*, 94(4):041903, 2009.

[51] Ankur Khare, Burak Himmetoglu, Melissa Johnson, David J. Norris, Matteo Cococcioni, and Eray S. Aydil. Calculation of the lattice dynamics and raman spectra of copper zinc tin chalcogenides and comparison to experiments. *Journal of Applied Physics*, 111(8):083707, 2012.

[52] Shiyou Chen, X. Gong, Aron Walsh, and Su-Huai Wei. Electronic structure and stability of quaternary chalcogenide semiconductors derived from cation cross-substitution of II-VI and I-III-VI_2 compounds. *Physical Review B*, 79(16):165211, apr 2009.

[53] Akihiro Kojima, Kenjiro Teshima, Yasuo Shirai, and Tsutomu Miyasaka. Organometal halide perovskites as visible-light sensitizers for photovoltaic cells. *Journal of the American Chemical Society*, 131(17):6050–6051, 2009.

[54] Woon Seok Yang, Byung-Wook Park, Eui Hyuk Jung, Nam Joong Jeon, Young Chan Kim, Dong Uk Lee, Seong Sik Shin, Jangwon Seo, Eun Kyu Kim, Jun Hong Noh, and Sang Il Seok. Iodide management in formamidinium-lead-halide–based perovskite layers for efficient solar cells. *Science*, 356(6345):1376–1379, 2017.

[55] Zhi-Kuang Tan, Reza Saberi Moghaddam, May Ling Lai, Pablo Docampo, Ruben Higler, Felix Deschler, Michael Price, Aditya Sadhanala, Luis M. Pazos, Dan Credgington, Fabian Hanusch, Thomas Bein, Henry J. Snaith, and Richard H. Friend. Bright light-emitting diodes based on organometal halide perovskite. *Nature Nanotechnology*, 9(9):687–692, 2014.

[56] Javad Shamsi, Ahmed L. Abdelhady, Sara Accornero, Milena Arciniegas, Luca Goldoni, Ajay Ram Srimath Kandada, Annamaria Petrozza, and Liberato Manna. N-Methylformamide as a Source of Methylammonium Ions in the Synthesis of Lead Halide Perovskite Nanocrystals and Bulk Crystals. *ACS Energy Letters*, 1(5):1042–1048, 2016.

[57] Soranyel Gonzalez-Carrero, Laura Francis-Soriano, Maria Gonzalez-Bajar, Said Agouram, Raquel E. Galian, and Julia Perez-Prieto. The Luminescence of $CH_3NH_3PbBr_3$ Perovskite Nanoparticles Crests the Summit and Their Photostability under Wet Conditions is Enhanced. *Small*, pages 5245–5250, 2016.

[58] Quinten A. Akkerman, Marina Gandini, Francesco Di Stasio, Prachi Rastogi, Francisco Palazon, Giovanni Bertoni, James M. Ball, Mirko Prato, Annamaria Petrozza, and Liberato Manna. Strongly emissive perovskite nanocrystal inks for high-voltage solar cells. *Nature Energy*, 2(2):16194, 2016.

[59] Quinten A. Akkerman, Valerio D'Innocenzo, Sara Accornero, Alice Scarpellini, Annamaria Petrozza, Mirko Prato, and Liberato Manna. Tuning the optical properties of cesium lead halide perovskite nanocrystals by anion exchange reactions. *Journal of the American Chemical Society*, 137(32), 2015.

[60] Loredana Protesescu, Sergii Yakunin, Maryna I. Bodnarchuk, Franziska Krieg, Riccarda Caputo, Christopher H. Hendon, Ruo Xi Yang, Aron Walsh, and Maksym V. Kovalenko. Nanocrystals of Cesium Lead Halide Perovskites ($CsPbX_3$, X = Cl, Br, and I): Novel Optoelectronic Materials Showing Bright Emission with Wide Color Gamut. *Nano Letters*, 15(6):3692–3696, 2015.

[61] Jasmina A. Sichert, Yu Tong, Niklas Mutz, Mathias Vollmer, Stefan Fischer, Karolina Z. Milowska, Ramon García Cortadella, Bert Nickel, Carlos Cardenas-Daw, Jacek K. Stolarczyk, Alexander S. Urban, and Jochen Feldmann. Quantum Size Effect in Organometal Halide Perovskite Nanoplatelets. *Nano Letters*, 15(10):6521–6527, 2015.

[62] Quinten A. Akkerman, Silvia Genaro Motti, Ajay Ram Srimath Kandada, Edoardo Mosconi, Valerio D'Innocenzo, Giovanni Bertoni, Sergio Marras, Brett A. Kamino, Laura Miranda, Filippo De Angelis, Annamaria Petrozza, Mirko Prato, and Liberato Manna. Solution Synthesis Approach to Colloidal Cesium Lead Halide Perovskite Nanoplatelets with Monolayer-Level Thickness Control. *Journal of the American Chemical Society*, 138(3):1010–1016, 2016.

[63] Muhammad Imran, Francesco Di Stasio, Zhiya Dang, Claudio Canale, Ali Hossain Khan, Javad Shamsi, Rosaria Brescia, Mirko Prato, and Liberato Manna. Colloidal Synthesis of Strongly Fluorescent CsPbBr3 Nanowires with Width Tunable down to the Quantum Confinement Regime. *Chemistry of Materials*, 28(18):6450–6454, 2016.

[64] Javad Shamsi, Zhiya Dang, Paolo Bianchini, Claudio Canale, Francesco Di Stasio, Rosaria Brescia, Mirko Prato, Liberato Manna, Francesco Di Stasio, Rosaria Brescia, Mirko Prato, and Liberato Manna. Colloidal Synthesis of Quantum Confined Single Crystal $CsPbBr_3$ nanosheets with Lateral Size Control up to the micrometer Range. *Journal of the American Chemical Society*, 138(23):jacs.6b03166, 2016.

[65] Dandan Zhang, Samuel W. Eaton, Yi Yu, Letian Dou, and Peidong Yang. Solution-Phase Synthesis of Cesium Lead Halide Perovskite Nanowires. *Journal of the American Chemical Society*, 137(29):9230–9233, 2015.

[66] Yehonadav Bekenstein, Brent A. Koscher, Samuel W. Eaton, Peidong Yang, and A. Paul Alivisatos. Highly Luminescent Colloidal Nanoplates of Perovskite Cesium Lead Halide and Their Oriented Assemblies. *Journal of the American Chemical Society*, 137(51):16008–16011, 2015.

[67] Patrick Cottingham and Richard L. Brutchey. On the Crystal Structure of Colloidally Prepared $CsPbBr_3$ Quantum Dots. *Chem. Commun.*, pages 3–6, 2016.

[68] Abhishek Swarnkar, Ramya Chulliyil, Vikash Kumar Ravi, Mir Irfanullah, Arindam Chowdhury, and Angshuman Nag. Colloidal $CsPbBr_3$ Perovskite Nanocrystals: Luminescence beyond Traditional Quantum Dots. *Angewandte Chemie - International Edition*, 54(51):15424–15428, 2015.

[69] Yi Yu, Dandan Zhang, Christian Kisielowski, Letian Dou, Nikolay Kornienko, Yehonadav Bekenstein, Andrew B. Wong, A. Paul Alivisatos, and Peidong Yang. Atomic Resolution Imaging of Halide Perovskites. *Nano Letters*, 16(12):7530–7535, 2016.

[70] Grzegorz Gabka, Piotr Bujak, Jan Żukrowski, Damian Zabost, Kamil Kotwica, Karolina Malinowska, Andrzej Ostrowski, Ireneusz Wielgus, Wojciech Lisowski, Janusz W. Sobczak, Marek Przybylski, and Adam Pron. Non-injection synthesis of monodisperse Cu-Fe-S nanocrystals and their size dependent properties. *Phys. Chem. Chem. Phys.*, 18(22):15091–15101, 2016.

[71] Sandeep Ghosh, Tommaso Avellini, Alessia Petrelli, Ilka Kriegel, Roberto Gaspari, Guilherme Almeida, Giovanni Bertoni, Andrea Cavalli, Francesco Scotognella, Teresa Pellegrino, and Liberato Manna. Colloidal $CuFeS_2$ nanocrystals: Intermediate Fe d-band leads to high photothermal conversion efficiency. *Chemistry of Materials*, 28(13):4848–4858, 2016.

[72] M. Knoll and E. Ruska. The electron microscope. *Zeitschrift für Physik*, 79(9-10):699, 1932.

[73] Rolf Erni, Marta D. Rossell, Christian Kisielowski, and Ulrich Dahmen. Atomic-resolution imaging with a sub-50-pm electron probe. *Physical Review Letters*, 102(9), 2009.

[74] David B. Williams and C. Barry Carter. *Transmission Electron Microscopy A Textbook for Material Science*. Springer, 2009.

[75] Manfred von Ardenne. Das Elektronen-Rastermikroskop - Theoretische Grundlagen. *Zeitschrift für Physik*, 109(9-10):553–572, 1938.

[76] A. V. Crewe. Scanning electron microscopes: is high resolution possible? *Science*, 154(3750):729–38, 1966.

[77] A. V. Crewe, J. Wall, and J. Langmore. Visibility of Single Atoms. *Science*, 168(3937):1338–1340, 1970.

[78] M. M. J. Treacy, A Howie, and C. J. Wilson. Z contrast of platinum and palladium catalysts. *Philosophical Magazine A*, 38(5):569–585, 1978.

[79] S. J. Pennycook and D. E. Jesson. High-resolution incoherent imaging of crystals. *Physical Review Letters*, 64(8):938–941, 1990.

[80] P E Batson, N Dellby, and O L Krivanek. Sub-angstrom resolution using aberration corrected electron optics. *Nature*, 418(6898):617–620, 2002.

[81] P. D. Nellist. Direct Sub-Angstrom Imaging of a Crystal Lattice. *Science*, 305(5691):1741–1741, 2004.

[82] Thomas Altantzis. *Three-Dimensional Characterization of Atomic Clusters, Nanoparticles and their Assemblies by Advanced Transmission Electron Microscopy*. PhD thesis, Antwerp, 2015.

[83] J. M. Cowley and A. F. Moodie. The scattering of electrons by atoms and crystals. I. A new theoretical approach. *Acta Crystallographica*, 10(10):609–619, 1957.

[84] K. Ishizuka and N. Uyeda. A new theoretical and practical approach to the multislice method. *Acta Crystallographica Section A*, 33(5):740–749, 1977.

[85] EJ Kirkland. *Advanced computing in electron microscopy*. Springer, 2010.

[86] G Cliff and G W Lorimer. The quantitative analysis of thin specimens. *Journal of Microscopy*, 103(2):203–207, 1975.

[87] M Watanabe, M Kanno, and E Okunishi. Atomic-Resolution Elemental Mapping by EELS and XEDS in Aberration Corrected STEM. *JEOL News*, 45(1):8–15, 2010.

[88] J I Goldstein and D B Williams. X-ray analysis in the TEM/STEM. *Scanning Electron Microscopy*, I:651–662, 1977.

[89] M. Watanabe and D. B. Williams. The quantitative analysis of thin specimens: A review of progress from the Cliff-Lorimer to the new zeta-factor methods. *Journal of Microscopy*, 221(2):89–109, 2006.

[90] Peter Schlossmacher, Dmitri O. Klenov, Bert Freitag, Sebastian Von Harrach, and Andy Steinbach. Nanoscale Chemical Compositional Analysis with an Innovative S/TEM-EDX System. *Microscopy and Analysis Nanotechnology Supplement*, 24:S5–S8, 2010.

[91] E. F. Rauch and M. Véron. Automated crystal orientation and phase mapping in TEM. *Materials Characterization*, 98:1–9, 2014.

[92] R. Vincent and P. A. Midgley. Double conical beam-rocking system for measurement of integrated electron diffraction intensities. *Ultramicroscopy*, 53(3):271–282, 1994.

[93] Jean Luc Rouviere, Armand Béché, Yannick Martin, Thibaud Denneulin, and David Cooper. Improved strain precision with high spatial resolution using nanobeam precession electron diffraction. *Applied Physics Letters*, 103(24), 2013.

[94] T.A. White, A.S. Eggeman, and P.A. Midgley. Is precession electron diffraction kinematical? Part I:. *Ultramicroscopy*, 110(7):763–770, 2010.

[95] Benedikt Haas. *Development of Quantitative Diffraction and Imaging Based Techniques for Scanning Transmission Electron Microscopy*. PhD thesis, Université Grenoble Alpes, 2017.

[96] Niels de Jonge and Frances M. Ross. Electron microscopy of specimens in liquid. *Nature Nanotechnology*, 6(11):695–704, 2011.

[97] Jong Min Yuk, Jungwon Park, Peter Ercius, Kwanpyo Kim, Daniel J Hellebusch, Michael F Crommie, Jeong Yong Lee, a Zettl, and a Paul Alivisatos. High-resolution EM of colloidal nanocrystal growth using graphene liquid cells. *Science*, 336(6077):61–4, apr 2012.

[98] Jeanne Ayache, Luc Beaunier, Jacqueline Boumendil, Gabrielle Ehret, and Danièle Laub. *Sample Preparation Handbook for Transmission Electron Microscopy methodology*. Springer, 2010.

[99] Emilie Klecha, Dorothée Ingert, and Marie P. Pileni. How the level of ordering of 2D nanocrystal superlattices is controlled by their deposition mode. *Journal of Physical Chemistry Letters*, 1(10):1616–1622, 2010.

[100] Matteo Cargnello, Vicky V. T. Doan-Nguyen, Thomas R. Gordon, Rosa E. Diaz, Eric a. Stach, Raymond J. Gorte, Paolo Fornasiero, and Christopher B. Murray. Control of Metal Nanocrystal Size Reveals Metal-Support Interface Role for Ceria Catalysts. *Science*, 341(6147):771–3, 2013.

[101] R F Egerton, P Li, and M Malac. Radiation damage in the TEM and SEM. *Micron*, 35(6):399–409, jan 2004.

[102] D R G Mitchell. Contamination mitigation strategies for scanning transmission electron microscopy. *Micron*, 73(2015):36–46, 2015.

[103] Luiz H. G. Tizei, Yung-Chang Lin, Ang-Yu Lu, Lain-Jong Li, and Kazu Suenaga. Electron energy loss spectroscopy of excitons in two-dimensional-semiconductors as a function of temperature. *Applied Physics Letters*, 108(16):163107, 2016.

[104] Johannes Schindelin, Ignacio Arganda-Carreras, Erwin Frise, Verena Kaynig, Mark Longair, Tobias Pietzsch, Stephan Preibisch, Curtis Rueden, Stephan Saalfeld, Benjamin Schmid, Jean-Yves Tinevez, Daniel James White, Volker Hartenstein, Kevin Eliceiri, Pavel Tomancak, and Albert Cardona. Fiji: an open-source platform for biological-image analysis. *Nature methods*, 9(7):676–82, 2012.

[105] Zhifeng Ren, Yucheng Lan, Hui Wang, Dezhi Wang, and Gang Chen. Grids for applications in high-temperature high-resolution transmission electron microscopy. *Journal of Nanotechnology*, 2010.

[106] A K Geim and K.S. Novoselov. The rise of graphene. *Nature Mater.*, 6(3):183–191, 2007.

[107] David M. Larson, Kenneth H. Downing, and Robert M. Glaeser. The surface of evaporated carbon films is an insulating, high-bandgap material. *Journal of Structural Biology*, 174(2):420–423, 2011.

[108] Jannik C. Meyer, Franz Eder, Simon Kurasch, Viera Skakalova, Jani Kotakoski, Hye Jin Park, Siegmar Roth, Andrey Chuvilin, Sören Eyhusen, Gerd Benner, Arkady V. Krasheninnikov, and Ute Kaiser. Accurate measurement of electron beam induced displacement cross sections for single-layer graphene. *Physical Review Letters*, 108(19), 2012.

[109] U Kaiser, J Biskupek, J C Meyer, J Leschner, L Lechner, H Rose, M Stöger-Pollach, A N Khlobystov, P Hartel, H Müller, M Haider, S Eyhusen, and G Benner. Transmission electron microscopy at 20 kV for imaging and spectroscopy. *Ultramicroscopy*, 111(8):1239–46, 2011.

[110] Radosav S. Pantelic, Jannik C. Meyer, Ute Kaiser, and Henning Stahlberg. The application of graphene as a sample support in transmission electron microscopy. *Solid State Communications*, 152(15):1375–1382, 2012.

[111] Matthew G. Panthani, Colin M. Hessel, Dariya Reid, Gilberto Casillas, Miguel José-Yacamán, and Brian A. Korgel. Graphene-supported high-resolution TEM and STEM imaging of silicon nanocrystals and their capping ligands. *Journal of Physical Chemistry C*, 116(42):22463–22468, 2012.

[112] Matteo Cargnello, Chen Chen, Benjamin T. Diroll, Vicky V. T. Doan-Nguyen, Raymond J. Gorte, and Christopher B. Murray. Efficient removal of organic ligands from supported nanocrystals by fast thermal annealing enables catalytic studies on well-defined active phases. *Journal of the American Chemical Society*, 137(21):6906–6911, 2015.

[113] Tugce Akdas, Monica Distaso, Susanne Kuhri, Benjamin Winter, Balaji Birajdar, Erdmann Spiecker, Dirk M. Guldi, and Wolfgang Peukert. The effects of post-processing on the surface and the optical properties of copper indium sulfide quantum dots. *Journal of Colloid and Interface Science*, 445:337–347, 2015.

[114] J. Seo, S. J. Kim, W. J. Kim, R. Singh, M. Samoc, A. N. Cartwright, and P. N. Prasad. Enhancement of the photovoltaic performance in PbS nanocrystal:P3HT hybrid composite devices by post-treatment-driven ligand exchange. *Nanotechnology*, 20:095202, 2009.

[115] Qijie Guo, Hugh W Hillhouse, and Rakesh Agrawal. Synthesis of Cu_2ZnSnS_4 Nanocrystal Ink and Its Use for Solar Cells. pages 11672–11673, 2009.

[116] Shannon C. Riha, Bruce A. Parkinson, and Amy L. Prieto. Solution-Based Synthesis and Characterization of Cu_2ZnSnS_4 Nanocrystals. *Journal of the American Chemical Society*, 131(34):12054–12055, 2009.

[117] Chet Steinhagen, Matthew G Panthani, Vahid Akhavan, Brian Goodfellow, Bonil Koo, and Brian a Korgel. Synthesis of Cu_2ZnSnS_4 nanocrystals for use in low-cost photovoltaics. *Journal of the American Chemical Society*, 131(35):12554–5, sep 2009.

[118] Michelle D Regulacio, Chen Ye, Suo Hon Lim, Michel Bosman, Enyi Ye, Shiyou Chen, Qing-Hua Xu, and Ming-Yong Han. Colloidal nanocrystals of wurtzite-type Cu_2ZnSnS_4: facile noninjection synthesis and formation mechanism. *Chemistry (Weinheim an der Bergstrasse, Germany)*, 18(11):3127–31, mar 2012.

[119] Wei-chang Chang Yang, Caleb K. Miskin, Nathaniel J. Carter, Rakesh Agrawal, Eric A. Stach, A Stach, and Eric A. Stach. Compositional inhomogeneity of multinary semiconductor nanoparticles: A case study of Cu_2ZnSnS_4. *Chemistry of Materials*, 26(24):6955–6962, 2014.

[120] Kaiwen Sun, Chang Yan, Fangyang Liu, Jialiang Huang, Fangzhou Zhou, John A. Stride, Martin Green, and Xiaojing Hao. Over 9% Efficient Kesterite Cu_2ZnSnS_4 Solar Cell Fabricated by Using Zn1–xCdxS Buffer Layer. *Advanced Energy Materials*, 6(12):4–9, 2016.

[121] Mei Li, Wen-Hui Zhou, Jie Guo, Yan-Li Zhou, Ze-Liang Hou, Jie Jiao, Zheng-Ji Zhou, Zu-Liang Du, and Si-Xin Wu. Synthesis of Pure Metastable Wurtzite CZTS Nanocrystals by Facile One-Pot Method. *JOURNAL OF PHYSICAL CHEMISTRY C*, 116:26507–26516, 2012.

[122] Joel Ming Rui Tan, Yih Hong Lee, Srikanth Pedireddy, Tom Baikie, Xing Yi Ling, and Lydia Helena Wong. Understanding the synthetic pathway of a single-phase quarternary semiconductor using surface-enhanced Raman scattering: A case of wurtzite Cu_2ZnSnS_4 nanoparticles. *Journal of the American Chemical Society*, 136(18):6684–6692, 2014.

[123] Christopher a Cattley, Cheng Cheng, Simon M Fairclough, Laura M Droessler, Neil P Young, Jamie H Warner, Jason M Smith, Hazel E Assender, and Andrew a R Watt. Low temperature phase selective synthesis of Cu_2ZnSnS_4 quantum dots. *Chemical communications*, 49(36):3745–7, may 2013.

[124] Ajay Singh, Hugh Geaney, Fathima Laffir, and Kevin M Ryan. Colloidal synthesis of wurtzite Cu_2ZnSnS_4 nanorods and their perpendicular assembly. *Journal of the American Chemical Society*, 134(6):2910–3, feb 2012.

[125] Claudia Coughlan and Kevin M. Ryan. Complete study of the composition and shape evolution in the synthesis of Cu_2ZnSnS_4 (CZTS) semiconductor nanocrystals. *CrystEngComm*, 17(36):6914–6922, 2015.

[126] Haoran Yang, Luis A. Jauregui, Genqiang Zhang, Yong P. Chen, and Yue Wu. Nontoxic and abundant copper zinc tin sulfide nanocrystals for potential high-temperature thermoelectric energy harvesting. *Nano Letters*, 12(2):540–545, 2012.

[127] Alexey Shavel, Doris Cadavid, Maria Ibáñez, Alex Carrete, and Andreu Cabot. Continuous production of Cu_2ZnSnS_4 nanocrystals in a flow reactor. *Journal of the American Chemical Society*, 134(3):1438–1441, 2012.

[128] Jordan W. Thomson, Kaz Nagashima, Peter M. MacDonald, and Geoffrey A. Ozin. From sulfur-amine solutions to metal sulfide nanocrystals: Peering into the oleylamine-sulfur black box. *Journal of the American Chemical Society*, 133(13):5036–5041, 2011.

[129] Chao Zou, Lijie Zhang, Deshang Lin, Yun Yang, Qiang Li, Xiangju Xu, Xi'an Chen, and Shaoming Huang. Facile synthesis of Cu_2ZnSnS_4 nanocrystals. *CrystEngComm*, 13(10):3310, 2011.

[130] Xiaotang Lu, Zhongbin Zhuang, Qing Peng, and Yadong Li. Wurtzite Cu_2ZnSnS_4 nanocrystals: a novel quaternary semiconductor. *Chemical communications*, 47(11):3141–3, mar 2011.

[131] Hsueh-Chung Liao, Meng-Huan Jao, Jing-Jong Shyue, Yang-Fang Chen, and Wei-Fang Su. Facile synthesis of wurtzite copper–zinc–tin sulfide nanocrystals from plasmonic djurleite nuclei. *J. Mater. Chem. A*, 1(2):337–341, 2013.

[132] Joel van Embden, Anthony S. R. Chesman, and Jacek J. Jasieniak. The Heat-Up Synthesis of Colloidal Nanocrystals. *Chemistry of Materials*, page 150220215346007, 2015.

[133] Sigma Aldrich. Oleylamine data sheet.

[134] Stefanos Mourdikoudis and Luis M Liz-Marzan. Oleylamine in Nanoparticle Synthesis. *Chemistry of Materials*, 2013.

[135] Wernfried Haas, Thomas Rath, Andreas Pein, Johannes Rattenberger, Gregor Trimmel, and Ferdinand Hofer. The stoichiometry of single nanoparticles of copper zinc tin selenide. *Chemical communications*, 47(7):2050–2, feb 2011.

[136] Aurélie Lefrançois. *Synthèse de nanocristaux de type Chalcopyrite en vue d'applications en cellules solaires*. PhD thesis, Université Joseph Fourier, 2014.

[137] Claudia Coughlan, Ajay Singh, and Kevin M Ryan. Systematic Study into the Synthesis and Shape Development in Colloidal $CuIn_xGa_{1-x}S_2$ Nanocrystals. *Chemistry of Materials*, pages 653–661, 2013.

[138] Andrew D. Collord and Hugh W. Hillhouse. Composition control and formation pathway of CZTS and CZTGS nanocrystal inks for kesterite solar cells. *Chemistry of Materials*, 27(5):1855–1862, 2015.

[139] Budhika G. Mendis, Mervyn D. Shannon, Max Cj Goodman, Jon D. Major, Richard Claridge, Douglas P. Halliday, and Ken Durose. Direct observation of Cu, Zn cation disorder in Cu_2ZnSnS_4 solar cell absorber material using aberration corrected scanning transmission electron microscopy. *Progress in Photovoltaics: Research and Applications*, 22:24–34, 2014.

[140] Nessrin Kattan, Bo Hou, David J. Fermín, and David Cherns. Crystal structure and defects visualization of Cu_2ZnSnS_4 nanoparticles employing transmission electron microscopy and electron diffraction. *Applied Materials Today*, 1(1):52–59, 2015.

[141] N. A. Kattan, I. J. Griffiths, D. Cherns, and D. J. Fermín. Observation of anti-site domain boundaries in Cu_2ZnSnS_4 by atomic-resolution transmission electron microscopy. *Nanoscale*, 8(30):14369–14373, 2016.

[142] Reza R Zamani, Maria Ibáñez, Martina Luysberg, Nuria García-Castelló, Lothar Houben, Joan Daniel Prades, Vincenzo Grillo, Rafal E Dunin-Borkowski, Joan Ramón Morante, Andreu Cabot, and Jordi Arbiol. Polarity-Driven Polytypic Branching in Cu-Based Quaternary Chalcogenide Nanostructures. *ACS nano*, 8(3):2290–2301, 2014.

[143] Lewys Jones, Hao Yang, Timothy J. Pennycook, Matthew S. J. Marshall, Sandra Van Aert, Nigel D. Browning, Martin R. Castell, and Peter D. Nellist. Smart Align—a new tool for robust non-rigid registration of scanning microscope data. *Advanced Structural and Chemical Imaging*, 1(1):8, 2015.

[144] R. McLeod, J. Kowal, P. Ringler, and H. Stahlberg. Robust image alignment for cryogenic transmission electron microscopy. *Journal of Structural Biology*, 197, 2017.

[145] Xiahan Sang and James M. LeBeau. Revolving scanning transmission electron microscopy: Correcting sample drift distortion without prior knowledge. *Ultramicroscopy*, 138:28–35, 2014.

[146] Martin Hytch, Jean-Luc Putaux, and Jean-Michel Penisson. Measurement of the displacement field of dislocations to 0.03 Å by electron microscopy. *Nature*, 423(May):270–273, 2003.

[147] Jian-Min Zuo, Amish B Shah, Honggyu Kim, Yifei Meng, Wenpei Gao, and Jean-Luc Rouviére. Lattice and strain analysis of atomic resolution Z-contrast images based on template matching. *Ultramicroscopy*, 136:50–60, 2014.

[148] Benedikt Haas, Robert A. McLeod, Thomas Auzelle, Bruno Daudin, Joël Eymery, Frédéric Lançon, Jian-Min Zuo, and Jean-Luc Rouvière. Picometre-precision atomic structure of inversion domain boundaries in GaN. *The 16th European Microscopy Congress, Lyon, France*, 2016.

[149] A. Ritscher, A. Franz, S. Schorr, and M. Lerch. Off-stoichiometric CZTS: Neutron scattering investigations on mechanochemically synthesized powders. *Journal of Alloys and Compounds*, 689:271–277, 2016.

[150] Laura Elisa Valle Rios, Kai Neldner, Galina Gurieva, and Susan Schorr. Existence of off-stoichiometric single phase kesterite. *Journal of Alloys and Compounds*, 657:408–413, 2016.

[151] Georgian Nedelcu, Loredana Protesescu, Sergii Yakunin, Maryna I. Bodnarchuk, Matthias J. Grotevent, and Maksym V. Kovalenko. Fast Anion-Exchange in Highly Luminescent Nanocrystals of Cesium Lead Halide Perovskites $CsPbX_3$, X = Cl, Br, I. *Nano Letters*, 15(8):5635–5640, 2015.

[152] A. M. Glazer. The classification of tilted octahedra in perovskites. *Acta Crystallographica Section B Structural Crystallography and Crystal Chemistry*, 28(11):3384–3392, 1972.

[153] Kyosuke Kishida, Kengo Goto, and Haruyuki Inui. Electron diffraction of ABX3 perovskites with both layered ordering of A cations and tilting of BX6 octahedra. *Acta Crystallographica Section B: Structural Science*, 65(4):405–415, 2009.

[154] S. Bernal, F. J. Botana, J. J. Calvino, C. Lòpez-Cartes, J. A. Pérez-Omil, and J. M. Rodrìguez-Izquierdo. The interpretation of HREM images of supported metal catalysts using image simulation: profile view images. *Ultramicroscopy*, 72(3-4):135–164, 1998.

[155] D. M. Trots, S. V. Myagkota, and A. S. Voloshinovskii. Crystal structure and thermal expansion of $CsPbBr_3$ in the range of 12-300 K. Technical report, Desy Annual Report, 2009.

[156] Zhiya Dang, Rosaria Brescia, Q. A. Akkerman, J. Shamsi, M Prato, and L. Manna. High-resolution tem study of colloidal cesium lead bromide nanocrystals. In *EMC 2016*, 2016.

[157] Mingzhi Zhang, Zhiping Zheng, Qiuyun Fu, Zheng Chen, Jianle He, sen Zhang, Liang Yan, Yunxiang Hu, and Wei Luo. Growth and characterization of the all-inorganic lead halide perovskite semiconductor $CsPbBr_3$ single crystals. *CrystEngComm*, 2017.

[158] Federica Bertolotti, Loredana Protesescu, Maksym V. Kovalenko, Sergii Yakunin, Antonio Cervellino, Simon J.L. Billinge, Maxwell W. Terban, Jan Skov Pedersen, Norberto Masciocchi, and Antonietta Guagliardi. Coherent Nanotwins and Dynamic Disorder in Cesium Lead Halide Perovskite Nanocrystals. *ACS Nano*, 11(4):3819–3831, 2017.

[159] M. Brennan, Masaru Kuno, and S. Rouvimov. TEM Analysis of CsPbBr3 Nanocrystals: Challenges and Perspectives. *Microscopy and Microanalysis*, 23(S1):2096–2097, 2017.

[160] Melody G. Campbell, Anchi Cheng, Axel F. Brilot, Arne Moeller, Dmitry Lyumkis, David Veesler, Junhua Pan, Stephen C. Harrison, Clinton S. Potter, Bridget Carragher, and Nikolaus Grigorieff. Movies of ice-embedded particles enhance resolution in electron cryo-microscopy. *Structure*, 20(11):1823–1828, 2012.

[161] Bernhard Schaffer, Werner Grogger, and Gerald Kothleitner. Automated spatial drift correction for EFTEM image series. *Ultramicroscopy*, 102(1):27–36, 2004.

[162] M. Klinger. More features, more tools, more CrysTBox. *Journal of Applied Crystallography*, 50, 2017.

[163] J M Zuo, I Vartanyants, M Gao, R Zhang, and L a Nagahara. Atomic resolution imaging of a carbon nanotube from diffraction intensities. *Science*, 300(5624):1419–21, may 2003.

[164] Zhiya Dang, Javad Shamsi, Francisco Palazon, Muhammad Imran, Quinten A. Akkerman, Sungwook Park, Giovanni Bertoni, Mirko Prato, Rosaria Brescia, and Liberato Manna. In Situ Transmission Electron Microscopy Study of Electron Beam-Induced Transformations in Colloidal Cesium Lead Halide Perovskite Nanocrystals. *ACS Nano*, 11(2):2124–2132, 2017.

[165] Zhiya Dang, Javad Shamsi, Quinten A. Akkerman, Muhammad Imran, Giovanni Bertoni, Rosaria Brescia, and Liberato Manna. Low-Temperature Electron Beam-Induced Transformations of Cesium Lead Halide Perovskite Nanocrystals. *ACS Omega*, 2(9):5660–5665, 2017.

[166] Younan Xia, Yujie Xiong, Byungkwon Lim, and Sara E. Skrabalak. Shape-controlled synthesis of metal nanocrystals: Simple chemistry meets complex physics? *Angewandte Chemie - International Edition*, 48(1):60–103, 2009.

[167] Taylor J Woehl, James E Evans, Ilke Arslan, William D Ristenpart, and Nigel D Browning. Direct in situ determination of the mechanisms controlling nanoparticle nucleation and growth. *ACS nano*, 6(10):8599–610, oct 2012.

[168] Tao Li, Andrew J. Senesi, and Byeongdu Lee. Small Angle X-ray Scattering for Nanoparticle Research. *Chemical Reviews*, 116(18):11128–11180, 2016.

[169] Benjamin Abécassis, Fabienne Testard, Olivier Spalla, and Philippe Barboux. Probing in situ the nucleation and growth of gold nanoparticles by small-angle X-ray scattering. *Nano Lett.*, 7(6):1723–1727, 2007.

[170] Z. H. Sun, H. Oyanagi, M. Uehara, H. Nakamura, K. Yamashita, A. Fukano, and H. Maeda. Study on initial kinetics of CdSe nanocrystals by a combination of in situ X-ray absorption fine structure and microfluidic reactor. *Journal of Physical Chemistry C*, 113(43):18608–18613, 2009.

[171] D. J. Chadi. Atomic and electronic structures of reconstructed Si(100) surfaces. *Physical Review Letters*, 43(1):43–47, 1979.

[172] P E Laibinis, G M Whitesides, D L Allara, Y.-T. Tao, A N Parikh, and R G Nuzzo. Comparison of the Structures and Wetting Properties of Self-Assembled Monolayers of Normal-Alkanethiols on the Coinage Metal-Surfaces, Cu, Ag, Au. *Journal Of The American Chemical Society*, 113(19):7152–7167, 1991.

[173] Yadong Yin and a Paul Alivisatos. Colloidal nanocrystal synthesis and the organic-inorganic interface. *Nature*, 437(7059):664–670, 2005.

[174] Maksym V. Kovalenko, Marcus Scheele, and Dmitri V. Talapin. Colloidal Nanocrystals with Molecular Metal Chalcogenide Surface Ligands. *Science*, 324(5933):1417–1420, 2009.

[175] Angshuman Nag, Maksym V. Kovalenko, Jong Soo Lee, Wenyong Liu, Boris Spokoyny, and Dmitri V. Talapin. Metal-free Inorganic Ligands for Colloidal Nanocrystals: S^{2-}, HS^{-}, Se^{2-}, HSe^{-}, Te^{2-}, HTe^{-}, $TeS_3{}^{2-}$, OH^{-}, and NH^{2-} as Surface Ligands. *Journal of the American Chemical Society*, 133(27):10612–10620, 2011.

[176] Anna Llordés, Guillermo Garcia, Jaume Gazquez, and Delia J Milliron. Tunable near-infrared and visible-light transmittance in nanocrystal-in-glass composites. *Nature*, 500:323–327, 2013.

[177] Teresa Pellegrino, Liberato Manna, Stefan Kudera, Tim Liedl, Dmitry Koktysh, Andrey L. Rogach, Simon Keller, Joachim Rädler, Giovanni Natile, and Wolfgang J. Parak. Hydrophobic nanocrystals coated with an amphiphilic polymer shell: A general route to water soluble nanocrystals. *Nano Letters*, 4(4):703–707, 2004.

[178] Danylo Zherebetskyy, Marcus Scheele, Yingjie Zhang, Noah Bronstein, Christopher Thompson, David Britt, Miquel Salmeron, Paul Alivisatos, and Lin-Wang Wang. Hydroxylation of the surface of PbS nanocrystals passivated with oleic acid. *Science*, 344(6190):1380–4, 2014.

[179] S Ithurria, M D Tessier, B Mahler, R P S M Lobo, B Dubertret, and Al L Efros. Colloidal nanoplatelets with two-dimensional electronic structure. *Nature materials*, 10(12):936–41, 2011.

[180] Xiaogang Peng, Liberato Manna, Weidong Yang, Juanita Wickham, Erik Scher, Andreas Kadavanich, and A P Alivisatos. Shape control of CdSe nanocrystals. *Nature*, 404(6773):59–61, 2000.

[181] R Nuzzo, B Zegarski, and L Dubois. Fundamental studies of the chemisorption of organosulfur compounds on gold (111). Implications for molecular self-assembly on gold surfaces. *Journal Of The American Chemical Society*, 1987.

[182] L H Dubois and R G Nuzzo. Synthesis, Structure, and Properties of Model Organic Surfaces. *Annual Review of Physical Chemistry*, 43(1):437–463, 1992.

[183] Michael J Hostetler, Jennifer J Stokes, and Royce W Murray. Infrared Spectroscopy of Three-Dimensional Self-Assembled Monolayers: a N-Alkanethiolate Monolayers on Gold Cluster Compounds. *Langmuir*, 12(15):3604–3612, 1996.

[184] Antonella Badia, Louis Cuccia, Linette Demers, Fred Morin, and R. Bruce Lennox. Structure and dynamics in alkanethiolate monolayers self-assembled on gold nanoparticles: A DSC, FT-IR, and deuterium NMR study. *Journal of the American Chemical Society*, 119(11):2682–2692, 1997.

[185] Loredana Protesescu, Maarten Nachtegaal, Oleksandr Voznyy, Olga Borovinskaya, Aaron J. Rossini, Lyndon Emsley, Christophe Copéret, Detlef Gunther, Edward H. Sargent, and Maksym V. Kovalenko. Atomistic description of thiostannate-capped CdSe nanocrystals: Retention of four-coordinate SnS_4 motif and preservation of Cd-rich stoichiometry. *Journal of the American Chemical Society*, 137(5):1862–1874, 2015.

[186] Zeger Hens and José C. Martins. A solution NMR toolbox for characterizing the surface chemistry of colloidal nanocrystals. *Chemistry of Materials*, 25(8):1211–1221, 2013.

[187] Bernd Fritzinger, Richard K. Capek, Karel Lambert, José C. Martins, and Zeger Hens. Utilizing self-exchange to address the binding of carboxylic acid ligands to CdSe quantum dots. *Journal of the American Chemical Society*, 132(29):10195–10201, 2010.

[188] Christopher B. Murray, Cherie R Kagan, and Moungi G Bawendi. Synthesis and characterization of monodisperse nanocrystals and close packed nanocrystal assembles. *Annual review of materials science*, 30:545–610, 2000.

[189] Hedi Mattoussi, Andrew Cumming, Christopher Murray, Moungi Bawendi, and Raymond Ober. Properties of CdSe nanocrystal dispersions in the dilute regime: Structure and interparticle interactions. *Physical Review B*, 58(12):7850–7863, 1998.

[190] Philipp Schapotschnikow, Bob Hommersom, and Thijs J H Vlugt. Adsorption and binding of ligands to CdSe nanocrystals. *Journal of Physical Chemistry C*, 113(29):12690–12698, 2009.

[191] Michael A. Boles, Daishun Ling, Taeghwan Hyeon, and Dmitri V. Talapin. The surface science of nanocrystals. *Nature Materials*, 15(2):141–153, 2016.

[192] Alexander H. Ip, Susanna M. Thon, Sjoerd Hoogland, Oleksandr Voznyy, David Zhitomirsky, Ratan Debnath, Larissa Levina, Lisa R. Rollny, Graham H. Carey, Armin Fischer, Kyle W. Kemp, Illan J. Kramer, Zhijun Ning, André J. Labelle, Kang Wei Chou, Aram Amassian, and Edward H. Sargent. Hybrid passivated colloidal quantum dot solids. *Nature Nanotechnology*, 7(9):577–582, 2012.

[193] Nicholas C Anderson, Mark P Hendricks, Joshua J Choi, and Jonathan S Owen. On the Dynamic Stoichiometry of Metal Chalcogenide Nanocrystals: Spectroscopic Studies of Metal Carboxylate Binding and Displacement. *Journal of the American Chemical Society*, 2:11457–11471, 2013.

[194] Patrick R. Brown, Donghun Kim, Richard R. Lunt, Ni Zhao, Moungi G. Bawendi, Jeffrey C. Grossman, and Vladimir Bulović. Energy level modification in lead sulfide quantum dot thin films through ligand exchange. *ACS Nano*, 8(6):5863–5872, 2014.

[195] C.M. Chuang, P. R Brown, V. Bulović, and M.G. Bawendi. Improved performance and stability in quantum dot solar cells through band alignment engineering. *Nature Materials*, 13:796–801, 2014.

[196] Elena V. Shevchenko, Dmitri V. Talapin, Nicholas A. Kotov, Stephen O'Brien, and Christopher B. Murray. Structural diversity in binary nanoparticle superlattices. *Nature*, 439(7072):55–9, 2006.

[197] Jinwook Lee, Vikram C. Sundar, Jason R. Heine, Moungi G. Bawendi, and Klavs F. Jensen. Full color emission from II-VI semiconductor quantum dot-polymer composites. *Advanced Materials*, 12(15):1102–1105, 2000.

[198] Dmitri V. Talapin, Jong Soo Lee, Maksym V. Kovalenko, and Elena V. Shevchenko. Prospects of colloidal nanocrystals for electronic and optoelectronic applications. *Chemical Reviews*, 110(1):389–458, 2010.

[199] Dmitri V. Talapin and Jonathan Steckel. Quantum dot light-emitting devices. *MRS Bulletin*, 38:685–691, 2013.

[200] Dmitri V Talapin and Christopher B Murray. PbSe nanocrystal solids for n- and p-channel thin film field-effect transistors. *Science*, 310(5745):86–9, 2005.

[201] Joseph M. Luther, Matt Law, Song Qing, Craig L. Perkins, Matthew C. Beard, and Arthur J. Nozik. Structural, optical, and electrical properties of self assembled films of PbSe nanocrystals treated with 1,2-ethanedithiol. *ACS Nano*, 2(2):271–280, 2008.

[202] Ji Hyuk Choi, Aaron T. Fafarman, Soong Ju Oh, Dong Kyun Ko, David K. Kim, Benjamin T. Diroll, Shin Muramoto, J. Greg Gillen, Christopher B. Murray, and Cherie R. Kagan. Bandlike transport in strongly coupled and doped quantum dot solids: A route to high-performance thin-film electronics. *Nano Letters*, 12(5):2631–2638, 2012.

[203] Kyungnam Kim, Chang-Soo Han, and Sohee Jeong. Design and synthesis of photostable multi-shell Cd-free nanocrystal quantum dots for LED applications. *Journal of Materials Chemistry*, 22(40):21370, 2012.

[204] Andrew Shabaev, Alexander L. Efros, and Alexei L. Efros. Dark and photoconductivity in ordered array of nanocrystals. *Nano Letters*, 13(11):5454–5461, 2013.

[205] Jiang Tang, Kyle W. Kemp, Sjoerd Hoogland, Kwang S. Jeong, Huan Liu, Larissa Levina, Melissa Furukawa, Xihua Wang, Ratan Debnath, Dongkyu Cha, Kang Wei Chou, Armin Fischer, Aram Amassian, John B. Asbury, and Edward H. Sargent. Colloidal-quantum-dot photovoltaics using atomic-ligand passivation. *Nature Materials*, 10(10):765–771, 2011.

[206] Maksym V. Kovalenko, Richard D. Schaller, Dorota Jarzab, Maria A. Loi, and Dmitri V. Talapin. Inorganically functionalized PbS-CdS colloidal nanocrystals: Integration into amorphous chalcogenide glass and luminescent properties. *Journal of the American Chemical Society*, 134(5):2457–2460, 2012.

[207] Elena V. Shevchenko, Maryna I. Bodnarchuk, Maksym V. Kovalenko, Dmitri V. Talapin, Rachel K. Smith, Shaul Aloni, Wolfgang Heiss, and A. Paul Alivisatos. Gold/iron oxide core/hollow-shell nanoparticles. *Advanced Materials*, 20(22):4323–4329, 2008.

[208] Francisco de la Peña, Tomas Ostasevicius, Vidar Tonaas Fauske, Pierre Burdet, Petras Jokubauskas, Magnus Nord, Eric Prestat, Mike Sarahan, Katherine E. MacArthur, Duncan N. Johnstone, Joshua Taillon, Jan Caron, Tom Furnival, Alberto Eljarrat, Stefano Mazzucco, Vadim Migunov, Thomas Aarholt, Michael Walls, Florian Winkler, Ben Martineau, Gaël Donval, Eric R. Hoglund, Ivo Alxneit, Ida Hjorth, Luiz Fernando Zagonel, Andreas Garmannslund, Christoph Gohlke, Ilya Iyengar, and Huang-Wei Chang. hyperspy/hyperspy: Hyperspy 1.3, May 2017.

[209] Sara Bals, Marianna Casavola, Marijn a van Huis, Sandra Van Aert, K Joost Batenburg, Gustaaf Van Tendeloo, and Daniël Vanmaekelbergh. Three-dimensional atomic imaging of colloidal core-shell nanocrystals. *Nano letters*, 11(8):3420–4, 2011.

[210] Sandra Van Aert, Kees J Batenburg, Marta D Rossell, Rolf Erni, and Gustaaf Van Tendeloo. Three-dimensional atomic imaging of crystalline nanoparticles. *Nature*, 470(7334):374–377, 2011.

[211] M C Scott, Chien-Chun Chen, Matthew Mecklenburg, Chun Zhu, Rui Xu, Peter Ercius, Ulrich Dahmen, B C Regan, and Jianwei Miao. Electron tomography at 2.4 Å resolution. *Nature*, 483(7390):444–7, mar 2012.

[212] Ali Shakouri. Recent Developments in Semiconductor Thermoelectric Physics and Materials. *Annual Review of Materials Research*, 41(1):399–431, 2011.

[213] D M Rowe. Thermoelectrics handbook: macro to nano. *Thermoelectrics Handbook Macro to Nano*, 80(10):1014, 2005.

[214] Ken Ichiro Gondaira. Self-consistent electronic structures of magnetic semiconductors by a discrete variational X calcuation. Chalcopyrite $CuFeS_2$. *Physical Review B*, 24(6):3349–3353, 1981.

[215] Daxin Liang, Ruoshui Ma, Shihui Jiao, Guangsheng Pang, and Shouhua Feng. A facile synthetic approach for copper iron sulfide nanocrystals with enhanced thermoelectric performance. *Nanoscale*, 4(20):6265, 2012.

[216] G Jeffrey Snyder and Eric S Toberer. Complex thermoelectric materials. *Nature materials*, 7(2):105–114, 2008.

[217] Kuan-ting Chen, Chung-Jie Chiang, and Dahtong Ray. Hydrothermal synthesis of chalcopyrite using an environmental friendly chelating agent. *Materials Letters*, 95(0):172–174, 2013.

[218] Yu Hsiang A Wang, Ningzhong Bao, and Arunava Gupta. Shape-controlled synthesis of semiconducting $CuFeS_2$ nanocrystals. *Solid State Sciences*, 12(3):387–390, 2010.

[219] Prashant Kumar, Sitharaman Uma, and Rajamani Nagarajan. Precursor driven one pot synthesis of wurtzite and chalcopyrite $CuFeS_2$. *Chemical communications*, 49(186):7316–8, 2013.

[220] T Rueda, M P Morales, and A Hernando. Ligand Exchange in Gold-Coated FePt Nanoparticles. *IEEE Transactions on Magnetics*, 44(11):2816–2819, 2008.

[221] Xu Liu, Jialiang Huang, Fangzhou Zhou, Fangyang Liu, Kaiwen Sun, Chang Yan, John A. Stride, and Xiaojing Hao. Understanding the Key Factors of Enhancing Phase and Compositional Controllability for 6 % Efficient Pure-Sulfide Cu_2ZnSnS_4 Solar Cells Prepared from Quaternary Wurtzite Nanocrystals. *Chemistry of Materials*, 28(11):3649–3658, 2016.

[222] Xuelian Yu, Alexey Shavel, Xiaoqiang An, Zhishan Luo, Maria Ibáñez, and Andreu Cabot. Cu_2ZnSnS_4-Pt and Cu_2ZnSnS_4-Au Heterostructured Nanoparticles for Photocatalytic Water Splitting and Pollutant Degradation. *Journal of the American Chemical Society*, 136(26):9236–9239, 2014.

[223] Maria Ibáñez, Zhishan Luo, Aziz Genç, Laura Piveteau, Silvia Ortega, Doris Cadavid, Oleksandr Dobrozhan, Yu Liu, Maarten Nachtegaal, Mona Zebarjadi, Jordi Arbiol, Maksym V. Kovalenko, and Andreu Cabot. High-performance thermoelectric nanocomposites from nanocrystal building blocks. *Nature Communications*, 7(May 2015):10766, 2016.

[224] Kostiantyn Kravchyk, Loredana Protesescu, Maryna I. Bodnarchuk, Frank Krumeich, Maksym Yarema, Marc Walter, Christoph Guntlin, and Maksym V. Kovalenko. Monodisperse and inorganically capped Sn and Sn/SnO_2 nanocrystals for high-performance Li-ion battery anodes. *Journal of the American Chemical Society*, 135(11):4199–4202, 2013.

[225] Minglu Liu and Robert Y. Wang. Size-Dependent Melting Behavior of Colloidal In, Sn, and Bi Nanocrystals. *Scientific Reports*, 5:16353, 2015.

Publications and communications

Peer-reviewed articles

1. L. Vaure, Y. Liu, D. Cadavid, **F. Agnese**, D. Aldakov, S. Pouget, A. Cabot, P. Reiss, P. Chenevier, Doping and Surface Effects of $CuFeS_2$ Nanocrystals Used in Thermoelectric Nanocomposites. **ChemNanoMat**. doi:10.1002/cnma.201800188

2. M. Gromova, A. Lefrancois, L. Vaure, **F. Agnese**, D. Aldakov, A. Maurice, D. Djurado, C. Lebrun, A. de Geyer, T. Schulli, S. Pouget, P. Reiss, Growth Mechanism and Surface State of $CuInS_2$ Nanocrystals Synthesized with Dodecanethiol. **J. Am. Chem. Soc.**, 139, 44, 15748-15759, 2017.

3. L. Mattera, S. Bhuckory, K.D. Wegner, X. Qiu, **F. Agnese**, C. Lincheneau, T. Senden, D. Djurado, L.J. Charbonnière, N. Hildebrandt, P. Reiss, Compact quantum dot-antibody conjugates for FRET immunoassays with subnanomolar detection limits. *Nanoscale*, 8:11275-11283, 2016

4. J.K. Molloy, C. Lincheneau, M.M. Karimdjy, **F. Agnese**, L. Mattera, C. Gateau, P. Reiss, D. Imbert, M. Mazzanti, Sensitisation of visible and NIR lanthanide emission by InP/ZnS quantum dots in bi-luminescent hybrids. *Chem.Commun.*, 52:4577-4580, 2016

5. G. Gabka, P. Bujak, M. Gryszel, A. Ostrowski, K. Malinowska, G. Z. Zukowska, **F. Agnese**, A. Pron, P. Reiss Synthesis and surface chemistry of high quality wurtzite and kesterite Cu_2ZnSnS_4 nanocrystals using tin(II) 2-ethylhexanoate as a new tin source. *Chem. Commun.*, 51:12985-12988, 2015

International communications

- **F. Agnese**, A. Lefrançois, S. Pouget, L. Vaure, O. Makrygenni, F. Chandezon, P.Bayle-Guillemaud, H. Okuno, P. Reiss, J.L. Rouviere, Investigating the Nucleation and Growth of Quaternary Cu_2ZnSnS_4 Nanocrystals, *16th European Microscopy Congress*, EMC, Lyon (France), September 2016 (poster)

Summary

The investigations of semiconductor nanocrystals (NCs) led to fascinating scientific results in optoelectronic devices. To fulfil certain requirements, i.e. cheaper costs, higher efficiencies, environmentally friendly components, new methods are explored in solution-processing, band gap and energy level engineering. Particularly, the method of synthesis can alter the optoelectronic properties. Therefore, a better understanding of the complex factors during synthesis will lead to improved performances. Advanced electron microscopy provides a precise way to gather information about morphology, crystal structure and chemical composition of materials with a spatial resolution down to the atomic level. The first part of this thesis deals with the optimisation of the synthesis and sample preparation for high-resolution transmission electron microscopy (HRTEM). The second part deals with the growth mechanism of Cu_2ZnSnS_4 NCs synthesised by a colloidal method. The morphology and stoichiometry of the samples extracted at different time intervals are characterised by HRTEM and electron dispersion X-ray spectroscopy (EDS). Two complementary methods, Nanobeam Precession Electron Diffraction (NPED) and High-Resolution Scanning Transmission Electron Microscopy by High Angle Annular Dark-Field Imaging (HRSTEM-HAADF), provide an in-depth crystal structure characterisation. Moreover, the crystal structure of $CsPbBr_3$ NCs is solved by probing STEM-HAADF simulations. This approach can differentiate cubic and orthorhombic crystal structures, which is otherwise impossible by diffraction techniques. Finally, the influence of synthesis methods on the morphology and crystal structure of $CuFeS_2$ NCs is investigated by HRTEM for thermoelectric applications.

Résumé

Les recherches sur les nanocristaux semiconducteur (NCs) ont conduit à des résultats scientifiques fascinants, spécialement pour l'application en dispositifs optoelectroniques. Afin de répondre à certaines exigences comme des coûts mineurs, des gains d'efficacité, des composants respectueux de l'environnement, etc., des nouvelles méthodes sont explorées : dans les procédés en solution, dans l'ingénierie de bande et des niveaux d'énergie. En particulier, la méthode de synthèse peut influencer les propriétés optoélectroniques. Par conséquent, une meilleure compréhension des facteurs complexes pendant la synthèse entraînera une amélioration des performances. La microscopie électronique avancée fournit un moyen précis de recueillir des informations sur la morphologie, la structure cristalline et la composition chimique des matériaux avec une résolution spatiale au niveau atomique. La première partie de cette thèse traite de la synthèse et de la préparation des échantillons pour la microscopie électronique à transmission en haute résolution (HRTEM). La deuxième partie traite du mécanisme de croissance des NCs Cu_2ZnSnS_4 synthétisés par une méthode colloïdale. La morphologie et la stoechiométrie des intermédiaires de réaction extraits après différents intervalles de temps sont déterminés par HRTEM et analyse dispersive de rayons X en énergie (EDS). Deux méthodes complémentaires, la diffraction par nanofaisceau d'électrons en précession (NPED) et la microscope électronique en transmission par balayage à haute résolution avec imagerie en champ sombre avec détecteur annulaire à grand angle (HRSTEM-HAADF) permettent une profonde caractérisation de la structure cristalline. En outre, la structure cristalline de NCs $CsPbBr_3$ est résolue avec simulations de STEM-HAADF. Cet approche peut différencier entre structures cristallines cubiques et orthorhombiques, impossible avec techniques de diffraction traditionnelles. Enfin, l'influence des méthodes de synthèse sur la morphologie et sur la structure cristalline de NCs $CuFeS_2$ pour applications dans le domaine de la thermoélectricité est analysée par HRTEM.